

## Editorial corner – a personal view

### Is it possible to strengthen rigid polymers by adding low aspect ratio nanofillers?

M. Q. Zhang\*

Materials Science Institute, Sun Yat-sen (Zhongshan) University, 510275 Guangzhou, P. R. China

When polymer nanocomposites emerged over twenty years ago, represented by the application of clay/nylon-6 nanocomposites at Toyota Central R&D Labs, they were considered as revolutionary alternative to microcomposites. As the interface between nanofillers and matrix would constitute large area within the bulk material, properties of polymer nanocomposites were expected to be greatly improved. With growing experience, however, it seems that enhancement of mechanical properties of rigid polymers (which are so named to distinguish them from rubbers and gels) resulting from addition of low aspect ratio nanofillers (e.g., clay, nanoparticles, etc.) is not so easy as people imagine. In general, stiffening characterized by increase of modulus can be acquired due to the inherent rigidity of inorganic nanofillers. Toughening is also possible when nanofillers are capable of highly mobile under applied stress, which leads to greater ability of energy dissipation and hence higher ductility of nanocomposites. The strategy has been evidenced by nanoclay/poly(vinylidene fluoride) or polystyrene (Adv. Mater., DOI: [10.1002/adma.200400984](https://doi.org/10.1002/adma.200400984)), nano-SiO<sub>2</sub>/polypropylene or polystyrene (Adv. Mater., DOI: [10.1002/adma.200602611](https://doi.org/10.1002/adma.200602611)), and carbon nanotubes/polypropylene (J. Mater. Chem., DOI: [10.1039/C1JM14474J](https://doi.org/10.1039/C1JM14474J)). Nevertheless, the reported strengthening effect is far from satisfactory no matter how the composites are prepared. The poor load-bearing capability of the low aspect ratio nanofillers should take the main responsibility.

It is worth noting that the results of our recent exploration indicate that the problem might be hopefully solved (J. Mater. Chem., DOI: [10.1039/C2JM16097H](https://doi.org/10.1039/C2JM16097H)).

We found that when nano-SiO<sub>2</sub> is present in drawn polypropylene, the aligned chains in amorphous regions can be tied by the well distributed nanofillers to share the stress together. Above the critical content of nanoparticles or drawing ratio, the nanoparticles form percolated network throughout the matrix, facilitating stress transfer in the amorphous phases during tensile test. Additionally, the nanoparticles favor microfibrillation of matrix polymer in the late stage of tensile testing (note: the microfibrils are mainly constituted by the crystalline phases). As a result, the high strength covalent bonds of macromolecules in both amorphous and crystalline phases are brought into full play. The matrix acts as the key load-bearer, while nano-SiO<sub>2</sub> gives indispensable assistance. This is different from the mechanism involved in conventional fiber/polymer composites.

Our approach is not a total solution for the aforesaid problem and needs optimization for specific polymers, but it demonstrates the possibility of strengthening rigid linear polymers with low aspect ratio nanofillers. Continuous efforts are needed in this aspect to find out new strengthening mechanism.



Prof. Dr. Ming Qiu Zhang  
Member of International Advisory Board

\*Corresponding author, e-mail: [ceszmq@mail.sysu.edu.cn](mailto:ceszmq@mail.sysu.edu.cn)

© BME-PT

# Effect of homopolymer poly(vinyl acetate) on compatibility and mechanical properties of poly(propylene carbonate)/poly(lactic acid) blends

J. Gao, H. Bai, Q. Zhang, Y. Gao, L. Chen, Q. Fu\*

Department of Polymer Science and Materials, Sichuan University, State Key Laboratory of Polymer Materials Engineering, 610065 Chengdu, P.R. China

Received 18 March 2012; accepted in revised form 17 May 2012

**Abstract.** A small amount of homopolymer poly(vinyl acetate) (PVAc) is used to compatibilize the biodegradable blends of poly(propylene carbonate) (PPC) and poly(lactic acid) (PLA). Scanning electron microscopy (SEM) and differential scanning calorimetry (DSC) results show that PVAc is selectively localized in the PLA phase and at the interface between PPC and PLA phases. As a result, these interface-localized PVAc layers act as not only a compatibilizer to improve the phase dispersion significantly but also a bridge to increase the interfacial adhesion between PPC and PLA phases dramatically. Both of them are believed to be responsible for the enhancement in mechanical properties. This work provides a simple avenue to fabricate eco-friendly PPC/PLA blends with high performance, and in some cases, reducing the demand for petroleum-based plastics such as polypropylene.

**Keywords:** mechanical properties, poly(propylene carbonate), poly(lactic acid), poly(vinyl acetate), compatibility

## 1. Introduction

Recently, much effort has been devoted to developing biodegradable and renewable resource-derived polymers because of the worldwide environment concerns and sustainability issues resulted from petroleum-based polymers. Poly(propylene carbonate) (PPC), derived from carbon dioxide (CO<sub>2</sub>) and propylene oxide, is one such polymer attracting great research attention. The utilization of CO<sub>2</sub> as one of the synthetic monomers can largely reduce the dependence on petroleum resources and the emission of CO<sub>2</sub> contributing to the greenhouse effect [1–4]. Generally, PPC exhibits excellent tensile toughness and transparency. However, its inferior tensile strength and low glass transition temperature ( $T_g$ , around 35°C) are the major drawbacks to prevent it from widely practical applications [5, 6]. Therefore,

melt blending of PPC with various biodegradable polymers, such as poly(3-hydroxybutyrate) (PHB) [7], poly(butylene succinate) (PBS) [8], poly(ethylene-co-vinyl alcohol) (EVOH) [9], and starch [10], has drawn much attention to obtain PPC materials with good biodegradability and improved properties. Poly(lactic acid) (PLA) is another promising biodegradable polymer derived from renewable resources (e.g., corn, wheat, or rice). It exhibits a potential as an effective reinforcing agent for PPC due to its high strength and stiffness [11, 12]. On the other hand, its inherent brittleness can be simultaneously improved by the flexible PPC as a toughening agent [13].

It is well-known that the mechanical properties of a polymer blend are greatly dependent on its phase morphology and interfacial adhesion [14–16]. How-

\*Corresponding author, e-mail: [qiangfu@scu.edu.cn](mailto:qiangfu@scu.edu.cn)

ever, most polymer pairs are incompatible thermodynamically. The coarse phase morphology and poor interfacial adhesion often give rise to unfavorable property combinations in the blends [17]. Although PPC and PLA have been reported to be partially compatible, compatibilization is also required to further improve its phase morphology and then endow the blend with desirable properties [18]. The introduction of well-defined block or graft copolymers into immiscible polymer blends is the most popular compatibilization strategy [19, 20]. Unfortunately, to the best of our knowledge, no commercially available block copolymer can be used as an effective compatibilizer for PPC/PLA blends at this time. Moreover, the *in situ* formation of graft copolymers by reactive blending is often not straightforward. In very limited investigations, another strategy, i.e. adding random copolymer or homopolymer, has been successfully used to improve the compatibilization of incompatible blends [21, 22]. In these cases, the selective localization of compatibilizer at the interface between the blend components is of vital importance to manipulate interface properties. Selective localization of a third component in incompatible binary blends is mainly attributed to the difference in the affinity between the third component and the blend components [23, 24]. Generally, the effective compatibilizer (e.g. well-designed block copolymer) prefers to locate at the phase interface as a result of the similar affinity to each of the matrix components. In previous works, poly(vinyl acetate) (PVAc) has been demonstrated to be compatible with both PPC and PLA [25, 26]. Therefore, in this contribution, a small amount of PVAc (10 wt%) was introduced into PPC/PLA blends. It is expected that PVAc could be mainly located at the phase interface as a compatibilizer to reduce interfacial tension and suppress coalescence of discrete domains, and thus leading to a significant improvement in mechanical performance of the PPC/PLA blends.

## 2. Experimental

### 2.1. Materials

Maleic anhydride end-capped poly (propylene carbonate) (PPC) was supplied by Changchun Institute of Applied Chemistry, Chinese Academy of Science. Its weight-average molecular weight ( $M_w$ ) was  $2.48 \cdot 10^5$  g/mol and  $M_w/M_n$  was 3.2. Poly(lactic acid) (PLA), with  $M_w = 1.59 \cdot 10^5$  g/mol and  $M_w/M_n = 2.75$ , was purchased from Haizheng Biomaterial Co. (Zhejiang, China). The  $M_w$  of poly(vinyl acetate) (PVAc) used in this work was about  $1.7 \cdot 10^5$  g/mol, and was provided by Acros organics USA. The chemical structures of PPC, PLA and PVAc are given in Figure 1.

### 2.2. Preparation of blends

PPC/PLA blends with and without PVAc were prepared by direct melt compounding in a HAAKE torque rheometer (Thermo Fisher Scientific, USA) at 50 rpm for 7 min. And the temperature was set at 150°C, which ensured that PPC and PVAc will not decompose. The content of PVAc was set as 10 wt% in the ternary blends. Specimens for tensile and dynamic mechanical measurements were compression molded at 150°C under a pressure of 10 MPa and then cut into dumb-bell shaped sheets (about 1 mm in thickness). Before being used, all materials were dried in a vacuum oven at 45°C for 24 h.

### 2.3. Characterization

Dynamic mechanical properties (DMA) were conducted using a TA Instruments Q800 dynamic mechanical analyzer (USA) in a film-tension mode at a frequency of 1 Hz. The temperature ranged from -10 to 90°C at a heating rate of 3°C/min. The tensile-fractured surfaces of the specimens were characterized by using an Inspect F field-emission SEM (FEI Company, USA) with 5–20 kV accelerating voltage. For the observation of phase morphologies, the specimens were first cryogenically fractured in liquid nitrogen. Then the PPC

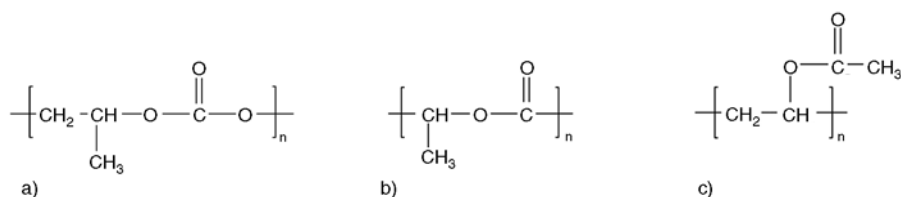


**Figure 1.** Chemical structures of (a) PPC, (b) PLA, and (c) PVAc

phase and PVAc were etched away in a mixed solution of anhydrous ethanol and acetone (1:1, v/v) at room temperature for 6 h. To determine the dispersion state of PVAc in the blends, anhydrous methanol was also used as an etching agent to selectively dissolve the PVAc phase at room temperature for 12 h. Before SEM characterization, both the etched surfaces and tensile-fractured surfaces were coated with a thin layer of gold.

A Netzsch DSC 204 Phoenix (Germany) was used to investigate the effect of PVAc on the crystallization behavior of PPC/PLA blends. The specimens (about 5 mg) were first heated from room temperature to 190°C rapidly and then kept at this temperature for 5 min to eliminate the thermal history. The cooling curves were recorded from 190 to 0°C at a cooling rate of 2°C/min. The values of crystallization temperature ( $T_c$ ) could be obtained from the cooling curves. All measurements were carried out under a nitrogen atmosphere.

All FTIR spectra were recorded at 4 cm<sup>-1</sup> resolution using a Thermo Scientific Nicolet 6700 spectrometer equipped with Smart iTR attenuated total reflection (ATR) accessory. Tensile testing was performed using an Instron 4302 universal tensile testing machine (USA) with a crosshead speed of 10 mm/min at 23°C. The results reported were the average from at least five specimens for each testing.

### 3. Results and discussion

#### 3.1. Compatibility and phase morphology

The compatibility of PPC/PLA blends was evaluated by DMA. Figure 2 shows the plots of dynamic loss modulus versus temperature for PPC, PLA, and 50PPC/50PLA blend with and without PVAc. The glass transition temperature ( $T_g$ ) can be obtained from the peak in the plots. Neat PPC and PLA exhibit the glass transition at 27.1 and 55.0°C, respectively.

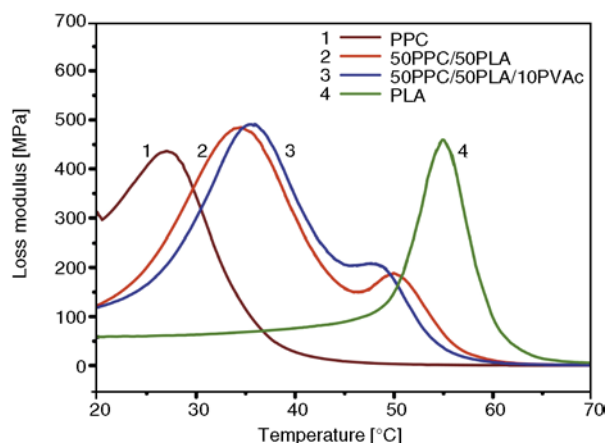


**Figure 2.** Loss modulus of PPC, PLA, and 50PPC/50PLA blend with and without PVAc as a function of temperature

As previously reported by Ma *et al.* [18], the  $T_g$  of both PPC and PLA shifts significantly towards each other in the blend, suggesting that PPC and PLA are partially compatible. More importantly, adding a small amount of PVAc (10 wt%) into the blend gives rise to not only a clearly increased  $T_g$  of PPC (from 34.5 to 36.0°C) but also a decreased  $T_g$  of PLA (from 50.0 to 47.7°C). Similar results have also been obtained from 30PPC/70PLA and 70PPC/30PLA blends with and without PVAc, as shown in Table 1. Evidently, the difference in the values of  $T_g$  between PPC and PLA decreases clearly with the introduction of PVAc, indicating that PVAc can act as a good compatibilizer for the PPC/PLA blends. The enhanced compatibility between PPC and PLA by adding PVAc can be further proved from the changes in the phase morphology of PPC/PLA blends with and without PVAc, as presented in Figure 3. It is obvious that 70PPC/30PLA blend exhibits a typical sea-island morphology, in which PLA domains are dispersed in the PPC matrix (Figure 3a), while 50PPC/50PLA blend exhibits a co-continu-

**Table 1.** Glass transition temperatures ( $T_g$ ) and Mechanical Properties of PPC/PLA blends with and without PVAc

Samples	$T_{g,PPC}$ [°C]	$T_{g,PLA}$ [°C]	Tensile strength [MPa]	Young's modulus [MPa]	Elongation at break [%]
PPC	27.1	–	6.2±0.5	121±40	988±40
70PPC/30PLA	32.2	a)	17.3±1.5	1104±80	118±35
70PPC/30PLA/10PVAc	34.0	a)	28.5±3.0	1434±150	187±60
50PPC/50PLA	34.5	50.0	28.3±1.0	1588±80	6±10
50PPC/50PLA/10PVAc	36.0	47.7	40.2±2.5	1787±100	65±10
30PPC/70PLA	37.1	53.3	45.6±3.2	1965±40	28±11
30PPC/70PLA/10PVAc	37.7	52.0	50.7±1.5	1960±80	40±5
PLA	–	55.0	59.8±2.0	2164±85	4±1

a) can not be determined from the loss modulus plots

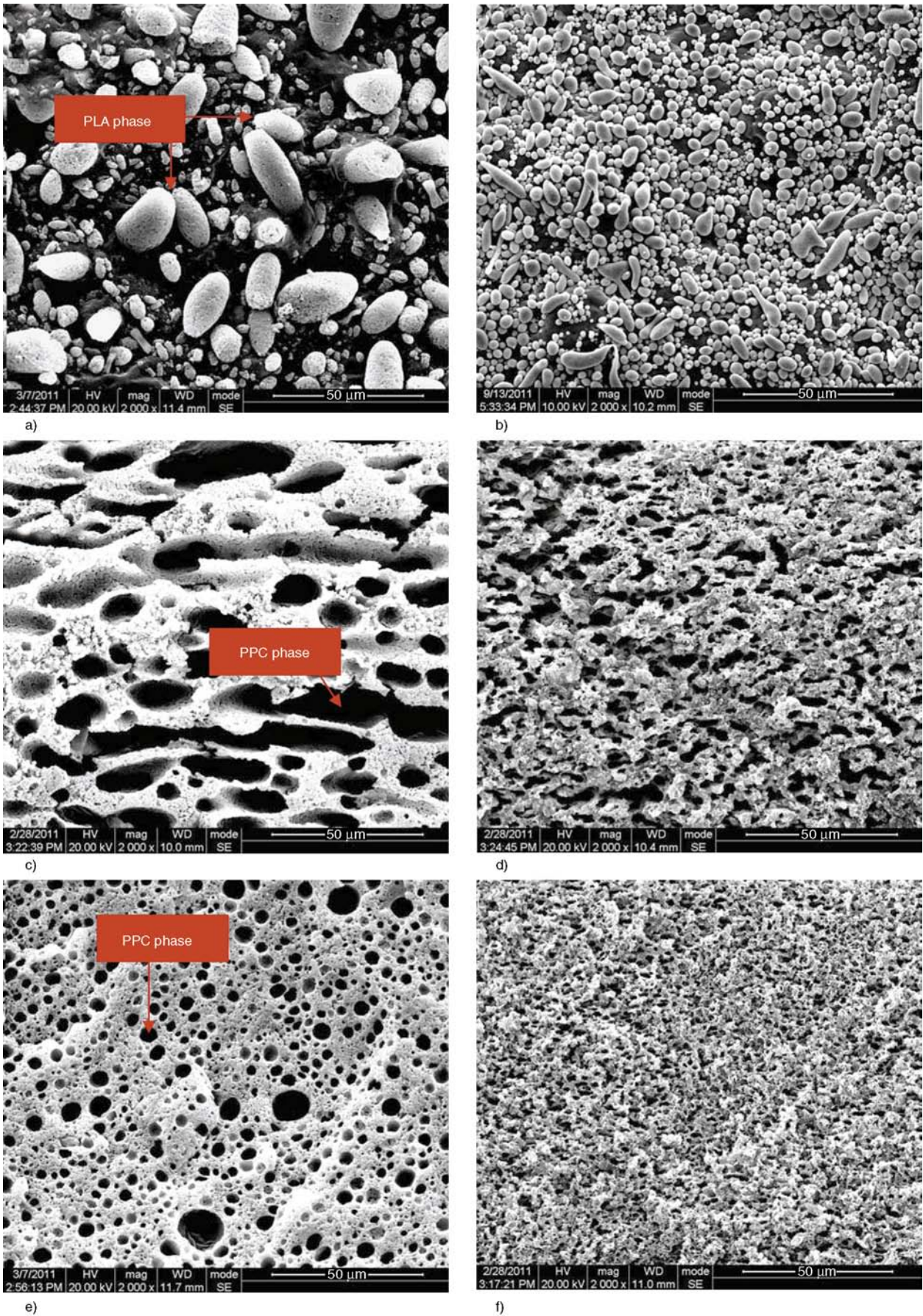


**Figure 3.** SEM micrographs of PPC/PLA blends with and without PVAc: (a) 70 PPC/30PLA, (b) 70PPC/30PLA/10PVAc, (c) 50PPC/50PLA, (d) 50PPC/50PLA/10PVAc, (e) 30PPC/70PLA, and (f) 30PPC/70PLA/10PVAc

ous morphology (Figure 3c). With increasing PLA content up to 70 wt%, however, the primarily continuous PPC phase is gradually transformed into dispersed droplets, followed by more and more dispersed PLA droplets in the PPC matrix coalesce together, forming another typical sea-island morphology (Figure 3e). Very interestingly, with the addition of PVAc, a much finer and more uniform phase structure is presented, which is similar to the results of introducing well-designed block copolymers into incompatible polymer blends [27]. For the compatibilized blend, the dispersed phase in the SEM micrographs is attributed to PPC-rich phase because the PVAc also can be etched away in the

mixed solution. For example, the size of dispersed PPC domains in the 30PPC/70PLA blend ranges from 5 to 15  $\mu\text{m}$ , whereas in the 30PPC/70PLA/10PVAc PPC-rich dispersed phase is significantly decreased to less than 5  $\mu\text{m}$  (Figure 3e and 3f). This further demonstrates that PVAc can improve the compatibility between PPC and PLA significantly. The improved compatibility may origin from the selective localization of PVAc in PPC/PLA blends. This assumption is well supported by another morphological observation of the blends as shown in Figure 4. Because it is very difficult to clarify the dispersion state of PVAc in the blends through SEM images of the cryogenically fractured surfaces (Fig-

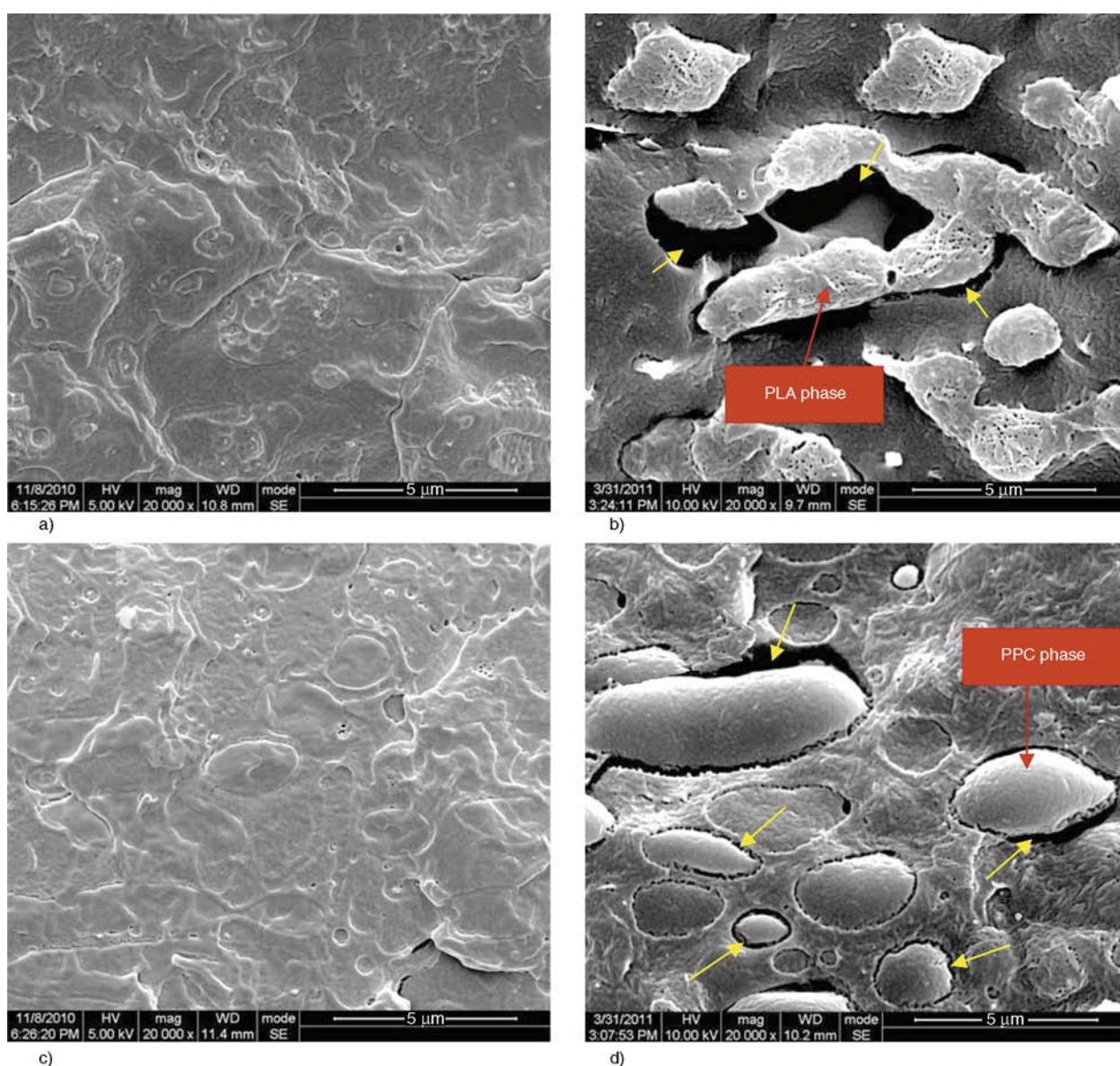


**Figure 4.** SEM micrographs show the dispersion of PVAc in (a, b) 70PPC/30PLA/10PVAc and (c, d) 30PPC/70PLA/10PVAc blends. (a) and (c) are the images of cryogenically fractured surfaces, while (b) and (d) are the subsequently etched surfaces. PVAc was selective dissolved by anhydrous methanol as shown by the arrows.

ure 4a and 4c), PVAc was selective removed from the blends by anhydrous methanol (both PPC and PLA cannot be dissolved in anhydrous methanol). As shown in Figure 4b and 4d, the dark holes represent the removed PVAc phase. Clearly, PVAc is selectively located at the interface between PPC and PLA phases as highlighted by the arrows. Furthermore, a fraction of PVAc may be dispersed in the PLA phase, evidenced by the existence of some tiny dark holes in the PLA droplets (Figure 4b). This indicates that PVAc may have a higher affinity to PLA than to PPC. In this case, a small amount of the PVAc has a tendency to migrate from the phase interface to the PLA phase during melt blending. The dispersion of PVAc in the PLA phase can also be confirmed by the results of DSC measured crystallization behavior of PPC/PLA blends with and without PVAc. As clearly shown in Figure 5, for 30PPC/70PLA and 50PPC/50PLA blends, no apparent changes in  $T_c$  of PLA can be observed compared to neat PLA. Similar result has been found in PPC/PHB blends, where the crystallization of PHB is independent of the presence of PPC [7]. However, with the addition of PVAc, a significant decrease of  $T_c$  appears in both the PLA and PPC/PLA blends. Because the shift degree of the two  $T_c$ -s are almost equivalent, the depressed crystallization of PLA in PPC/PLA/PVAc blends should be attributed to the PVAc dispersed in the PLA phase. The strong interaction between PVAc and PLA may play a negative role for the crystallization of PLA by hindering the movement and rearrangement of molecular chains. In particular, the  $T_c$  of PLA in 70PPC/30PLA blend is much lower than that in 30PPC/70PLA or 50PPC/

50PLA blend, indicating the confined crystallization of PLA in the case of PPC being a continuous phase (Figure 3e).

### 3.2. Molecular mechanisms for the compatibilization

Due to the similar chemical structures of the three polymers, the possible molecular mechanisms for the interactions between the interface-localized PVAc and the two matrix components (i.e. PPC and PLA) are analyzed with FTIR spectra of PPC, PLA, and their blends with and without PVAc. As shown in Figure 6, in the C=O stretching vibration region, the absorption peak of PLA at  $1747\text{ cm}^{-1}$  shifts significantly towards lower wavenumber with the addition of 50 wt% PPC due to the specific intermolecular interactions between PPC and PLA, such as  $\text{C=O}\cdots\text{O=C}$  dipole-dipole interaction [18]. More

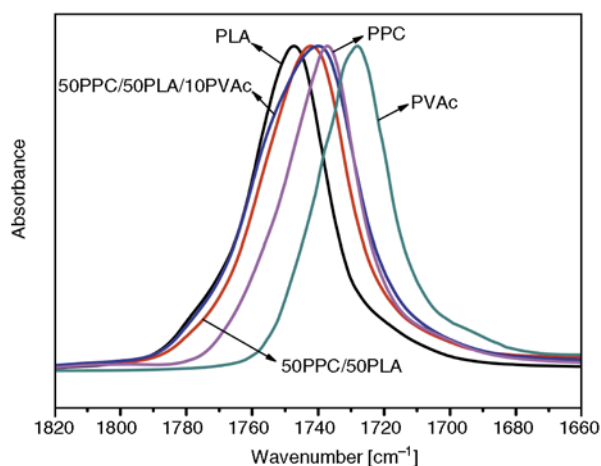


**Figure 6.** Normalized FTIR spectra of C=O stretching bands for PPC, PLA, PVAc and PPC/PLA blends with and without PVAc

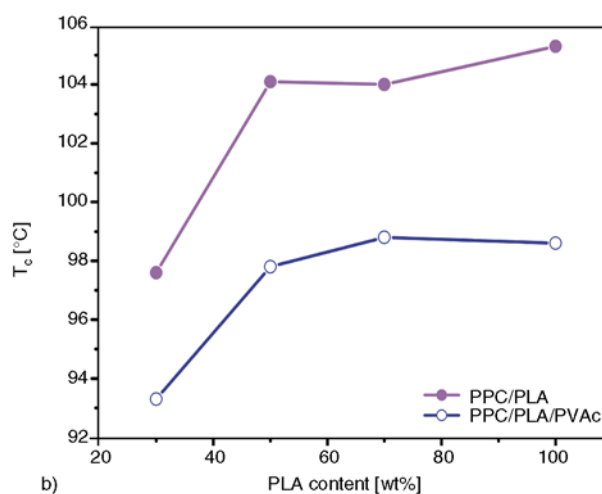
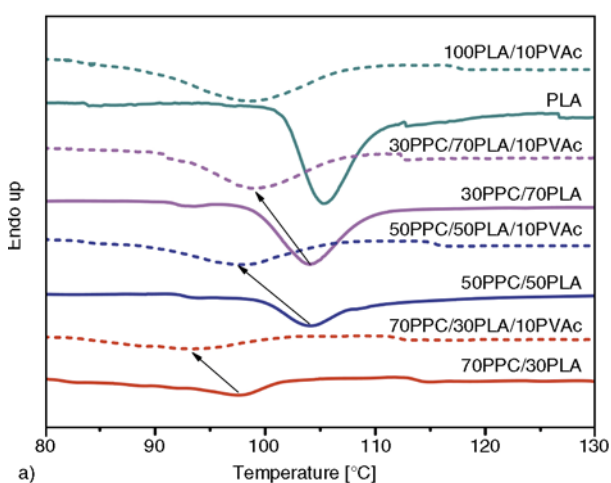


**Figure 5.** (a) DSC cooling curves of PPC/PLA blends with and without PVAc, and (b) crystallization temperature ( $T_c$ ) as a function of PLA content

importantly, it is interesting to note that the addition of PVAc into the PPC/PLA blend gives rise to not only a peak shifting of the C=O stretching band (from 1742 to 1739  $\text{cm}^{-1}$ ) but also an obvious peak broadening, suggesting that PVAc is likely to improve the interaction between PPC and PLA molecules. The potential molecular mechanisms for the enhanced interaction may be the  $\text{CH}_3 \cdots \text{O}=\text{C}$  interaction, as in the case for PHB/PLA/PVAc blends proposed by El-Hadi [28]. To give a direct evidence on the validity of this assumption, the FTIR spectra of neat PPC, PLA, and PPC/PVAc and PLA/PVAc blends were measured. Unfortunately, because the chemical constitution of PVAc is very similar to those of PPC and PLA (Figure 1), both the absorption peaks assigned to the  $\text{CH}_3$  deformation bands and those corresponding to the C=O stretching vibration bands overlap for PPC/ PVAc and PLA/PVAc blends, then the spectra become complicated and it is difficult to reveal the direct interaction according to the changes in peak position and peak shape. Maybe as the literature reported, the interaction between C=O groups of PLA and  $\text{CH}_3$  groups of PVAc is considered to be the main contribution to the compatibility between PLA and PVAc [26]. This type of hydrogen bonding has also been reported to exist in PLLA/PDLA stereocomplex [29]. For PPC/PVAc blends, such weak hydrogen bonding is likely to favor the compatibility due to the fact that PPC and PLA have similar C=O groups in main chains. Because of the delicate difference between the FTIR spectra, the exact molecular mechanisms need further investigation and will be reported in further work.

From above discussion, it is obvious that the compatibility between PPC and PLA is improved dra-

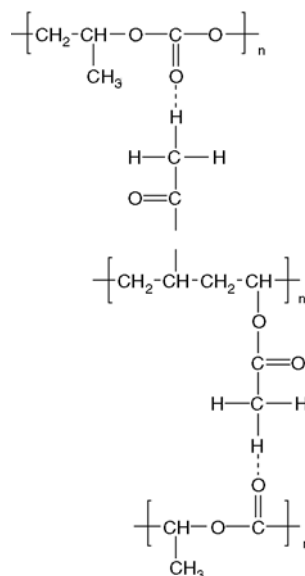


**Figure 7.** Schematic representation of the possible compatibilizing mechanism of PVAc in PPC/PLA blends

matically upon of PVAc, which is selectively dispersed at the phase interface and in the PLA phase. At the current stage of this study, we give a briefly schematic representation of the possible compatibilizing mechanism of PVAc in the binary blends, as shown in Figure 7. These interface-localized PVAc can act as a compatibilizer to reduce the interfacial tension through specific intermolecular interactions with the two matrix components (i.e. PPC and PLA) and hinder the domains coalescence during blending, thus leading to a much refined phase morphology.

### 3.3. Mechanical properties

As discussed in the *introduction*, the phase morphology of multiphase polymer blends plays a crucial role in determining their performance. Therefore, with the addition of a small amount of PVAc

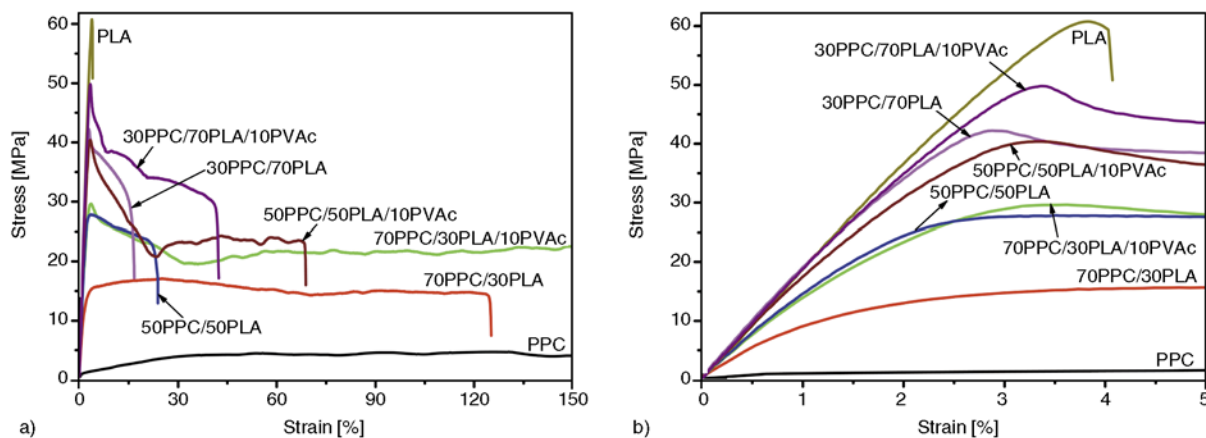


**Figure 8.** (a) stress-strain curves of of PPC/PLA blends with and without PVAc, and (b) enlarged part of the curves



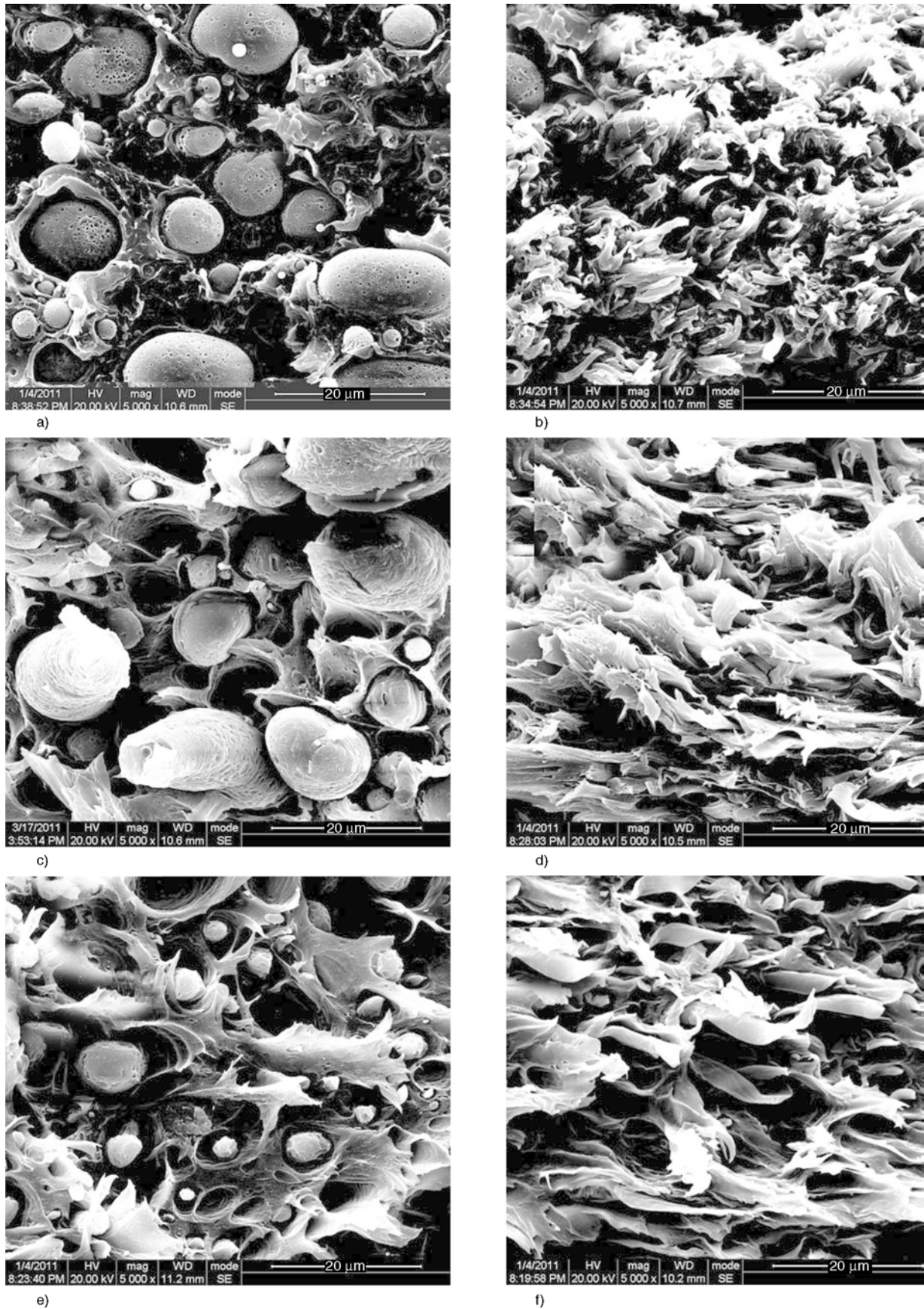


**Figure 9.** SEM micrographs of tensile-fractured surfaces of PPC/PLA blends with and without PVAc: (a) 70PPC/30PLA, (b) 70PPC/30PLA/10PVAc, (c) 50PPC/50PLA, (d) 50PPC/50PLA/10PVAc, (e) 30PPC/70PLA, and (f) 30PPC/70PLA/10PVAc

**Table 2.** Mechanical properties of PPC/PLA blends (70/30) with (2–10 wt%) and without PVAc

Samples	Tensile strength [MPa]	Young's modulus [MPa]	Elongation at break [%]
70PPC/30PLA	17.3±1.5	1104±80	118±35
70PPC/30PLA/2PVAc	21.5±3.0	1206±100	130±55
70PPC/30PLA/5PVAc	28.0±1.0	1388±130	196±65
70PPC/30PLA/10PVAc	28.5±3.0	1434±150	187±60

in the PPC/PLA blends, the enhancement in the mechanical properties is expected because of the significant improvement in the phase dispersion. Figure 8 shows the stress-strain curves of PPC, PLA and their blends with and without PVAc. The mechanical properties are summarized in Table 2. Clearly, although the tensile strength and Young's modulus increase steadily with increasing PLA contents, PPC/PLA binary blends exhibit a relatively low ductility (the elongation at break is much lower than that of neat PPC) probably due to the weak interfacial adhesion between PPC and PLA phases. However, as expected, the evident enhancements in both the strength and the ductility are observed upon adding 10 wt% PVAc. For example, the tensile strength and elongation at break increase from 28.3 MPa and 36% for 50PPC/50PLA blend to 40.2 MPa and 65% for 50PPC/50PLA/10PVAc blend, respectively. In addition, the Young's modulus of PPC/PLA/PVAc ternary blends displays a slight enhancement with respect to that of PPC/PLA binary blends. Note that, even for 70PPC/30PLA/10PVAc blend where PPC as the dominant component, the tensile strength and Young's modulus still remain as high as about 26.5 and 1434 MPa, respectively, which are comparable to those of widely used polypropylene (PP) [30]. Obviously, the PPC/PLA blend modified with a small amount of PVAc exhibits a potential to be used as a sustainable alternative to petroleum-based polymers.

In order to clarify the fracture mechanisms responsible for the improved mechanical properties, tensile-fractured surfaces of PPC/PLA blends with and without PVAc are observed by SEM. As shown in Figure 9, PPC/PLA binary blend shows an intensive interfacial debonding between PPC and PLA phases (most of the dispersed domains are pulled out from the matrix rather than being broken), suggesting a relatively weak interfacial interaction. Moreover, the domains are as large as 20  $\mu\text{m}$  (Figure 9a and 9c),

which leads to the large voids through interfacial debonding and subsequently not only reduce the tensile strength but also develop into cracks. In contrast, for the PPC/PLA/PVAc ternary blends, the interfacial interaction is significantly improved by the interface-localized PVAc, which is able to promote the stress transfer between the two matrix phases and prevent the initiation of cracks at the phase interface [31, 32], then highly stretched and fibrillated ligaments are formed due to the matrix shear yielding (Figure 9b, 9d, 9f). On the other hand, compared with the coarse phase morphology in the PPC/PLA binary blend, the much finer one in the PPC/PLA/PVAc ternary blend is more favorable to trigger large-scale shear yielding [33].

Based on the results presented above, it can be concluded that the improvement in the mechanical properties of PPC/PLA blends with the addition of 10 wt% PVAc should be mainly attributed to the remarkably improved phase dispersion and the enhanced interfacial bonding through the bridge effect of the interface-localized PVAc.

#### 4. Conclusions

Homopolymer PVAc has been successfully used to improve the compatibilization of partially compatible PPC/PLA blends. During melting blending, PVAc is selectively dispersed at the interface between the two matrix phases and in the PLA phase. The interface-localized PVAc acts as not only a compatibilizer to improve the phase morphology remarkably but also as a bridge to enhance the interfacial bonding, which are mainly responsible for the significant increase in the mechanical properties.

#### Acknowledgements

We would like to express our sincere thanks to Changchun Institute of Applied Chemistry for kindly providing the PPC, and the National Natural Science Foundation of China for financial support (21034005, 51121001).

#### References

- [1] Sugimoto H., Inoue S.: Recent progress in the synthesis of polymers based on carbon dioxide. *Pure and Applied Chemistry*, **78**, 1823–1834 (2006). DOI: [10.1351/pac200678101823](https://doi.org/10.1351/pac200678101823)
- [2] Tan C-S., Hsu T-J.: Alternating copolymerization of carbon dioxide and propylene oxide with a rare-earth-metal coordination catalyst. *Macromolecules*, **30**, 3147–3150 (1997). DOI: [10.1021/ma961725j](https://doi.org/10.1021/ma961725j)

- [3] Lu X-B., Shi L., Wang Y-M., Zhang R., Zhang Y-J., Peng X-J., Zhang Z-C., Li B.: Design of highly active binary catalyst systems for CO<sub>2</sub>/epoxide copolymerization: Polymer selectivity, enantioselectivity, and stereochemistry control. *Journal of the American Chemical Society*, **128**, 1664–1674 (2006). DOI: [10.1021/ja056383o](https://doi.org/10.1021/ja056383o)
- [4] Chisholm M. H., Navarro-Llobet D., Zhou Z.: Poly(propylene carbonate). 1. More about poly(propylene carbonate) formed from the copolymerization of propylene oxide and carbon dioxide employing a zinc glutarate catalyst. *Macromolecules*, **35**, 6494–6504 (2002). DOI: [10.1021/ma020348+](https://doi.org/10.1021/ma020348+)
- [5] Qin Y. S., Chen L. J., Wang X. H., Zhao X. J., Wang F. S.: Enhanced mechanical performance of poly(propylene carbonate) via hydrogen bonding interaction with *o*-lauroyl chitosan. *Carbohydrate Polymers*, **84**, 329–334 (2011). DOI: [10.1016/j.carbpol.2010.11.045](https://doi.org/10.1016/j.carbpol.2010.11.045)
- [6] Yu T., Zhou Y., Zhao Y., Liu K., Chen E., Wang D., Wang F.: Hydrogen-bonded thermostable liquid crystalline complex formed by biodegradable polymer and amphiphilic molecules. *Macromolecules*, **41**, 3175–3180 (2008). DOI: [10.1021/ma7020562](https://doi.org/10.1021/ma7020562)
- [7] Yang D. Z., Hu P.: Miscibility, crystallization, and mechanical properties of poly(3-hydroxybutyrate) and poly(propylene carbonate) biodegradable blends. *Journal of Applied Polymer Science*, **109**, 1635–1642 (2008). DOI: [10.1002/app.28002](https://doi.org/10.1002/app.28002)
- [8] Pang M. Z., Qiao J. J., Jiao J., Wang S. J., Xiao M., Meng Y. Z.: Miscibility and properties of completely biodegradable blends of poly(propylene carbonate) and poly(butylene succinate). *Journal of Applied Polymer Science*, **107**, 2854–2860 (2008). DOI: [10.1002/app.27252](https://doi.org/10.1002/app.27252)
- [9] Jiao J., Wang S. J., Xiao M., Xu Y., Meng Y. Z.: Processability, property, and morphology of biodegradable blends of poly(propylene carbonate) and poly(ethylene-*co*-vinyl alcohol). *Polymer Engineering and Science*, **47**, 174–180 (2007). DOI: [10.1002/pen.20694](https://doi.org/10.1002/pen.20694)
- [10] Ma X., Chang P. R., Yu J., Wang N.: Preparation and properties of biodegradable poly(propylene carbonate)/thermoplastic dried starch composites. *Carbohydrate Polymers*, **71**, 229–234 (2008). DOI: [10.1016/j.carbpol.2007.05.033](https://doi.org/10.1016/j.carbpol.2007.05.033)
- [11] Chen B-K., Shen C-H., Chen S-C., Chen A. F.: Ductile PLA modified with methacryloyloxyalkyl isocyanate improves mechanical properties. *Polymer*, **51**, 4667–4672 (2010). DOI: [10.1016/j.polymer.2010.08.028](https://doi.org/10.1016/j.polymer.2010.08.028)
- [12] Hashima K., Nishitsuji S., Inoue T.: Structure-properties of super-tough PLA alloy with excellent heat resistance. *Polymer*, **51**, 3934–3939 (2010). DOI: [10.1016/j.polymer.2010.06.045](https://doi.org/10.1016/j.polymer.2010.06.045)
- [13] Huang Y., Wang J., Liao B., Chen M., Cong G.: Epoxy resins toughened by poly(propylene carbonate). *Journal of Applied Polymer Science*, **64**, 2457–2465 (1997). DOI: [10.1002/\(SICI\)1097-4628\(19970620\)64:12<2457::AID-APP20>3.0.CO;2-X](https://doi.org/10.1002/(SICI)1097-4628(19970620)64:12<2457::AID-APP20>3.0.CO;2-X)
- [14] Liu Z. H., Maréchal P., Jérôme R.: Blends of poly(vinylidene fluoride) with polyamide 6: Interfacial adhesion, morphology and mechanical properties. *Polymer*, **39**, 1779–1785 (1998). DOI: [10.1016/S0032-3861\(97\)00222-X](https://doi.org/10.1016/S0032-3861(97)00222-X)
- [15] Liu H., Song W., Chen F., Guo L., Zhang J.: Interaction of microstructure and interfacial adhesion on impact performance of polylactide (PLA) ternary blends. *Macromolecules*, **44**, 1513–1522 (2011). DOI: [10.1021/ma1026934](https://doi.org/10.1021/ma1026934)
- [16] Cigana P., Favis B. D., Albert C., Vu-Khanh T.: Morphology–interface–property relationships in polystyrene/ethylene–propylene rubber blends. 1. Influence of triblock copolymer interfacial modifiers. *Macromolecules*, **30**, 4163–4169 (1997). DOI: [10.1021/ma960995z](https://doi.org/10.1021/ma960995z)
- [17] Cao Y., Zhang J., Feng J., Wu P.: Compatibilization of immiscible polymer blends using graphene oxide sheets. *ACS Nano*, **5**, 5920–5927 (2011). DOI: [10.1021/nn201717a](https://doi.org/10.1021/nn201717a)
- [18] Ma X., Yu J., Wang N.: Compatibility characterization of poly(lactic acid)/poly(propylene carbonate) blends. *Journal of Polymer Science Part B: Polymer Physics*, **44**, 94–101 (2006). DOI: [10.1002/polb.20669](https://doi.org/10.1002/polb.20669)
- [19] Chun S. B., Han C. D.: Morphology of model A/B/(C-*block*-D) ternary blends and compatibilization of two immiscible homopolymers A and B with a C-*block*-D copolymer. *Macromolecules*, **33**, 3409–3424 (2000). DOI: [10.1021/ma9918708](https://doi.org/10.1021/ma9918708)
- [20] Feng H., Ye C., Tian J., Feng Z., Huang B.: Compatibilization effect of graft copolymer on immiscible polymer blends: 1. LLDPE/SBS/LLDPE-*g*-PS systems. *Polymer*, **39**, 1787–1792 (1998). DOI: [10.1016/S0032-3861\(97\)00269-3](https://doi.org/10.1016/S0032-3861(97)00269-3)
- [21] Zhang W., Fu B. X., Seo Y., Schrag E., Hsiao B., Mather P. T., Yang N-L., Xu D., Ade H., Rafailovich M., Sokolov J.: Effect of methyl methacrylate/polyhedral oligomeric silsesquioxane random copolymers in compatibilization of polystyrene and poly(methyl methacrylate) blends. *Macromolecules*, **35**, 8029–8038 (2002). DOI: [10.1021/ma020725i](https://doi.org/10.1021/ma020725i)
- [22] Moussaif N., Jérôme R.: Compatibilization of immiscible polymer blends (PV/PVDF) by the addition of a third polymer (PMMA): Analysis of phase morphology and mechanical properties. *Polymer*, **40**, 3919–3932 (1999). DOI: [10.1016/S0032-3861\(98\)00620-X](https://doi.org/10.1016/S0032-3861(98)00620-X)

- [23] Gödel A., Kasaliwal G., Pötschke P.: Selective localization and migration of multiwalled carbon nanotubes in blends of polycarbonate and poly(styrene-acrylonitrile). *Macromolecular Rapid Communications*, **30**, 423–429 (2009).  
DOI: [10.1002/marc.200800549](https://doi.org/10.1002/marc.200800549)
- [24] Wu D., Lin D., Zhang J., Zhou W., Zhang M., Zhang Y., Wang D., Lin B.: Selective localization of nanofillers: Effect on morphology and crystallization of PLA/PCL blends. *Macromolecular Chemistry and Physics*, **212**, 613–626 (2011).  
DOI: [10.1002/macp.201000579](https://doi.org/10.1002/macp.201000579)
- [25] Li Y., Shimizu H.: Compatibilization by homopolymer: Significant improvements in the modulus and tensile strength of PPC/PMMA blends by the addition of a small amount of PVAc. *ACS Applied Materials and Interfaces*, **1**, 1650–1655 (2009).  
DOI: [10.1021/am900314k](https://doi.org/10.1021/am900314k)
- [26] Gajria A. M., Davé V., Gross R. A., McCarthy S. P.: Miscibility and biodegradability of blends of poly(lactic acid) and poly(vinyl acetate). *Polymer*, **37**, 437–444 (1996).  
DOI: [10.1016/0032-3861\(96\)82913-2](https://doi.org/10.1016/0032-3861(96)82913-2)
- [27] Chen B., Li X., Xu S., Tang T., Zhou B., Huang B.: Compatibilization effects of block copolymers in high density polyethylene/syndiotactic polystyrene blends. *Polymer*, **43**, 953–961 (2002).  
DOI: [10.1016/S0032-3861\(01\)00660-7](https://doi.org/10.1016/S0032-3861(01)00660-7)
- [28] El-Hadi A. M.: Effect of processing conditions on the development of morphological features of banded or nonbanded spherulites of poly(3-hydroxybutyrate) (PHB) and polylactic acid (PLLA) blends. *Polymer Engineering and Science*, **51**, 2191–2202 (2011).  
DOI: [10.1002/pen.21991](https://doi.org/10.1002/pen.21991)
- [29] Zhang J. M., Sato H., Tsuji H., Noda I., Ozaki Y.: Differences in the  $\text{CH}_3 \cdots \text{O}=\text{C}$  interactions among poly(L-lactide), poly(L-lactide)/poly(D-lactide) stereocomplex, and poly(3-hydroxybutyrate) studied by infrared spectroscopy. *Journal of Molecular Structure*, **735–736**, 249–257 (2005).  
DOI: [10.1016/j.molstruc.2004.11.033](https://doi.org/10.1016/j.molstruc.2004.11.033)
- [30] Arranz-Andrés J., Peña B., Benavente R., Pérez E., Cerrada M. L.: Influence of isotacticity and molecular weight on the properties of metallocenic isotactic polypropylene. *European Polymer Journal*, **43**, 2357–2370 (2007).  
DOI: [10.1016/j.eurpolymj.2007.03.034](https://doi.org/10.1016/j.eurpolymj.2007.03.034)
- [31] Wu D., Zhang Y., Zhang M., Yu W.: Selective localization of multiwalled carbon nanotubes in poly( $\epsilon$ -caprolactone)/polylactide blend. *Biomacromolecules*, **10**, 417–424 (2009).  
DOI: [10.1021/bm801183f](https://doi.org/10.1021/bm801183f)
- [32] Filippone G., Dintcheva N. T., La Mantia F. P., Acierno D.: Selective localization of organoclay and effects on the morphology and mechanical properties of LDPE/PA11 blends with distributed and co-continuous morphology. *Journal of Polymer Science Part B: Polymer Physics*, **48**, 600–609 (2010).  
DOI: [10.1002/polb.21928](https://doi.org/10.1002/polb.21928)
- [33] Jang B. Z., Uhlmann D. R., Sande J. B. V.: The rubber particle size dependence of crazing in polypropylene. *Polymer Engineering and Science*, **25**, 643–651 (1985).  
DOI: [10.1002/pen.760251011](https://doi.org/10.1002/pen.760251011)

# Morphology, mechanical properties and thermal degradation kinetics of PMMA-zirconia nanocomposites prepared by melt compounding

T. E. Motaung<sup>1</sup>, A. S. Luyt<sup>1\*</sup>, M. L. Saladino<sup>2</sup>, D. C. Martino<sup>2</sup>, E. Caponetti<sup>2,3</sup>

<sup>1</sup>Department of Chemistry, University of the Free State (Qwaqwa Campus), Private Bag X13, 9866 Phuthaditjhaba, South Africa

<sup>2</sup>Department of Chemistry 'S.Cannizzaro', University of Palermo, Parco d'Orleans II-Viale delle Scienze pad.17, I-90128 Palermo, Italy

<sup>3</sup>Centro Grandi Apparecchiature-UniNetLab, University of Palermo, Via F. Marini 14, I-90128 Palermo, Italy

Received 16 March 2012; accepted in revised form 23 May 2012

**Abstract.** Zirconia nanoparticles were synthesized by means of a sol-gel method and embedded in poly(methyl methacrylate) (PMMA) by melt compounding. The zirconia was well dispersed in the PMMA matrix, with only a few clusters, especially for the highest investigated zirconia content. NMR results showed heteronuclear dipolar interactions involving the carbons and the surrounding hydrogen nuclei. The effect of the amount of zirconia, in the range of 1–5 wt%, on the thermo-mechanical properties and thermal degradation kinetics of PMMA was also investigated by means of dynamic mechanical analysis (DMA), thermogravimetric analyses (TGA), and Fourier-transform infrared spectroscopy (FTIR). The presence of zirconia showed a decrease in the storage and loss moduli at lower temperatures, probably due to a plasticization effect. The presence of zirconia in PMMA slightly increased its thermal stability, but the activation energies of thermal degradation for the nanocomposites were significantly lower, at degrees of conversion higher than 0.3, than those of pure PMMA.

**Keywords:** nanocomposites, PMMA, zirconia, morphology, dynamic mechanical analysis, thermal degradation

## 1. Introduction

Nanocomposite materials, based on a polymer matrix and inorganic nanoparticle fillers, have drawn considerable attention in recent years, due to improvements in various properties including electrical, thermal, optical and other mechanical properties [1–5]. Poly(methyl methacrylate)/zirconia (PMMA-ZrO<sub>2</sub>) is one of the most important nanocomposites that has been applied for the increasing demands of optical waveguides, ophthalmic lenses, antireflection coatings and adhesives for optical components. Several methods including *in situ* polymerization, sol-gel methods for the preparation of nanoparticles, and *in situ* emulsion polymerization

have been used to prepare the nanocomposites. FTIR, TEM and UV investigations showed that zirconia nanoparticles were generally homogeneously dispersed in the polymer matrix at primary particle size level and that the composites were transparent [6–12].

TGA analyses of PMMA-ZrO<sub>2</sub> nanocomposites in air and nitrogen atmospheres, where a sol-gel method was used for the preparation of the nanocomposites, showed three degradation steps with the thermal stability increasing in the presence of zirconia [10, 11]. However, the onset temperatures of the second step in nitrogen and of the third step in air of the nanocomposites were lower. This was

\*Corresponding author, e-mail: [LuytAS@qwa.ufs.ac.za](mailto:LuytAS@qwa.ufs.ac.za)

related to different mechanisms of thermal degradation in air and nitrogen atmospheres. The kinetic results showed that the values of activation energy ( $E_a$ ) for the degradation of the nanocomposites in air were higher than that of pure PMMA. In nitrogen the  $E_a$  values of thermal degradation for the first and last stages were larger than that of PMMA. The increase was associated with the action of the nanoparticles to inhibit the formation of free radicals. A similar reason was given by Wang *et al.* [13] in a study of synergistic flame-retarded systems consisting of nano-ZrO<sub>2</sub> and triphenylphosphate for PMMA prepared by a solution mixing process. They observed more significant increases in the thermal stability of the PMMA-ZrO<sub>2</sub> nanocomposites in air than in nitrogen.

DMA analysis of PMMA-ZrO<sub>2</sub> nanocomposites prepared via *in situ* emulsion polymerization, showed higher storage and loss moduli, glass transition ( $T_g$ ) and elastic modulus than PMMA in the glassy state [6–8, 12]. This was related to the reinforcing effect of the zirconia nanoparticles. However, in the rubbery state, the PMMA modulus was independent of the filler content, which was attributed to the weak interaction between the polymer and filler at high temperatures. It was found that the pendulum hardness of PMMA-ZrO<sub>2</sub> nanocomposites quickly increased with increasing ZrO<sub>2</sub> content, even for low content, and that there was steady increment of scratch resistance with increasing zirconia content. The hardness and abrasion behaviour was attributed to the gel effect on PMMA-ZrO<sub>2</sub> nanocomposites by ZrO<sub>2</sub> nanoparticles during polymerization.

Hu *et al.* [10] prepared PMMA-ZrO<sub>2</sub> nanocomposites by modifying non-aqueous synthesized ZrO<sub>2</sub> nanoparticles with methacryloxypropyltrimethoxysilane (MPS) in tetrahydrofuran, dispersing MPS-functionalized ZrO<sub>2</sub> nanoparticles in MMA and performing *in situ* bulk polymerization with controlled pre-polymerization time. They found that the ZrO<sub>2</sub> enhanced rigidity without loss of toughness, though not remarkable. This was attributed to bonding between the polymer and the functionalized zirconia. The results were in line with the study of Hu *et al.* [6], where an increase in elastic modulus was observed.

The purpose of this study was to prepare PMMA-ZrO<sub>2</sub> nanocomposites through a melt compounding

method. Zirconia was prepared using a sol-gel method. Both nanoparticles and composites were characterized using X-ray diffractometry (XRD), transmission electron microscopy (TEM), <sup>13</sup>C cross-polarization magic-angle spinning nuclear magnetic resonance (<sup>13</sup>C{<sup>1</sup>H} CP-MAS NMR), dynamic mechanical analysis (DMA), thermogravimetric analyses (TGA), and Fourier-transform infrared (FTIR) spectroscopy. The effect of the presence and amount of zirconia nanoparticles on the thermal and mechanical properties, as well as the thermal degradation kinetics, of the PMMA will be discussed.

## 2. Experimental

### 2.1. Materials

Tetra-*n*-propylzirconate (TPZ, Aldrich), capronic acid (Aldrich), ethanol (Eurobase), ammonium hydroxide (NH<sub>4</sub>OH, Aldrich) were used as received without further purification. Commercial grade poly(methyl methacrylate) (PMMA, Altuglas® V920T) produced by Bayer Materials Science, Italy and having a melt flow rate at 230°C/3.8 kg of 1 g/10 min, and an  $M_w = 350\,000$ , was used in pellet form. The polymer was dried at 120°C overnight under static vacuum before processing.

### 2.2. Zirconia preparation

The ZrO<sub>2</sub> nanoparticles were prepared according to the sol-gel method reported by Bondioli *et al.* [14].

### 2.3. Preparation of the composites

The PMMA pellets were thoroughly mixed with 1, 2 and 5 wt% zirconia for 10 min at 200°C and 30 rpm in a 50 mL internal mixer of a Brabender Plastograph from Duisburg, Germany. The mixed samples were melt-pressed into 1 mm thick sheets at 200°C for 5 min.

### 2.4. Analysis methods

Oriented finite element analysis (OFE) was carried out on a Carlo Erba EA 1110 apparatus in order to determine the residual carbon content in the zirconia particles.

TEM micrographs were acquired by using a JEM-2100 (JEOL, Japan) electron microscope operating at 200 kV accelerating voltage equipped with an X-ray energy dispersive spectrometer (EDS, Oxford, model INCA ENERGY-200T) for analysis of elements. Few tens of milligrams of powders were dis-

persed in 2 mL of isopropanol and a small drop of the dispersion was deposited on a 300 mesh carbon-coated copper grid, which was introduced into the TEM chamber analysis after the complete solvent evaporation. Nanocomposite thin samples of about 50 nm in thickness were cut using a Leica EM UC6 ultramicrotome equipped with a Leica EMFC6 cryo-camera and a diamond blade. The thin samples thus obtained were deposited onto copper grids.

XRD patterns were recorded in the 2–70° 2 $\theta$  range at steps of 0.05° and a counting time of 5 s/step on a Philips PW 1050 diffractometer, equipped with a Cu tube and a scintillation detector beam. The X-ray generator worked at 40 kV and 30 mA. The instrument resolution (divergent and antiscatter slits of 0.5°) was determined using standards free from the effect of reduced crystallite size and lattice defects. Diffraction patterns were analyzed according to the Rietveld method [15] using the programme MAUD [16].

The  $^{13}\text{C}\{^1\text{H}\}$  CP-MAS NMR spectra were obtained at room temperature with a Bruker Avance II 400 MHz (9.4 T) spectrometer operating at 100.63 MHz for the  $^{13}\text{C}$  nucleus with a MAS rate of 10 kHz, 400 scans, a contact time of 1.5 s and a repetition delay of 2 sec. The optimization of the Hartmann-Hahn condition [17] was obtained using an adamantane sample. Each sample was placed in a 4 mm zirconia rotor with KEL-F caps using silica as filler to avoid inhomogeneities inside the rotor. The proton spin–lattice relaxation time in the rotating frame  $T_{1\rho}(\text{H})$  was indirectly determined, with the *variable spin lock* (VSL) pulse sequence, by the carbon nucleus observation using a 90°– $\tau$ –spin-lock pulse sequence prior to cross-polarization [18]. The data acquisition was performed by  $^1\text{H}$  decoupling with a delay time,  $\tau$ , ranging from 0.1 to 7.5 ms and a contact time of 1.5 ms. The  $T_{\text{CH}}$  values for all carbon signals of PMMA were obtained through variable contact time (VCT) experiments [19]. The contact times used in the (VCT) experiments were 0.05, 0.1, 0.2, 0.3, 0.4, 0.5, 0.6, 0.8, 1.0, 1.2, 1.5, 2.0, 2.5, 3.0, 3.5, 4.0, 4.5, 5.0, 6.0 and 7.0 ms. The proton spin–lattice relaxation time in the laboratory frame  $T_1(\text{H})$  was determined, with the saturation recovery pulse sequence [20], by the carbon nucleus observation using a 90°– $\tau$ –90° pulse sequence prior to cross polarization with a delay time  $\tau$  ranging from 0.01 to 3 s.

The dynamic mechanical analysis (DMA) of the blends and composites was performed from 40 to 180°C in the bending mode at a heating rate of 5°C min $^{-1}$  and a frequency of 1 Hz using a Perkin Elmer Diamond DMA from Waltham, Massachusetts, U.S.A.

Thermogravimetric analysis (TGA) was performed in a Perkin Elmer TGA7 from Waltham, Massachusetts, U.S.A. The analyses were done under flowing nitrogen at a constant flow rate of 20 mL min $^{-1}$ . Samples (5–10 mg) were heated from 25 to 600°C at different heating rates. The degradation kinetic analysis was done using the following two methods. The Flynn-Wall-Ozawa method is an isoconversional linear method based on Equation (1):

$$\ln\beta = c - 1.053 \frac{E_a}{RT} \quad (1)$$

where  $\beta$  heating rate in K min $^{-1}$ ,  $c$  is constant,  $E_a$  activation energy in kJ mol $^{-1}$ ,  $R$  universal gas constant, and  $T$  temperature in K. The plot of  $\ln\beta$  vs.  $1/T$ , obtained from the TGA curves recorded at several heating rates, should be a straight line. The activation energy can be evaluated from its slope. The second method is Kissinger-Akahira-Sunose which it is based on Equation (2)

$$\ln \frac{\beta}{T^2} = \ln \frac{AR}{E_a \cdot g(\alpha)} - \frac{E_a}{RT} \quad (2)$$

where  $\beta$ ,  $E_a$ ,  $R$  and  $T$  were defined before,  $\alpha$  fraction of conversion,  $A$  pre-exponential factor and  $g(\alpha)$  algebraic expression for integral methods. From the TGA curves recorded at different heating rates  $\beta$ , temperatures  $T$  were determined at the conversions  $\alpha = 10\sim 90\%$ . The activation energies were calculated from the slope of the straight lines of  $\ln(\beta/T^2)$  versus  $1/T$ .

The thermogravimetric analysis-Fourier-transform infrared (TGA-FTIR) analyses were performed in a Perkin Elmer STA6000 simultaneous thermal analyzer from Waltham, Massachusetts, U.S.A. The analyses were done under flowing nitrogen at a constant flow rate of 20 mL min $^{-1}$ . Samples (20–25 mg) were heated from 30 to 600°C at 10°C min $^{-1}$  and held for 4 min at 600°C. The furnace was linked to the FTIR (Perkin Elmer Spectrum 100, Massachusetts, U.S.A.) with a gas transfer line. The volatiles were scanned over a 400–4000 cm $^{-1}$  wavenumber range at a resolution of 4 cm $^{-1}$ . The

FTIR spectra were recorded in the transmittance mode at different temperatures during the thermal degradation process.

### 3. Results and discussion

The elemental analysis of zirconia particles shows a significant carbon content of 7.2% and a hydrogen content of 4.4%. These residues can be attributed to an incomplete sol-gel reaction of the zirconia precursor tetra-n-propylzirconate (TPZ).

The XRD patterns of the  $ZrO_2$  powder, pure PMMA and of the composites are reported in Figure 1. The analysis of the XRD patterns was performed using the Rietveld method [15]. The pattern of zirconia powder is described in terms of two crystalline phases: 80( $\pm$ 3) wt% of tetragonal [S.G. P42/mnm,  $a = 3.6205(\pm 1)$  Å and  $c = 5.14245(\pm 1)$  Å, average crystallite size 180 Å( $\pm$ 3)] and 20( $\pm$ 3) wt% of monoclinic [S.G. P21/c,  $a = 5.03(\pm 1)$  Å,  $b = 5.06(\pm 1)$  Å,  $c = 5.04(\pm 1)$  Å and  $\beta = 98.7^\circ$ , average crystallite size 500( $\pm$ 30) Å] Baddeleyite. The diffraction pattern of PMMA shows a broad diffraction peak at  $2\theta = 14^\circ$ , typical of an amorphous material, together with two bands of lower intensities centred at 29.7 and 41.7°. The XRD patterns of the PMMA- $ZrO_2$  nanocomposites having 1, 2 and 5 wt% of  $ZrO_2$  show the bands of PMMA together with the peaks of the zirconia in which the intensity increases with zirconia quantity. This suggests that zirconia maintains its structure in the composite and that the orientation of the PMMA chains is not influenced by the filler.

Some TEM micrographs and the EDS spectrum of zirconia powder are reported in Figure 2. Aggre-

gates with a large number of particles (more than 30) of different sizes are observed. In each aggregate bigger, quite thick particles (around 200–400 nm) are surrounded by smaller spongy particles (50–100 nm). The EDS spectrum shows the characteristic peaks of Zr and O in the sample, together with nickel and the copper of the grid. The TEM micrographs of the PMMA- $ZrO_2$  nanocomposite having 5 wt% of zirconia, reported in Figure 3, show aggregates constituted of many small particles of 100 and 200 nm in size having spongy surfaces dispersed in the polymer. The TEM micrographs of the PMMA- $ZrO_2$  nanocomposites having 1 and 2 wt% of zirconia still show some aggregation, but to a lower extent, and the nanoparticle dispersion looks better (Figures 4 and 5).

The DMA curves of the pure PMMA, and the PMMA composites having 1, 2 and 5 wt% of zirconia are shown in Figure 6. The presence of zirconia shows a decrease in the storage and loss moduli at lower temperatures, which could be the result of more free space for molecular vibration in the presence of the inorganic (nano)particles. Above the glass transition temperature the 2 and 5% zirconia containing nanocomposites have storage moduli similar to PMMA, but the 1% containing nanocomposite has higher storage modulus values. It seems as if effective immobilization of the polymer chains only takes place at the lower zirconia content. The  $\tan \delta$  curves, shown in Figure 6c, confirm that the presence of zirconia did not have a significant influence, except for the nanocomposite containing 1 wt%  $ZrO_2$ , which shows a little increase in the glass transition temperature. These results are surprising because a rigidity increase of the polymer chains is generally observed at higher filler content [21]. They could, however, be explained by considering the aggregation of particles at higher filler quantity. Aggregation would reduce the exposed surface area of the nanoparticles and decrease the extent of interaction of these particles with the polymer, thereby reducing the immobilization of the polymer chains by the nanoparticles.

The TGA curves of the pure PMMA and of the composites having 1, 2 and 5 wt% of zirconia are reported in Figure 7. All the samples show single-step degradation and an increase in char content with an increase in the zirconia content. The amount of char is in line with the amount of zirconia ini-

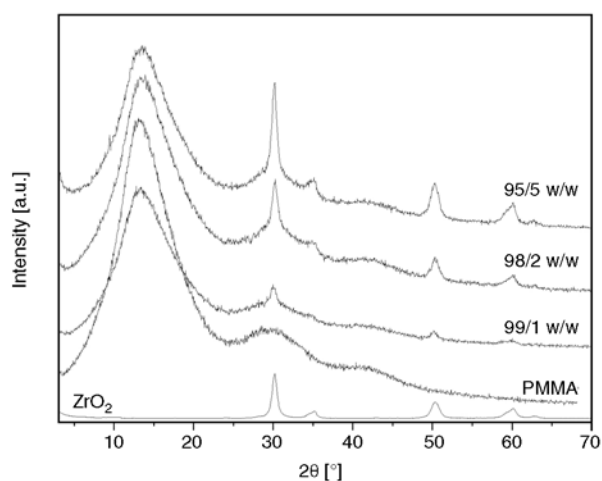


**Figure 1.** XRD patterns of zirconia powder, pure PMMA and of the PMMA- $ZrO_2$  nanocomposites



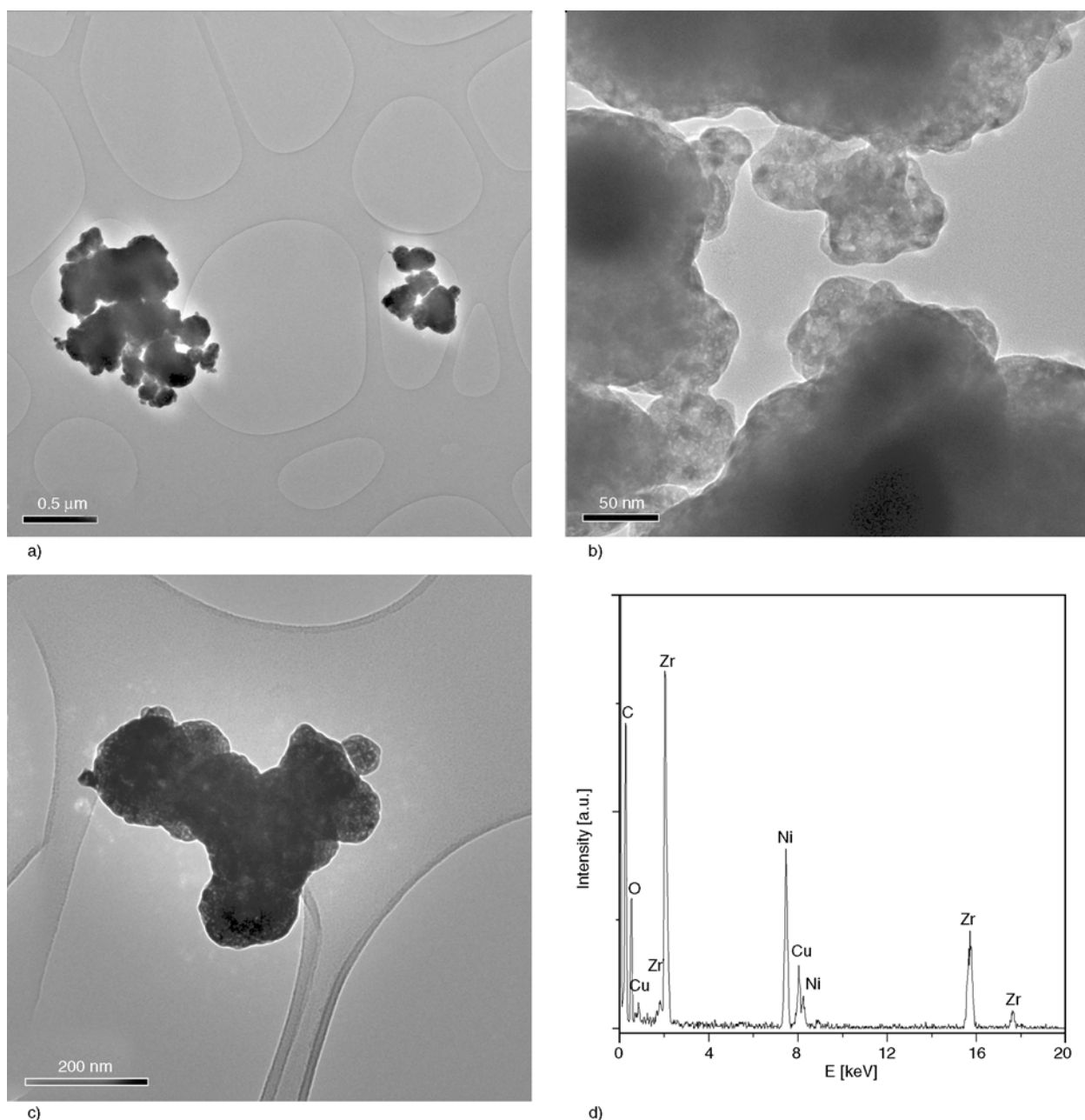


**Figure 2.** TEM micrographs (a–c) and EDS spectrum (d) of zirconia powder

tially mixed into the sample (Table 1). The standard deviation values suggest that the nanoparticles dispersion in the polymer matrix was fairly homogeneous, except for the 5% zirconia containing sample which has a very high standard deviation value. This is probably the result of a large number of aggregates formed in this nanocomposite, as observed from the TEM micrographs and according to the hypothesis made when discussing the  $\tan \delta$  data. The presence of zirconia in PMMA slightly increased its thermal stability, but the thermal stability does not increase with increasing amount of zirconia.

**Table 1.** Char content values for all PMMA-zirconia nanocomposites

Sample	Char content [%]
98/1 w/w PMMA-ZrO <sub>2</sub>	1.33±0.11
98/2 w/w PMMA-ZrO <sub>2</sub>	2.10±0.13
98/5 w/w PMMA-ZrO <sub>2</sub>	4.88±1.10

This is probably due to interactions between the zirconia and the free radicals formed during degradation which immobilized the free radicals and retarded the degradation process. It is possible that the nanoparticles also interacted with the volatile decompo-

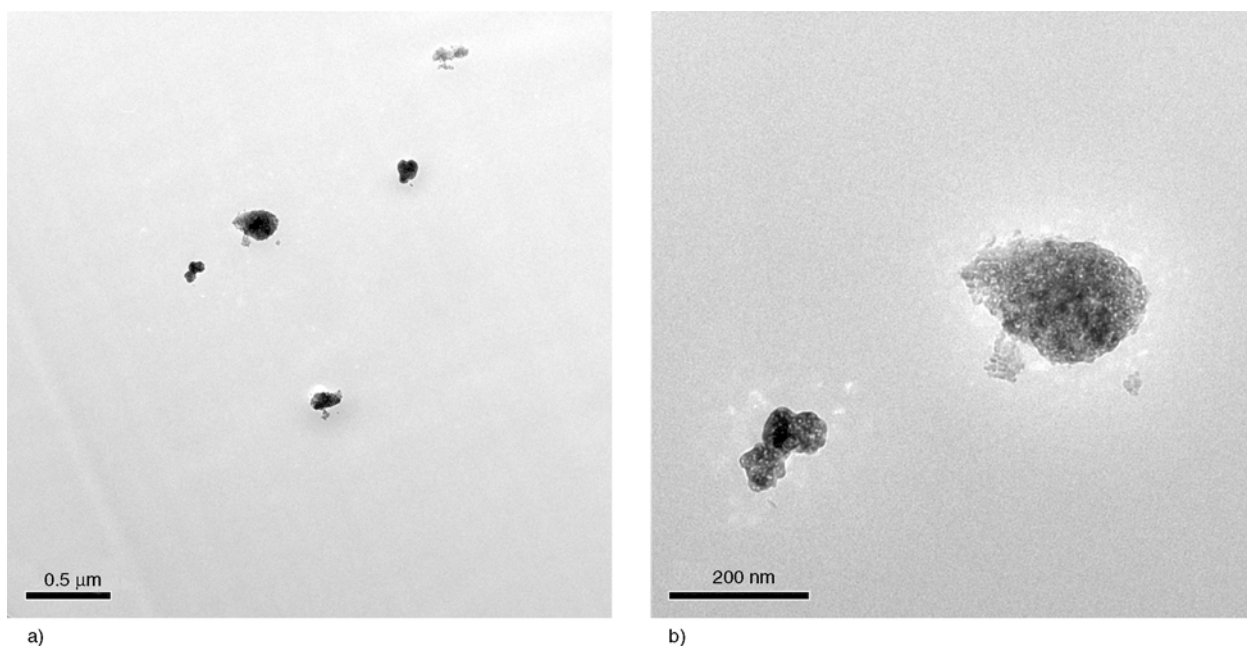


**Figure 3.** TEM micrographs of the 5 wt% PMMA-ZrO<sub>2</sub> nanocomposite at different magnifications

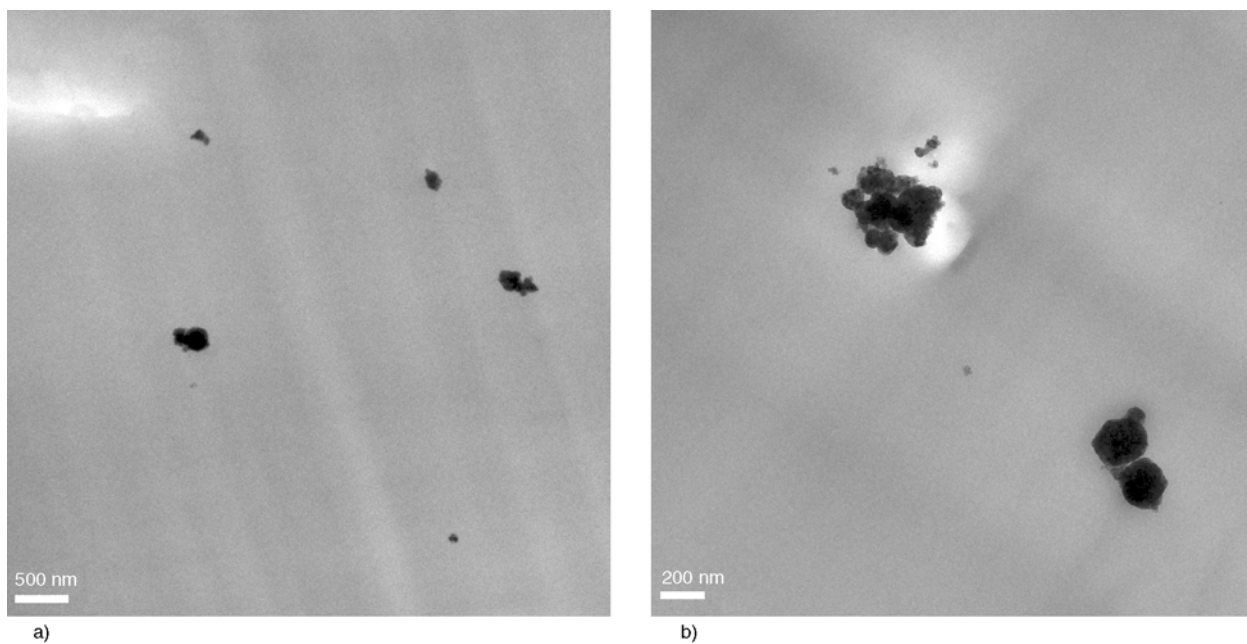


**Figure 4.** TEM micrographs of the 1 wt% PMMA-ZrO<sub>2</sub> nanocomposite at different magnifications

sition products and in the process retarded its diffusion out of the sample.

From the TGA curves of PMMA and PMMA-zirconia (5 wt%) at heating rates of 3, 5, 7 and 9°C min<sup>-1</sup> the isoconversional graphs of  $\ln\beta$  versus  $1/T$  according to Equation (1) were plotted, and of  $\ln(\beta/T^2)$  versus  $1/T$  according to Equation (2). The activation energy values were calculated from the slopes of the isoconversional plots. Both isoconversional methods give similar values of the activation energies within experimental uncertainty. Figure 8 illus-

trates the relationship between the activation energies and the degree of conversion.

The activation energy values of pure PMMA and its nanocomposites generally show an increase with the degree of conversion. However, those of the nanocomposites slightly decrease after 80% mass loss. The activation energy values of the nanocomposite are slightly higher than those of pure PMMA up to about 30% mass loss, which is in line with the higher thermal stabilities observed in Figure 7. However, the differences between the two sets of

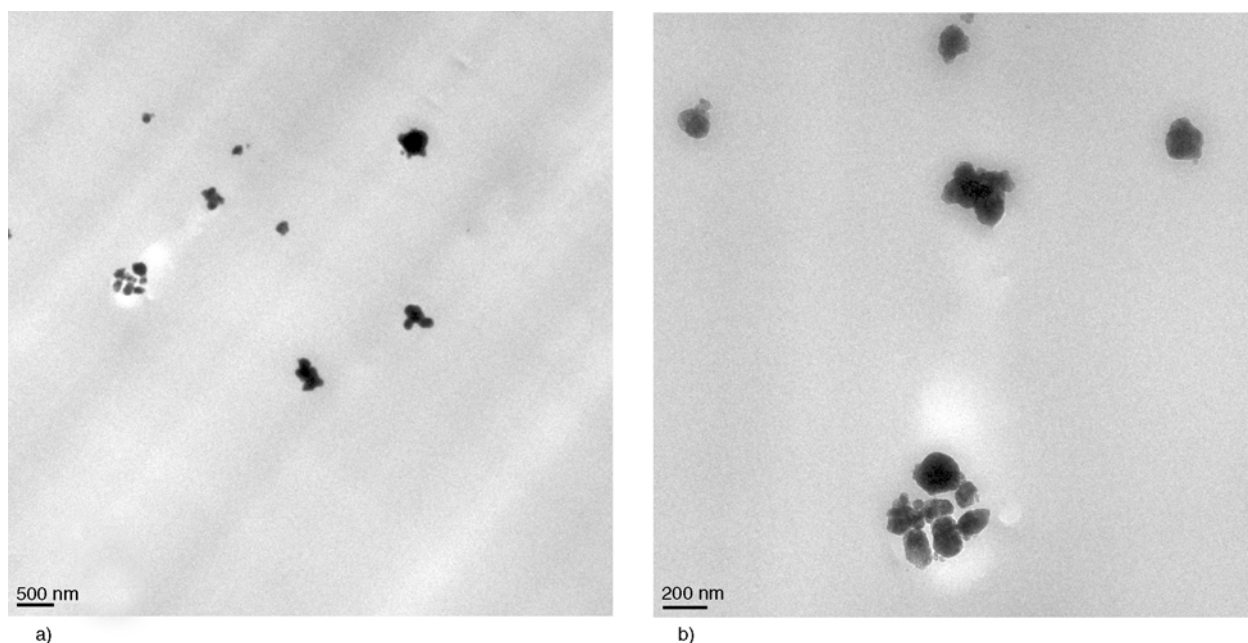


**Figure 5.** TEM micrographs of the 2 wt% PMMA-ZrO<sub>2</sub> nanocomposite at different magnifications

values increase with increasing degree of conversion. The lower activation energy values for the nanocomposite at higher conversions may be related to strong interactions between zirconia and the free radicals formed during degradation, giving rise to the nanoparticles having a catalytic effect on the PMMA degradation during the more advanced stages of degradation [22, 23].

TGA-FTIR analyses were done to establish the nature of the degradation product(s), and to confirm the observations from the kinetic analysis of the thermal degradation of PMMA and PMMA-zirconia (5 wt%). All the spectra almost perfectly match the known spectrum of methyl metacrylate (MMA), which confirms the primary degradation as that of de-polymerization (Figure 9). The peak around 2966 cm<sup>-1</sup> is assigned to the CH<sub>3</sub> and CH<sub>2</sub> stretching vibrations, whereas their bending vibration appears around 1451 cm<sup>-1</sup> for CH<sub>2</sub> and 1314 cm<sup>-1</sup> for CH<sub>3</sub>. The carbonyl absorption vibration appears around 1744 cm<sup>-1</sup> and the stretching vibration for C–O is around 1167 cm<sup>-1</sup>. The peak at 2336 cm<sup>-1</sup> is related to the asymmetric stretching mode of CO<sub>2</sub>. No new peaks or peak shifts were observed for the nanocomposite samples. There is a clear increase in peak intensity for all the characteristic peaks with increasing temperature, it reaches a maximum, and decreases again with further increase in temperature.

The PMMA-zirconia (5 wt%) sample shows the same spectra and a similar trend (Figure 9b). The peaks at 314°C for PMMA are more intense than the corresponding peaks of the PMMA nanocomposite. The intensities of the peaks for PMMA seem to reach a maximum between 346 and 360°C, while those of the nanocomposite reach a maximum at 360°C. This confirms that the initial release of MMA volatiles is retarded when zirconia nanoparticles are present, whether it is because of an inhibition of the decomposition process or because of a stronger interaction between zirconia and the MMA molecules. The interaction between PMMA or MMA and the zirconia nanoparticles therefore played a significant role in modifying the degradation kinetics.

In order to investigate this aspect, solid state NMR measurements were performed. The <sup>13</sup>C{<sup>1</sup>H} CP-MAS NMR spectra of PMMA and of the composite having 5% of zirconia are reported in Figure 10. Five peaks are present in all the spectra: peak 1 at 17 ppm is related to the methyl group, peak 2 at 45 ppm to the methylene group, peak 3 at 52 ppm to the quaternary carbon of polymeric chain, peak 4 at 56 ppm to the methoxyl group, and peak 5 at 177 ppm to the carbonyl carbon, according to literature [20]. No modification in the chemical shift and in the band shape is observed in the PMMA-ZrO<sub>2</sub> composite spectrum indicating that no chemical modification occurred in the polymer.

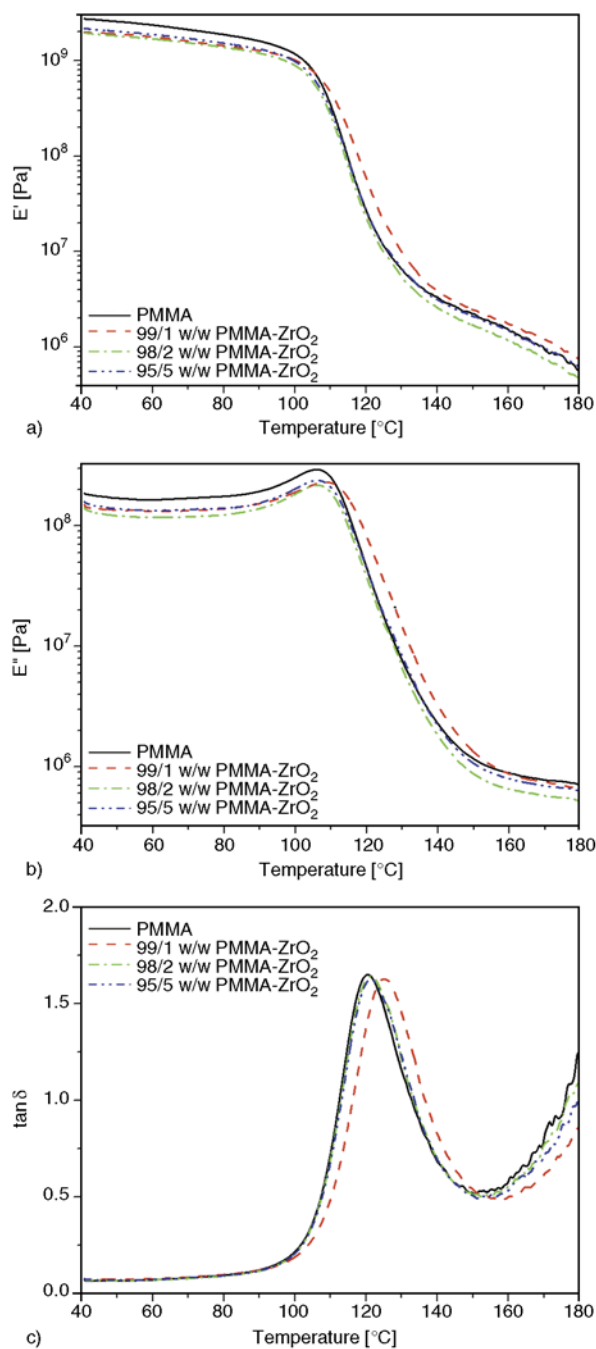


**Figure 6.** (a) Storage modulus, (b) loss modulus and (c)  $\tan \delta$  curves of PMMA and PMMA-ZrO<sub>2</sub> nanocomposites

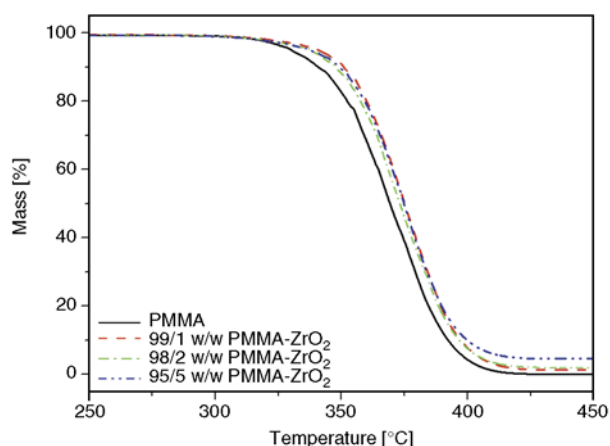


**Figure 7.** TGA curves of PMMA and PMMA-ZrO<sub>2</sub> nanocomposites

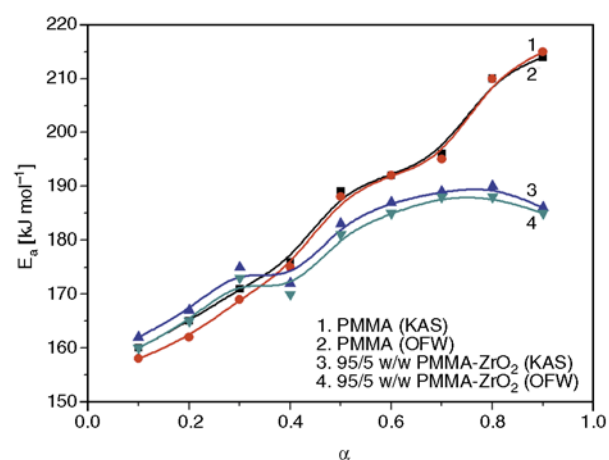


**Figure 8.**  $E_a$  values obtained by the OFW and KAS degradation kinetics methods

The spin-lattice relaxation time in the laboratory frame  $T_1(H)$ , and in the rotating frame  $T_{1\rho}(H)$ , and the cross-polarization time  $T_{CH}$  were determined through solid-state NMR measurements in order to evaluate the dynamic modifications occurring in the polymeric chain of the PMMA matrix after composite formation. The  $T_1(H)$ ,  $T_{1\rho}(H)$ , and  $T_{CH}$  values obtained from each peak in the <sup>13</sup>C spectra of all the samples are reported in Table 2.

**Table 2.** Relaxation time values for all the peaks in the <sup>13</sup>C spectra of the PMMA and the PMMA-ZrO<sub>2</sub> composite having the 5 wt% of filler

ppm	$T_1(H)$ [s]		$T_{1\rho}(H)$ [ms]		$T_{CH}$ [ $\mu$ s]	
	PMMA	PMMA-ZrO <sub>2</sub>	PMMA	PMMA-ZrO <sub>2</sub>	PMMA	PMMA-ZrO <sub>2</sub>
178	0.70±0.02	0.71±0.02	18.1±0.5	22.9±0.9	1306±167	1105±126
56	0.71±0.03	0.70±0.03	20.4±0.9	19.5±0.7	254±79	185±26
52	0.71±0.01	0.70±0.01	16.2±0.2	20.7±0.3	339±42	268±22
45	0.71±0.01	0.69±0.01	17.0±0.2	19.6±0.3	614±33	713±41
17	0.71±0.01	0.74±0.02	19.3±0.4	21.9±0.3	320±36	261±21

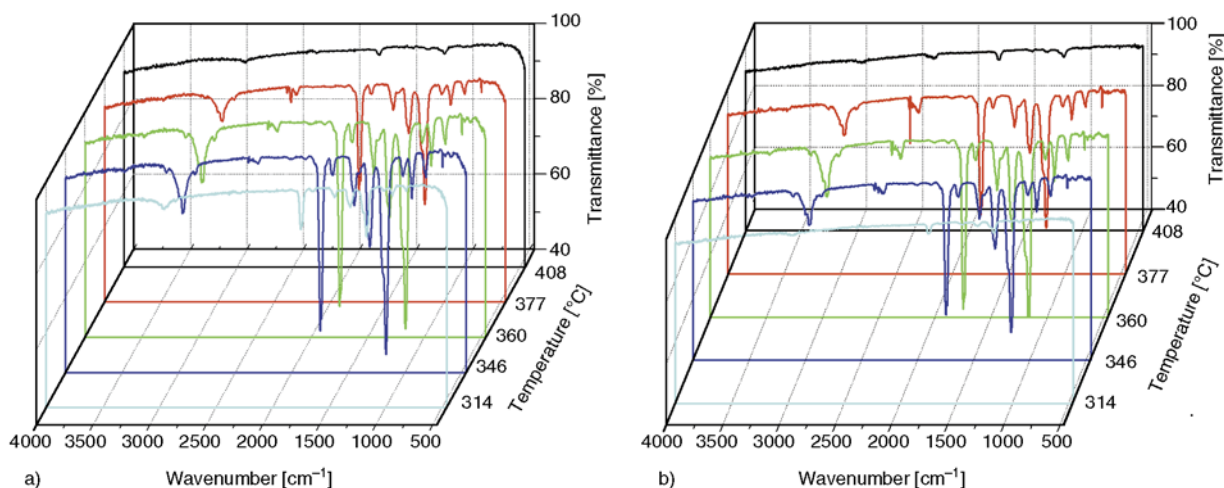


**Figure 9.** FTIR spectra at different temperatures during the thermal degradation in a TGA of (a) PMMA and (b) 95/5 w/w PMMA/ZrO<sub>2</sub> at a heating rate of 10°C min<sup>-1</sup>

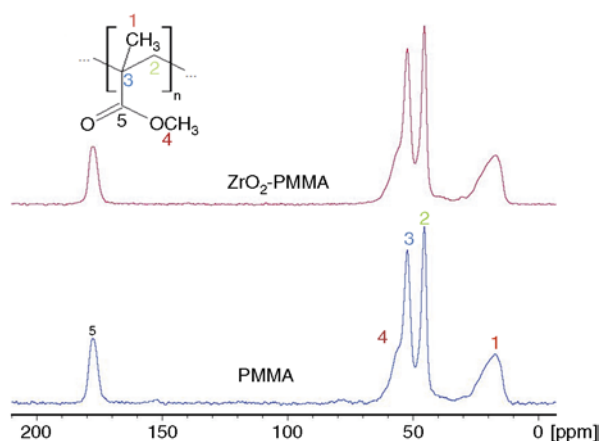


**Figure 10.** <sup>13</sup>C{<sup>1</sup>H} CP-MAS NMR spectra of PMMA and the 95/5 w/w PMMA/ZrO<sub>2</sub> nanocomposite. Numbers on the peaks identify the carbon atoms

The presence of the filler in the PMMA matrix did not significantly affect the  $T_1(H)$  values. This indicates that the composite was dynamically homogeneous in a range from tens to hundreds of nanometres. The presence of the ZrO<sub>2</sub> in the PMMA causes an increase of the  $T_{1\rho}(H)$  values indicating an increase in the polymer stiffness due to the presence of the filler. This effect is correlated with distances ranging from tens to hundreds of angstroms. In fact, the  $T_{1\rho}(H)$  parameter is inversely proportional to the spectral density of motion in the kHz frequency region. These motions reflect the dynamic behaviour of a polymeric chain in a range of a few nanometres. Larger  $T_{1\rho}(H)$  values result in an increase in the rigidity of a polymer. The  $T_{CH}$  value decrease indicates that there was an increase in the heteronu-

clear dipolar interactions involving the carbons and the surrounding hydrogen nuclei indicating an increase in the polymer rigidity [24, 25]. It is, however, possible that the effect is not strong enough to give rise to an observable change in a macroscopic property like the  $T_g$  of a polymer.

#### 4. Conclusions

Zirconia was successfully prepared by a sol-gel method and XRD analysis confirmed that the powder was composed of a mixture of tetragonal and monoclinic Baddeleyite. The elemental analysis showed evidence of the presence of carbon in the powder. PMMA-zirconia nanocomposites were prepared using a melt compounding method and were systematically investigated as a function of zirconia amount from 1 to 5 wt%. The XRD results showed that the zirconia nanoparticles maintained their structure and did not induce orientation of the PMMA chains. TEM analysis showed that the nanoparticles were well dispersed in the PMMA matrix, with some agglomerates, especially for the highest investigated zirconia content. NMR analysis indicated that the filler increased the rigidity of the polymer.

The char content values from TGA confirmed the homogenous dispersion by zirconia nanoparticles within PMMA matrix at low zirconia contents. The degradation of the polymer and the release of volatile products occurred at higher temperatures in the presence of zirconia and an increase in zirconia content showed negligible influence on the thermal

stability of PMMA. The presence of the nanoparticles also reduced the activation energy of degradation of PMMA at higher conversions.

### Acknowledgements

The authors would like to thank MIUR for supporting this research through the COOPERLINK 2009 Prot. CII098ZQLT ‘Sintesi e caratterizzazione di compositi polimetilmetacrilato e nano-TiO<sub>2</sub>/-ZrO<sub>2</sub>’. The National Research Foundation in South Africa and the University of the Free State are acknowledged for financial support of the research. TEM-EDS and NMR experimental data were provided by Centro Grandi Apparecchiature–UniNetLab–Università di Palermo funded by P.O.R. Sicilia 2000–2006, Misura 3.15 Azione C Quota Regionale.

### References

- [1] Zufikar M. A., Mohammad A. W., Hilal N.: Preparation and characterization of novel porous PMMA-SiO<sub>2</sub> hybrid membranes. *Desalination*, **192**, 262–270 (2006). DOI: [10.1016/j.desal.2005.09.022](https://doi.org/10.1016/j.desal.2005.09.022)
- [2] Sun X., Chen X., Liu X., Qu S.: Optical properties of poly(methyl methacrylate)-titania nanostructure thin films containing ellipsoid-shaped titania nanoparticles from ex-situ sol-gel method at low growth temperature. *Applied Physics B: Lasers and Optics*, **103**, 391–398 (2011). DOI: [10.1007/s00340-010-4265-6](https://doi.org/10.1007/s00340-010-4265-6)
- [3] Ahmad S., Ahmad S., Agnihotry S. A.: Synthesis and characterization of *in situ* prepared poly(methyl methacrylate) nanocomposites. *Bulletin of Materials Science*, **30**, 31–35 (2007). DOI: [10.1007/s12034-007-0006-9](https://doi.org/10.1007/s12034-007-0006-9)
- [4] Xie X-L., Liu Q-X., Li R. K-Y., Zhou X-P., Zhang Q-X., Yu Z-Z., Mai Y-W.: Rheological and mechanical properties of PVC/CaCO<sub>3</sub> nanocomposites prepared by *in situ* polymerization. *Polymer*, **45**, 6665–6673 (2004). DOI: [10.1016/j.polymer.2004.07.045](https://doi.org/10.1016/j.polymer.2004.07.045)
- [5] Saladino M. L., Zanutto A., Martino D. C., Spinella A., Nasillo G., Caponetti E.: Ce:YAG nanoparticles embedded in a PMMA matrix: Preparation and characterization. *Langmuir*, **26**, 13442–13449 (2010). DOI: [10.1021/la9042809](https://doi.org/10.1021/la9042809)
- [6] Hu Y., Zhou S., Wu L.: Surface mechanical properties of transparent poly(methyl methacrylate)/zirconia nanocomposites prepared by *in situ* bulk polymerization. *Polymer*, **50**, 3609–3616 (2009). DOI: [10.1016/j.polymer.2009.03.028](https://doi.org/10.1016/j.polymer.2009.03.028)
- [7] Wang H., Xu P., Zhong W., Shen L., Du Q.: Transparent poly(methyl methacrylate)/silica/zirconia nanocomposites with excellent thermal stabilities. *Polymer Degradation and Stability*, **87**, 319–327 (2005). DOI: [10.1016/j.polymdegradstab.2004.08.015](https://doi.org/10.1016/j.polymdegradstab.2004.08.015)
- [8] Wang Y., Zhang D., Shi L., Li L., Zhang J.: Novel transparent ternary nanocomposite films of trialkoxysilane-capped poly(methyl methacrylate)/zirconia/titania with incorporating networks. *Materials Chemistry and Physics*, **110**, 463–470 (2008). DOI: [10.1016/j.matchemphys.2008.03.006](https://doi.org/10.1016/j.matchemphys.2008.03.006)
- [9] Atik M., Luna F. P., Messaddeq S. H., Aegerter V.: Ormocer (ZrO<sub>2</sub>-PMMA) films for stainless steel corrosion protection. *Journal of Sol-Gel Science and Technology*, **8**, 517–522 (1997). DOI: [10.1007/BF02436892](https://doi.org/10.1007/BF02436892)
- [10] Hu Y., Gu G., Zhou S., Wu L.: Preparation and properties of transparent PMMA/ZrO<sub>2</sub> nanocomposites using 2-hydroxyethyl methacrylate as a coupling agent. *Polymer*, **52**, 122–129 (2011). DOI: [10.1016/j.polymer.2010.11.020](https://doi.org/10.1016/j.polymer.2010.11.020)
- [11] Messaddeq S. H., Pulcinelli S. H., Santilli C. V., Guastaldi A. C., Massaddeq Y.: Microstructure and corrosion resistance of inorganic-organic (ZrO<sub>2</sub>-PMMA) hybrid coating on stainless steel. *Journal of Non-Crystalline Solids*, **247**, 164–170 (1999). DOI: [10.1016/S0022-3093\(99\)00058-7](https://doi.org/10.1016/S0022-3093(99)00058-7)
- [12] Wang X., Wu L., Li J.: Influence of nanozirconia on the thermal stability of poly(methyl methacrylate) prepared by *in situ* bulk polymerization. *Journal of Applied Polymer Science*, **117**, 163–170 (2010). DOI: [10.1002/app.31970](https://doi.org/10.1002/app.31970)
- [13] Wang X., Wu L., Li J.: Synergistic flame retarded poly(methyl methacrylate) by nano-ZrO<sub>2</sub> and triphenylphosphate. *Journal of Thermal Analysis and Calorimetry*, **103**, 741–746 (2011). DOI: [10.1007/s10973-010-1050-z](https://doi.org/10.1007/s10973-010-1050-z)
- [14] Bondioli F., Cannillo V., Fabbri E., Messori M.: Preparation and characterization of epoxy resins filled with submicron spherical zirconia particles. *Polimery*, **51**, 794–798 (2006).
- [15] Young R. A.: *The Rietveld method*. Oxford University Press, Oxford (1993).
- [16] Lutterotti L., Gialanella S.: X-ray diffraction characterization of heavily deformed metallic specimens. *Acta Metallurgica*, **46**, 101–110 (1998). DOI: [10.1016/S1359-6454\(97\)00222-X](https://doi.org/10.1016/S1359-6454(97)00222-X)
- [17] Hartmann S. R., Hahn E. L.: Nuclear double resonance in the rotating frame. *Physical Review Online Archive*, **128**, 2042–2053 (1962). DOI: [10.1103/PhysRev.128.2042](https://doi.org/10.1103/PhysRev.128.2042)
- [18] Lau C., Mi Y.: A study of blending and complexation of poly(acrylic acid)/poly(vinyl pyrrolidone). *Polymer*, **43**, 823–829 (2002). DOI: [10.1016/S0032-3861\(01\)00641-3](https://doi.org/10.1016/S0032-3861(01)00641-3)
- [19] Conte P., Spaccini R., Piccolo A.: State of the art of CPMAS <sup>13</sup>C-NMR spectroscopy applied to natural organic matter. *Progress in Nuclear Magnetic Resonance Spectroscopy*, **44**, 215–223 (2004). DOI: [10.1016/j.pnmrs.2004.02.002](https://doi.org/10.1016/j.pnmrs.2004.02.002)

- [20] Alamo R. G., Blanco J. A., Carrilero I., Fu R.: Measurement of the  $^{13}\text{C}$  spin–lattice relaxation time of the non-crystalline regions of semicrystalline polymers by a cp MAS-based method. *Polymer*, **43**, 1857–1865 (2002).  
DOI: [10.1016/S0032-3861\(01\)00761-3](https://doi.org/10.1016/S0032-3861(01)00761-3)
- [21] Saladino M. L., Motaung T. E., Luyt A. S., Spinella A., Nasillo G., Caponetti E.: The effect of silica nanoparticles on the morphology, mechanical properties and thermal degradation kinetics of PMMA. *Polymer Degradation and Stability*, **97**, 452–459 (2012).  
DOI: [10.1016/j.polymdegradstab.2011.11.006](https://doi.org/10.1016/j.polymdegradstab.2011.11.006)
- [22] Vassiliou A. A., Chrissafis K., Bakiaris D. N.: Thermal degradation kinetics of *in situ* prepared PET nanocomposites with acid-treated multi-walled carbon nanotubes. *Journal of Thermal Analysis and Calorimetry*, **100**, 1063–1071 (2010).  
DOI: [10.1007/s10973-009-0426-4](https://doi.org/10.1007/s10973-009-0426-4)
- [23] Majoni S., Su S., Hossenlopp J. M.: The effect of boron-containing layered hydroxy salt (LHS) on the thermal stability and degradation kinetics of poly (methyl methacrylate). *Polymer Degradation and Stability*, **95**, 1593–1604 (2010).  
DOI: [10.1016/j.polymdegradstab.2010.05.033](https://doi.org/10.1016/j.polymdegradstab.2010.05.033)
- [24] Geppi M., Ciardelli F., Veracini C. A., Forte C., Cecchin G., Ferrari P.: Dynamics and morphology of polyolefinic elastomers by means of  $^{13}\text{C}$  and  $^1\text{H}$  solid-state n.m.r. *Polymer*, **38**, 5713–5723 (1997).  
DOI: [10.1016/S0032-3861\(97\)00134-1](https://doi.org/10.1016/S0032-3861(97)00134-1)
- [25] Koenig J. L.: *Spectroscopy of polymers*. Elsevier Science (1999).

# Structure, morphology, and mechanical properties of polysiloxane elastomer composites prepared by *in situ* polymerization of zinc dimethacrylate

Y. Meng<sup>1,2</sup>, Z. Wei<sup>1,2</sup>, Y. L. Lu<sup>1,2</sup>, L. Q. Zhang<sup>1,2\*</sup>

<sup>1</sup>Key Laboratory of Beijing City for Preparation and Processing of Novel Polymer Materials, Beijing University of Chemical Technology, 100029 Beijing, PR China

<sup>2</sup>State Key Laboratory of Organic-Inorganic Composites, Beijing University of Chemical Technology, 100029 Beijing, PR China

Received 18 March 2012; accepted in revised form 24 May 2012

**Abstract.** Methyl vinyl silicone rubber/zinc dimethacrylate (VMQ/ZDMA) composites were prepared through *in situ* polymerization of ZDMA monomers during the peroxide curing. The polymerization conversion of ZDMA and morphology of the VMQ/ZDMA composites were studied. The results showed that most of the ZDMA monomers participated in the *in situ* polymerization during the cross-linking of the VMQ matrix and uniform nanophases were formed in the composites. The ‘dissolving-diffusion’ model was used to explain the micro-nano transformation of ZDMA. According to the model, a uniform nano-dispersed structure could be obtained through the *in situ* reaction even though the initial dispersion of ZDMA in the blends was poor. In addition, tensile tests of VMQ/ZDMA composites showed that ZDMA had a significant reinforcement on the mechanical properties of VMQ, and the best mechanical properties were obtained when the amounts of peroxide and ZDMA were 5 and 40 phr, respectively. The gross crosslink density and ionic crosslink density increased as the amount of ZDMA increased, but the covalent crosslink density decreased slightly. These results indicated that the ionic crosslink structure had a significant effect on the mechanical properties of VMQ/ZDMA composites.

**Keywords:** nanocomposites, reinforcements, silicone rubber, zinc dimethacrylate

## 1. Introduction

Because of its unique chemical structure, silicone rubber exhibits a list of excellent properties including a large degree of flexibility, climate and oxidation resistance, thermal stability, low electrical conductivity, biocompatibility, low surface tension, and high permeability [1, 2]. As a result of these excellent properties, silicone rubber is widely used in aerospace industry, automobile industry, electronic industry and biomedical applications [2–5]. However, silicone rubber has low mechanical strength because of the weak intermolecular forces between polymer chains [6], and the weak mechanical prop-

erties seriously limit the practical application of silicone rubber [7]. Therefore, improving the mechanical properties of silicone rubber is of foremost importance. At present, fumed or precipitated silica is most commonly used to reinforce silicone rubber; other fillers like clays, graphite, carbon nanotubes, and polyhedral oligomeric silsesquioxanes have also been reported to be effective reinforcing agents [8–12]. However, it is very difficult for nano-sized particles to disperse in a polymer matrix with low viscoelasticity, and a long mixing time and high dispersion energy are required to obtain fine dispersion. Hence, it is meaningful to find new methods

\*Corresponding author, e-mail: [zhanglq@mail.buct.edu.cn](mailto:zhanglq@mail.buct.edu.cn)



and reinforcing agents with good processability, fine dispersion, and high reinforcing effect to improve the mechanical properties of silicone rubber. The ‘*in situ* reaction’ technique is an effective method to obtain fine dispersion of fillers in a polymer matrix. Generally, two ‘*in situ* reaction’ methods can be used for the preparation of rubber composites: the ‘sol-gel’ method and the ‘*in situ* polymerization’ method. An example of the ‘sol-gel’ method is the ‘sol-gel’ hydrolysis of alkoxy silanes (organosilicates) to form silica *in situ* within a polymer matrix [13–17]. Ning *et al.* [15] carried out many studies on reinforcing polydimethylsiloxane by the *in situ* precipitation of silica, and found that the generated particles were dispersed at the nano-level and considerable reinforcement of the elastomer could be achieved. Other particles generated *in situ*, for example, titania, have been also reported to have a good reinforcement on elastomers [16, 17]. However, the cost of this method is higher than that of conventional ‘*ex situ*’ methods [8]. In the ‘*in situ* polymerization’ method, reactive monomers are polymerized to generate reinforcing particles. Among the reactive monomers, metal salts of unsaturated carboxylic acids are the typical monomers widely used to improve the properties of elastomers [18–24, 26–32]. Wen *et al.* [21] synthesized particles of acrylate(1,10-phenanthroline)bis(2-thenoyltrifluoroacetate) samarium [Sm(TTA)<sub>2</sub>-(AA)(Phen)], which combined the good fluorescence property of Sm(TTA)<sub>3</sub>(Phen) and the reactivity of acrylic acid with radicals, and used the particles to prepare HNBR/Sm(TTA)<sub>2</sub>-(AA)(Phen) composites. It was suggested that a fine dispersion of the particles in HNBR was obtained due to the *in situ* reaction. Lu *et al.* [22, 23] added zinc dimethacrylate (ZDMA) into different kinds of elastomers and found that uniform nanophases were formed by the *in situ* polymerization of ZDMA and the mechanical properties of the resulting composites were significantly improved. The ‘*in situ* polymerization’ method is relatively simpler and less expensive than the ‘sol-gel’ method, and its reinforcing effect is more remarkable.

In this study, we attempted to improve the properties of methyl vinyl silicone rubber (VMQ) by the ‘*in situ* reaction’ method. We selected ZDMA as the

reinforcing agent because ZDMA shows better reinforcement than most of other metal salts of unsaturated carboxylic acids do [26]. VMQ/ZDMA composites with different amounts of peroxide and ZDMA were prepared, and the polymerization conversion of ZDMA, the morphology and the crosslink structure of these VMQ/ZDMA composites were studied. The effect of peroxide content and ZDMA content on the mechanical properties of the VMQ/ZDMA composites was also investigated.

## 2. Experimental

### 2.1. Materials

VMQ having 0.15% vinyl substituent and a molecular weight of 550 000 g/mol was obtained from Chenguang Chemical Research Institute, Sichuan, China. Zinc Dimethacrylate (ZDMA) (grade Saret 634) was purchased from Sartomer Co., USA. The peroxide used was 2,5-bis(tert-butylperoxy)-2,5-dimethyl hexane (DBPMH), which was purchased from Akzo Nobel Cross-Linking Peroxide Co., Ltd., Ningbo, China.

### 2.2. Preparation of VMQ/ZDMA composites

At room temperature, silicone rubber and ZDMA were mixed on a two-roll mill for 15 minutes, followed by the addition of DBPMH. The resulting blends were cured at 160°C in an electrically heated hydraulic press for their respective optimal cure time ( $t_{90}$ ) obtained from the curing curve.

The ZDMA/DBPMH blend was prepared as follows: (1) the ZDMA and DBPMH (ZDMA/DBPMH 6:1, weight ratio) were dispersed in acetone to obtain a turbid liquid (DBPMH can dissolve in acetone but ZDMA can't); (2) after being stirred for 24 hours at room temperature, the prepared turbid liquid was dried at 60°C to remove acetone, and then the ZDMA/DBPMH blend was obtained.

### 2.3. Measurements

#### 2.3.1. Curing characteristics of VMQ blends

Curing characteristics of VMQ blends were determined with an oscillating disc rheometer (M2000-FA) made by Gotech Testing Machines (Dong Guan) Co. LTD. The curing dynamics of the rubbers were characterized at 160°C with an angular displacement of 0.5°.

### 2.3.2. Fourier transform infrared spectroscopy (FTIR)

FTIR analysis was performed on an FTIR spectrometer (Tensor 27, Bruker Optik GmbH Co., Germany). The scan range was 4000 to 600  $\text{cm}^{-1}$  with a resolution of 4  $\text{cm}^{-1}$ .

### 2.3.3. X-ray diffraction (XRD)

X-ray diffraction (XRD) analysis was carried out on a Rigaku D/Max 2500 X-ray diffractometer (Rigaku Inc., Sendagaya, Japan) with  $\text{Cu K}\alpha$  radiation (at 40 kV and 100 mA). The scanning was performed in the diffraction angle ( $2\theta$ ) range from 3 to 40° at a rate of 5°/min.

### 2.3.4. Scanning electron microscopy (SEM)

Scanning electron microscopy observations were performed on an S4700 field emission scanning electron microscope (Hitachi Co., Japan) at a voltage of 20 kV.

### 2.3.5. Polarizing optical microscopy (POM)

The VMQ/ZDMA blends before vulcanization were difficult to observe on a scanning electron microscope or transmission electron microscope because they were very viscous fluids. Instead, the VMQ/ZDMA blends were observed on a polarizing optical microscope (ZEISS Axioskop 40A, Germany). In this technique, the samples were heated to 160°C on a hot-stage, and the morphology change during the peroxide curing was recorded.

### 2.3.6. Transmission electron microscopy (TEM) and high resolution transmission electron microscopy (HRTEM)

Both transmission electron microscopy (TEM) and high resolution transmission electron microscopy (HRTEM) were performed to observe the morphology of VMQ/ZDMA composites. TEM was carried out on an H-800-1 transmission electron microscope (Hitachi Co., Japan) and HRTEM was carried out on a JEM-3010 transmission electron microscope (Hitachi Co., Japan). The thin sections for TEM and HRTEM experiments were cut by a microtome at -100°C and collected on cooper grids.

### 2.3.7. Differential scanning calorimetry (DSC)

DSC measurements were carried out on STARE system DSC 1 instrument (Mettler-Toledo Interna-

tional Inc., Switzerland). The sample was heated from 30 to 350°C under nitrogen atmosphere with the heating rate of 10°C/min. For isothermal DSC analysis, the sample were heated to 160°C rapidly and kept at 160°C for 20 minutes.

### 2.3.8. Mechanical properties

Tensile tests were performed on a CTM 4104 tensile tester (SANS, Shenzhen, China) at a cross-head speed of 500 mm/min and a temperature of 25±2°C according to Chinese Standards GB/T528-1998 and GB/T529-1999.

### 2.3.9. Measurements of crosslink density

The crosslink density was determined by equilibrium swelling. A certain amount of samples (about 0.15 g) was swollen in toluene in a sealed vessel at 25±0.2°C for 5 days. Then the samples were taken out and immediately weighed on an analytical balance after the surface toluene was blotted off with tissue paper. Subsequently, the samples were dried in a vacuum oven at 80°C for one day to remove all the solvent and weighed again. The crosslink density of the samples ( $\nu_e$ ) was calculated by the Flory-Rehner equation (Equation (1)) [25]:

$$\nu_e = \frac{\ln(1 - \nu_2) + \nu_2 + \chi\nu_2}{V_0 \left( \nu_2^{1/3} - \frac{\nu_2}{2} \right)} \quad (1)$$

where  $V_0$  is the molar volume of the solvent (106.54  $\text{cm}^3/\text{mol}$  for toluene),  $\chi$  is the interaction parameter of VMQ and toluene and is taken as 0.465 here [6], and  $\nu_2$  is the volume fraction of the polymer in the vulcanizate swollen to equilibrium. The parameter  $\nu_2$  was calculated by Equation (2):

$$\nu_2 = \frac{\frac{m_0\phi(1-\alpha)}{\rho_2}}{\frac{m_0\phi(1-\alpha)}{\rho_2} + \frac{m_1 - m_2}{\rho_1}} \quad (2)$$

where  $m_0$ ,  $m_1$  and  $m_2$  are the masses of original sample, sample swollen to equilibrium, and dried sample, respectively,  $\phi$  is the mass fraction of VMQ in the original sample,  $\rho_1$  and  $\rho_2$  are the density of toluene and density of gum VMQ vulcanizate, respectively, and  $\alpha$  is the mass loss of gum VMQ vulcanizate during swelling.

For the measurements of covalent crosslink density, samples (about 0.5 mm in thickness) were swollen

in a mixture of dilute hydrochloric acid (1 mol/L) and acetone (the volume ratio of dilute hydrochloric acid and acetone is 1:9) for 2 days to destroy the ionic network, and then placed for 3 days in a Soxhlet extractor containing acetone, and vacuum dried. The crosslink density of samples before acidolysis ( $v_e$ ) and the crosslink density of samples after acidolysis ( $v_{e1}$ ) present the gross crosslink density and the covalent crosslink density, respectively, and the ionic crosslink density ( $v_{e2}$ ) was calculated by subtracting  $v_{e1}$  from  $v_e$ .

### 3. Results and discussion

#### 3.1. Polymerization conversion of ZDMA

To verify the *in situ* reaction of ZDMA in VMQ matrix during the peroxide curing, transmission FTIR spectroscopy was performed. The FTIR spectra of ZDMA, ZDMA after heat treatment at 160°C for 15 min (the optimum curing time  $t_{90}$  of the blend), ZDMA/DBPMH blend, ZDMA/DBPMH blend after heat treatment at 160°C for 15 min, VMQ/ZDMA blend, and VMQ/ZDMA composite are shown in Figure 1. In the spectrum of ZDMA (Figure 1 curve a), the bands at 1560 and 1420  $\text{cm}^{-1}$  are attributed to the symmetrical and anti-symmetrical vibrations of  $\text{COO}^-$ ; the band at 1651  $\text{cm}^{-1}$  is assigned to the stretching vibration of  $\text{C}=\text{C}$ . After heat treatment, those characteristic peaks of ZDMA can be still observed (Figure 1 curve b), illustrating that ZDMA is stable at 160°C. For ZDMA/DBPMH blend (Figure 1 curve c and curve d), however, the band at 1651  $\text{cm}^{-1}$  has disappeared after the heat

treatment. This result confirms that ZDMA has a high reactivity and most of ZDMA particles have reacted with the peroxide. In the spectrum of VMQ/ZDMA blend (Figure 1 curve e), the two sharp bands at 1015  $\text{cm}^{-1}$  and 1087  $\text{cm}^{-1}$  are attributed to the stretching vibration of  $\text{Si-O-Si}$ , and the sharp band at 796  $\text{cm}^{-1}$  is attributed to the stretching vibration of  $\text{Si-C}$ . The  $\text{C}=\text{C}$  characteristics of ZDMA can be still observed in the blends, although the intensity of the peaks decreases as a result of the concentration effect. In the spectrum of VMQ/ZDMA composite (Figure 1 curve f), the band at 1651  $\text{cm}^{-1}$  has disappeared, indicating that most of the ZDMA participated in the *in situ* reaction in the VMQ matrix during the peroxide curing.

X-ray diffraction (XRD) analysis was carried out to further verify the *in situ* reaction of ZDMA during the peroxide curing. Figure 2 shows the XRD patterns of ZDMA, ZDMA after heat treatment at 160°C for 15 min, ZDMA/DBPMH blend, ZDMA/DBPMH blend after heat treatment at 160°C for 15 min, VMQ/ZDMA blend, and VMQ/ZDMA composite. ZDMA is highly crystalline and shows strong peaks at  $2\theta$  of 9.8, 11.0, 11.9, 16.7 and 22.1°, as shown in Figure 2 curve a. From the XRD patterns of ZDMA before and after heat treatment, it can be seen that there is almost no difference, meaning that the crystal structure of ZDMA was not destroyed by the heat treatment. The main characteristic peaks of ZDMA can be still observed in the ZDMA/DBPMH blend before heat treatment, as shown in Figure 2 curve c; after heat treatment, however, none of

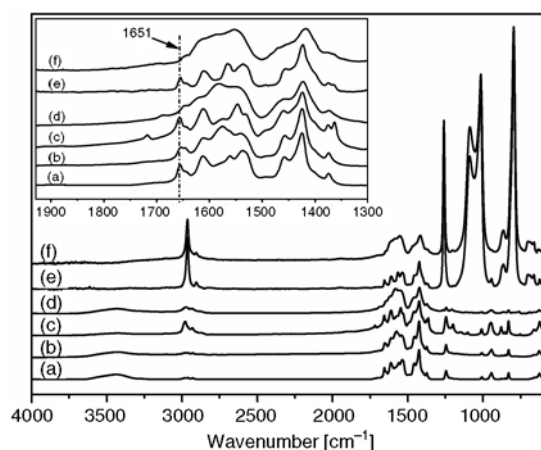


**Figure 1.** FTIR spectra of ZDMA (a) before and (b) after heat treatment, ZDMA/DBPMH blend (c) before and (d) after heat treatment and VMQ/ZDMA (100/40) composites containing 5 phr DBPMH (e) before and (f) after cured

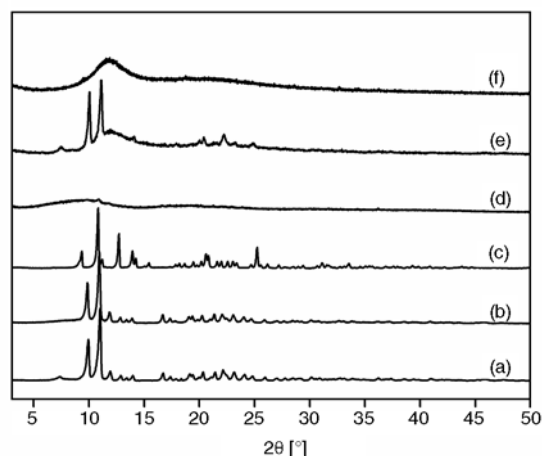


**Figure 2.** XRD patterns of ZDMA (a) before and (b) after heat treatment, ZDMA/DBPMH blend (c) before and (d) after heat treatment and VMQ/ZDMA (100/40) composites containing 5 phr DBPMH (e) before and (f) after cured

those peaks can be detected (Figure 2 curve d). The result reveals that almost all the ZDMA crystals have transformed to amorphous state, which further confirms the reaction of ZDMA. In the pattern for the VMQ/ZDMA blend (Figure 2 curve e), the strong characteristic peaks of ZDMA at  $2\theta = 9.8$  and  $11.0^\circ$  can be observed clearly. However, only a very broad diffraction peak of the VMQ matrix at  $2\theta = 11.8^\circ$  can be detected in the VMQ/ZDMA composite, as shown in Figure 2 curve f. The result suggests that most of the ZDMA particles have participated in the *in situ* reaction during the peroxide curing and formed amorphous phases, consisting with the conclusion from the FTIR analysis.

On the basis of the above results and the results of previous studies on the *in situ* reactions of ZDMA [22, 27, 28], the possible chemical reactions in the VMQ/ZDMA blend during the peroxide curing are represented in Figure 3. During the peroxide curing, the peroxide is first decomposed to form free radi-

cals, which will react with the ZDMA monomers and silicone rubber chains to form ZDMA radicals and VMQ radicals, respectively. A ZDMA radical initiates its monomer to form a poly-ZDMA radical, which will be terminated with another poly-ZDMA radical to form poly-ZDMA or terminated with a VMQ radical to form grafted poly-ZDMA. Simultaneously, the covalent bonds between the rubber chains are formed by the reaction of VMQ radicals.

### 3.2. Morphology analysis

The SEM image in Figure 4a shows the morphology of the original ZDMA particles. These particles are in the shape of rod (ratio of length to diameter,  $L/D = 5$  and length  $5\text{--}50\ \mu\text{m}$ ). The polarizing optical microscopy (POM) image of the VMQ/ZDMA blend is shown in Figure 4b. The dark phase is the silicone rubber matrix (silicone rubber is amorphous at room temperature), and the bright phase represents the ZDMA crystals. The size and shape of the ZDMA particles in the VMQ matrix don't change much over those of the original ZDMA particles shown in the SEM image (Figure 4a) because the shear stress generated by the silicone rubber is too low to grind the ZDMA particles. It implies that it is difficult to get a good dispersion of ZDMA in VMQ matrix via simple mechanical blending. After curing, however, the bright phases have darkened or disappeared, as shown in Figure 4c, implying that the crystalline structure of ZDMA was destroyed in the peroxide curing, possibly because of the *in situ* reaction of ZDMA. In the cured VMQ/ZDMA composites, some amorphous particles at the micro-level can be observed. These particles are probably composed of unreacted ZDMA and poly-ZDMA particles generated by the polymerization of ZDMA.

Some previous studies focused on the transformation of metal salts of unsaturated carboxylic acids

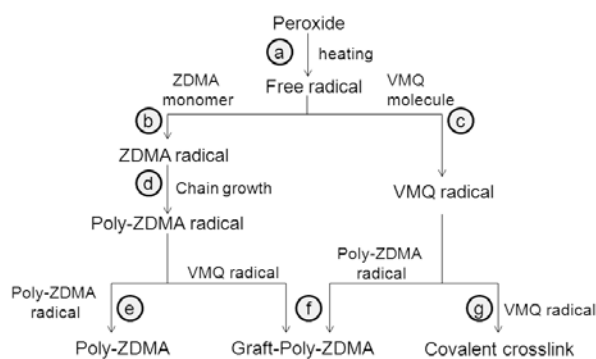


**Figure 3.** In-situ reaction in VMQ/ZDMA blend during peroxide curing: (a) decomposition of peroxide by heating, (b) ZDMA is initiated to form ZDMA radical, (c) VMQ is initiated to form VMQ radical, (d) chain growth of poly-ZDMA, (e) termination of poly-ZDMA chain, (f) graft reaction between VMQ and poly-ZDMA, and (g) generation of covalent crosslinks

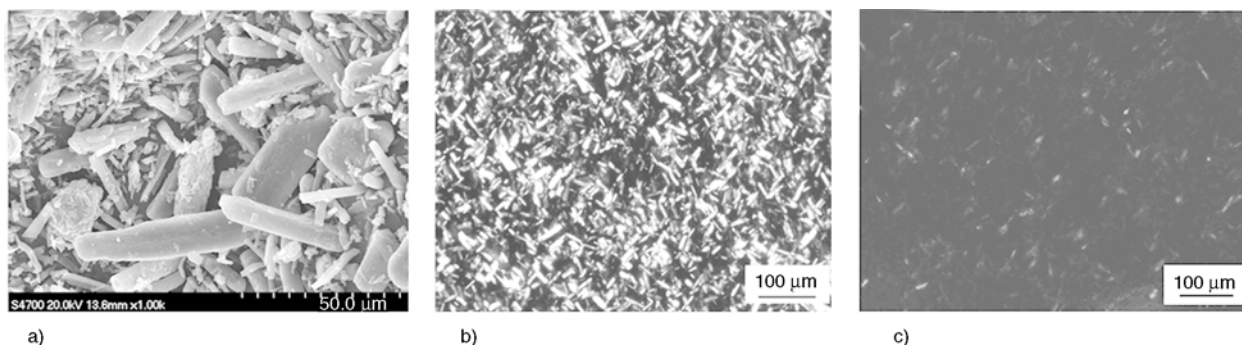


**Figure 4.** (a) SEM micrograph of ZDMA, and POM images of (b) uncured and (c) cured VMQ/ZDMA (100/40) composites containing 5 phr DBPMH

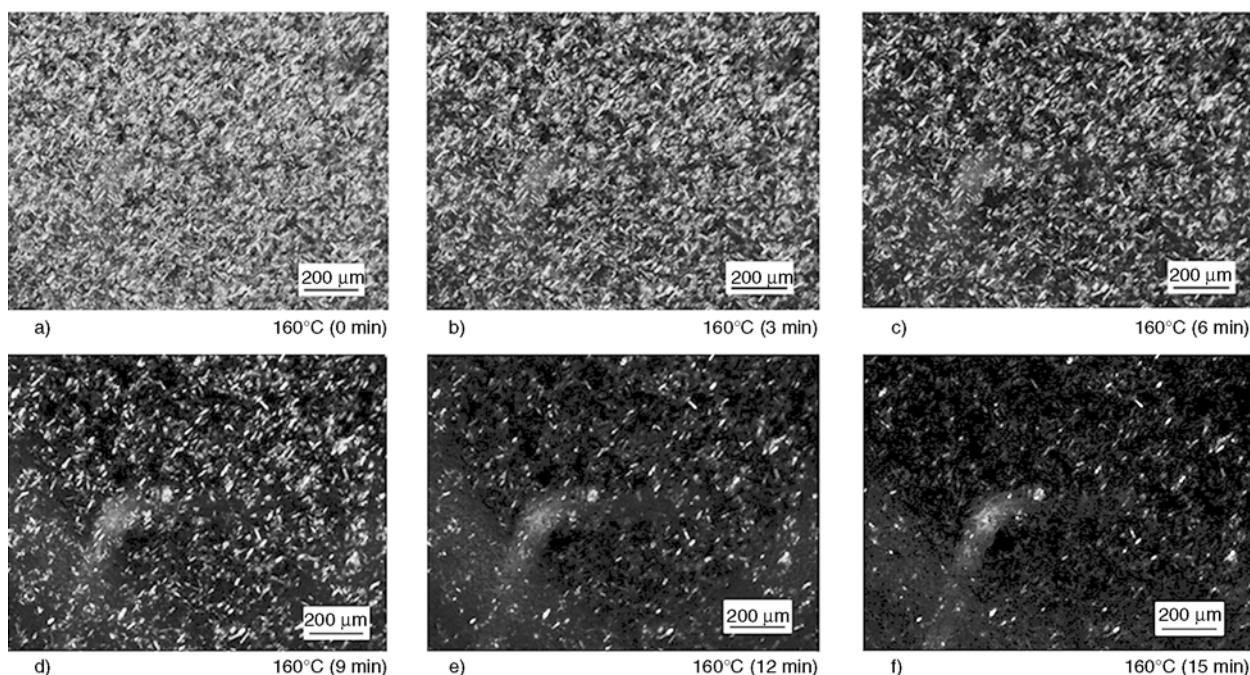


**Figure 5.** POM images of VMQ/ZDMA blends (100/40) containing 5 phr DBPMH during the heat treatment

by contrasting the morphology of the vulcanizates to that of the blends [23, 27]. In the present study, we used POM to observe the transformation of ZDMA crystals *in situ* during the peroxide curing. The change of the ZDMA crystals, as shown in Figure 5, was recorded by the polarizing optical microscope for 15 minutes. During the peroxide curing, the size of ZDMA crystals decreases gradually, and almost all the crystals disappear at the end. As illustrated in the XRD analysis, the reaction of ZDMA induced by peroxide radicals can destroy the crystalline structure. Therefore, the disappearance of ZDMA crystals in the VMQ/ZDMA blend during the peroxide curing is probably attributed to the *in situ* reaction of ZDMA. Besides, the melting of ZDMA crystals and the dissolving of ZDMA into silicone rubber are also possible reasons for the disappearance of ZDMA crystals. To further study the transformation of ZDMA crystals in silicone rubber at high temperature, the thermal behavior of ZDMA was investigated by DSC, as shown in Figure 6. The DSC heating curve (Figure 6a) shows two endothermic peaks at 186 and 218°C, corresponding to two different ZDMA crystalline structure. At high temperature (about 300°C), a strong exothermic peak can be observed, indicating that some reaction of ZDMA occurs. In the isothermal DSC curve of ZDMA at 160°C (Figure 6b), neither endothermic nor exothermic peak can be observed, implying that

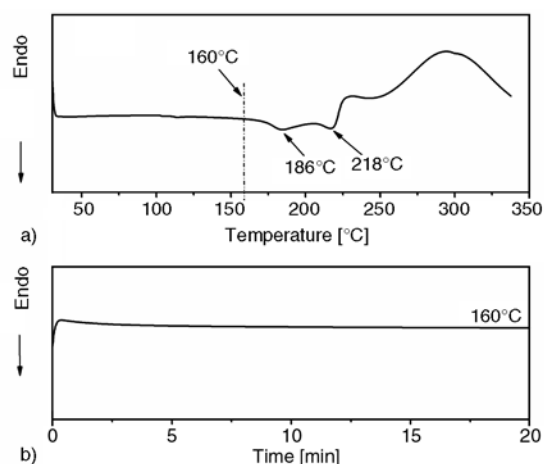


**Figure 6.** DSC curves of ZDMA under nitrogen atmosphere (a) DSC heating curve, (b) isothermal DSC curve

ZDMA is quite stable at 160°C and the disappearance of ZDMA crystals during the peroxide curing should not be attributed to the crystal melting. Figure 7 shows the transformation of ZDMA in the VMQ/ZDMA blend without peroxide when the blend was kept at 160°C for 15 min. At the beginning of heating process, the size of ZDMA decreases gradually, probably due to the dissolving of ZDMA into silicone rubber since the melting of crystals does not occur according to the DSC analysis. However, great quantities of ZDMA crystals can be still observed at the end of heating process. Comparing the POM images of VMQ/ZDMA blend containing peroxide with those of VMQ/ZDMA blend

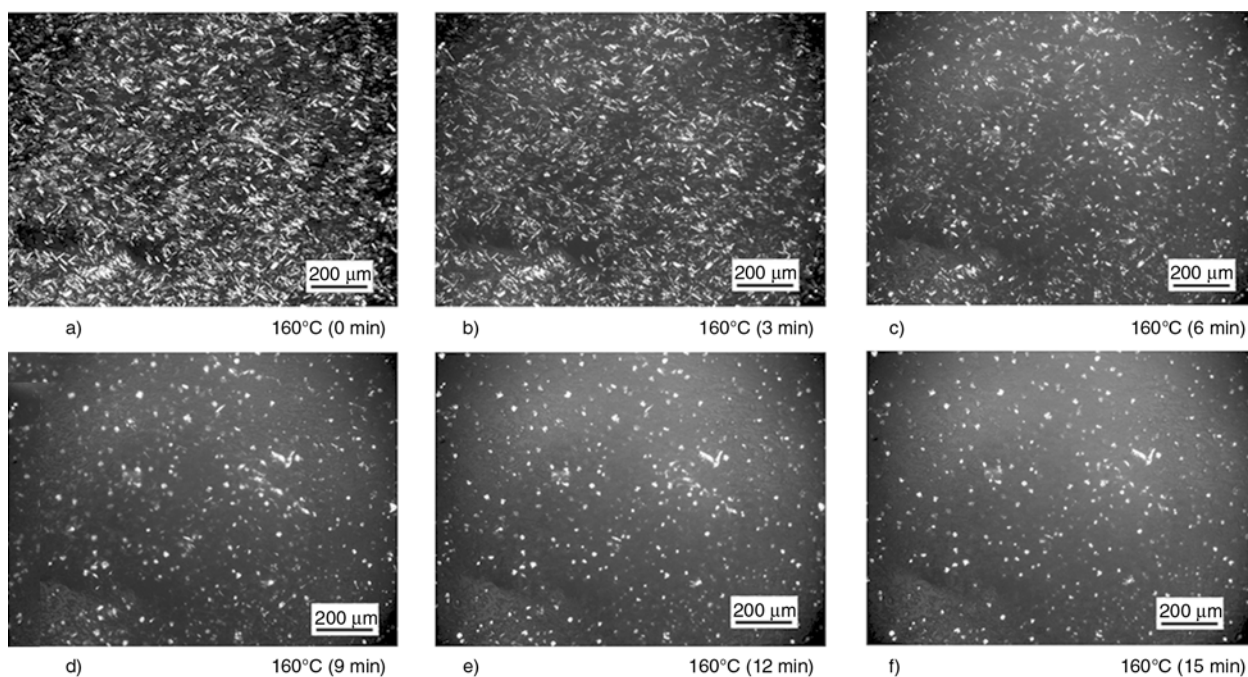


**Figure 7.** POM images of VMQ/ZDMA blends (100/40) without peroxide during the heat treatment

without peroxide, we can conclude that the *in situ* reaction of ZDMA during the peroxide curing plays an important role on the transformation of ZDMA from crystalline state to amorphous state.

Transmission electron microscopy (TEM) and high resolution transmission electron microscopy (HRTEM) were performed to observe the morphology of VMQ/ZDMA composites at the nano-level. Figure 8a shows the TEM morphology of VMQ/ZDMA composites. In the VMQ/ZDMA composites, micro-level particles can still be observed. However, the crystalline structure of these particles was likely destroyed because the crystals would split from the VMQ matrix to form cavities during the preparation of the samples. In the TEM photograph at high magnification, uniform dark phases at the nano-level can be observed, as shown in Figure 8a<sub>1</sub>. The HRTEM images given in Figure 8b–d clearly show that there are significant amounts of nano-dispersed structures (the darker phase) forming in the composites. These nano-dispersed structures, which are about 5–10 nm in diameter, represent poly-ZDMA aggregates or poly-ZDMA ionic clusters [23, 28–32] produced by the *in situ* polymerization of ZDMA during the peroxide curing.

The TEM observations indicate that uniform nano-level dispersion can be obtained via the *in situ* reaction method even though the original dispersion of ZDMA is poor. The ‘dissolving-diffusion’ mecha-

nism of nanodispersion generation, which has been accepted by some researchers [28, 31, 32], was used to illustrate the transformation of ZDMA in VMQ matrix, as shown in Figure 9. During the peroxide curing, the ZDMA monomers dissolved in the VMQ matrix and on the surface of the micro-level ZDMA crystals homo-polymerize or graft onto the silicone rubber chains with peroxide. The generated poly-ZDMA particles separate from the ZDMA crystals and disperse in the VMQ matrix. As a result, the inner monomers of the ZDMA crystals are exposed for further reaction, and the size of ZDMA particles decreased gradually. On the other hand, because of the formation of grafted poly-ZDMA, the compatibility between the silicone rubber and ZDMA is probably improved to some extent. The improved compatibility is beneficial to further diffusion of ZDMA monomers. With the *in situ* polymerization, the dissolving-diffusion balance of the ZDMA monomers in the VMQ matrix is broken, leading to a continual diffusion of these monomers from the particles into the matrix to participate in the *in situ* polymerization. Ultimately, a nano-dispersion is obtained.

### 3.3. Mechanical properties

We studied the effect of ZDMA on the mechanical properties of VMQ because ZDMA has been shown to be an effective reinforcing agent for elastomers

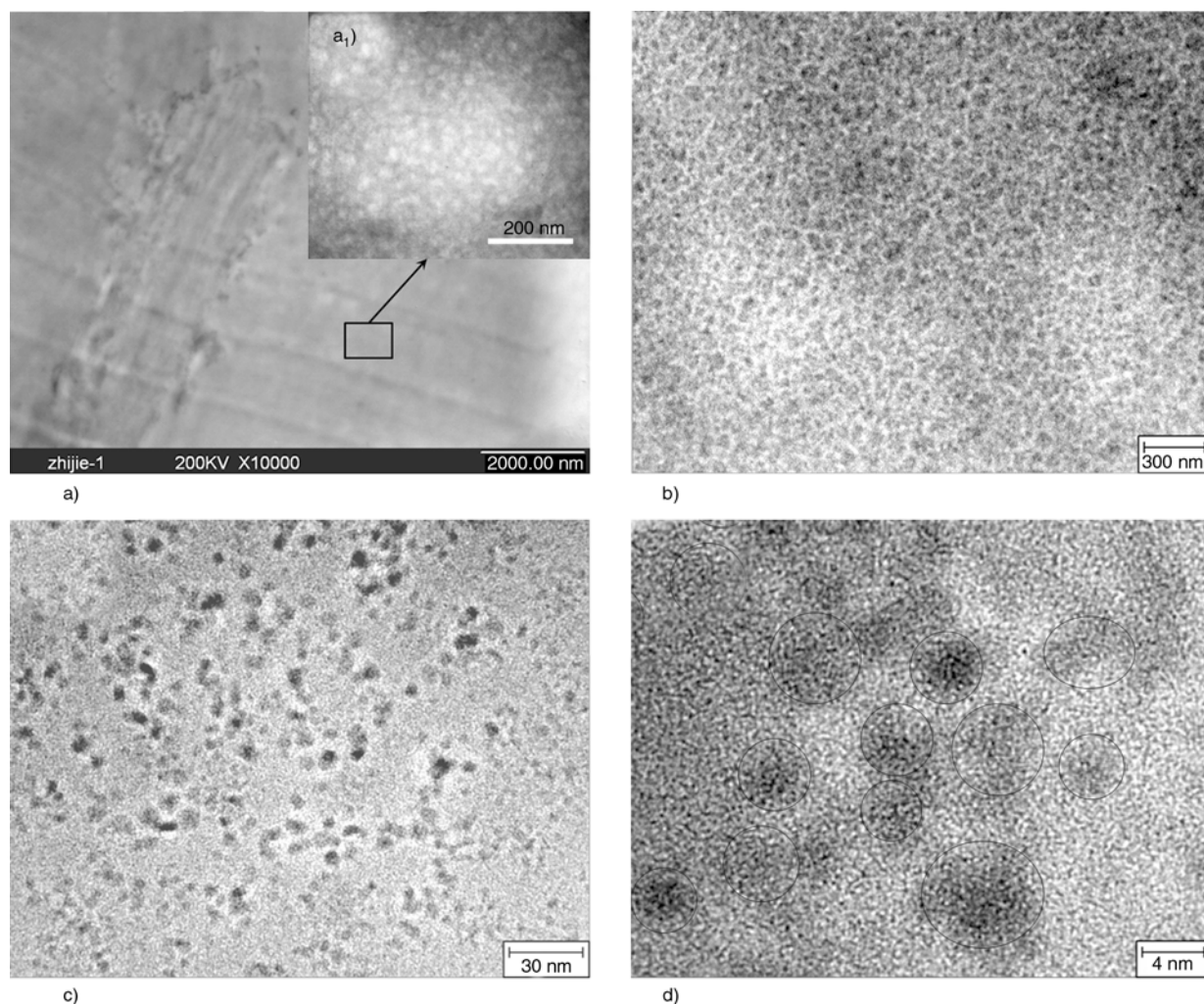


**Figure 8.** (a) TEM morphology and (c–d) HRTEM morphology of the cured VMQ/ZDMA composite containing 40 phr ZDMA and 5 phr DBPMH

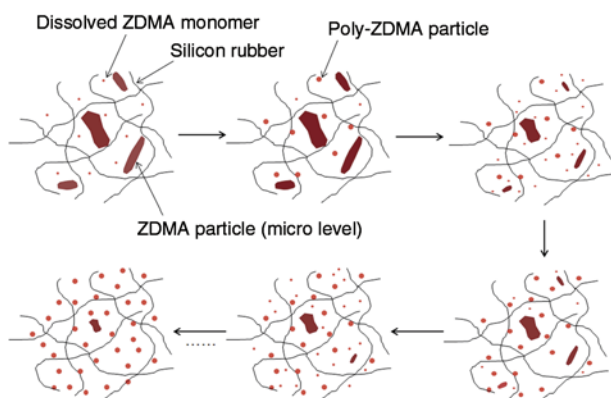


**Figure 9.** Schematic representation for the formation of nanophases in silicone rubber matrix during the peroxide curing

[22]. Since a considerable amount of radicals generated by peroxide was consumed by ZDMA, the amount of peroxide should be an important factor for the mechanical properties of VMQ/ZDMA composites. In this work, the effect of the amount of

peroxide on the mechanical properties of VMQ/ZDMA was investigated first. Table 1 show the mechanical properties of VMQ/ZDMA (100/30) composites. With increasing the amount of DBPMH, the modulus at 100% strain and Shore A hardness increase, but the elongation at break decreases gradually. The tensile strength shows a maximum value of 4.08 MPa when the amount of DBPMH is 5 phr. The amount of ZDMA also affects the tear strength of VMQ/ZDMA composites. With increasing the amount of DBPMH, the tear strength increase at first and then tends to stable when the amount of ZDMA is higher than 3 phr. The content of DBPMH has little influence on the permanent set of VMQ/ZDMA composites, and the value keeps at a low level for all the samples (below 5%). Additionally, it can be seen that the elongation at break (over 350%) is still high even when the amount of DBPMH is as high as 6 phr. It is a characteristic

**Table 1.** Mechanical properties of VMQ/ZDMA (100/30) composites with different amount of DBPMH

Samples	100% modulus [MPa]	Tensile strength [MPa]	Shore A hardness [°]	Tear strength [kN/m]	Elongation at break [100%]	Permanent set [100%]
DBPMH 1 phr	0.30 (±0.01)	1.16 (±0.02)	21	4.20 (±0.05)	529 (±28)	4
DBPMH 2 phr	0.51 (±0.03)	2.24 (±0.06)	30	7.31 (±0.25)	483 (±20)	4
DBPMH 3 phr	0.67 (±0.03)	2.75 (±0.08)	35	8.22 (±0.10)	423 (±20)	3
DBPMH 4 phr	0.83 (±0.04)	3.64 (±0.21)	39	8.42 (±0.34)	409 (±18)	2
DBPMH 5 phr	0.95 (±0.03)	4.08 (±0.21)	40	8.08 (±0.41)	380 (±17)	2
DBPMH 6 phr	0.97 (±0.04)	3.70 (±0.07)	40	8.18 (±0.52)	363 (±17)	2

property of metal salts of unsaturated carboxylic acids that they impart high strength and hardness, while allowing the rubber to retain a high elongation at break [29].

The effect of amount of ZDMA on the mechanical properties of VMQ/ZDMA composites was investigated next. Figure 10 shows the curing characteristics of VMQ/ZDMA blends containing 5 phr DBPMH. The maximum torque (MH) decreases with increasing the amount of ZDMA, but the minimum torque (ML) doesn't change much. Generally, the difference between maximum torque and minimum torque (MH–ML) is related to the crosslink density of the composites; for a given formula, high value corresponds to high crosslink density. The result implies that the incorporation of ZDMA will affect the crosslink structure of silicone rubber. Additionally, the optimum curing time ( $t_{90}$ ) increases greatly when ZDMA is incorporated into VMQ matrix, probably ascribed to the consumption of peroxide radicals by ZDMA.

The mechanical properties of VMQ/ZDMA composites containing 5 phr DBPMH are shown in Table 2. The tensile strength and elongation at break exhibit maximums when the amount of ZDMA is 40 and 30 phr, respectively. The maximum tensile

strength is 4.50 MPa and the maximum elongation at break is 380%. The tear strength also shows a maximum (9.05 kN/m) when the amount of ZDMA is 50 phr. Both the modulus at 100% strain and Shore A hardness increase significantly with increasing the amount of ZDMA. The permanent set of VMQ/ZDMA composites also increases with increasing the amount of ZDMA, but the value keeps at a low level for all the samples (below 5%). Considering the mechanical properties of gum VMQ vulcanizate shown in Table 2 (ZDMA 0 phr), we can conclude that ZDMA has a significant reinforcing effect on VMQ. For example, when 40 phr ZDMA is incorporated into VMQ matrix, both the tensile strength and tear strength increase by more than 10 times. The typical stress-strain curves of VMQ/ZDMA composites with different amount of ZDMA are presented in Figure 11. It can be seen that the incorporation of ZDMA can greatly increase the modulus of VMQ vulcanizates, especially at the low elongation.

In summary, both the amount of peroxide and the amount of ZDMA play important roles on the mechanical properties of VMQ/ZDMA composites. The best mechanical properties of VMQ/ZDMA composites are obtained when the DBPMH amount

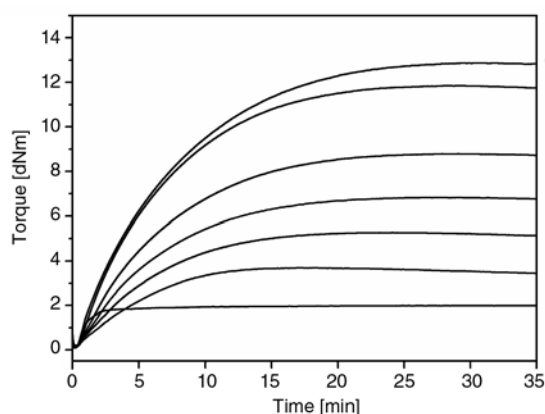


**Figure 10.** The curing curves of VMQ/ZDMA blends with different amount of ZDMA

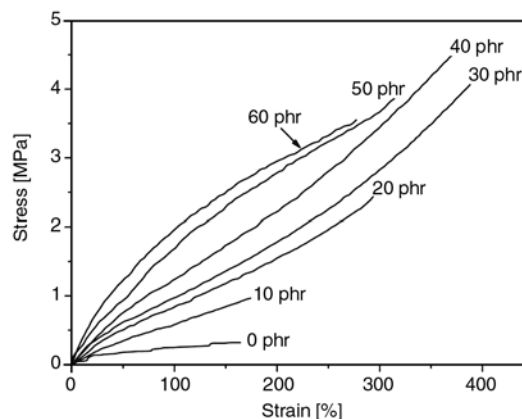


**Figure 11.** Stress-strain curves of VMQ/ZDMA blends with different amount of ZDMA



**Table 2.** Mechanical properties of VMQ/ZDMA composites with different amount of ZDMA

Samples	100% modulus [MPa]	Tensile strength [MPa]	Shore A hardness [°]	Tear strength [kN/m]	Elongation at break [100%]	Permanent set [100%]
ZDMA 0 phr	0.25 (±0.06)	0.35 (±0.13)	19	0.67 (±0.04)	160 (±22)	0
ZDMA 10 phr	0.54 (±0.05)	0.97 (±0.13)	32	3.04 (±0.22)	163 (±28)	0
ZDMA 20 phr	0.78 (±0.03)	2.48 (±0.07)	35	4.73 (±0.28)	292 (±19)	2
ZDMA 30 phr	0.95 (±0.03)	4.08 (±0.21)	40	8.08 (±0.41)	380 (±17)	2
ZDMA 40 phr	1.37 (±0.04)	4.50 (±0.15)	45	8.71 (±0.14)	373 (±11)	4
ZDMA 50 phr	1.75 (±0.03)	3.93 (±0.10)	53	9.05 (±0.33)	313 (±13)	4
ZDMA 60 phr	1.96 (±0.06)	3.64 (±0.09)	57	8.95 (±0.42)	276 (±24)	4

and VMQ amount are 5 and 40 phr, respectively. However, the reinforcing effect of ZDMA is lower on silicone rubber than on other elastomers such as HNBR, EPDM, and NBR, possibly because of the poor dispersion of ZDMA in the VMQ blend. The TEM and POM images showed that large ZDMA particles cannot diffuse completely into the VMQ matrix to form a uniform nanodispersion, but become amorphous particles at the micro-level instead. These micro-level particles have a negative effect on the mechanical properties.

### 3.4. Crosslink structure of VMQ/ZDMA composites

The competitive reactions of peroxide-initiated polymerization of ZDMA and cross linking of polymer occur simultaneously during the peroxide curing of the blend. In rubber/ZDMA composites, there are not only covalent crosslinks between the rubber chains but also ionic crosslinks mainly formed by the grafted poly-ZDMA, as shown in Figure 12. Because the ionic crosslinks have been known [22, 29, 30] to play an important role on the mechanical properties of rubber/ZDMA composites, it is significant and necessary to investigate the crosslink structure of the VMQ/ZDMA composites.

Figure 13 shows the FTIR spectra of VMQ/ZDMA composites before and after acidolysis. After aci-

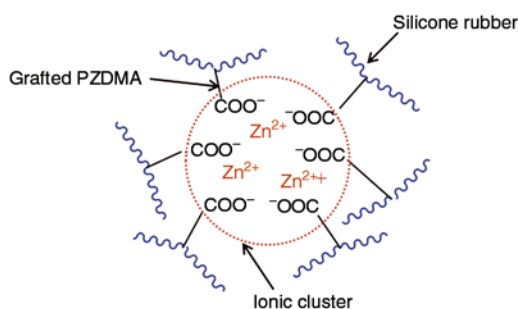


**Figure 12.** Schematic representation of ionic crosslink

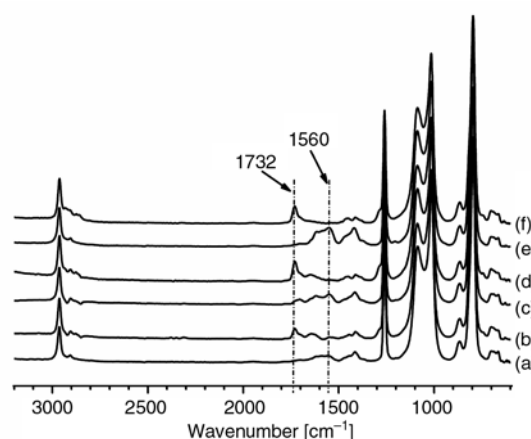


**Figure 13.** FTIR spectra of samples: (a) VMQ/ZDMA (100/20) vulcanizate before acidolysis, (b) VMQ/ZDMA (100/20) vulcanizate after acidolysis, (c) VMQ/ZDMA (100/40) vulcanizate before acidolysis, (d) VMQ/ZDMA (100/40) vulcanizate after acidolysis, (e) VMQ/ZDMA (100/60) vulcanizate before and (f) VMQ/ZDMA (100/60) vulcanizate after acidolysis

dolysis, the band corresponding to  $\text{-COO-}$  at  $1560\text{ cm}^{-1}$  has disappeared, and a new stretching vibration band corresponding to  $\text{-COOH}$  was observed at  $1732\text{ cm}^{-1}$ . These results confirmed that the hydrolysis of poly-ZDMA was quite thorough, and almost all the  $\text{Zn}^{2+}$  had been replaced by  $\text{H}^+$  during hydrolysis. The FTIR spectra also confirmed that parts of the poly-ZDMA were grafted onto silicone rubber chains during the peroxide curing because both the ungrafted poly-ZDMA and residual unreacted ZDMA could be extracted from the samples during the Soxhlet extraction treatment.

Figure 14 shows that with increasing the amount of ZDMA, the gross crosslink density and ionic crosslink density of VMQ/ZDMA composites increase gradually, but the covalent crosslink density decreases slightly. Looking at the results of the

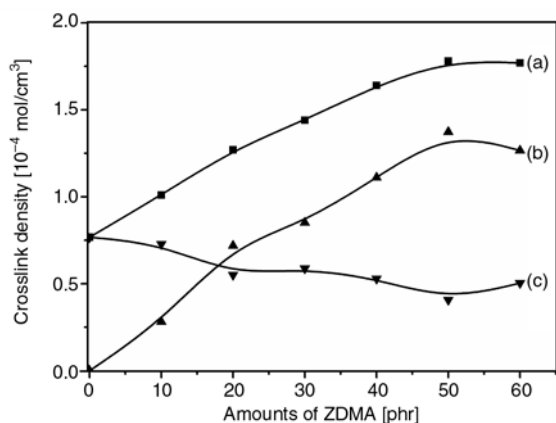


**Figure 14.** Effect of ZDMA loading on the crosslink density of VMQ/ZDMA composites containing 5 phr DBPMH: (a) gross crosslink density, (b) ionic crosslink density and (c) covalent crosslink density

crosslink density and the mechanical properties of VMQ/ZDMA composites, we can conclude that the ionic crosslink structure has a close relationship with the mechanical properties. The composite with high ionic crosslink density exhibits high hardness and modulus at 100% strain; high ionic crosslink density is also favorable to high tensile strength and elongation at break at the low ZDMA contents. However, the ionic crosslink content is lower in VMQ/ZDMA composites than in other rubber/ZDMA composites such as HNBR/ZDMA composites and NBR/ZDMA composites. For example, in the VMQ/ZDMA composite containing 40 phr ZDMA, ionic crosslinks account for only 67% of gross crosslinks, but the content of ionic crosslinks is higher than 85% in HNBR/ZDMA composites [31]. The low content of vinyl substituent (0.15%) in silicone rubber is possibly one reason for the low content of ionic crosslinks. As illustrated in Figure 3, grafted poly-ZDMA is formed by the reaction between poly-ZDMA radicals and VMQ radicals. Because of the low content of VMQ radicals, which are mainly generated from the vinyl substituent, the content of grafted poly-ZDMA is low. As a result, the VMQ/ZDMA composites have relatively low contents of ionic crosslinks. Additionally, the poor dispersion of ZDMA in VMQ blends decreases the contact area of the ZDMA particles and VMQ matrix and would do harm to the grafting reaction, leading to a low content of ionic crosslinks.

#### 4. Conclusions

During the peroxide curing, ZDMA homo-polymerized to form poly-ZDMA or grafted onto silicone rubber chains to form grafted poly-ZDMA, and the conversion of ZDMA was almost complete as shown by the FTIR and XRD analyses. Because of the *in situ* reaction of ZDMA, the micro-level ZDMA particles gradually got smaller. In the composites, a uniform nano-dispersed structure (the aggregation of poly-ZDMA and grafted poly-ZDMA) was formed. A ‘dissolving-diffusion’ model was used in previous studies to illustrate the transformation of ZDMA in the VMQ matrix. This model suggests that a uniform nano-dispersed structure can be obtained via the *in situ* reaction even though the initial dispersion of ZDMA in the blend is poor. ZDMA has a significant reinforcement for silicone rubber. Both the amount of peroxide and the amount of ZDMA affect the mechanical properties of VMQ/ZDMA composites significantly, and the best mechanical properties of VMQ/ZDMA composites are obtained when the amount of DBPMH and the amount of ZDMA are 5 and 40 phr, respectively. The addition of ZDMA into VMQ introduced a large amount of ionic crosslinks, which plays an important role on the mechanical properties. As the amount of ZDMA increases, the gross crosslink density and ionic crosslink density increase, but the covalent crosslink density decreases slightly.

#### Acknowledgements

This research was financially supported by the National Science Fund for Distinguished Young Scholars (50725310) and the Program for Changjiang Scholars and Innovative Research Team in University (PCSIRT, IRT0807).

#### References

- [1] Clarson S. J.: Silicones and silicone-modified materials: A concise overview. in ‘Synthesis and properties of silicones and silicone-modified materials’ (eds.: Clarson S. J., Fitzgerald J. J., Owen M. J., Smith S. D., Van Dyke M. E.) American Chemical Society, Washington, Vol 838, 1–10 (2003). DOI: [10.1021/bk-2003-0838.ch001](https://doi.org/10.1021/bk-2003-0838.ch001)
- [2] Mark J. E.: Overview of siloxane polymers. in ‘Silicones and silicone-modified materials’ (eds.: Clarson S. J., Fitzgerald J. J., Owen M. J., Smith S. D.) American Chemical Society, Washington, Vol 729, 1–10 (2000). DOI: [10.1021/bk-2000-0729.ch001](https://doi.org/10.1021/bk-2000-0729.ch001)

- [3] McMillin C. R.: Biomedical applications of rubbers and elastomers. *Rubber Chemistry and Technology*, **79**, 500–519 (2006).  
DOI: [10.5254/1.3547948](https://doi.org/10.5254/1.3547948)
- [4] Sandén R.: Castable silicone based heat insulations for jet engines. *Polymer Testing*, **21**, 61–64 (2002).  
DOI: [10.1016/S0142-9418\(01\)00048-4](https://doi.org/10.1016/S0142-9418(01)00048-4)
- [5] Saleem A., Fromann L., Soever A.: Fabrication of extrinsically conductive silicone rubbers with high elasticity and analysis of their mechanical and electrical characteristics. *Polymers*, **2**, 200–210 (2010).  
DOI: [10.3390/polym2030200](https://doi.org/10.3390/polym2030200)
- [6] Xu Q., Pang M., Zhu L., Zhang Y., Feng S.: Mechanical properties of silicone rubber composed of diverse vinyl content silicone gums blending. *Materials and Design*, **31**, 4083–4087 (2010).  
DOI: [10.1016/j.matdes.2010.04.052](https://doi.org/10.1016/j.matdes.2010.04.052)
- [7] Ahmad Z., Mark J. E.: Biomimetic materials: Recent developments in organic-inorganic hybrids. *Materials Science and Engineering: C*, **6**, 183–196 (1998).  
DOI: [10.1016/S0928-4931\(98\)00044-7](https://doi.org/10.1016/S0928-4931(98)00044-7)
- [8] Paul D. R., Mark J. E.: Fillers for polysiloxane ('silicone') elastomers. *Progress in Polymer Science*, **35**, 893–901 (2010).  
DOI: [10.1016/j.progpolymsci.2010.03.004](https://doi.org/10.1016/j.progpolymsci.2010.03.004)
- [9] LeBaron P. C., Pinnavaia T. J.: Clay nanolayer reinforcement of a silicone elastomer. *Chemistry of Materials*, **13**, 3760–3765 (2001).  
DOI: [10.1021/cm010982m](https://doi.org/10.1021/cm010982m)
- [10] Frogley M. D., Ravich D., Wagner H. D.: Mechanical properties of carbon nanoparticle-reinforced elastomers. *Composites Science and Technology*, **63**, 1647–1654 (2003).  
DOI: [10.1016/S0266-3538\(03\)00066-6](https://doi.org/10.1016/S0266-3538(03)00066-6)
- [11] Liu L., Tian M., Zhang W., Zhang L., Mark J. E.: Crystallization and morphology study of polyhedral oligomeric silsesquioxane (POSS)/polysiloxane elastomer composites prepared by melt blending. *Polymer*, **48**, 3201–3212 (2007).  
DOI: [10.1016/j.polymer.2007.03.067](https://doi.org/10.1016/j.polymer.2007.03.067)
- [12] Pan G., Mark J. E., Schaefer D. W.: Synthesis and characterization of fillers of controlled structure based on polyhedral oligomeric silsesquioxane cages and their use in reinforcing siloxane elastomers. *Journal of Polymer Science Part B: Polymer Physics*, **41**, 3314–3323 (2003).  
DOI: [10.1002/polb.10695](https://doi.org/10.1002/polb.10695)
- [13] Alexandru M., Cazacu M., Doroftei F., Ignat M., Timpu D., Grigoras C. V., Simionescu B. C.: On the morphology and potential application of polydimethylsiloxane-silica-titania composites. *Express Polymer Letters*, **5**, 188–196 (2011).  
DOI: [10.3144/expresspolymlett.2011.17](https://doi.org/10.3144/expresspolymlett.2011.17)
- [14] Mark J. E., Pan S.-J.: Reinforcement of polydimethylsiloxane networks by *in-situ* precipitation of silica: A new method for preparation of filled elastomers. *Macromolecular Rapid Communications*, **3**, 681–685 (1982).  
DOI: [10.1002/marc.1982.030031006](https://doi.org/10.1002/marc.1982.030031006)
- [15] Ning Y.-P., Tang M.-Y., Jiang C.-Y., Mark J. E., Roth W. C.: Particle sizes of reinforcing silica precipitated into elastomeric networks. *Journal of Applied Polymer Science*, **29**, 3209–3212 (1984).  
DOI: [10.1002/app.1984.070291022](https://doi.org/10.1002/app.1984.070291022)
- [16] Bokobza L., Diop A. L.: Reinforcement of poly(dimethylsiloxane) by sol-gel *in situ* generated silica and titania particles. *Express Polymer Letters*, **4**, 355–363 (2010).  
DOI: [10.3144/expresspolymlett.2010.45](https://doi.org/10.3144/expresspolymlett.2010.45)
- [17] Wen J., Mark J. E.: Synthesis, structure, and properties of poly(dimethylsiloxane) networks reinforced by *in situ*-precipitated silica-titania, silica-zirconia, and silica-alumina mixed oxides. *Journal of Applied Polymer Science*, **58**, 1135–1145 (1995).  
DOI: [10.1002/app.1995.070580707](https://doi.org/10.1002/app.1995.070580707)
- [18] Song S.-S., Qi H.-B., Wu Y.-P.: Preparation and properties of water-absorbent composites of chloroprene rubber, starch, and sodium acrylate. *Polymers for Advanced Technologies*, **22**, 1778–1785 (2011).  
DOI: [10.1002/pat.1671](https://doi.org/10.1002/pat.1671)
- [19] Yin D. H., Zhang Y., Peng Z. L., Zhang Y. X.: A comparison between the SBR vulcanizates reinforced by magnesium methacrylate added directly or prepared *in situ*. *European Polymer Journal*, **39**, 99–105 (2003).  
DOI: [10.1016/S0014-3057\(02\)00171-4](https://doi.org/10.1016/S0014-3057(02)00171-4)
- [20] Du A., Peng Z., Zhang Y., Zhang Y.: Effect of magnesium methacrylate on the mechanical properties of EVM vulcanizate. *Polymer Testing*, **21**, 889–895 (2002).  
DOI: [10.1016/S0142-9418\(02\)00025-9](https://doi.org/10.1016/S0142-9418(02)00025-9)
- [21] Wen S., Zhang X., Hu S., Zhang L., Liu L.: Influence of *in-situ* reaction on luminescent properties of samarium-complex/hydrogenated acrylonitrile-butadiene composites. *Polymer*, **50**, 3269–3274 (2009).  
DOI: [10.1016/j.polymer.2009.05.009](https://doi.org/10.1016/j.polymer.2009.05.009)
- [22] Lu Y., Liu L., Tian M., Geng H., Zhang L.: Study on mechanical properties of elastomers reinforced by zinc dimethacrylate. *European Polymer Journal*, **41**, 589–598 (2005).  
DOI: [10.1016/j.eurpolymj.2004.10.012](https://doi.org/10.1016/j.eurpolymj.2004.10.012)
- [23] Lu Y., Liu L., Yang C., Tian M., Zhang L.: The morphology of zinc dimethacrylate reinforced elastomers investigated by SEM and TEM. *European Polymer Journal*, **41**, 577–588 (2005).  
DOI: [10.1016/j.eurpolymj.2004.10.019](https://doi.org/10.1016/j.eurpolymj.2004.10.019)
- [24] Guo B. C., Chen F., Chen W. W., Lei Y. D., Jia D. M.: Reinforcement of nitrile rubber by *in situ* formed zinc disorbate. *Express Polymer Letters*, **4**, 529–538 (2010).  
DOI: [10.3144/expresspolymlett.2010.67](https://doi.org/10.3144/expresspolymlett.2010.67)
- [25] Flory P. J., Krigbaum W. R.: Statistical mechanics of dilute polymer solutions II. *Journal of Chemical Physics*, **18**, 1086–1094 (1950).  
DOI: [10.1063/1.1747866](https://doi.org/10.1063/1.1747866)

- [26] Gao G., Zhang Z., Zheng Y., Jin Z.: Effect of magnesium methacrylate and zinc methacrylate on bond properties of thermal insulation material based on NBR/EPDM blends. *Journal of Applied Polymer Science*, **113**, 3901–3909 (2009).  
DOI: [10.1002/app.30415](https://doi.org/10.1002/app.30415)
- [27] Lu Y., Liu L., Shen D., Yang C., Zhang L.: Infrared study on *in situ* polymerization of zinc dimethacrylate in poly( $\alpha$ -octylene-co-ethylene) elastomer. *Polymer International*, **53**, 802–808 (2004).  
DOI: [10.1002/pi.1462](https://doi.org/10.1002/pi.1462)
- [28] Saito Y., Nishimura K., Asada M., Toyoda A.: Polymerization behavior of zinc methacrylate study of zinc methacrylate/rubber/peroxide compounds; Part 2 (in Japanese). *Japanese Rubber Society*, **67**, 867–872 (1994).
- [29] Peng Z., Liang X., Zhang Y., Zhang Y.: Reinforcement of EPDM by *in situ* prepared zinc dimethacrylate. *Journal of Applied Polymer Science*, **84**, 1339–1345 (2002).  
DOI: [10.1002/app.10112](https://doi.org/10.1002/app.10112)
- [30] Nie Y., Huang G., Qu L., Zhang P., Weng G., Wu J.: Cure kinetics and morphology of natural rubber reinforced by the *in situ* polymerization of zinc dimethacrylate. *Journal of Applied Polymer Science*, **115**, 99–106 (2010).  
DOI: [10.1002/app.31045](https://doi.org/10.1002/app.31045)
- [31] Wei Z., Lu Y., Yan S., Meng Y., Zhang L.: Dramatic influence of curing temperature on micro–nano structure transform of HNBR filled with zinc dimethacrylate. *Journal of Applied Polymer Science*, **124**, 288–295 (2012).  
DOI: [10.1002/app.34615](https://doi.org/10.1002/app.34615)
- [32] Ikeda T., Yamada B., Tsuji M., Sakurai S.: *In situ* copolymerization behaviour of zinc dimethacrylate and 2-(*N*-ethylperfluoro-octanesulphonamido)ethyl acrylate in hydrogenated nitrile–butadiene rubber during peroxide crosslinking. *Polymer International*, **48**, 446–454 (1999).  
DOI: [10.1002/\(SICI\)1097-0126\(199906\)48:6<446::AID-PI159>3.0.CO;2-9](https://doi.org/10.1002/(SICI)1097-0126(199906)48:6<446::AID-PI159>3.0.CO;2-9)

# Upgrading of recycled polypropylene by preparing flame retarded layered composite

B. Bodzay<sup>1\*</sup>, M. Fejős<sup>1</sup>, K. Bocz<sup>1</sup>, A. Toldy<sup>1,2</sup>, F. Ronkay<sup>2</sup>, Gy. Marosi<sup>1</sup>

<sup>1</sup>Budapest University of Technology and Economics, Faculty of Chemical Technology and Biotechnology, Department of Organic Chemistry and Technology, Budafoki út 8., H-1111 Budapest, Hungary

<sup>2</sup>Budapest University of Technology and Economics, Faculty of Mechanical Engineering, Department of Polymer Engineering, Műegyetem rkp. 3., H-1111 Budapest, Hungary

Received 26 January 2012; accepted in revised form 6 June 2012

**Abstract.** Upgrading of polypropylene waste was performed by different composite technologies, in order to improve the flame retardancy combined with preserved or improved mechanical properties. The polymer waste of density below 900 kg/m<sup>3</sup> is originated from end-of-life vehicles (ELV) after comminution, density separation and comprehensive analysis. Intumescent flame retardant system was used for reducing the flammability; while chopped glass fibre reinforcement was used to compensate the deterioration of mechanical properties caused by flame retardant additives. In mixed composite beside of flame retardants, the reinforcement effect of glass fibre can not be realized; therefore with modification of composite structure (but maintaining the composition) a multilayer composite was developed, which contains 65.5% of recycled polymer, where the core is reinforced with glass fibre covered by flame retarded shell layers. Enhanced flame retardancy (4 min longer time to escape) was achieved by using this layered composite compared to the mixed composite, thus the time to escape could be extended only with modification of composite structure.

**Keywords:** polymer composites, recycling, multilayer structure, flame retardant, glass fibre reinforced

## 1. Introduction

According to a recent market analysis the application of recycled polymers in the automotive industry is still not usual because of their poor properties [1]. Although the acceptable upper limit for the application of secondary plastics in combination with primary raw materials changes in a wide range (20-100%), the use of secondary plastic materials is still lower than required by the European legislation (COM/2001/0031, 99/31/EC, 2000/53/EC, 2002/96/EC, 2003/108/EC) aiming at fostering the development of environmental-friendly technologies with reduction of waste [2].

Secondary plastics have low market value because of their uneven composition and purity; however,

their value can be increased by separation in order to obtain relatively homogeneous fractions upgraded with reinforcement, functionalization, restabilization and flame retardancy [3, 4].

In the field of transportation both mechanical and flame retardant properties play important role in the material development [5]. The application of flame retardant additives usually considerably deteriorates the mechanical properties [6–10]. In order to fulfil these antagonistic requirements polymer composites of layered (or sandwich) structure can be a solution.

Concerning the flame retardancy of layered composite structures, it should be noted, that the non-homogeneous nature of the core composite materi-

\*Corresponding author, e-mail: [bbodzay@mail.bme.hu](mailto:bbodzay@mail.bme.hu)

© BME-PT

als may cause problems, especially if the adhesion between the layers is not adequate. Delamination of the skin, uneven melting of the core and skin, and edge effects are the factors that must be taken into consideration evaluating the flame retardancy results. Using usual bench-scale test methods such as the Cone Calorimeter test the core composites may not react as a solid homogeneous material would be expected to [11]. If halogen-free solution is required the flammability of polypropylene (PP) is mostly reduced by application of intumescent additives [12, 13]. Application of intumescent flame retardant additives is favourable because of their low toxicity, action in solid state and suppressed smoke evolution in case of fire [14]. Considering the enhancement of mechanical properties of the composites, fibre-reinforcement offers a cost-effective solution. Besides providing high strength, stiffness and impact properties, the inorganic fibres possess other advantages, such as inflammability, therefore they are widely utilized in thermosets and thermoplastics [15]. The environmentally and ecologically harmless glass fibres are often used as reinforcement also in flame retarded composites [16]. The application of polymer waste as matrix of composites is both ecologic and economic solution providing driving force to reuse the plastic waste in a competitive form. Matko and his co-workers [9] have developed a method for rendering pure polypropylene flame retardant with additives consisting of mainly recycled materials, which reduce considerably the material costs. Strongly reduced heat release rate and high flame retardancy classification was achieved with application of recycled ground tires, and recycled polyurethane in PP, at the expense of the deteriorated mechanical properties. Therefore the aim of this study was to find a cost-effective and environmentally friendly way for producing useful materials of higher value from polymer waste by improving the flame retardancy combined with preserved or improved mechanical properties. In the present approach composites containing glass fibre reinforced recycled polypropylene core covered with flame retarded secondary polymer layers were designed. Whilst most of the papers dealing with polymer waste perform only model experiments using mixtures of pure polymers, in this work real industrial car shredder, obtained from end-of-life cars, was used as secondary raw material.

## 2. Materials and methods

### 2.1. Materials

The recycled polypropylene (ASR  $\rho < 900 \text{ kg/m}^3$ ) supplied by Alcufer Ltd., (Fehérvárcsúrgó, Hungary) separated to density fractions, originated from light fraction of automobile shredder residue (ASR) obtained from shredding of end-of-life vehicles (ELV). After a comprehensive component analysis (Fourier transform infrared spectroscopy – FTIR, Raman, thermogravimetry – TG, differential scanning calorimetry – DSC) [17], it was found that below the density of  $900 \text{ kg/m}^3$  the main polymer component is polypropylene ( $> 78 \%$ ), melt flow rate (MFR) ( $190^\circ\text{C}$ ,  $2.16 \text{ kg}$ )  $2.14 \text{ g}/10 \text{ min}$  and its inorganic filler residue content (determined by heating under mass loss calorimeter with heating wire of  $900^\circ\text{C}$ , which means approx.  $650^\circ\text{C}$  on the surface of the samples) is lower than  $0.75 \text{ mass}\%$ , containing mainly talc, calcium-carbonate and short glass fibre. As some of the inorganic fillers undergo decomposition at this temperature the inorganic filler content is somewhat higher than the determined residue.

As reinforcing material in the core of the layered structure and in the mixed polyolefin composite chopped glass fibre (GF) (DS 2200-13P) 3B – Fibreglass Company (Battice, Belgium) (Table 1) was used.

The contained intumescent flame retardant (IFR), applied in the flame retarded shell, consisted of ammonium polyphosphate (APP) (Exolit AP 422) Clariant GmbH. (Kornkamp, Germany), recycled polyurethane (RecPUR) Amatech-Polycel Inc. (Erie, Pennsylvania, USA), glyceryl-monostearate (GMS) (Estol) Chemiplast Ltd. (Budapest, Hungary) and ethylene-vinyl-acetate (EVA) (Ibucell K100), H.B. Fuller (St Paul, MN, USA). This intumescent flame retardant system was successfully applied in polyolefin matrix in our previous work [9]. The APP is the phosphorous containing flame retardant additive which forms intumescent char with application of recycled PUR as a carbon source. GMS was used as a compatibilizer and EVA to improve the flexibility.

**Table 1.** Properties of the DS 2200-13P type glass fibre

Property	Unit	E-glass
Fibre length	mm	4
Diameter	$\mu\text{m}$	13
Moisture content	%	max. 0.05
Solid content	%	0.5

## 2.2. Preparation of samples

**Compounding:** the components were homogenized in a Brabender Plasti Corder (PL 2000) Brabender GmbH & Co. KG (Duisburg, Germany) equipped by a 50 cm<sup>3</sup> kneader chamber, at 190°C, with a rotor speed of 50 rpm, for 10 min.

**Compression moulding of the test sheets:** the compounds were compressed in a Collin P 200 E Dr. Collin GmbH (Ebersberg, Germany) laboratory compression moulding machine at 190°C, with 10 bar, for 10 min, the layered composites were prepared at 180°C, 50 bar for 10 min. The sample thickness was 4 mm.

## 2.3. Evaluation methods

**Comparative mechanical tests** were carried out by ZWICK Z020 universal tester Zwick GmbH & Co. KG (Ulm, Germany). The tensile test speed was 10 mm/min with clamping distance of 80 mm using rectangular strip specimens with cross-section of 4 mm × 10 mm. Tensile strength and tensile modulus were calculated from the force-displacement curves obtained from the tensile test. The three-point bending measurements were also carried out using Zwick Z020 device at 64 mm gauge length and 5 mm/min crosshead speed, following the ISO-178 standard. The tests were carried out at room temperature and average values were calculated from the results of five test specimens. SEM pictures were taken of the composites by JSM 6380LA type JEOL (Tokyo) Scanning Electron Microscope. The *flame retardant performance* was characterized by limiting oxygen index (LOI) according to the standard ASTM D 2863 and UL-94 (ASTM D 635, ASTM D 3801) flammability measurements. While limiting oxygen index gives information about ignitability in controlled atmosphere, UL-94 classification (HB-worst, V2, V1, V0-best) is used for determination of dripping and fire spreading rate. For investigation of surface flammability UL 94 - 5VA&5VB (ASTM D 5048) was used, which dis-

tinguishes 5VA (non-burning), and 5VB (through-burning) materials.

The Mass Loss type Cone Calorimeter tests were carried out by the device of Fire Testing Technology Inc. (East Grinstead, England) instrument, following the procedures in ASTM E 906 standard method for measuring heat release of materials during their burning. The results of 3 measurements were averaged. Square specimens (100 mm × 100 mm × 4 mm) were irradiated at a heat flux of 50 kW/m<sup>2</sup>. This method is based on the principle of direct measurement of the convective and radiant heat liberated using a mass loss calorimeter fitted with thermopiles. Thermocouples are embedded in the mass loss calorimeters' chimney to measure the temperature of the gases directly. By calibrating them by combustion methane gas at each heat flux, heat release values for each sample can be determined throughout the experiments. It makes also possible to monitor the change of sample mass during the burning process.

## 3. Results and discussion

In order to upgrade the selected polymer waste fraction (< 900 kg/m<sup>3</sup>), flame retardant additives and reinforcing fibres were introduced into composite materials with two technologies. In case of mixed composite (RMC) the components were homogenized in an internal mixer and hot-pressed to obtain 4 mm thick homogeneous material, while the other composite had a layered structure (RLC) consisting of a 2 mm thick reinforced core layer (RC) and two 1 mm thick flame retarded outer layers (RS) pressed together see in Figure 1.

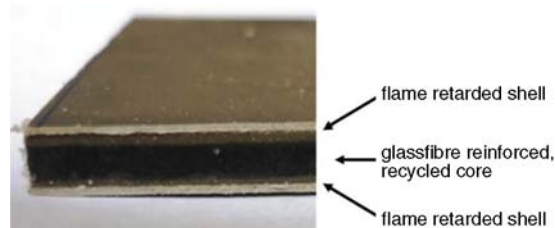


**Figure 1.** The structure of the layered composite

**Table 2.** Composition of the shell, core layers and composites

Materials	Recycled shell (RS)	Recycled core (RC)	Recycled composites (RMC, RLC)
Recycled matrix (ASR $\rho < 0.9$ g/cm <sup>3</sup> )	36%	70%	53.0%
EVA	13%	–	6.5%
GMS	1%	–	0.5%
APP	25%	–	12.5%
Recycled PUR	25%	–	12.5%
Glass fibre	–	30%	15. %

The layers of the ‘sandwich’ composite were also investigated separately. The composition of the samples is summarized in Table 2.

The composites having high waste content including the recycled matrix and recycled PUR as an additive (RS: 61%, RC: 70%, RMC, RLC: 65.5%) are advantageous from economical and environmental aspects.

In order to compare the efficiency of the different composite technologies (mixed and layered composites) their flame retardant and mechanical properties of the sandwich composites and their each layer were determined.

### 3.1. Flammability

The LOI and UL-94 results are summarized in Table 3. It can be concluded that the intumescent shell, as expected, reached V-0 UL-94 level of fire retardancy and much higher LOI (28) than the core material (HB and 19 respectively). If the components are simply mixed together the UL-94 classification remained HB, and the LOI values increased only with 2 units (21), which means that it is still very combustible in air. Applying flame retarded layer as an outer shell of layered composite, the UL-94 level remained HB, however, the LOI increased from 19 to 25. During the UL-94 classification of layered composite structures the cross section of the sample is exposed to fire during the ignition, therefore the core of the layered composites, being the most ignitable layer of the material, determines the achieved classification. Taking into account the possible application areas of this material, it is quite clear that only the outer layers (the surface), will be exposed to fire, the classification of the shell in case of layered composites is more relevant. The UL-94 5VA&5VB surface flammability test (Table 3) verifies that similarly to the shell, the layered composite reaches also the best (5VA) classification in contrast to the core and mixed composite (5VB) results.

**Table 3.** LOI and UL-94 ratings

Samples	LOI [%]	UL-94	Burning rate [mm/min]	UL-94 5VA & 5VB
Recycled matrix	19	HB	31.1	–
Recycled core (RC)	19	HB	24.7	5VB
Recycled shell (RS)	28	V-0	–	5VA
Recycled mixed composite (RMC)	21	HB	25.5	5VB
Recycled layered composite (RLC)	25	HB	3.6	5VA

Although the composition of the mixed and layered composites is exactly the same, the application of layered structure causes improvement in the oxygen index from 21 (RMC) in case of mixed composite to 25 (RLC) at layered composites, furthermore significantly (by approx. 80%) reduces the burning rate as well.

Concerning the heat release rate (HRR) results shown in Figure 2 the core contains only 70% PP and 30% glass fibre which helps the heat diffusion; therefore the pHRR is reduced compared to the RecPP. The 4 mm thick flame retarded shell causes more than 4 min shift in the time of peak heat release rate owing to the formed intumescent char on the surface of the material. This layer is intact up to 500 s, then it loses its protecting effect. The intumescent flame retardant system significantly (by 70%) reduced the peak heat release rate (pHRR) of both mixed and layered composites compared to the matrix materials. However, comparing the two technologies applied for producing the composites, it is clear that the application of layered structure delayed the time to pHRR and also the intensive burning by approx. 200 s. After 200 s the shell layer lost its protecting effect and the HRR values approached the curves of mixed composites. Con-

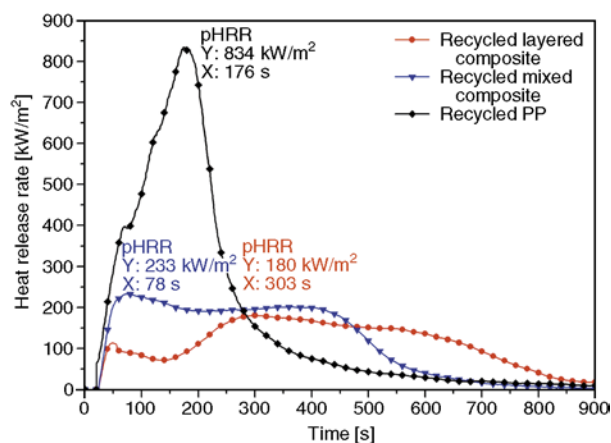


**Figure 2.** Heat release rate results of the mixed and layered composites



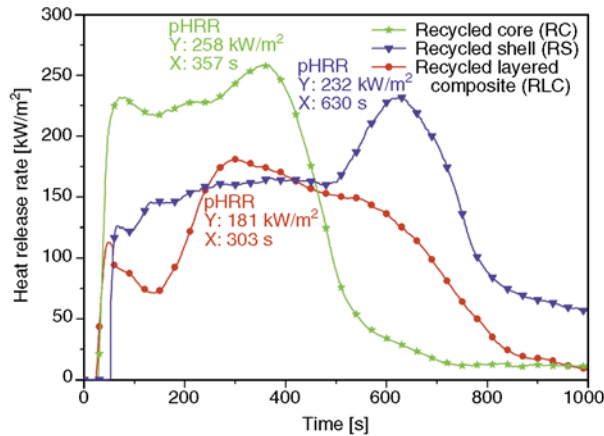


**Figure 3.** Heat release rate results of the layered (sandwich) composite, core and shell materials

sequently if the whole amount of the FR additives is concentrated into the surface layer both the intensity and the time of pHRR decreases.

In order to understand more details of this behaviour, the layers and the layered composite are compared in Figure 3. Surprisingly the HRR curve of layered structure runs lower at the beginning than that of shell with higher overall FR content and the loss of the protective function occurs earlier than in case of shell tested alone (RS). The difference occurs because the glass fibre in the core of the layered structure, having flame retarded layer of 1 mm on the surface, helped the heat diffusion under the surface [12]. Thus the pHRR was reduced at the initial phase (until 250 s). Later on in case of the 4 mm thick shell material the accumulated heat leads to decomposition of the surface structure and breakdown of its protecting effect, leading to a second intensive peak of heat release. It does not occur with the layered composite in which the heat is carried away by the heat conductive sublayer, therefore the protecting effect of the intumescent char is similar to the shell material but this protection effect lasts until the end of test. No significant cracks or delamination occurred at the surface of the composite see on

**Table 4.** Numeric results of mass loss calorimeter tests

Samples	Time of peak heat release rate <sup>a</sup> [s]	Peak heat release rate (pHRR) <sup>b</sup> [kW/m <sup>2</sup> ]	Total heat released (THR) <sup>c</sup> [MJ/m <sup>2</sup> ]
Recycled matrix	176	834	155
Recycled core (RC)	357	258	112
Recycled shell (RS)	630	232	136
Recycled mixed composite (RMC)	78	233	102
Recycled layered composite (RLC)	303	181	100

<sup>a</sup>deviation of method ±5 s

<sup>b</sup>deviation of method ±39kW/m<sup>2</sup>

<sup>c</sup>deviation of method ±3 MJ/m<sup>2</sup>

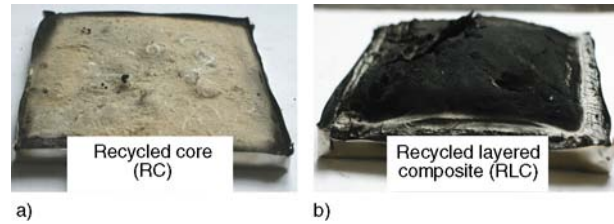


**Figure 4.** Residues after burning; recycled core (a), recycled layered composite (b)

Figure 4b compared to the uncovered residue made of glass fibres of the recycled core (RC) (Figure 4a).

The total heat released (THR) was approximately the same during the burning of both mixed and layered composites (see Table 4), but in case of the layered one, the main heat release step was prolonged by 220 s (almost 4 minutes) in time compared to the mixed one, due to the protecting effect of the outer flame retarded layers, where the intumescent flame retardants were concentrated. Furthermore the amount of residue after burning was significantly increased in case of RLC (see Table 5). The most surprising result of Table 4 is the lower amount of total heat released of the composites than that of shell material in spite of their less fire retardant content. It can not be explained merely by the presence of 15% non-combustible glass fibre, consideration of the preserved protecting capability of their surface layer, as described at the explanation of Figure 3, is also required.

Based on the results in Figure 2 and 3 and Table 4 it can be concluded that the layered composite is the more advantageous than the shell (containing dou-

**Table 5.** The residue of the samples after burning

Samples	Residue
Recycled matrix (ASR $\rho < 900 \text{ kg/m}^3$ )	0.7%
Recycled shell (RS)	17%
Recycled core (RC)	30.5%
Recycled mixed composite (RMC)	13%
Recycled layered composite (RLC)	16%

ble amount of flame retardant), because of the decrease in the peak HRR, the shift of its position by approx. 200 s and the significantly reduced THR. The combined application of FR shell and reinforced core of enhanced heat conductivity layers in the form of layered composites resulted in a synergistic effect, both in terms of total heat released and peak of HRR.

### 3.2. Mechanical properties

The main mechanical properties of the samples were evaluated by tensile and flexural tests in order to trace the changes caused by different additives. In comparison to the matrix (RecPP), the tensile strength of the flame retardant containing shell (RS) was reduced by 50% (Figure 5a). Applying glass fibre reinforcement the tensile strength of the core (RC) could be increased by 25% compared to the matrix. The reinforcement effect of the same amount of glass fibre in the mixed composite (RMC) was not enough to balance the negative effect of flame retardant system, thus the tensile strength shows slight (14.7 MPa) decrease compared to the matrix

(16.1 MPa). In case of layered structure better compensation can be achieved, therefore this structure is considered more favourable than the mixed one in terms of tensile strength.

The tensile moduli of the materials are shown in Figure 5b. While the presence of the flame retardant additives slightly diminishes the stiffness, the reinforcement with glass fibre raises it significantly. The tensile moduli of all composite samples prepared either by mixing (RMC) or by layering technology (RLC) are approximately similar to that of core material (RC): ~1.2 GPa. It is surprising because the glass fibre content in these composites is less than in the core material. It seems that the FR components and the macromolecules adsorbed in their interlayers compensate the lower content of the reinforcing fibres in this respect.

Figures 6a and 6b summarize the results of the flexural tests. Similarly to the mechanical properties showed previously, the flexural strength and modulus of the flame retardant containing samples decreased, but the glass fibre significantly improved them.

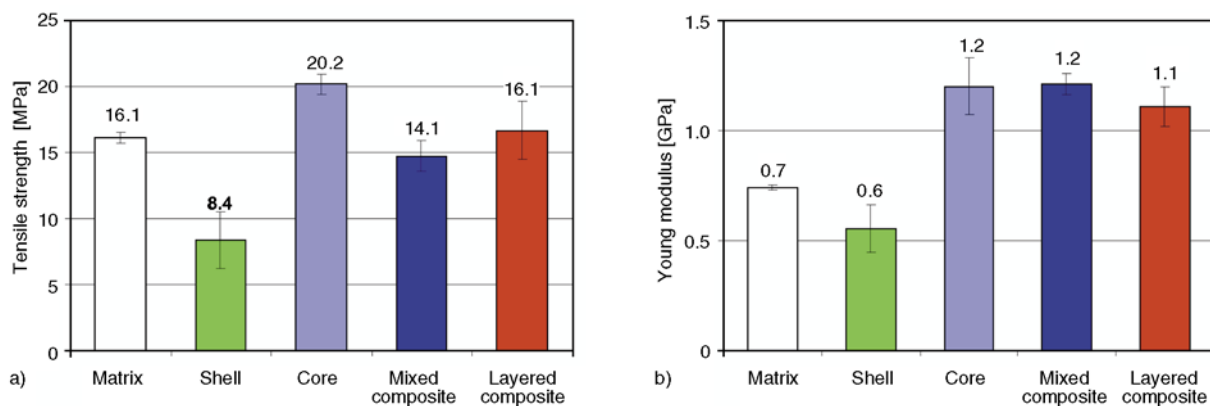


Figure 5. Tensile strength (a) and modulus (b) of the recycled samples

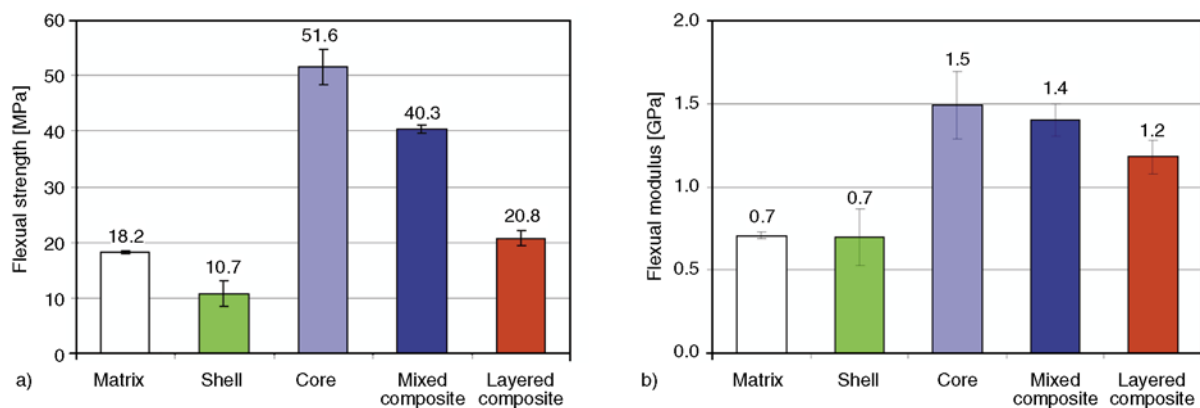
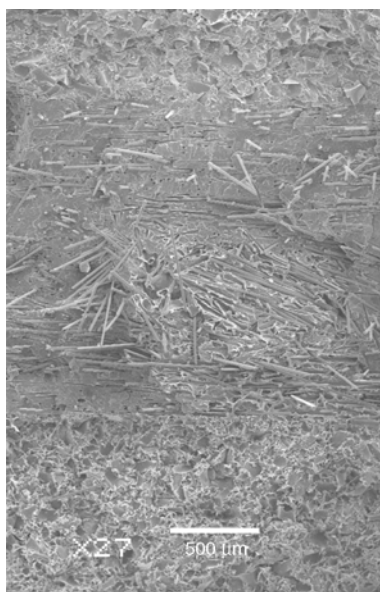


Figure 6. Flexural strength (a) and modulus (b) of the recycled samples



**Figure 7.** SEM picture of layered composite

As it was expected, the results of the mixed composite (RMC) are between the core (RC) and shell (RS) or reference matrix, but the flexural properties of the layered composites (RLC) are somewhat worse than those of the mixed composites, because the reinforcement is concentrated in the middle layer of the composite, which can admit higher flexibility, but attains the flexural strength of the matrix. Application of this recycled layered structure as an internal element of cars, such as dashboard it has to be flexible, because of the slight deformation of each car element, therefore EVA was used for this purpose. In this point of view, the layer composite shows better moduli than the mixed one. Nevertheless, it can be stated, that besides improved fire retardancy also the tensile and flexural properties of the layered composites reach the mechanical properties of the reference matrix.

Based on the SEM picture (Figure 7) it can be stated, that the orientation of the fibres is not considerable, it can be observed only near the surface of the core (interlayer). It is assumed that the compression moulding process did not induce any fibre orientation effects which might influence the mechanical properties.

#### 4. Conclusions

The aim of this work was to find a cost-effective, environmentally friendly way for upcycling of polypropylene waste in order to produce useful materials of higher value. Different composite tech-

nologies were used to improve the flame retardancy besides constant or improved mechanical properties using recycled polypropylene and layered structure. Chopped glass fibre was used as reinforcing agent in recycled polypropylene waste separated from automotive shredder residue (ASR), with density below  $900 \text{ kg/m}^3$ , and intumescent flame retardant system served for the reduction of flammability with application of recycled polyurethane as a charring agent. Layered structure was used in order to eliminate the deterioration of mechanical properties caused by flame retardant additives. The application of the flame retarded shell material decreased the peak of HRR of the sandwich composites by approx. 80% in comparison to recycled PP matrix and increased the LOI from 19 of the core material to 24. The mechanical properties of the flame retarded recycled layered composite reached the properties of the reference polypropylene, therefore the composites containing recycled materials are still proper for certain engineering applications.

#### Acknowledgements

The recycling of polymer waste was promoted by an EU7 framework with the title of ‘Magnetic sorting and ultrasound sensor technologies for production of high purity secondary polyolefins from waste’ (W2PLASTICS, No. 212782), and by Recytech project (TECH\_08\_A4/2-2008-142) called ‘Elaboration of Recycling Technologies for non-metallic automotive and electronic waste avoiding further deposition of organic materials subsidized by the National Development Agency (NFÜ)’. The publishing of this paper was supported by the Hungarian Scientific Research Fund (OTKA PD 72722), the János Bolyai Scholarship of the Hungarian Academy of Science and the ERA Chemistry (code NN 82426). This work is connected to the scientific program of the ‘Development of quality-oriented and harmonized R+D+I strategy and functional model at BME’. This project is supported by the New Hungary Development Plan (Project ID: TÁMOP-4.2.1/B-09/1/KMR-2010-0002). The work reported in this paper has been developed in the framework of the project ‘Talent care and cultivation in the scientific workshops of BME’ project. This project is supported by the grant TÁMOP-4.2.2.B-10/1-2010-0009.

#### References

- [1] Toldy A., Bodzay B., Tieren M.: Recycling of mixed polyolefin wastes. *Environmental Engineering and Management Journal*, **8**, 967–971 (2009).
- [2] Bellmann K., Khare A.: European response to issues in recycling car plastics. *Technovation*, **19**, 721–734 (1999).  
DOI: [10.1016/S0166-4972\(99\)00081-4](https://doi.org/10.1016/S0166-4972(99)00081-4)

- [3] Bocz K., Toldy A., Kmetty Á., Bárány T., Igricz T., Marosi Gy.: Development of flame retarded self-reinforced composites from automotive shredder plastic waste. *Polymer Degradation and Stability*, **97**, 221–227 (2012).  
DOI: [10.1016/j.polyimdegradstab.2011.12.029](https://doi.org/10.1016/j.polyimdegradstab.2011.12.029)
- [4] Fávaro S. L., Ganzerli T. A., de Carvalho Neto A. G. V., da Silva O. R. R. F., Radovanovic E.: Chemical, morphological and mechanical analysis of sisal fiber-reinforced recycled high-density polyethylene composites. *Express Polymer Letters*, **4**, 465–473 (2010).  
DOI: [10.3144/expresspolymlett.2010.59](https://doi.org/10.3144/expresspolymlett.2010.59)
- [5] Marsh G.: Fire-safe composites for mass transit vehicles. *Reinforced Plastics*, **46**, 26–30 (2002).  
DOI: [10.1016/S0034-3617\(02\)80157-6](https://doi.org/10.1016/S0034-3617(02)80157-6)
- [6] Nachtigall S. M. B., Miotto M., Schneider E., Mauler R. S., Forte M. M. C.: Macromolecular coupling agents for flame retardant materials. *European Polymer Journal*, **42**, 990–999 (2006).  
DOI: [10.1016/j.eurpolymj.2005.10.017](https://doi.org/10.1016/j.eurpolymj.2005.10.017)
- [7] Chiu S-H., Wang W-K.: Dynamic flame retardancy of polypropylene filled with ammonium polyphosphate, pentaerythritol and melamine additives. *Polymer*, **39**, 1951–1955 (1998).  
DOI: [10.1016/S0032-3861\(97\)00492-8](https://doi.org/10.1016/S0032-3861(97)00492-8)
- [8] Almeras X., Le Bras M., Hornsby P., Bourbigot S., Marosi Gy., Keszei S., Poutch F.: Effect of fillers on the fire retardancy of intumescent polypropylene compounds. *Polymer Degradation and Stability*, **82**, 325–331 (2003).  
DOI: [10.1016/S0141-3910\(03\)00187-3](https://doi.org/10.1016/S0141-3910(03)00187-3)
- [9] Matkó Sz., Répási I., Szabó A., Bodzay B., Anna P., Marosi Gy.: Fire retardancy and environmental assessment of rubbery blends of recycled polymers. *Express Polymer Letters*, **2**, 126–132 (2008).  
DOI: [10.3144/expresspolymlett.2008.17](https://doi.org/10.3144/expresspolymlett.2008.17)
- [10] Huang N. H., Chen Z. J., Wang J. Q., Wei P.: Synergistic effects of sepiolite on intumescent flame retardant polypropylene. *Express Polymer Letters*, **4**, 743–752 (2010).  
DOI: [10.3144/expresspolymlett.2010.90](https://doi.org/10.3144/expresspolymlett.2010.90)
- [11] Grenier A. T., Dembsey N. A., Barnett J. R.: Fire characteristics of cored composite materials for marine use. *Fire Safety Journal*, **30**, 137–159 (1998).  
DOI: [10.1016/S0379-7112\(97\)00059-3](https://doi.org/10.1016/S0379-7112(97)00059-3)
- [12] Liu Y., Deng C-L., Zhao J., Wang J-S., Chen L., Wang Y-Z.: An efficiently halogen-free flame-retardant long-glass-fiber-reinforced polypropylene system. *Polymer Degradation and Stability*, **96**, 363–370 (2011).  
DOI: [10.1016/j.polyimdegradstab.2010.02.033](https://doi.org/10.1016/j.polyimdegradstab.2010.02.033)
- [13] Zhang S., Horrocks A. R.: A review of flame retardant polypropylene fibres. *Progress in Polymer Science*, **28**, 1517–1538 (2003).  
DOI: [10.1016/j.progpolymsci.2003.09.001](https://doi.org/10.1016/j.progpolymsci.2003.09.001)
- [14] Horacek H., Grabner R.: Advantages of flame retardants based on nitrogen compounds. *Polymer Degradation and Stability*, **54**, 205–215 (1996).  
DOI: [10.1016/S0141-3910\(96\)00045-6](https://doi.org/10.1016/S0141-3910(96)00045-6)
- [15] Kumar K. S., Ghosh A. K., Bhatnagar N.: Mechanical properties of injection molded long fiber polypropylene composites, Part I: Tensile and flexural properties. *Polymer Composites*, **28**, 259–266 (2007).  
DOI: [10.1002/pc.20298](https://doi.org/10.1002/pc.20298)
- [16] Pozzi P., Taurino R., Zanasi T., Andreola F., Barbieri L., Lancellotti I.: New polypropylene/glass composites: Effect of glass fibers from cathode ray tubes on thermal and mechanical properties. *Composites Part A: Applied Science and Manufacturing*, **41**, 435–440 (2010).  
DOI: [10.1016/j.compositesa.2009.12.001](https://doi.org/10.1016/j.compositesa.2009.12.001)
- [17] Vajna B., Bodzay B., Toldy A., Farkas I., Igricz T., Marosi Gy.: Analysis of car shredder polymer waste with Raman mapping and chemometrics. *Express Polymer Letters*, **6**, 107–119 (2012).  
DOI: [10.3144/expresspolymlett.2012.12](https://doi.org/10.3144/expresspolymlett.2012.12)

# Preparation and characterization of multifunctional free-standing Ni/epoxy composite films

X. J. Shen<sup>1,2</sup>, Y. Liu<sup>1</sup>, Q. P. Feng<sup>1</sup>, H. M. Xiao<sup>1</sup>, S. Y. Fu<sup>1\*</sup>, K. Friedrich<sup>3,4</sup>

<sup>1</sup>Technical Institute of Physics and Chemistry, Chinese Academy of Sciences, 100190 Beijing, China

<sup>2</sup>Graduate School, Chinese Academy of Sciences, 100039 Beijing, China

<sup>3</sup>Institute for Composite Materials (IVW GmbH), Technical University of Kaiserslautern, 67663 Kaiserslautern, Germany

<sup>4</sup>CEREM, King Saud University, Riyadh, Saudi Arabia

Received 12 April 2012; accepted in revised form 8 June 2012

**Abstract.** A new method is reported on preparation of multifunctional free-standing Ni/epoxy composite films with comprehensive physical properties under an applied magnetic field. A water soluble poly(vinyl alcohol) film is used as an inter-layer film to separate epoxy resin and glass wafer. Ultrafine Ni particles are incorporated into a self-designed flexible-type transparent epoxy resin to get composite films. For the purpose of comparison, random Ni/epoxy composite films are also prepared in the absence of the applied magnetic field. The aligned composite films are endowed with promising optical, mechanical, electrical, and ferromagnetic properties. The specific resistance is 4–9 orders lower in the vertical direction than that in the horizontal plane and the squareness ratio in the vertical direction is about 50% higher than in the horizontal plane. Meanwhile, their transmittance is much higher than that of the random composites. The anisotropies in their electrical and ferromagnetic properties are very useful material characteristics that may be explored for many applications.

**Keywords:** polymer composites, electrical conductivity, ferromagnetic property, transmittance

## 1. Introduction

With the rapid development of modern sciences and technologies, new materials with comprehensive physical properties are desired to meet the requirements of multifunctional devices [1–4]. Especially, optically transparent, mechanically flexible but electrically conductive and ferromagnetic material films are very useful in practical applications for flexible multifunctional devices in various electronic and electro-optical [5, 6], magneto-optical recording [7, 8], surface mount [9, 10] and new sensor technologies [11, 12]. Polymer based composites are nowadays more and more considered as promising candidates for this kind of applications [13–15].

Transparent polymers such as poly(vinyl alcohol) (PVA) and epoxy resin, etc. can be made to be

mechanically flexible [16, 17], but they are completely electrical insulators and nonmagnetic materials. In order to make them electrically conductive and ferromagnetic, functional particles such as Ni and Co, etc. must be incorporated to form micro- and nano-composites [13, 15, 18–20]. Thermosetting polymers have the advantages such as ease of processability and low cost of production, etc. Epoxy resins are a class of extensively used thermosetting polymers and their multifunctional composites have wide applications in surface mount, space and electronic technologies [14, 15, 21]. Unfortunately, the resultant composites usually become opaque by the introduction of functional particles. This is due to the fact that the refractive index mismatches between organic polymers and inorganic particles [22]. It is thus of great significance to

\*Corresponding author, e-mail: [syfu@mail.ipc.ac.cn](mailto:syfu@mail.ipc.ac.cn)

develop transparent conductive and ferromagnetic composites based on epoxy resins. However, little work has been reported yet on transparent epoxy composite films with comprehensive physical properties. Moreover, free standing films have some advantages such as easy operation and flexibility in practical applications for multifunctional devices. It is still a great challenge to develop free standing composite films based on epoxy resins since epoxy resins are strongly adhesive to various substrates [23–25].

Epoxy and its composite films can be prepared on various substrates [15, 26–28]. Epoxy films were synthesized by coating epoxy polymer on low carbon steel substrates degreased with organic solvents [26, 27]. Epoxy–polyester films were prepared on stainless steel substrate by electrostatic spray deposition [28]. The magnetic conductor micro-sized Ni powders and filaments were added to the epoxy matrix and then mixed thoroughly, finally the composite films were then obtained on a flat glass substrate [15]. However, it is hard to prepare free-standing epoxy composite films as mentioned above. In order to prepare free-standing epoxy composite films, release oil agent or polytetrafluoroethylene (PTFE) can be used to assist in peeling off epoxy composite films from substrates, but it is hard to form complete and good quality epoxy composite films due to large contact angles of epoxy resins with release oil agent or PTFE. Thus, it is of great importance to prepare free-standing epoxy composite films via a new approach.

In this work, a new method is developed for successful preparation of free-standing epoxy composite films. One key point here is that a water soluble PVA film is used as the interlayer film to separate epoxy resin and glass substrate. The PVA film has not only a small contact angle with epoxy resin but can also be water-soluble so that complete and high quality epoxy and composite films can be easily formed. In order to create transparent composite films, the as-prepared ultrafine monodisperse Ni particles with uniform sizes are aligned in the epoxy matrix by an applied magnetic field to allow light to transmit in the vertical direction. To get flexible epoxy and composite films, brittle epoxy resins can be modified using flexible modifiers [29–32]. This was realized by adding a flexible diamine to the epoxy resin matrix [33]. The aligned composites

showed obvious anisotropies in electrical and ferromagnetic properties and such anisotropies are very useful material characteristics that can be exploited for many applications [13–15, 34, 35]. For the purpose of comparison and as reference materials, the random composite films were also prepared by a conventional direct mixing method.

## 2. Experimental

### 2.1. Materials

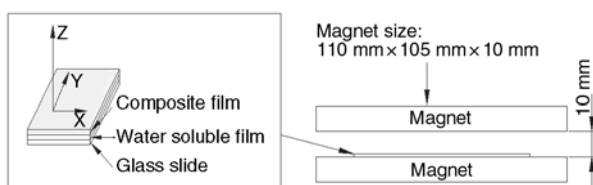
Ultrafine Ni particles with a diameter of about 114 nm were synthesized in our laboratory via a simple surfactant-free solvothermal method [36]. The matrix used was a transparent epoxy resin based on bisphenol-A (WS615) with an epoxy value of 0.50–0.56, purchased from Wuxi Resin Factory, Wuxi, China. The hardener was composed of flexible diamine (Jeffamine D-230, molecular weight  $M_w = 230$ , amine equivalent weight = 57.5) obtained from Huntsman Chemical Co., Salt Lake City, Utah, USA and alicyclic amine WK-6822 (amine value =  $260 \pm 10$ ) obtained from Wells Sheng Intl. Trading Co., Guangzhou, China.  $\gamma$ -glycidoxypropyltrimethoxysilane (KH-560) bought from Nanjing & Compton Co. Nanjing, China, was used as coupling agent. Flexible diamine (D-230) was used to modify the epoxy resin in order to get flexible epoxy composite films after curing [33]. The water soluble polyvinyl alcohol (PVA) film (Q-type) purchased from Yongan SYF Water Soluble Films Co., Ltd., Yongan, China was employed as the interlayer film to separate epoxy resin and glass substrate for an easy preparation of free-standing epoxy composite films.

### 2.2. Preparation of free-standing composite films

The compositions for preparing the composite films are shown in Table 1. Firstly, ultrafine monodisperse Ni particles, coupling agent and hardener were mixed in a conical flask and sonicated for 20 min. Then, the equivalent amount of the epoxy resin was mixed with the above mixture by ultrasonic treatment for 10 min. Afterwards, the suspension was degassed with a vacuum pump to eliminate air bubbles. When the air bubbles were sufficiently removed, 0.3 g of the resultant mixture was spread on a water soluble PVA film which was pre-coated on a glass slide substrate coated with vac-

**Table 1.** Formulations for preparation of epoxy and Ni/epoxy composite films

Sample code	Ni weight [g]	Ni content [wt%]	Bisphenol-A (WS615) [g]	D-230 [g]	WK6822 [g]	KH-560 [g]	Applied magnetic field
Pure epoxy	–	–	3.10	0.60	0.60	0.11	–
A	0.02	0.5	3.10	0.60	0.60	0.11	no
B	0.09	2.0	3.10	0.60	0.60	0.11	no
C	0.28	6.0	3.10	0.60	0.60	0.11	no
A <sub>m</sub>	0.02	0.5	3.10	0.60	0.60	0.11	yes
B <sub>m</sub>	0.09	2.0	3.10	0.60	0.60	0.11	yes
C <sub>m</sub>	0.28	6.0	3.10	0.60	0.60	0.11	yes

**Figure 1.** Schematic of the fixture for the curing of the composite samples under the applied magnetic field

uum silicon grease. The use of such a PVA interlayer film was necessary to easily obtain free-standing epoxy and composite films. Without using a PVA film as an interlayer, the epoxy resin would strongly adhere to the glass, making it very difficult to be free-standing.

The experimental fixture consisted of two permanent magnets in order to apply a magnetic field during the curing of the composites, as illustrated in Figure 1. The magnets with the pole section area of 110 mm × 105 mm and the pole-to-pole gap of 10 mm could produce a magnetic field of ca. 63 680 A/m. The samples were cured at room temperature for 6 h, and then 80°C for 4 h in the presence of the applied magnetic field. When the samples were cooled down to room temperature, the composite films along with the water soluble film were peeled off from the glass substrates. They were then placed in an 80°C hot water till the water soluble film was completely dissolved. Finally, the high-quality free-standing composite films of about 150–200 μm thickness were readily prepared. For the purpose of comparison, the samples were also prepared in the absence of the applied magnetic field under the same curing condition. Thus, the samples with three different Ni contents of 0.5, 2.0 and 6.0 wt% were synthesized.

### 2.3. Characterization and measurement

Scanning electron microscope (SEM) images were obtained to characterize the morphology and dispersion of the ultrafine Ni particles, using a Hitachi S-4300 microscope (Hitachi Co., Ltd., Tokyo,

Japan). The phase purity of the products was determined by X-ray diffraction (XRD) (D8 focus, Bruker Co., Karlsruhe, Germany) with a Cu K $\alpha$  radiation ( $\lambda = 1.5418 \text{ \AA}$ ). Top- and side-view micrographs were taken by an optical polarized microscope (Leica DM 2500M with an attached digital camera, DH-HV3100FC, Leica Microsystems Co., Wetzlar, Germany). The side-view samples were prepared by cryo-fracture via liquid nitrogen. The transmittance spectra of the films were detected using a UV–Vis spectrophotometer (U-3900, Hitachi Co., Ltd., Tokyo, Japan). The DC specific resistance was measured by a high-resistance & microcurrent meter (EST121, Beijing Institute of Labor Protection, Beijing, China). For the electrical conductivity measurement, the sample surfaces were pasted by silver paste with an area of 5 mm × 5 mm to ensure a perfect electrical contact. The area of the silver paste was large enough and thus the measured conductivity was independent of the contact area of the silver paste. Three measurements of the conductivity were conducted for each sample. The magnetic measurement was carried out at room temperature for the as-prepared samples, using a vibrating sample magnetometer (VSM 7307, Lakeshore Co., Westerville, USA) with a maximum magnetic field of 796 kA/m. The contact angle was measured by an automatic contact angle meter (SL200B, Solon Information & Technology Co., Shanghai, China).

## 3. Results and discussion

### 3.1. Characterization of Ni particles and contact angle of epoxy with base substrate materials

Ultrafine monodisperse Ni particles with a diameter of  $113.7 \pm 7.1 \text{ nm}$  were synthesized via a solvothermal method at a reaction temperature of 100°C for 3 h [36]. Figure 2a illustrates the as-synthesized spherical Ni particles. The size of the Ni particles

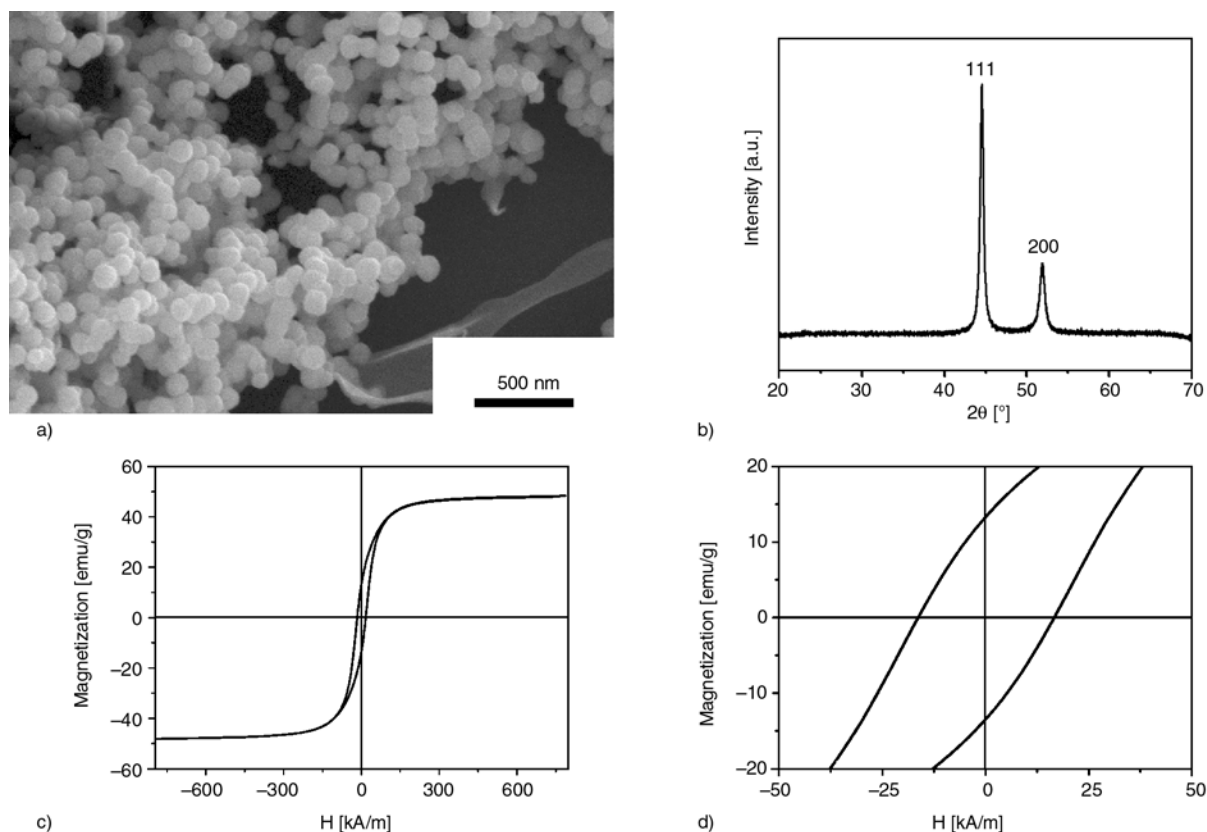


**Figure 2.** (a) SEM image, (b) XRD pattern and (c) hysteresis loops at room temperature of the as-prepared ultrafine nickel particles as well as (d) enlarged part of (c)

prepared under such a reaction condition showed no dependence on the reaction time [36], i.e. the following polymerization will not affect the size of the Ni particles. The X-ray powder diffraction (XRD) pattern of the ultrafine Ni particles is displayed in Figure 2b. The two peaks detected for the Ni sample are assigned to diffractions from the (111) and (200) planes of the face-centered cubic (fcc) Ni structure, respectively [36]. This is consistent with the values in the standard card (JCPDS card No. 4-485). No impurity peaks were detected in the experimental range, thus indicating the formation of pure Ni particles. The magnetic hysteresis measurement of the ultrafine Ni particles was carried out at room temperature in an applied magnetic field, sweeping from  $-796$  to  $796$  kA/m. Figure 2c and 2d shows the room temperature magnetic hysteresis curves of the as-prepared samples. The ultrafine Ni particles show ferromagnetic behavior with a saturation magnetization ( $M_s$ ) of about  $48.24$  emu/g and a remanence ( $M_r$ ) of about  $13.39$  emu/g. Meanwhile, they have a relatively high coercivity ( $H_c$ ) of  $16\,484$  A/m, compared with the coercive force value ( $56$  A/m) of the bulk one at room temperature [37].

In order to show the advantages of the PVA interlayer film over normally used PTFE or release oil agents for preparing epoxy films, the contact angles of the epoxy resin with these base materials were measured. The contact angles of epoxy resin with PTFE or release oil coated glass substrate were obtained to be  $45.4$  and  $38.6$  degrees, respectively. In contrast, the contact angle with the water soluble film was much smaller, amounting to just an angle of  $17.6$  degrees. Hence, it is much easier to form epoxy and composite films based on the water soluble PVA film than based on the PTFE or release oil agents. If the epoxy was spread directly on a glass substrate, the formed epoxy film could not be peeled off from the substrate due to the strong adhesion between the epoxy and the glass. Therefore, the advantage of the present work is that there is no need of peeling off the epoxy composite films from the water soluble PVA interlayer film, but just by simply dissolving the water soluble PVA substrate.

### 3.2. Transmittance of Ni/epoxy composite films

The top-view and side-view optical micrographs of both the aligned and random 2.0 wt% Ni/epoxy



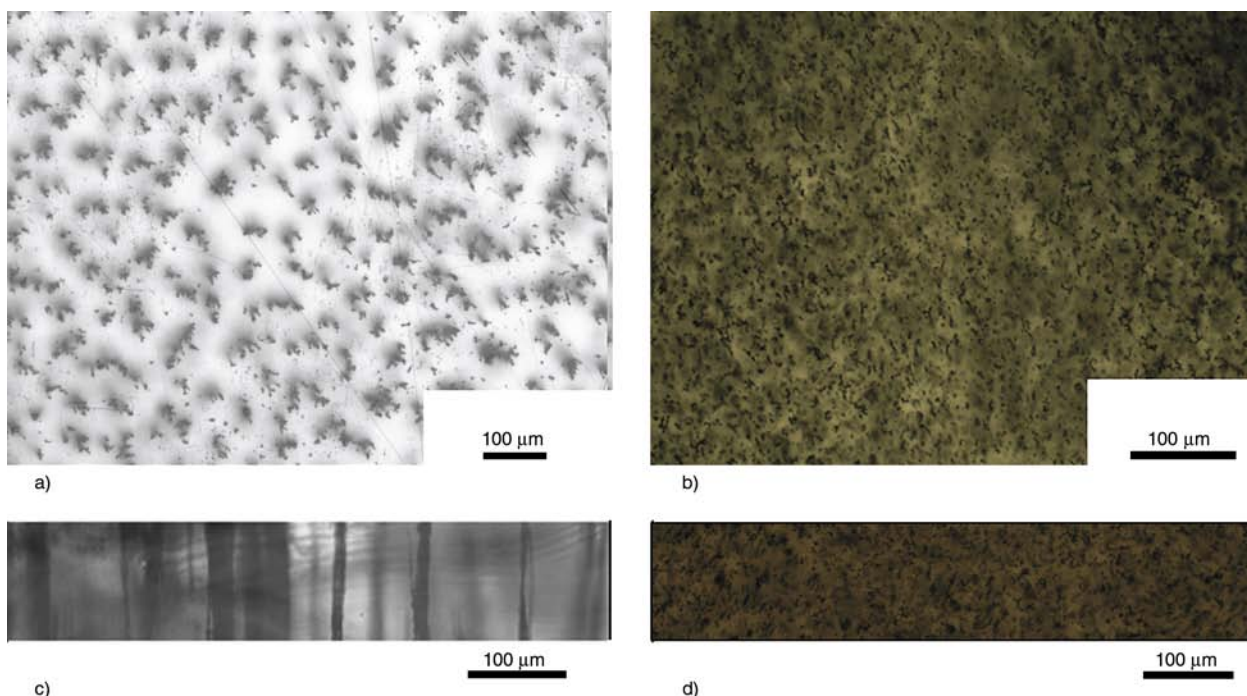


**Figure 3.** (a, b) Top-view (along the  $z$ -axis shown in Figure 1) and (c, d) side-view optical micrographs of the Ni/epoxy composite films (left  $B_m$  and right B)

composites are displayed in Figure 3. It reveals that the Ni columns in the composite medium are aligned along the magnetic field, and they are separated and spaced from each other (Figure 3a and 3c).

When the ultrafine Ni particles are uniformly dispersed in the epoxy matrix and subjected to a unidirectional magnetic field, they are aligned into a chain configuration to minimize the magnetostatic energy. Because they are in a fluid epoxy medium before curing, the Ni particles will move to minimize the potential energy of the system. The resultant magnetic dipoles in the neighboring columns repel each

other, thus positioning the columns towards an equilibrium spacing [14]. The surface tension of the epoxy matrix prevents the undesirable overgrowth of the Ni columns beyond the thickness of the layer. The magnetically aligned conductive structure is retained after the epoxy matrix is cured. Moreover, most of the columns extend throughout the whole thickness of the composite film. Figure 3b and 3d show the top-view and side-view optical micrographs of the composite medium prepared in the absence of the applied magnetic field. As predicted, the ultrafine Ni particles were distributed randomly

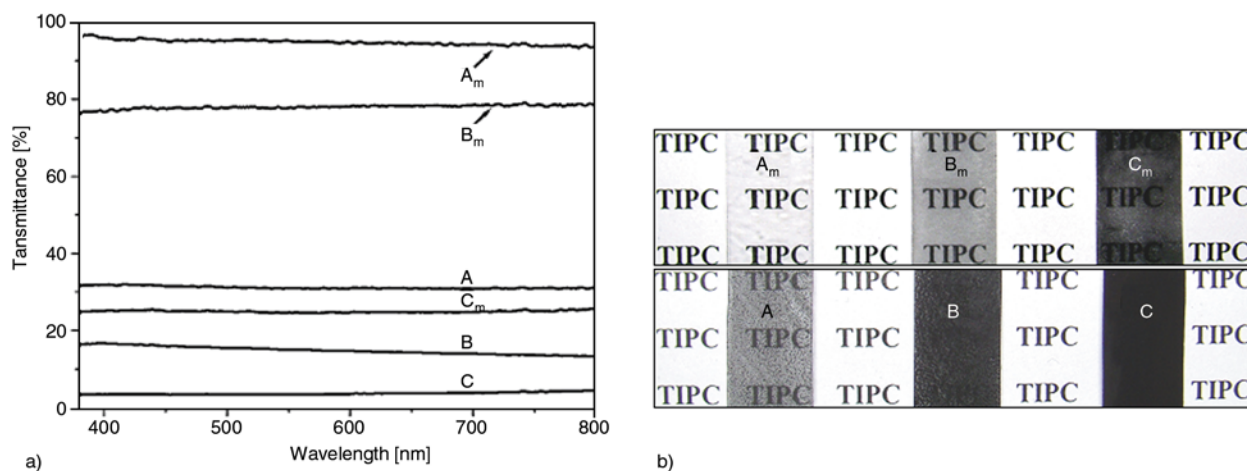


**Figure 4.** (a) UV-vis transmittance spectra of the Ni/epoxy composite films (calibrated against the pure epoxy film) along the vertical direction, and (b) digital photographs of the Ni/epoxy composite samples

in the epoxy matrix. This would bring about an opaque composite medium, which is confirmed in Figure 4.

Figure 4a shows the effect of the Ni alignment on the transmittance and transparency of the composite films with different Ni contents, whereby the data were calibrated against a pure epoxy sample. It can be seen that the transmittance of the composite films is dramatically improved by the alignment of the ultrafine Ni particles induced under the applied magnetic field. Therefore, a relatively higher transmittance and transparency have been observed for the aligned composites than for the random composites with the same Ni contents. However, there will be increased light scattering and blockage for both the random and aligned composites as the Ni particle content increases. Besides, an altered refractive index in the strained polymer material near the ultrafine Ni particles will also cause a loss in transmittance [14]. Therefore, a higher Ni content will lead to more severe light scattering and blockage, and the transmittance of the composite films decreases dramatically as the Ni content increases (Figure 4a). The corresponding transparency shown in Figure 4b confirms this tendency.

### 3.3. Electrical resistance and mechanical flexibility of Ni/epoxy composite films

The epoxy composites consisted of epoxy and ferromagnetic ultrafine Ni particles. The ultrafine Ni particles created aligned columns along the applied magnetic field, as shown in Figure 3a and 3c. The ferromagnetic ultrafine Ni particles are magnetized under the applied magnetic field, and these magnetized particles interact with adjacent particles due to their polarity. Finally, a columned structure of ultrafine Ni particles is formed due to repulsion of Ni particles in the as-prepared composites after they are cured. As a result, the current will primarily

flow along the direction of the applied magnetic field. To demonstrate this fact, the electrical conductivity in both the vertical ( $z$ -axis) direction and horizontal plane was measured. For the vertical measurement, the composite film was sandwiched between two copper electrodes, with a thin layer of silver paste at the interface between the copper electrodes

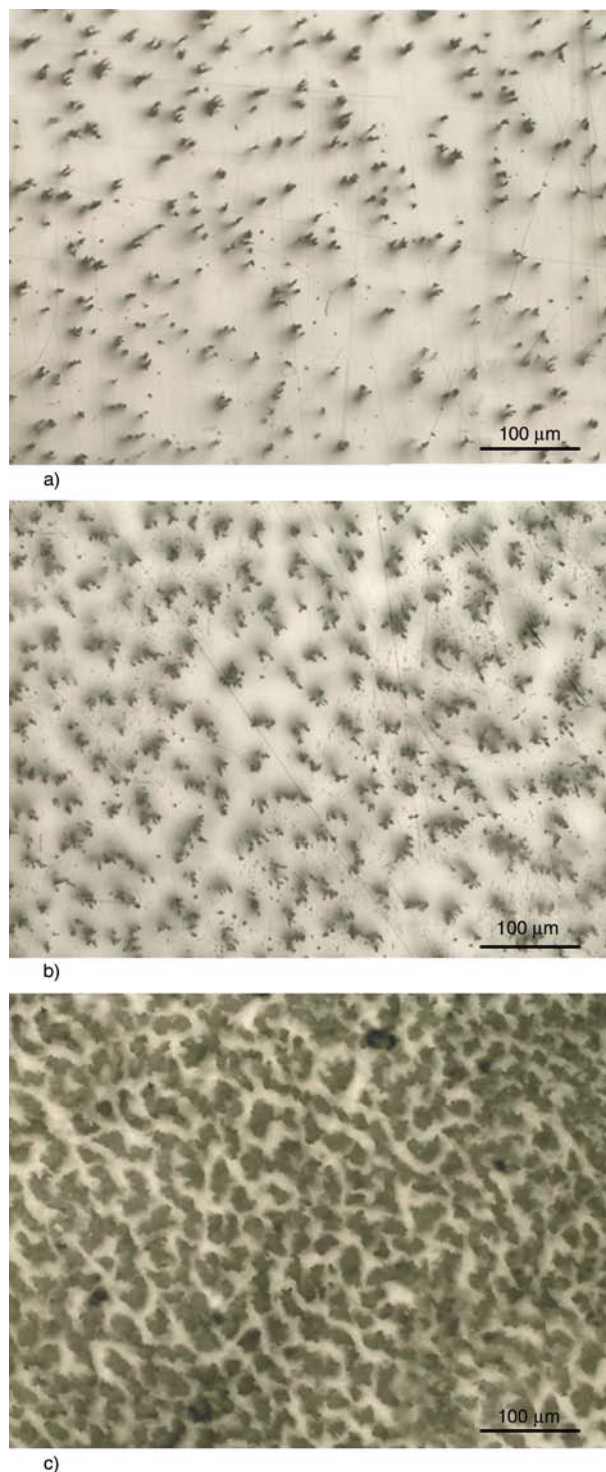
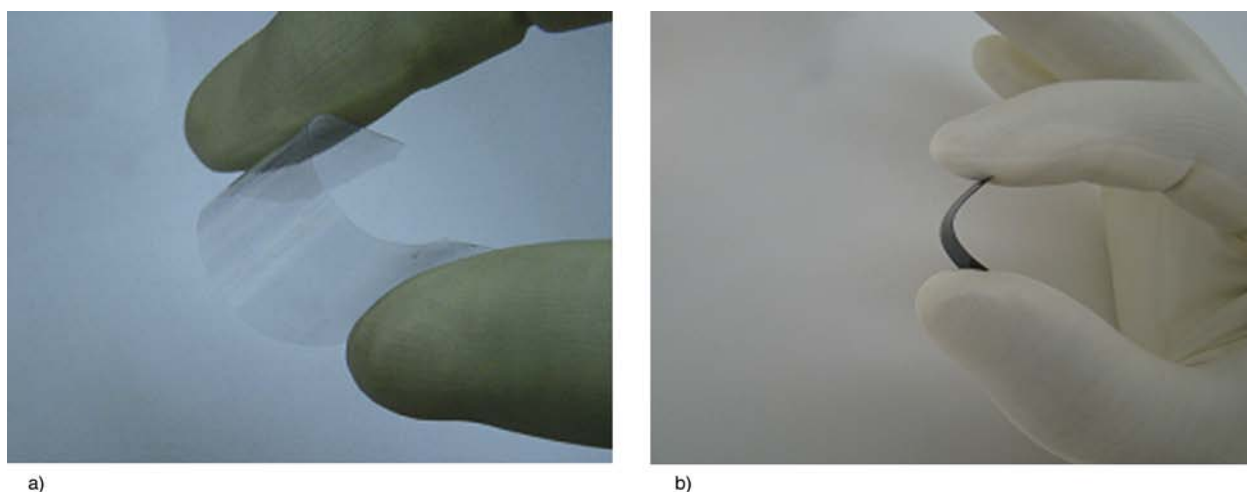


Figure 5. Top-view optical micrographs of the aligned Ni/epoxy composites: (a)  $A_m$ , (b)  $B_m$  and (c)  $C_m$

Table 2. Specific resistance of the pure epoxy film and the Ni/epoxy composite films

Sample code	Specific resistance of the horizontal plane [ $\Omega \cdot \text{cm}$ ]	Specific resistance of the vertical direction [ $\Omega \cdot \text{cm}$ ]
Pure epoxy film	$8.4 \cdot 10^{14}$	$9.5 \cdot 10^{14}$
A	$4.8 \cdot 10^{14}$	$6.0 \cdot 10^{14}$
B	$2.3 \cdot 10^{13}$	$1.6 \cdot 10^{13}$
C	$4.6 \cdot 10^{12}$	$3.4 \cdot 10^{12}$
$A_m$	$3.8 \cdot 10^{12}$	$6.8 \cdot 10^{10}$
$B_m$	$5.5 \cdot 10^{13}$	$2.4 \cdot 10^5$
$C_m$	$5.9 \cdot 10^{13}$	$2.3 \cdot 10^4$



**Figure 6.** Digital photographs of the composite films bent by fingers: (a)  $A_m$  and (b)  $C_m$

and the composite film to reduce the contact resistance. The horizontal electrical property of the composites was measured directly by two copper electrodes which clamp the two ends of the sample, respectively. All the electrical properties of the composites were measured at room temperature.

The corresponding results for the specific resistance are presented in Table 2. It can be seen that the specific resistance of the composite films decreases as the Ni content increases. This is easy to understand since the distance between Ni particles is reduced by the increase of the Ni content, so that it becomes easy for the Ni particles to contact with each other. For the aligned composites ( $A_m$ ,  $B_m$  and  $C_m$ ), the average diameters of the Ni columns are about 8, 23 and 37  $\mu\text{m}$  for the composite films, respectively, as shown in Figure 5. Moreover, the average distances among the Ni columns can be evaluated from over 10 measurements to be about 49, 44 and 20  $\mu\text{m}$ , respectively. Table 2 shows further that the specific resistances of the composite films ( $A_m$ ,  $B_m$  and  $C_m$ ) prepared in the presence of the applied magnetic field are 4–9 orders lower in the vertical direction than in the horizontal plane. This is because the ultrafine Ni particles were aligned to form columns throughout the whole thickness of the aligned composite film when the magnetic field was applied. Thus, these columns serve as electrically conducting pathways. This anisotropy in the electrical property is a useful material characteristic that may be exploited for electronic device applications [14, 15]. However, the normal composite samples (A, B, C) prepared in the absence of a magnetic field show an isotropy in the specific resistance. This is because

the ultrafine Ni particles were randomly dispersed in the epoxy matrix.

Figure 6 illustrates that the as-synthesized composite films are also very flexible. When bending the composite films, they will not be destroyed. After releasing of bending force, the composite films recover to their original shapes. In addition, repeated bending and unbending of the films up to ten times or more does not change this good behavior, thus demonstrating their excellent mechanical flexibility. Moreover, the flexibility of the samples was tested according to the standard ASTM D4338-97(2011)e1. The flexibility value of the films is defined as the diameter of the smallest mandrel over which four out of five test specimens do not break. The obtained flexibility for the samples of  $A_m$ ,  $B_m$  and  $C_m$  is respectively 4.0, 5.4 and 6.8 mm. And the flexibility of the samples (A, B and C) is also equal to 4.0, 5.4 and 6.8 mm, respectively. The good flexibility of these films is mainly due to the fact that the epoxy matrix modified by the flexible diamine (D-230) is flexible, as it was also done in our previous work for severe cryogenic engineering application [33]. Moreover, the specific resistance was measured for the composite films after repeated bending and unbending, and their specific resistance maintains their original values. This confirms that the composite films keep their integrity due to their excellent flexibility.

#### 3.4. Ferromagnetic property of Ni/epoxy composite films

The hysteresis measurements of the composites were carried out at room temperature in an applied

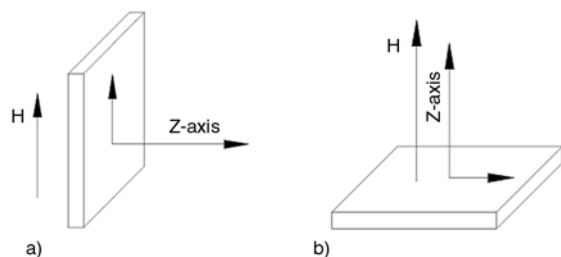


**Figure 7.** Schematic illustration of the VSM experiment in a magnetic field with different directions: (a) horizontal and (b) vertical

magnetic field sweeping from  $-796$  to  $796$  kA/m in the horizontal plane as well as in the vertical direction (Figure 7). The hysteresis loops for the aligned composite films are exhibited in Figure 8, whereby the hysteresis loops for the random composites were not presented for simplicity. The Ni/epoxy composites display a typical ferromagnetic behavior, indicating that the ferromagnetic characteristics of the ultrafine Ni particles were not altered by the preparation process of the composites. The results for the ferromagnetic properties are summarized in Table 3. It shows that the coercivity of the composite samples is about  $16\ 000$ – $16\ 875$  A/m, which is approximately the same as for the pure ultrafine Ni particles. This means, the applied magnetic field has a negligible effect on the coercivity of the composite films. On the other hand, both the saturation magnetization ( $M_s$ ) and remanence ( $M_r$ ) of the composite films increase as the Ni content increases from  $0.5$  to  $6.0$  wt% (Table 3).

In order to investigate the effect of the applied magnetic field on the magnetic anisotropy of the samples, a comparison in the squareness ratio ( $M_r/M_s$ ) of the samples is presented in Table 4. For the aligned composite films, when measuring in the horizontal plane (direction), the  $M_r/M_s$  of the samples is  $0.18$ ,  $0.23$  and  $0.24$ , for  $A_m$ ,  $B_m$  and  $C_m$ , respectively; when measuring in the vertical direction, the  $M_r/M_s$  of the three samples amounts to  $0.27$ ,  $0.35$  and  $0.36$ .

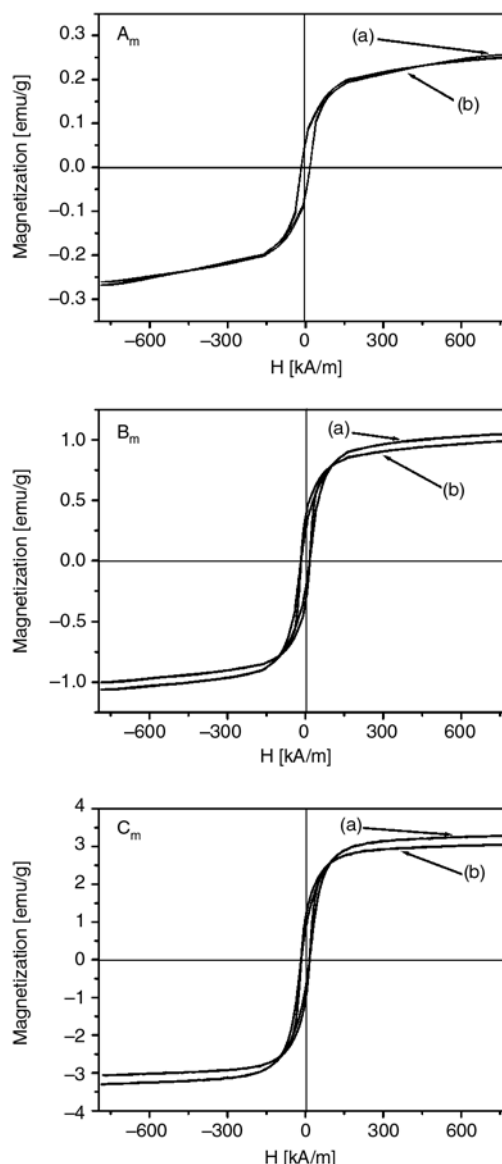


**Figure 8.** Hysteresis loops of the composite films ( $A_m$ ,  $B_m$  and  $C_m$ ): (a) horizontal and (b) vertical

The obvious difference (about 50%) in the squareness ratio between the horizontal and vertical directions indicates that an obvious magnetic anisotropy has been induced in the aligned composite films. For the random samples (A, B and C), the  $M_r/M_s$

**Table 3.** Saturation magnetization, remanence and coercivity of the Ni/epoxy composite films

Sample code	$M_s$ [emu/g]		$M_r$ [emu/g]		Coercivity [A/m]	
	Horizontal	Vertical	Horizontal	Vertical	Horizontal	Vertical
A	0.2622	0.2687	0.0603	0.0564	16687	16659
B	1.1319	1.0433	0.2717	0.2400	16701	16670
C	3.2646	3.1125	0.9141	0.8093	16029	15989
$A_m$	0.2775	0.2770	0.0500	0.0748	16571	16870
$B_m$	1.0550	0.9993	0.2427	0.3498	16610	16728
$C_m$	3.2964	3.0525	0.7911	1.099	16083	16115

**Table 4.** Squareness ratio ( $M_r/M_s$ ) of the Ni/epoxy composite films

Sample code	Squareness ratio ( $M_r/M_s$ )	
	Horizontal	Vertical
A	0.23	0.21
B	0.24	0.23
C	0.28	0.26
Am	0.18	0.27
Bm	0.23	0.35
Cm	0.24	0.36

ratio shows approximately equal values in the two directions and thus their ferromagnetic property is isotropic.

The most promising potential application of such films is in surface mount technology [14], where comprehensive physical and mechanical properties are required for epoxy composites. To make such films, the optimal concentration of the Ni particles should be about 2.0 wt%, and the film thickness should be below 200  $\mu\text{m}$  to get a high quality composite film with comprehensive physical properties.

#### 4. Conclusions

In summary, optically transparent, mechanically flexible, but electrically conductive and ferromagnetic free-standing Ni/epoxy composite films have been prepared via a new approach. The composites are based on the incorporation of as-prepared ultra-fine monodisperse Ni particles into a self-designed flexible-type transparent epoxy resin under an applied magnetic field. A water soluble poly(vinyl alcohol) film was used as the interlayer to separate epoxy resin and glass substrate so that epoxy and composite films could be easily obtained. It was shown that the Ni particles were aligned in the composite films prepared under an applied magnetic field, while the Ni particles in the reference composites prepared in the absence of an applied magnetic field showed a random filler distribution. The aligned composite films exhibited clear anisotropies in the electrical and ferromagnetic properties and a relatively higher optical transparency. Due to their comprehensive physical properties and great anisotropies in electrical and ferromagnetic properties, the aligned composite films are promising for practical applications in multifunctional electronic and electro-optical devices.

#### Acknowledgements

This work is financially supported by the National Natural Science Foundation of China (Nos. 10972216, 51073169 and 11002142) and Beijing Municipal Natural Science Foundation (No. 2122055). One of us, S. Y. Fu, is grateful to the Alexander von Humboldt Foundation for support of his research stay at IVW, Kaiserslautern, Germany, in March 2012.

#### References

- [1] Liao L., Zhang Z., Yan B., Zheng Z., Bao Q. L., Wu T., Li C. M., Shen Z. X., Zhang J. X., Gong H., Li J. C., Yu T.: Multifunctional CuO nanowire devices: p-type field effect transistors and CO gas sensors. *Nanotechnology*, **20**, 085203/1–085203/8 (2009). DOI: [10.1088/0957-4484/20/8/085203](https://doi.org/10.1088/0957-4484/20/8/085203)
- [2] Das J., Kalinikos B. A., Barman A. R., Patton C. E.: Multifunctional dual-tunable low loss ferrite-ferroelectric heterostructures for microwave devices. *Applied Physics Letters*, **91**, 172516/1–172516/3 (2007). DOI: [10.1063/1.2802577](https://doi.org/10.1063/1.2802577)
- [3] Li S., Tay Y. Y., Sun C. Q.: Separation of lattice structural and electronic effects on physical properties with nanotechnology. *Journal of Electroceramics*, **21**, 91–98 (2008). DOI: [10.1007/s10832-007-9078-6](https://doi.org/10.1007/s10832-007-9078-6)
- [4] Zhang C.-S., Ni Q.-Q., Fu S.-Y., Kurashiki K.: Electromagnetic interference shielding effect of nanocomposites with carbon nanotube and shape memory polymer. *Composites Science and Technology*, **67**, 2973–2980 (2007). DOI: [10.1016/j.compscitech.2007.05.011](https://doi.org/10.1016/j.compscitech.2007.05.011)
- [5] Sierros K. A., Hecht D. S., Banerjee D. A., Morris N. J., Hu L., Irvin G. C., Lee R. S., Cairns D. R.: Durable transparent carbon nanotube films for flexible device components. *Thin Solid Films*, **518**, 6977–6983 (2010). DOI: [10.1016/j.tsf.2010.07.026](https://doi.org/10.1016/j.tsf.2010.07.026)
- [6] de Villoria R. G., Hart A. J., Wardle B. L.: Continuous high-yield production of vertically aligned carbon nanotubes on 2D and 3D substrates. *ACS Nano*, **5**, 4850–4857 (2011). DOI: [10.1021/nn2008645](https://doi.org/10.1021/nn2008645)
- [7] Baba K., Takase F., Miyagi M.: Magnet-optic media composed of ferromagnetic metal island films for glass and semiconductor substrates. *Electronics Letters*, **32**, 222–224 (1996). DOI: [10.1049/el:19960151](https://doi.org/10.1049/el:19960151)
- [8] Yokoyama T., Nakagawa T., Takagi Y.: Magnetic circular dichroism for surface and thin film magnetism: Measurement techniques and surface chemical applications. *International Reviews in Physical Chemistry*, **27**, 449–505 (2008). DOI: [10.1080/01442350802127608](https://doi.org/10.1080/01442350802127608)

- [9] Ramkumar S. M., Srihari K.: A novel anisotropic conductive adhesive for lead-free surface mount electronics packaging. *Journal of Electronic Packaging*, **129**, 149–156 (2007).  
DOI: [10.1115/1.2721086](https://doi.org/10.1115/1.2721086)
- [10] Lu D., Wong C. P.: Novel conductive adhesives for surface mount applications. *Journal of Applied Polymer Science*, **74**, 399–406 (1999).  
DOI: [10.1002/\(SICI\)1097-4628\(19991010\)74:2<399::AID-APP22>3.0.CO;2-F](https://doi.org/10.1002/(SICI)1097-4628(19991010)74:2<399::AID-APP22>3.0.CO;2-F)
- [11] Nam S-B., Yun G. J., Carletta J., Kim D-H., Binienda W.: A novel noncontact electromagnetic field-based sensor for the monitoring of resonant fatigue tests. *Smart Materials and Structures*, **20**, 035005/1–035005/13 (2011).  
DOI: [10.1088/0964-1726/20/3/035005](https://doi.org/10.1088/0964-1726/20/3/035005)
- [12] Adachi N., Yogo K., Ota T., Takahashi M., Ishiyama K.: Magneto-optical effect and ferromagnetic resonance of Bi-Fe garnet for high frequency electromagnetic sensor. *Journal of Applied Physics*, **109**, 07A506/1–07A506/3 (2011).  
DOI: [10.1063/1.3556709](https://doi.org/10.1063/1.3556709)
- [13] Zhang B., Xie C., Hu J., Wang H., Gui Y.: Novel 1–3 metal nanoparticle/polymer composites induced by hybrid external fields. *Composites Science and Technology*, **66**, 1558–1563 (2006).  
DOI: [10.1016/j.compscitech.2005.11.020](https://doi.org/10.1016/j.compscitech.2005.11.020)
- [14] Jin S., Tiefel T. H., Wolfe R., Sherwood R. C., Mottine J. J. Jr.: Optically transparent, electrically conductive composite medium. *Science*, **255**, 446–448 (1992).  
DOI: [10.1126/science.255.5043.446](https://doi.org/10.1126/science.255.5043.446)
- [15] Sancaktar E., Dilsiz N.: Anisotropic alignment of nickel particles in a magnetic field for electronically conductive adhesives applications. *Journal of Adhesion Science and Technology*, **11**, 155–166 (1997).  
DOI: [10.1163/156856197X00273](https://doi.org/10.1163/156856197X00273)
- [16] Kim M. J., Yoo J-B.: Electrical properties of transparent conductive CNT composite films. *Electronic Materials Letters*, **4**, 57–61 (2008).
- [17] Harada M., Ueda A., Miyazaki H., Ochi M.: Mechanical properties of the flexible-type epoxy/clay nanocomposites prepared by slurry method. *Journal of Applied Polymer Science*, **113**, 2256–2263 (2009).  
DOI: [10.1002/app.30396](https://doi.org/10.1002/app.30396)
- [18] Taucher-Mautner W., Kordesch K.: Studies of pasted nickel electrodes to improve cylindrical nickel–zinc cells. *Journal of Power Sources*, **132**, 275–281 (2004).  
DOI: [10.1016/j.jpowsour.2004.01.032](https://doi.org/10.1016/j.jpowsour.2004.01.032)
- [19] Zeng W., Tan S. T.: Preparation and EMI shielding properties of nickel-coated PET fiber filled epoxy composites. *Polymer Composites*, **27**, 24–29 (2006).  
DOI: [10.1002/pc.20094](https://doi.org/10.1002/pc.20094)
- [20] Park J-M., Wang Z-J., Kwon D-J., Jang J-H., DeVries K. L.: Interfacial evaluation and hydrophobicity of multi-functional Ni-nanopowder/epoxy composites for self-sensing and actuation. *Smart Materials and Structures*, **19**, 124006/1–124006/8 (2010).  
DOI: [10.1088/0964-1726/19/12/124006](https://doi.org/10.1088/0964-1726/19/12/124006)
- [21] Shinko Denki Kogyo K. K.: Lead frame for resin-moulded semiconductor device – has connection between holes etched into front and rear surfaces of element mound die pad. Japanese Patent, JP3006851-A (1991).
- [22] Li Y. Q., Fu S. Y., Yang Y., Mai Y. W.: Facile synthesis of highly transparent polymer nanocomposites by introduction of core–shell structured nanoparticles. *Chemistry of Materials*, **20**, 2637–2643 (2008).  
DOI: [10.1021/cm7033307](https://doi.org/10.1021/cm7033307)
- [23] Barletta M., Bellisario D.: Manufacture and characterization of free-standing epoxy-polyester films. *Progress in Organic Coatings*, **70**, 259–272 (2011).  
DOI: [10.1016/j.porgcoat.2010.09.029](https://doi.org/10.1016/j.porgcoat.2010.09.029)
- [24] Rath S. K., Chavan J. G., Sasane S., Jagannath, Patri M., Samui A. B., Chakraborty B. C.: Two component silicone modified epoxy foul release coatings: Effect of modulus, surface energy and surface restructuring on pseudobarnacle and macrofouling behavior. *Applied Surface Science*, **256**, 2440–2446 (2010).  
DOI: [10.1016/j.apsusc.2009.10.084](https://doi.org/10.1016/j.apsusc.2009.10.084)
- [25] Afzal A., Siddiqi H. M.: A comprehensive study of the bicontinuous epoxy–silica hybrid polymers: I. Synthesis, characterization and glass transition. *Polymer*, **52**, 1345–1355 (2011).  
DOI: [10.1016/j.polymer.2011.01.046](https://doi.org/10.1016/j.polymer.2011.01.046)
- [26] Posner R., Santa M., Grundmeier G.: Wet- and corrosive de-adhesion processes of water-borne epoxy film coated steel. *Journal of the Electrochemical Society*, **158**, C29–C35 (2011).  
DOI: [10.1149/1.3525239](https://doi.org/10.1149/1.3525239)
- [27] Santa M., Posner R., Grundmeier G.: Wet- and corrosive de-adhesion processes of water-borne epoxy film coated steel. *Journal of the Electrochemical Society*, **158**, C36–C41 (2011).  
DOI: [10.1149/1.3525240](https://doi.org/10.1149/1.3525240)
- [28] Barletta M., Gisario A.: The role of the substrate in micro-scale scratching of epoxy–polyester films. *Applied Surface Science*, **257**, 4449–4463 (2011).  
DOI: [10.1016/j.apsusc.2010.12.090](https://doi.org/10.1016/j.apsusc.2010.12.090)
- [29] Maiti P. K.: Polymer-insulating material for rated electrical applications. *Journal of Applied Polymer Science*, **117**, 2310–2315 (2010).  
DOI: [10.1002/app.32071](https://doi.org/10.1002/app.32071)
- [30] Kostrzewa M., Hausnerova B., Bakar M., Siwek E.: Effects of various polyurethanes on the mechanical and structural properties of an epoxy resin. *Journal of Applied Polymer Science*, **119**, 2925–2932 (2011).  
DOI: [10.1002/app.32974](https://doi.org/10.1002/app.32974)
- [31] Ratna D., Chakraborty B. C., Dutta H., Banthia A. K.: Nanoreinforcement of flexible epoxy using layered silicate. *Polymer Engineering and Science*, **46**, 1667–1673 (2006).  
DOI: [10.1002/pen.20628](https://doi.org/10.1002/pen.20628)

- [32] Nazir T., Afzal A., Siddiqi H. M., Ahmad Z., Dumon M.: Thermally and mechanically superior hybrid epoxy–silica polymer films via sol–gel method. *Progress in Organic Coatings*, **69**, 100–106 (2010).  
DOI: [10.1016/j.porgcoat.2010.05.012](https://doi.org/10.1016/j.porgcoat.2010.05.012)
- [33] Yang G., Fu S-Y., Yang J-P.: Preparation and mechanical properties of modified epoxy resins with flexible diamines. *Polymer*, **48**, 302–310 (2010).  
DOI: [10.1016/j.polymer.2006.11.031](https://doi.org/10.1016/j.polymer.2006.11.031)
- [34] Duan C-G., Velez J. P., Sabirianov R. F., Mei W. N., Jaswal S. S., Tsymbal E. Y.: Tailoring magnetic anisotropy at the ferromagnetic/ferroelectric interface. *Applied Physics Letters*, **92**, 122905/1–122905/3 (2008).  
DOI: [10.1063/1.2901879](https://doi.org/10.1063/1.2901879)
- [35] Wei H. X., Qin Q. H., Wen Z. C., Han X. F., Zhang X-G.: Magnetic tunnel junction sensor with Co/Pt perpendicular anisotropy ferromagnetic layer. *Applied Physics Letters*, **94**, 172902/1–172902/3 (2009).  
DOI: [10.1063/1.3126064](https://doi.org/10.1063/1.3126064)
- [36] Shen X-J., Yang J-P., Liu Y., Luo Y-S., Fu S-Y.: Facile surfactant-free synthesis of monodisperse Ni particles via a simple solvothermal method and their superior catalytic effect on thermal decomposition of ammonium perchlorate. *New Journal of Chemistry*, **35**, 1403–1409 (2011).  
DOI: [10.1039/c0nj00987c](https://doi.org/10.1039/c0nj00987c)
- [37] Liu Q., Liu H., Han M., Zhu J., Liang Y., Xu Z., Song Y.: Nanometer-sized nickel hollow spheres. *Advanced Materials*, **17**, 1995–1999 (2005).  
DOI: [10.1002/adma.200500174](https://doi.org/10.1002/adma.200500174)

# Properties of poly(lactic acid) nanocomposites based on montmorillonite, sepiolite and zirconium phosphonate

K. Fukushima<sup>1\*</sup>, A. Fina<sup>1</sup>, F. Geobaldo<sup>2</sup>, A. Venturello<sup>2</sup>, G. Camino<sup>1</sup>

<sup>1</sup>Department of Applied Science and Technology, Polytechnic of Turin, V.le Teresa Michel 5, 15121 Alessandria, Italy

<sup>2</sup>Department of Applied Science and Technology, Polytechnic of Turin, Corso Duca degli Abruzzi 24, 10129 Torino, Italy

Received 18 April 2012; accepted in revised form 22 June 2012

**Abstract.** Poly(lactic acid) (PLA) based nanocomposites based on 5 wt.% of an organically modified montmorillonite (CLO), unmodified sepiolite (SEP) and organically modified zirconium phosphonate (ZrP) were obtained by melt blending. Wide angle X-ray scattering (WAXS) and scanning electron microscopy (SEM) analysis showed a different dispersion level depending on the type and functionalisation of nanoparticles. Differential scanning calorimetric (DSC) analysis showed that PLA was able to crystallize on heating, and that the addition of ZrP could promote extent of PLA crystallization, whereas the presence of CLO and SEP did not significantly affect the crystallization on heating and melting behaviour of PLA matrix. Dynamic Mechanical Thermoanalysis (DMTA) results showed that addition of all nanoparticles brought considerable improvements in  $E'$  of PLA, resulting in a remarkable increase of elastic properties for PLA nanocomposites. The melt viscosity and dynamic shear moduli ( $G'$ ,  $G''$ ) of PLA nanocomposites were also enhanced significantly by the presence of CLO and SEP, and attributed to the formation of a PLA/nanoparticle interconnected structure within the polymer matrix. The oxygen permeability of PLA did not significantly vary upon addition of SEP and ZrP nanoparticles. Only addition of CLO led to about 30% decrease compared to PLA permeability, due to the good clay dispersion and clay platelet-like morphology. The characteristic high transparency of PLA in the visible region was kept upon addition of the nanoparticles. Based on these achievements, a high potential of these PLA nanocomposites in sustainable packaging applications could be envisaged.

**Keywords:** nanocomposites, PLA, montmorillonite clay, sepiolite, zirconium phosphonate

## 1. Introduction

During the past decade, the issue of sustainability has been high on the European Union (EU) agenda, encouraging academia and industry to develop sustainable alternatives thus aiming to preserve resources for future generations. The successful promotion and use of biological, renewable materials for the production of packaging materials will satisfy a number of the EU objectives [1]. To date, packaging materials have been, to a large extent, based on non-renewable materials. The only widely used renewable packaging materials are paper and board which are based on cellulose, the most abundant

renewable polymer world-wide. However, major efforts are under way to identify alternative non-food uses of agricultural crops and the production of packaging materials, based on polymer from agricultural sources, could become a major use of such crops [2–4].

Indeed such alternative bio-based packaging materials have attracted considerable research and development interest for long time [1, 4] and in recent years the materials are reaching the market. Among all bio-based biodegradable polymers studied, poly(lactic acid) (PLA) appears to be one of the most attractive polymers commercially available, because

\*Corresponding author, e-mail: [kikku.fukushima@gmail.com](mailto:kikku.fukushima@gmail.com)



of its biodegradability, ease of processing, transparency and price. In general, commercial PLA grades are copolymers of poly (L-lactic acid) and poly(D,L-lactic acid), which are produced from L-lactides and D,L-lactides respectively. The ratio of L-enantiomers to D,L-enantiomers is known to affect the properties of PLA [5, 6], i.e. whether the materials are semicrystalline or amorphous. There is increasing interest in using PLA for disposable degradable plastic articles; however, there are properties such as flexural properties, gas barrier properties, high melt viscosity and melt strength/elasticity during processing, that are often not good enough for some end-use applications, such as blow molding [7, 8]. To improve the physical properties of PLA, especially in terms of thermomechanical stability, addition of different fillers (nanoparticles) in PLA was explored [2, 9–11]. Most of the literature regarding nanocomposites is devoted to lamellar layered silicates, in particular organically modified montmorillonites due to their ability to significantly enhance several polymer physical properties as compared to unmodified layered silicate clays, including gas barrier, flame retardancy, thermal stability and influence on the polymer biodegradation rate [2, 12–14]; however, needle like phyllosilicates (sepiolites) and zirconium phosphate are also reported in literature [15–21].

Sepiolite is a layered hydrated magnesium silicate characterized by a needle like morphology based on alternated blocks of tunnels in the fibre direction [16] and very high surface area (BET  $374 \pm 7 \text{ m}^2/\text{g}$ ) [23] as compared to layered phyllosilicates (BET  $82 \pm 1 \text{ m}^2/\text{g}$ ) [23, 24]. The addition of sepiolite has been reported to lead an improvement of the mechanical properties in various polymers, such as poly(vinylidene fluoride) and poly(methyl methacrylate) [25, 26], poly(styrene butadiene) block copolymers [27], ethylene-propylene (EPM) compounds [28] and natural rubber [29]. Based on the few papers on PLA, Poly ( $\epsilon$ -caprolactone) (PCL), PP and Poly (butylene terephthalate) (PBT) [15, 16], the possibility of an unmodified sepiolite to well disperse in polymers by melt blending was evidenced and mainly attributed to the large concentration of surface silanols, spaced every 0,5 nm along the length of sepiolite needle [30–32], that are easily available for coupling reactions with local polarity on polymer chains.

Zirconium bis(monohydrogen orthophosphate) monohydrate,  $(\alpha\text{-Zr}(\text{HPO}_4)_2(\text{H}_2\text{O}))$  ( $\alpha\text{-ZrP}$ ), has a layered structure with many interesting properties, such as high density of grafted organic modifiers, high thermal stability [33], possible achievement of large aspect ratios, high elastic modulus and the potential to delaminate and become intercalated within the polymer [17, 18]. PLA/zirconium phosphate composites has been studied and showed intumescent flame-retardant properties [34]. However, to the best of our knowledge, no studies on layered zirconium phosphonate PLA nanocomposites have been reported for possible packaging applications.

The aim of this work is to improve melt viscosity, thermo-mechanical and gas barrier properties of PLA by mixing it with organically modified montmorillonite, unmodified sepiolite and modified zirconium phosphonate, and thus producing final PLA nanocomposites with properties able to enlarge the PLA application fields.

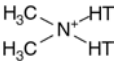
## 2. Experimental section

### 2.1. Materials

The poly(lactic acid) – PLA, 2002D –, average molecular weight 121 400 g/mol, ratio 96% L-lactide to 4% D-lactide units, MFR 6.4 g/10 min, was a commercial grade supplied by NatureWorks, Minneapolis Minnesota, USA. One commercial montmorillonite modified with a ditallow, dimethyl ammonium salt – CLOISITE 20A – was supplied by Southern Clay, Cheshire, UK, commercial unmodified sepiolite – PANGEL S9 – supplied by Tolsa, S.A, Madrid, Spain and  $\alpha$ -carboxyl-ethane zirconium phosphonate – ZrP 102 – (ultrapure >99%) were supplied by Prolabin & Tefarm, Perugia, Italy. The characteristics of the nanoparticles used in this work are listed in Table 1.

Prior to the melt blending, polymer matrix was dried at 70°C under vacuum for 4 h to achieve a residual moisture less than 190 ppm. Nanoparticles were dried at 100°C under vacuum for 10 h for CLO and SEP; and 4 h for ZrP to achieve residual moisture less than 250 ppm. Nanocomposites were prepared at 5% filler loading by melt blending using a Microextruder DSM Micro 15ml Twin Screw Compounder, with a mixing time of 5 min, at 180°C in nitrogen flow. The mixing was performed at two different rotor speeds: 60 rpm in the loading step and

**Table 1.** Characteristics of nanoparticles

Nanoparticle type	Commercial name	Modifier structure	Functional formula of nanoparticle	Notation in text
Montmorillonite <sup>a),b)</sup>	CLOISITE 20A		$M_x(Al_{4-x}Mg_x)Si_8O_{20}(OH)_4$ M: monovalent cation; x: degree of isomorphous substitution (between 0.5 and 1.3)	CLO
Sepiolite <sup>c)</sup>	PANGEL S9	None	$Si_{12}O_{30}Mg_8(OH)_4(H_2O)_4 \cdot 8H_2O$	SEP
$\alpha$ -carboxyl-ethane Zirconium phosphonate <sup>d)</sup>	ZrP 102	CH <sub>2</sub> CH <sub>2</sub> COOH	$Zr(O_3P(CH_2)_2COOH)_2$	ZrP

HT: hydrogenated linear alkyl chains: C<sub>8–18</sub>

<sup>a)</sup>Organic modifier content *ca.* 38 wt% according to CLOISITE 20A technical data sheet.

<sup>b)</sup>Functional formula taken from reference [2].

<sup>c)</sup>Functional formula taken from reference [22].

<sup>d)</sup>Functional formula taken from reference [35].

100 rpm during mixing. Sheets were obtained by compression molding in a hot-plate hydraulic press at 190°C and allowed to cool (*ca.* –10°C/min) to room temperature under pressure (60 Kgf/cm<sup>2</sup>). Morphological and thermo-mechanical characterizations were made on compression moulded 0.6 mm films, melt rheological measurements were carried out on compression moulded 1 mm films, optical transparency analyses were made on compression moulded 40–50  $\mu$ m films and oxygen gas barrier analyses were performed on compression moulded 320  $\mu$ m films (for PLA/ZrP) and on chill roll extruded 150–160  $\mu$ m films (for PLA, PLA/CLO and PLA/SEP). These last films were moulded at 180°C, passing the specimens by a chill roll with 150  $\mu$ m opening of several slits and allowed to cool to room temperature. In the case of PLA and PLA/CLO chill roll films, previous to the film cooling process to room temperature, these were biaxially stretched above PLA glass transition temperature (above 60°C) to obtain films with 50–70  $\mu$ m thick.

## 2.2. Characterization techniques

Wide Angle X-Ray Spectra (WAXS) were recorded using a Thermo ARL diffractometer X-tra 48, at room temperature in the range 1–30° (2 $\theta$ ) (step size = 0.02°, scanning rate = 2 s/step) by using filtered CuK $\alpha$  radiation ( $\lambda$  = 1.54 Å).

Scanning electron microscopy (SEM) was carried out on surfaces obtained after sectioning with a microtome diamond knife to avoid large surface roughness sputtered with gold, using a LEO 1400 VP Series (Carl Zeiss, Oberkochen, Germany) equipped with energy dispersive spectroscopy (EDS).

Transmission electron microscopy (TEM) analyses were performed with a high-resolution equipment.

Ultrathin sections of about 100 nm thick were cut at room temperature with a microtome equipped with a diamond knife and placed on a 200-mesh copper grid. Differential Scanning Calorimetry (DSC) tests were carried on a DSC Q100 TA Instruments (New Castle, DE, USA) under nitrogen atmosphere at a scanning rate of 10°C/min, sample size 3–5 mg in aluminium pans. Thermal history of samples was erased by a preliminary heating cycle at 10°C/min from –20°C to +280°C. The glass transition temperature ( $T_g$ ), cold crystallization temperature ( $T_{cc}$ ), melting temperature ( $T_m$ ), cold crystallization enthalpy ( $\Delta H_{cc}$ ) and melting enthalpy ( $\Delta H_m$ ) were determined from second heating scan at 10°C/min. Dynamic-Mechanical Thermal Analysis (DMTA) was performed on compression moulded 6 × 20 × 0.6 mm<sup>3</sup> films, using a DMA Q800 TA Instruments (New Castle, DE, USA) in tension film clamp. The temperature range analysed was from +20 to +80°C, at a heating rate of 2°C/min, 1 Hz frequency, in strain controlled mode, 15 micron of amplitude and static loading = 125% dynamic loading. At least two samples of each material were tested and the average value of these parameters for each material was calculated and reported. The estimated experimental error based on the Storage Modulus and Tan Delta deviations between repeated tests was *ca.* 10%.

Melt rheological measurements were performed on ARES instrument (New Castle, DE, USA) with a torque transducer capable of measurements over the range of 0.02 to 200 g·cm. Dynamic oscillatory shear measurements were performed by applying a time dependent strain of  $\gamma(t) = \gamma_0 \sin(\omega t)$  and the resultant shear stress is  $\sigma(t) = \gamma_0 [G' \cdot \sin(\omega t) + G'' \cdot \cos(\omega t)]$ , with  $G'$  and  $G''$  being the storage and loss modulus, respectively. Measurements were con-

ducted by using a set of 25 mm diameter parallel plates with a sample thickness of 1 mm. The strain amplitude was fixed to 1% for PLA/CLO and 10% for neat PLA and PLA/SEP systems, in order to obtain reasonable signal intensities even at low frequency ( $\omega$ ) to avoid the non linear response. For each type of material the limits of linear viscoelasticity were determined by performing strain sweeps at series of fixed  $\omega$ s. The dynamic viscoelastic curves were obtained by using the principle of time-temperature superposition and shifted to a common reference temperature of 190°C which was chosen as the most representative of a typical processing temperature of PLA.

Oxygen gas barrier properties were measured on compression moulded films of 5 cm<sup>2</sup> × 320 μm for PLA/ZrP, on chill roll moulded films of 50 cm<sup>2</sup> × 150–160 μm for PLA/SEP and on chill roll moulded films of 50 cm<sup>2</sup> × 50–70 μm for PLA and PLA/CLO, using a permeabilimeter MOCON OX-TRAN 2/21 (Minneapolis, USA). The experimental conditions were 23°C, 760 mm Hg pressure, 0% relative humidity and with permeant concentration of 100%. Two samples were tested for each type of material and average results of permeability (normalised on the thickness) are presented.

Optical transparency of PLA and PLA/composites was obtained using a UV-vis spectrometer CARY 500 (California, USA) on compression moulded 5 cm<sup>2</sup> × 40–50 μm. The analysis was performance in transmittance mode from 380–780 nm wavelength, UV-vis scan rate of 600 nm/min and Double Beam Mode. The cumulative transmission over visible spectra was measured to three samples of each material and the average value of these measure-

ments was reported for each material type. The estimated experimental error was *ca.* 10%.

### 3. Results and discussion

#### 3.1. Morphology

##### 3.1.1. Wide Angle X-ray analysis (WAXS)

The WAXS pattern of PLA is characterized by a broad amorphous halo with maximum approximately at  $2\theta = 17^\circ$  (not shown here). These results indicate that PLA matrix was not able to crystallize during the film cooling process (*ca.* 10°C/min), thus obtaining a completely amorphous structure for the polymer matrix at room temperature.

A similar broad WAXS halo with maximum at *ca.*  $2\theta = 17^\circ$  was observed for PLA/CLO and PLA/ZrP, indicating an amorphous structure of the polymer matrix in these specimens. This result suggests that the addition of these nanoparticles does not induce polymer crystallization under the conditions of film cooling carried out here.

The most significant features are indeed encountered in the lower angle range, which gives indication of the nanoparticles interlayer distance. Figure 1a and 1b represent the WAXS patterns of composites of PLA with CLO and ZrP, compared with the pristine nanoparticles. CLO is characterized by two diffraction peaks at  $2\theta = 3.5$  and  $7.2^\circ$  respectively (Figure 1a); the diffraction peak at  $2\theta = 3.5^\circ$  correspond to the crystalline plane (001) [11], whereas the weak peak at  $7.2^\circ$ , corresponding to an interlayer distance of 1.24 nm, is likely to be related to a low content of montmorillonite silicates layers without organic modifier insertion [11].

The PLA/CLO nanocomposite exhibited two diffraction peaks at  $2.4^\circ$  corresponding to an interlayer

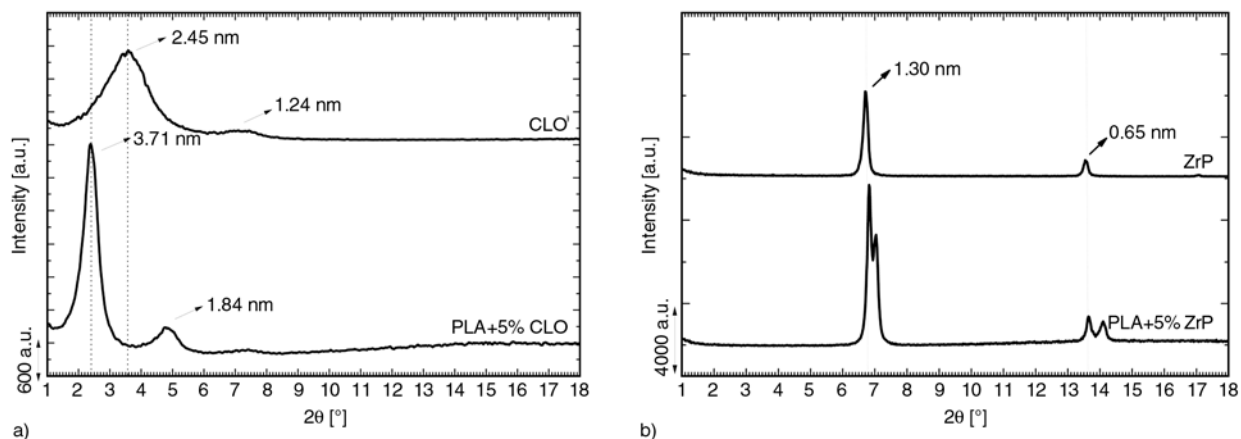


Figure 1. WAXS patterns of PLA based composites with 5% (a) CLO and (b) ZrP

spacing of 3.71 nm, and a secondary diffraction peak, ( $d_{002}$ ), at  $5.0^\circ$  [8, 11]. An increase in the interlayer spacing from 2.45 nm in the nanoclay filler to 3.71 nm in the PLA nanocomposite gave credit to some intercalation occurring during the component blending above the melting temperature of the polymer matrix. This finding showed the possibility of penetration of the PLA chains within the nanoclay galleries on shearing at high temperature.

This intercalation of polymer chains in the CLO silicate layers can be obtained thanks to chemical affinity between the polymer and the clay, originated from the hydrogen bonding between the carbonyl groups of the main chain of PLA molecules and the hydroxyl groups belonging to CLO surface silicate layers [2, 11, 15]. The presence of the organic modifier between CLO layers could also make possible the delamination of CLO silicate layers in PLA/CLO hybrid by high mixing torques during the melt blending process, despite, strong chemical interactions between the organic modifier molecules and PLA matrix would not be expected, considering the non-polar structure of this organic modifier [8].

Figure 1b shows the WAXS patterns of the pristine ZrP, showing two characteristic peaks at  $2\theta = 6.70^\circ$  and  $13.5^\circ$ , which are attributed to the (002) plane for organo-modified ZrP and pristine ZrP, respectively. Indeed, the main WAXS peak at  $6.70^\circ$  ( $d = 1.30$  nm) indicates greater separation of the ZrP layers by the presence of the carboxyl-ethane groups [20, 21, 35], whereas the weaker WAXS peak at  $13.5^\circ$  corresponds to the interlayer d-spacing of inorganic  $\alpha$ -ZrP as an impurity [19, 35, 36].

The WAXS patterns of PLA/ZrP hybrid do not show signs of intercalation of PLA into ZrP platelets, likely due to the insufficient interlayer thickness, which is significantly lower in ZrP as compared to CLO. Indeed, the presence of the sharp peaks at diffraction angles correspondent to ZrP confirms that, in these compounding conditions, the stacking of parallel zirconium phosphate sheets is not significantly modified.

No information is delivered by WAXS on dispersion of needle-shaped sepiolite in PLA, given the lack of periodic stacking of pristine nanoparticles.

### 3.1.2. Scanning electron microscopy (SEM)

All formulations were observed by SEM on surfaces to study the dispersion and distribution of nanoparticles. SEM micrographs at low magnification (not shown here) reveals no significant presence of agglomerated ( $> 10 \mu\text{m}$ ) inorganic nanoparticles regardless the composition. In PLA/CLO a very uniform distribution of small stacks of silicate layers can be observed in the polymer matrix, as shown in Figure 2a. The presence of clay layers is indeed highlighted by the cracks observable on diamond cut surfaces, which are not present in pristine PLA when prepared in the same way. Indeed, such cracks are attributed to delamination between polymer matrix and nanoclay stacks. TEM images (Figure 2b) confirmed the presence of both isolated nanoclay layers and stacks of a few clay layers.

In the case of PLA/SEP, nanofibres emerging from the polymer surface are clearly visible in SEM micrographs (Figure 3). Diameter of these fibres are in the range of 10 to 100 nm, therefore are

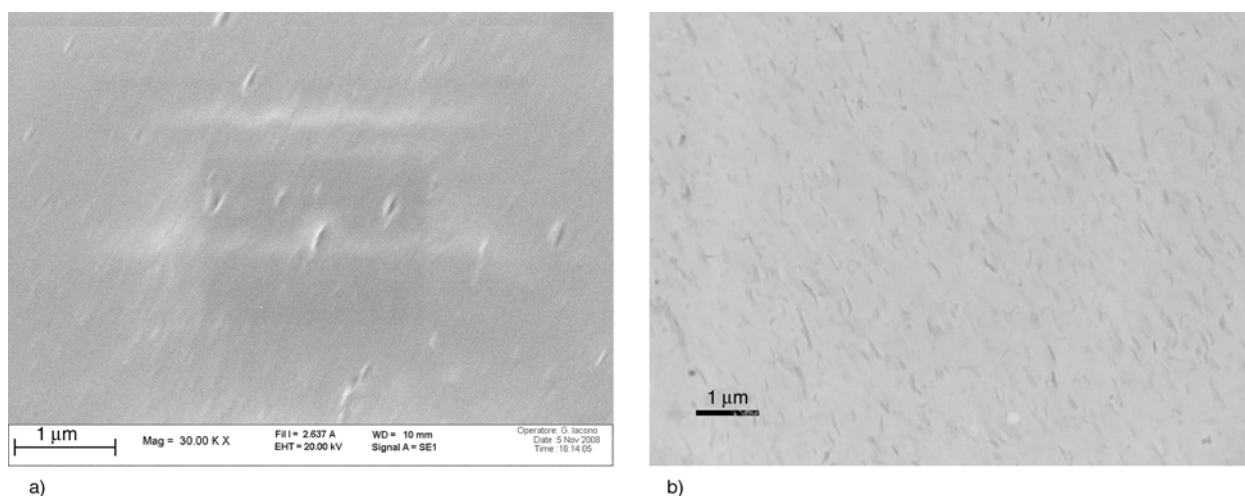


**Figure 2.** Scanning electron micrograph (a) and transmission electron micrograph (b) for PLA + 5% CLO

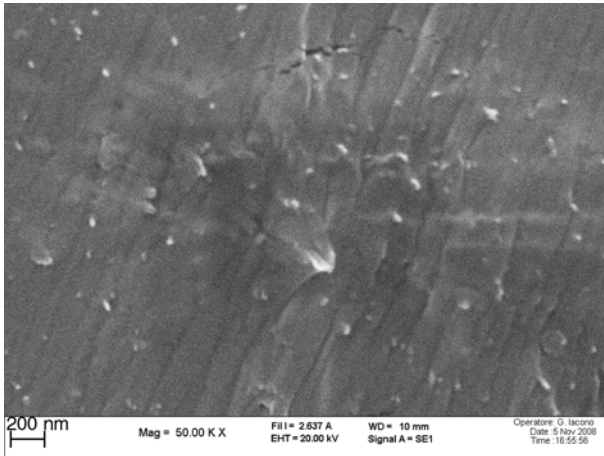


**Figure 3.** Scanning electron micrographs at 50 kX of magnification for PLA + 5% SEP. The cracks observed in the polymer matrix corresponds to matrix degradation under electron beam irradiation

assigned to single sepiolite needles and some bundles of a few individual sepiolite needles.

The addition of 5% ZrP (Figure 4) reveals the presence of ZrP micro-particles fairly distributed in the polymer surface. However, poor adhesion of the

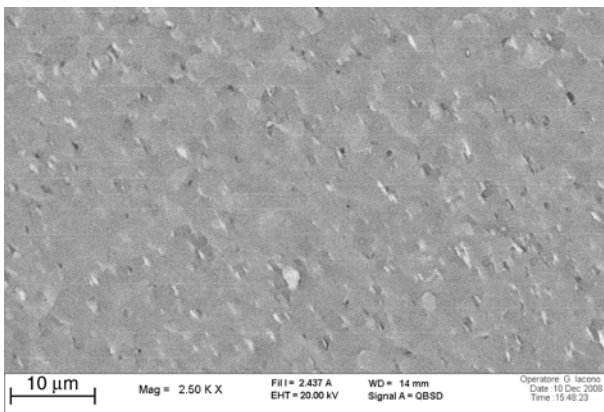


**Figure 4.** Scanning electron micrographs for PLA + 5% ZrP

microparticles is evidenced by the presence of holes left by detachment of some ZrP particles during mirotome cutting. Interestingly enough, SEM micrographs show that ZrP powder presents a plate-like structure and regular sheets, which can be related to the presence of very sharp WAXS peaks both in pristine ZrP and in the composite.

### 3.2. Thermal analysis (DSC)

Crystallisation of PLA nanocomposites was studied by means of DSC measurements. In Figure 5, cooling and second heating DSC plots for PLA and composites are reported. On cooling at a rate of 10°C/min (Figure 5a), the pure PLA does not exhibit any exothermic peak, evidencing that no crystallization takes place. Crystallization on cooling of PLA is not significantly affected by the addition of the nanoparticles, as evidenced by the identical DSC thermograms, confirming that all materials addressed here are not able to crystallise at cooling rates of 10°C/min or higher, in agreement with the WAXS analysis which evidenced fully amorphous structures.

Figure 5b reports the DSC thermograms of the second heating curves of PLA and PLA/nanocomposites. PLA partially crystallizes on heating at about 130°C (cold crystallization) giving a crystalline phase which melts with a peak endotherm at about 154°C [15, 37] (see Table 2).

Figure 5b and Table 2 show that the addition of CLO and SEP does not significantly affect the crystallization and melting behaviour of PLA, since no significant variations of cold crystallization temperature ( $T_{cc}$ ), enthalpy of cold crystallization ( $\Delta H_{cc}$ ),

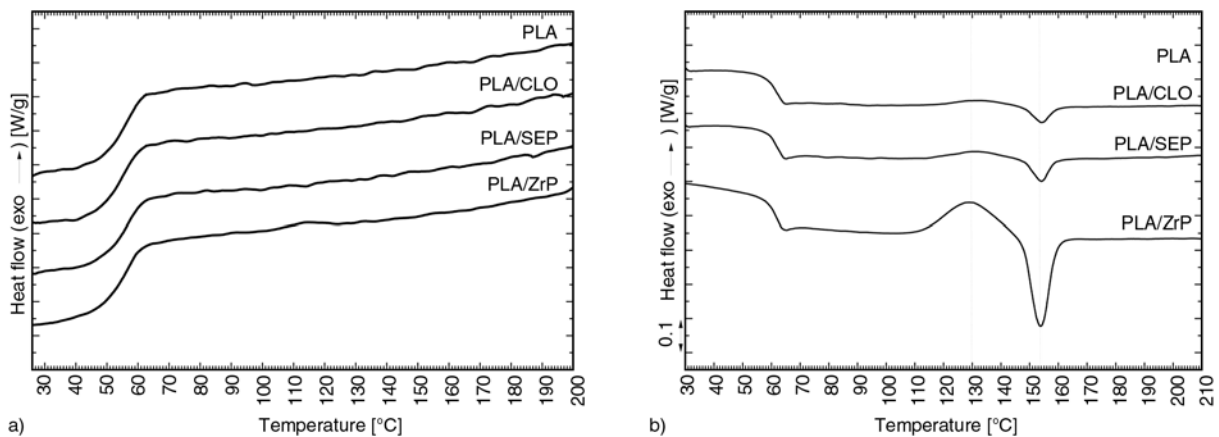


**Figure 5.** DSC thermograms of PLA and PLA/composites at (a) cooling and (b) second heating. Plots are vertically shifted for the sake of clarity.

**Table 2.** DSC data on PLA and PLA/nanocomposites obtained by second heating curves

Sample	$T_{cc}^{a)}$ [°C]	$\Delta H_{cc}$ [J/g]	$T_m^{a)}$ [°C]	$\Delta H_m$ [J/g]	$T_g$ [°C]
PLA	130	2	154	2	61
PLA + CLO	131	2	154	2	61
PLA + SEP	131	3	154	3	61
PLA + ZrP	129	11	154	12	60

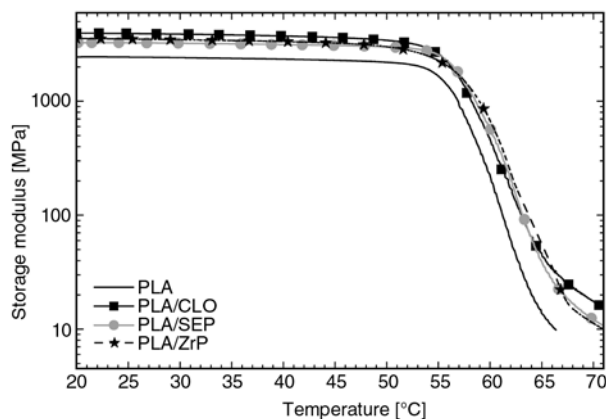
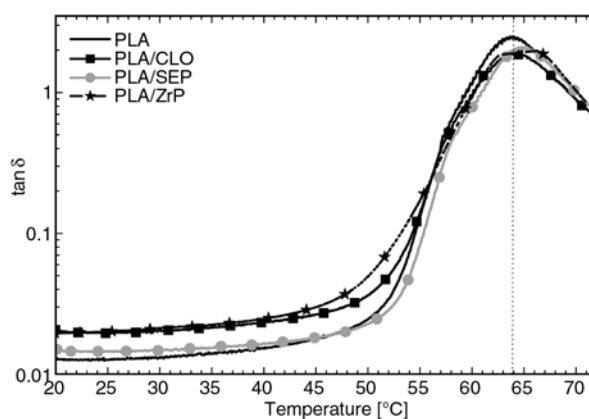
<sup>a)</sup>Temperatures quoted are peak temperatures

melting temperature ( $T_m$ ), melting enthalpy ( $\Delta H_m$ ) and glass transition temperature ( $T_g$ ) were observed. Addition of ZrP particles neither leads important variations in the  $T_{cc}$ ,  $T_m$  and  $T_g$  of PLA matrix, however, increases of the enthalpy of cold crystallization (*ca.* 9 J/g) and of the melting enthalpy of neat PLA (*ca.* 10 J/g) could be detected by the presence of these particles (see Figure 5b and Table 2). These increases of  $\Delta H_{cc}$  and  $\Delta H_m$  obtained by ZrP based composites indicate that the addition of these particles promotes extent of crystallization of the PLA on heating, which is most likely related to the regular distribution of ZrP micronic particles (previously verified through WAXS and SEM analysis) able to act as nucleating agents of PLA crystallization.

It is also possible that a higher dispersion level of CLO and SEP particles into the PLA as compared to ZrP, could interfere with polymer molecules crystallization instead of enhancing it. In general, it has been reported the possible nucleating effect of well dispersed organoclay layers on polymer crystallization of PLA [2, 9–11]; however, it has been also reported that high interactions between polymer matrix and nanoscale particles, can provoke that some polymer chains can be attached to the clay layers, and then partially immobilized and hindered from taking part in the flow process and their crystallization process [8, 38]. Accordingly, in addition to acting as nucleation agents, the silicates particles of CLO and SEP could also become retardant of crystallization, acting as physical hindrance if there are important interactions between polymer matrix and clay, and consequently obtaining insignificant changes in the crystallization and melting process of PLA.

### 3.3. Dynamic-mechanical thermal analysis (DMTA)

The dynamic-mechanical experiments of PLA and nanocomposites are reported in Figure 6, Figure 7

**Figure 6.** Temperature dependence of storage modulus ( $E'$ ) for PLA and PLA/composites**Figure 7.** Temperature dependence of  $\tan \delta$  for PLA and PLA/composites

and Table 3, showing the temperature dependence of Storage Modulus ( $E'$ ) and  $\tan \delta$  for all the studied materials. A general enhancement of  $E'$  below  $T_g$  was observed compared to neat PLA: at 20°C,  $E'$  increases of *ca.* 60, 35 and 45% were obtained for PLA/CLO, PLA/SEP and PLA/ZrP, respectively (Table 3). Higher enhancements of  $E'$  were observed above  $T_g$ : at 65°C increases of *ca.* 150, 120 and 170% were obtained for PLA/CLO, PLA/SEP and PLA/ZrP, respectively.

The dynamo-mechanical results show improvements in  $E'$  with the addition of all nanoparticles, indicating that addition of particles into PLA matrix results in a remarkable increase of elastic properties for PLA composites, more noticeable at higher temperatures (above 60°C), which means an increase of thermal-mechanical stability for the composites at high temperatures [38]. The increase of  $E'$  for composites with temperature compared to that of neat PLA may be attributed to a restriction in the movements of the polymer chains above  $T_g$  [2, 38]. How-

**Table 3.**  $E'$  and  $\tan\delta$  values of PLA and PLA/composites at 20 and 65°C. Estimated experimental error  $\pm 10\%$ 

Sample	$E'$ at 20°C [MPa]	$E'$ at 65°C [MPa]	T at $\tan\delta_{\max}$ [°C]
PLA	2429	13	64
PLA + CLO	3815	32	65
PLA + SEP	3264	28	64
PLA + ZrP	3529	35	65

ever, given the very low storage modulus values of neat PLA above  $T_g$ , these enhancement in modulus above this temperature have limited practical interest, absolute values for  $E'$  being below 50 MPa for all composites.

This improved strength has also been observed for other polymer/clay nanocomposites, depending on the degree of dispersion of clay in the polymer matrix [13, 15]. In the case of PLA nanocomposites in this study, all composites present  $E'$  improvements both below and above glass transition temperature, explained by strong interactions between the particles and PLA molecules originated from hydrogen bonding between the carbonyl groups of PLA and the hydroxyl groups belong to the structure of CLO, SEP and ZrP (see Table 1). Indeed, such interactions have been previously verified by other researchers in biopolymer nanocomposites based on similar nanoparticles rich of surface silanol groups (Si–OH) [21, 39, 40]. In this case, they have corroborated the possible spontaneous assembly of the biopolymer matrix and nanoparticles through hydrogen-bonding interactions, by the observed infrared perturbation of the O–H stretching vibrations assigned to the surface silanol groups. Interestingly enough, similar increases of  $E'$  were obtained upon the addition of ZrP into PLA as compared to CLO and SEP (even higher at 65°C), despite its low dispersion level into the PLA matrix according to WAXS and SEM analysis, and probably attributed to the high crystallinity of ZrP particles as well as to the very regular distribution of ZrP micronic particles along all the polymer matrix (see Figure 1b and 4).

The presence of the particles does not show significant shift of  $\tan\delta$  (Figure 7 and Table 3) for all composites compared to pure PLA, in agreement with DSC analysis.

### 3.4. Melt rheology

The rheological properties of polymer nanocomposites are directly related to their melt behavior during processing, such as extrusion or injection moulding. Moreover, rheology offers a mean to assess the level of filler dispersion in nanocomposites directly in the molten state, given that rheological properties of particle-filled materials are sensitive to the structure, particle size, shape and interface characteristics of the dispersed phase [2].

The rheological behavior was studied for the PLA nanocomposites containing well dispersed particles (CLO and SEP); the linear dynamic viscoelastic curves for these materials as well as neat PLA are shown in Figure 8. Both  $G'(\omega)$  and  $G''(\omega)$  moduli of nanocomposites increase at all frequencies as compared to PLA. At high frequencies, the values of  $G'(\omega)$  and  $G''(\omega)$  of neat PLA are practically unaffected by the presence of nanoparticles. However, at low frequency, the presence of nanoparticles CLO and SEP induces an increase of  $G'(\omega)$  and  $G''(\omega)$  compared to neat PLA (see Figure 8a, b). Indeed, at  $\omega < 10 \text{ rad}\cdot\text{s}^{-1}$  for PLA/CLO and  $\omega < 0.05 \text{ rad}\cdot\text{s}^{-1}$  for PLA/SEP, both  $G'(\omega)$  and  $G''(\omega)$  display a significantly diminished frequency dependence as compared to PLA. The lower frequency dependence and the higher absolute values of the dynamic moduli observed for PLA/CLO compared to PLA suggest the formation of a ‘network’ structure in the molten state [41]. This is explained by the presence of highly dispersed silicate layers of CLO which are incapable rotating freely and hence, by imposing small  $\omega$ , the relaxations of the structure are almost completely prevented. This type of prevented relaxation due to the highly geometric constrains of dispersed silicate layers leads to the marked presence of the pseudo-solid like behavior for PLA/CLO system [41]. Similar results are obtained for PLA/SEP, but only observing the achievement of a spatially linked structure determining  $G'(\omega)$  plateau for  $\omega < 0.05 \text{ rad}\cdot\text{s}^{-1}$ , probably due to its lower dispersion level as compared to PLA/CLO in accordance with SEM results and/or due to the different geometrical features compared to lamellar clay, i.e. needles vs platelets.

The complex viscosity  $[\eta^*(\omega)]$  curves are also shown in Figure 8c; it is possible to observe at low

$\omega$  region ( $\omega < 10 \text{ rad}\cdot\text{s}^{-1}$ ) that the neat PLA shows Newtonian behavior while PLA/CLO ( $\omega < 10 \text{ rad}\cdot\text{s}^{-1}$ ) and PLA/SEP ( $\omega < 0.05 \text{ rad}\cdot\text{s}^{-1}$ ) exhibit a considerable increase of the viscosity with decreasing  $\omega$ , especially in the case of PLA/CLO. This last behavior is associated to a solid-like behavior commented above, especially for CLO. By increasing the shear rates, shear thinning behavior was observed for CLO and SEP materials, indicating that these nanoparticles do not significantly influence viscosity at

higher frequencies, reaching  $[\eta^*(\omega)]$  values analogous to those found for neat polymer.

### 3.5. Oxygen barrier properties

The  $\text{O}_2$  gas permeability values of pure PLA and several composites are presented in Figure 9, showing that oxygen permeability of PLA does not vary significantly, taking into account the experimental error, upon addition of SEP and ZrP particles. Only addition of 5 wt% CLO leads to a decrease of the PLA oxygen permeability (by *ca.* 30%).

The higher oxygen barrier properties of CLO nanocomposites as compared to PLA can be explained by the concept of the tortuous path, given to its high clay dispersion, according to WAXS and SEM analysis, and its clay platelets like morphology which maximize the permeant path length due to the large length to width ratio [2]. In the case of SEP, the lack of barrier effect is likely related to its needle like morphology, which cannot play a considerable barrier role of oxygen molecules through the bulk material as compared to platelets morphology of CLO. In the case of ZrP based material, the low dispersion level of lamellar nanoparticles into PLA is assumed to cause the lack of significant effects on permeability.

For food packaging applications is widely common the use of Polystyrene (PS), Polypropylene (PP) and Polyethylene terephthalate (PET), given their good mechanical and oxygen barrier properties in this industrial field. The typical oxygen barrier values of these polymers are listed in Table 4; comparing these results with those obtained for neat PLA (see Figure 9), this results to be an alternative to PS and PP, in terms of oxygen barrier properties. The addition of CLO can decrease the oxygen permeation of neat

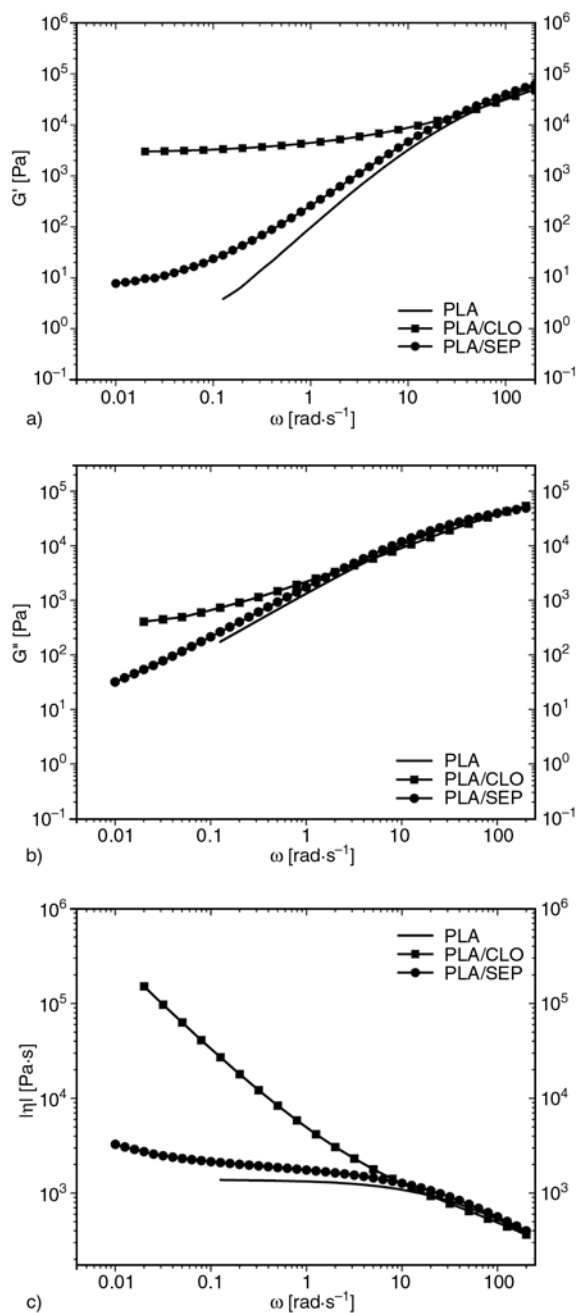


**Figure 8.** Reduced frequency dependence of (a) storage modulus  $[G'(\omega)]$ , (b) loss modulus  $[G''(\omega)]$ , and (c) complex viscosity  $[\eta^*(\omega)]$  at  $190^\circ\text{C}$  of neat PLA and PLA/composites

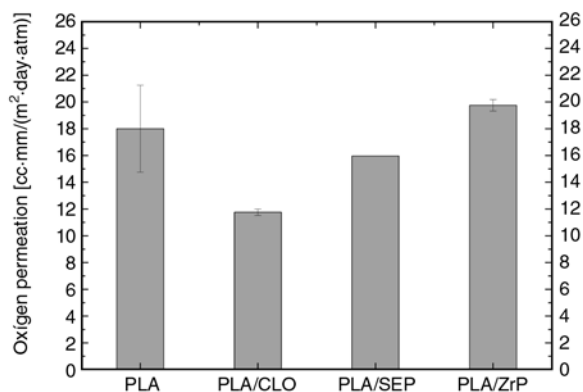


**Figure 9.** Oxygen gas permeability of PLA and PLA/composites, measured at  $23^\circ\text{C}$  and 0% relative humidity



**Table 4.** Oxygen permeation of PS, PP, PET films, values taken from Massey [42]

Reference	Oxygen permeation [cc·mm/(m <sup>2</sup> ·day·atm)]
Polystyrene (PS)	117–157
Polypropylene (PP)	59–102
Polypropylene oriented film (PPof)	59–63
Polyethylene terephthalate (PET) film	3

PLA; however, this decrease is not sufficient to reach the low permeability of PET. The deep understanding of chemical and physical interaction between CLO, SEP and ZrP particles and the polymer could result in the optimization of the melt blending conditions and clay content in order to obtain polymer nanocomposites with the reduced oxygen permeation required for materials with high oxygen barrier properties such as PET, contributing to the development of new bio-based polymer composites for food packaging applications.

### 3.6. Optical transparency

In polymer nanocomposites, it has been reported that film transparency is an effective index for providing information on the size of dispersed particles in the polymer matrix, typically observing aggregate domains larger than visible wavelength could obstruct light, leading to translucent or opaque films [21], while highly dispersed nanoparticles in a transparent polymer matrix result in optically clear nanocomposites in visible light given that the size of particles is smaller than the wavelength [2].

All films of neat PLA and PLA/composites obtained by compression moulding were optically transparent. Indeed, Table 5 shows the cumulative transmission over visible spectra (380–780 nm wavelength) on neat PLA and composites; these results show that the absorption in the visible region, taking into account the experimental error, is not significantly affected by the presence of any particle, therefore the characteristic transparency of PLA film of 50  $\mu\text{m}$

**Table 5.** UV-visible transmission average results of PLA and PLA/nanocomposites from 380–780 nm wavelength. Experimental error 10%.

Sample	Absorbance [A/ $\mu\text{m}$ ]	Transmission [%T/50 $\mu\text{m}$ ]
PLA	0.0081	39
PLA + CLO	0.0101	31
PLA + SEP	0.0066	43
PLA + ZrP	0.0096	33

thick is not considerable reduced in the presence of these particles.

## 4. Conclusions

Poly(lactic acid) (PLA) based nanocomposites prepared by adding 5 wt% filler content of organically modified montmorillonite (CLO) and unmodified sepiolite (SEP) were obtained by melt blending. WAXS and SEM analysis showed a good dispersion of CLO and SEP into the polymer matrix. PLA containing ZrP showed a limited dispersion on PLA matrix as compared to CLO, likely due to its significant lower interlayer thickness, leading to formation of a polymer microcomposite.

DSC analysis showed that neat PLA and composites presented no tendency to crystallise on cooling. Nevertheless, it was observed that PLA was able to crystallize on heating, and that the addition of ZrP can promote the extent of crystallization of the PLA on heating, which can be explained by the regular distribution of ZrP micronic particles able to act as efficient nucleating agents for PLA crystallization.

The dynamo-mechanical results showed improvements in  $E'$  with the addition of all particles, resulting in a remarkable increase of elastic properties for PLA composites, especially at temperatures close to the glass transition temperature. These  $E'$  increases were associated to possible interactions between the particles and PLA molecules originated from hydrogen bonding between the carbonyl group of PLA and the hydroxyl groups belong to the structure of CLO, SEP and ZrP. Interestingly, similar increases of  $E'$  were obtained upon the addition of ZrP into PLA as compared to CLO and SEP, despite its low dispersion level into the PLA matrix, possibly explained by the high crystallinity of ZrP particles as well as to the very regular distribution of ZrP micronic particles along all the polymer matrix.

The melt viscosity and dynamic shear moduli of nanocomposites were also enhanced significantly by the presence of CLO and SEP. The dynamic shear storage modulus,  $G'$ , and loss modulus,  $G''$  of these nanocomposites, exhibited less frequency dependence than pure PLA at a low frequency range. These results could be attributed to important interactions between PLA and nanocomposites, especially CLO, forming an interconnected structure within the PLA matrix.

The oxygen permeability of PLA did not significantly vary upon addition of SEP and ZrP particles. Only addition of CLO led to an important decrease of the PLA oxygen permeability. Optical transparency measurements showed the transparency of PLA in the visible region not to change significantly with the presence of particles, thus preserving the good optical properties typical of PLA. The improvements of viscous and/or elastic properties for PLA composites as well as the similar transparency and improved gas barrier properties could provide to these composites an opportunity in the field of packaging. Even more, it is reasonable to expect that by controlling the nanoparticle content and processing conditions, PLA based nanocomposites films with improved properties could be obtained for various purposes of industrial application.

### Acknowledgements

The authors would like to thank gratefully Dr. Simona Cecilia and Emilia Giofreddi for their great support and guidance throughout the measurements and analysis of rheological tests. This work was partially supported by the research project NAMATECH 'Nano-materials and -technologies for intelligent monitoring of safety, quality and traceability in confectionery products' in the frame of Piedmont Region Converging technologies call 2007.

### References

- [1] Weber C. L. J.: Biobased packaging materials for the food industry. Report by the EU Directorate 12 (2011).
- [2] Sinha Ray S., Okamoto M.: Polymer/layered silicate nanocomposites: A review from preparation to processing. *Progress in Polymer Science*, **28**, 1539–1641 (2003).  
DOI: [10.1016/j.progpolymsci.2003.08.002](https://doi.org/10.1016/j.progpolymsci.2003.08.002)
- [3] Coombs J., Hall K.: Non food agro-industrial research information (CD-rom version). CPL Publishing Services, Newbury (2000).
- [4] Mangan C.: The green chemical and polymers chain: Fair, agriculture and fisheries including agro-industry, food-technologies, forestry, aquaculture and rural development: 4<sup>th</sup> framework programme 1994–1998. European Commission, Luxembourg (1998).
- [5] Sinha Ray S., Okamoto M.: Biodegradable polylactide and its nanocomposites: Opening a new dimension for plastics and composites. *Macromolecular Rapid Communications*, **24**, 815–840 (2003).  
DOI: [10.1002/marc.200300008](https://doi.org/10.1002/marc.200300008)
- [6] Feijoo J. L., Cabedo L., Giménez E., Lagaron J. M., Saura J. J.: Development of amorphous PLA-montmorillonite nanocomposites. *Journal of Materials Science*, **40**, 1785–1788 (2005).  
DOI: [10.1007/s10853-005-0694-8](https://doi.org/10.1007/s10853-005-0694-8)
- [7] Singh R. P., Pandey J. K., Rutot D., Degée Ph., Dubois Ph.: Biodegradation of poly( $\epsilon$ -caprolactone)/starch blends and composites in composting and culture environments: The effect of compatibilization on the inherent biodegradability of the host polymer. *Carbohydrate Research*, **338**, 1759–1769 (2003).  
DOI: [10.1016/S0008-6215\(03\)00236-2](https://doi.org/10.1016/S0008-6215(03)00236-2)
- [8] Di Y., Iannace S., Di Maio E., Nicolais L.: Poly(lactic acid)/organoclay nanocomposites: Thermal, rheological properties and foam processing. *Journal of Polymer Science Part B: Polymer Physics*, **43**, 689–698 (2005).  
DOI: [10.1002/polb.20366](https://doi.org/10.1002/polb.20366)
- [9] Pollet E., Paul M-A., Dubois P.: New aliphatic polyester layered-silicate nanocomposites. in 'Biodegradable polymers and plastics, Vol 1.' (eds.: Chiellini E., Solaro R.) Kluwer, New York (2003).  
DOI: [10.1007/978-1-4419-9240-6\\_22](https://doi.org/10.1007/978-1-4419-9240-6_22)
- [10] Utracki L. A.: Basic elements of polymeric nanocomposites technology. in 'Clay- containing polymeric nanocomposites' (ed.: Utracki L. A.) Vol 1. Rapra, Shropshire (2004).
- [11] Pluta M., Galeski A., Alexandre M., Paul M-A., Dubois P.: Polylactide/montmorillonite nanocomposites and microcomposites prepared by melt blending: Structure and some physical properties. *Journal of Applied Polymer Science*, **86**, 1497–1506 (2002).  
DOI: [10.1002/app.11309](https://doi.org/10.1002/app.11309)
- [12] Chang J-H., Kim S. J., Joo Y. L., Im S.: Poly(ethylene terephthalate) nanocomposites by in situ interlayer polymerization: The thermo-mechanical properties and morphology of the hybrid fibers. *Polymer*, **45**, 919–926 (2004).  
DOI: [10.1016/j.polymer.2003.11.037](https://doi.org/10.1016/j.polymer.2003.11.037)
- [13] Utracki L. A., Sepehr M., Boccaleri E.: Synthetic, layered nanoparticles for polymeric nanocomposites (PNCs). *Polymers for Advanced Technologies*, **18**, 1–37 (2007).  
DOI: [10.1002/pat.852](https://doi.org/10.1002/pat.852)
- [14] Fukushima K., Abbate C., Tabuani D., Gennari M., Camino G.: Biodegradation of poly(lactic acid) and its nanocomposites. *Polymer Degradation and Stability*, **94**, 1646–1655 (2009).  
DOI: [10.1016/j.polymdegradstab.2009.07.001](https://doi.org/10.1016/j.polymdegradstab.2009.07.001)
- [15] Fukushima K., Tabuani D., Camino G.: Nanocomposites of PLA and PCL based on montmorillonite and sepiolite. *Materials Science and Engineering C*, **29**, 1433–1441 (2009).  
DOI: [10.1016/j.msec.2008.11.005](https://doi.org/10.1016/j.msec.2008.11.005)

- [16] Tartaglione G., Tabuani D., Camino G., Moisisio M.: PP and PBT composites filled with sepiolite: Morphology and thermal behaviour. *Composites Science and Technology*, **68**, 451–460 (2008).  
DOI: [10.1016/j.compscitech.2007.06.023](https://doi.org/10.1016/j.compscitech.2007.06.023)
- [17] Brandão L. S., Mendes L. C., Medeiros M. E., Sirelli L., Dias M. L.: Thermal and mechanical properties of poly(ethylene terephthalate)/lamellar zirconium phosphate nanocomposites. *Journal of Applied Polymer Science*, **102**, 3868–3876 (2006).  
DOI: [10.1002/app.24096](https://doi.org/10.1002/app.24096)
- [18] Sun L., Boo W. J., Browning R. L., Sue H.-J., Clearfield A.: Effect of crystallinity on the intercalation of monoamine in  $\alpha$ -zirconium phosphate layer structure. *Chemistry of Materials*, **17**, 5606–5609 (2005).  
DOI: [10.1021/cm051160i](https://doi.org/10.1021/cm051160i)
- [19] Boo W.-J., Sun L., Warren G. L., Moghbelli E., Pham H., Clearfield A., Sue H.-J.: Effect of nanoplatelet aspect ratio on mechanical properties of epoxy nanocomposites. *Polymer*, **48**, 1075–1082 (2007).  
DOI: [10.1016/j.polymer.2006.12.042](https://doi.org/10.1016/j.polymer.2006.12.042)
- [20] Boo W. J., Sun L. Y., Liu J., Clearfield A., Sue H.-J., Mullins M. J., Pham H.: Morphology and mechanical behavior of exfoliated epoxy/ $\alpha$ -zirconium phosphate nanocomposites. *Composites Science and Technology*, **67**, 262–269 (2007).  
DOI: [10.1016/j.compscitech.2006.08.012](https://doi.org/10.1016/j.compscitech.2006.08.012)
- [21] Wu H., Liu C., Chen J., Chang P. R., Chen Y., Anderson D. P.: Structure and properties of starch/ $\alpha$ -zirconium phosphate nanocomposite films. *Carbohydrate Polymers*, **77**, 358–364 (2009).  
DOI: [10.1016/j.carbpol.2009.01.002](https://doi.org/10.1016/j.carbpol.2009.01.002)
- [22] Choudalakis G., Gotsis A. D.: Permeability of polymer/clay nanocomposites: A review. *European Polymer Journal*, **45**, 967–984 (2009).  
DOI: [10.1016/j.eurpolymj.2009.01.027](https://doi.org/10.1016/j.eurpolymj.2009.01.027)
- [23] Tartaglione G., Tabuani D., Camino G.: Thermal and morphological characterisation of organically modified sepiolite. *Microporous and Mesoporous Materials*, **107**, 161–168 (2008).  
DOI: [10.1016/j.micromeso.2007.04.020](https://doi.org/10.1016/j.micromeso.2007.04.020)
- [24] Shariatmadari H., Mermut A. R.: Magnesium- and silicon-induced phosphate desorption in smectite-, palygorskite-, and sepiolite-calcite systems. *Soil Science Society of America Journal*, **63**, 1167–1173 (1999).  
DOI: [10.2136/sssaj1999.6351167x](https://doi.org/10.2136/sssaj1999.6351167x)
- [25] Herrero C. R., Morales E., Acosta J. L.: The influence of sepiolite on the dynamic moduli and thermal transition of compatible and incompatible blends based on poly(vinylidene fluoride). *Die Angewandte Makromolekulare Chemie*, **205**, 97–106 (1993).  
DOI: [10.1002/apmc.1993.052050108](https://doi.org/10.1002/apmc.1993.052050108)
- [26] Herrero C. R., Morales E., Acosta J. L.: Compatibilization of semicrystalline polymeric alloys through sepiolite addition. *Journal of Applied Polymer Science*, **51**, 1189–1197 (1994).  
DOI: [10.1002/app.1994.070510705](https://doi.org/10.1002/app.1994.070510705)
- [27] Acosta J. L., González L., Ojeda M. C., Del Río C.: Ionomer composites based on sepiolite/hydrogenated poly(styrene butadiene) block copolymer systems. *Journal of Applied Polymer Science*, **86**, 3512–3519 (2002).  
DOI: [10.1002/app.11113](https://doi.org/10.1002/app.11113)
- [28] González L., Rodríguez A., Marcos-Fernández A., Del Campo A.: Reinforcing effect and electrical properties of ethylene-propylene rubber filled with calcined sepiolite. *Journal of Applied Polymer Science*, **79**, 714–718 (2001).  
DOI: [10.1002/1097-4628\(20010124\)79:4<714::AID-APP160>3.0.CO;2-J](https://doi.org/10.1002/1097-4628(20010124)79:4<714::AID-APP160>3.0.CO;2-J)
- [29] Bokobza L., Chauvin J.-P.: Reinforcement of natural rubber: Use of in situ generated silicas and nanofibres of sepiolite. *Polymer*, **46**, 4144–4151 (2005).  
DOI: [10.1016/j.polymer.2005.02.048](https://doi.org/10.1016/j.polymer.2005.02.048)
- [30] Jones B. F., Galán E. S.: Sepiolite and palygorskite. *Mineralogical Society of America*, **19**, 631–674 (1988).
- [31] Ahlrichs J. L., Serna C., Serratos J. M.: Structural hydroxyls in sepiolites. *Clays and Clay Minerals*, **23**, 119–124 (1975).  
DOI: [10.1346/CCMN.1975.0230207](https://doi.org/10.1346/CCMN.1975.0230207)
- [32] Serratos J. M.: Surface properties of fibrous clay minerals (palygorskite and sepiolite). in ‘Proceedings of international clay conference 1978’ (Mortland M. M., Farme V. C.) Amsterdam, Elsevier, 99–110 (1979).
- [33] Clearfield A., Smith G. D.: Crystallography and structure of  $\alpha$ -zirconium bis(monohydrogen orthophosphate) monohydrate. *Inorganic Chemistry*, **8**, 431–436 (1969).  
DOI: [10.1021/ic50073a005](https://doi.org/10.1021/ic50073a005)
- [34] Liu X.-Q., Wang D.-Y., Wang X.-L., Chen L., Wang Y.-Z.: Synthesis of organo-modified  $\alpha$ -zirconium phosphate and its effect on the flame retardancy of IFR poly(lactic acid) systems. *Polymer Degradation and Stability*, **96**, 771–777 (2001).  
DOI: [10.1016/j.polymdegradstab.2011.02.022](https://doi.org/10.1016/j.polymdegradstab.2011.02.022)
- [35] Alberti G., Costantino U., Casciola M., Vivani R.: Proton conductivity of zirconium carboxy n-alkyl phosphonates with an  $\alpha$ -layered structure. *Solid State Ionics*, **46**, 61–68 (1991).  
DOI: [10.1016/0167-2738\(91\)90129-Y](https://doi.org/10.1016/0167-2738(91)90129-Y)
- [36] Costantino U., Vivani R., Zima V., Cernoskova E.: Thermoanalytical study, phase transitions, and dimensional changes of  $\alpha$ -Zr(HPO<sub>4</sub>)<sub>2</sub>·H<sub>2</sub>O large crystals. *Journal of Solid State Chemistry*, **132**, 17–23 (1997).  
DOI: [10.1006/jssc.1997.7385](https://doi.org/10.1006/jssc.1997.7385)

- [37] Fukushima K., Tabuani D., Abbate C., Arena M., Rizzarelli P.: Preparation, characterization and biodegradation of biopolymer nanocomposites based on fumed silica. *European Polymer Journal*, **47**, 139–152 (2011). DOI: [10.1016/j.eurpolymj.2010.10.027](https://doi.org/10.1016/j.eurpolymj.2010.10.027)
- [38] Di Y., Iannace S., Di Maio E., Nicolais L.: Nanocomposites by melt intercalation based on polycaprolactone and organoclay. *Journal of Polymer Science Part B: Polymer Physics*, **41**, 670–678 (2003). DOI: [10.1002/polb.10420](https://doi.org/10.1002/polb.10420)
- [39] Ruiz-Hitzky E., Darder M., Aranda P., del Burgo M. A. M., del Real G.: Bionanocomposites as new carriers for influenza vaccines. *Advanced Materials*, **21**, 4167–4171 (2009). DOI: [10.1002/adma.200900181](https://doi.org/10.1002/adma.200900181)
- [40] Ruiz-Hitzky E.: Molecular access to intracrystalline tunnels of sepiolite. *Journal of Materials Chemistry*, **11**, 86–91 (2001). DOI: [10.1039/b003197f](https://doi.org/10.1039/b003197f)
- [41] Sinha Ray S., Yamada K., Okamoto M., Ueda K.: New polylactide-layered silicate nanocomposites. 2. Concurrent improvements of material properties, biodegradability and melt rheology. *Polymer*, **44**, 857–866 (2003). DOI: [10.1016/S0032-3861\(02\)00818-2](https://doi.org/10.1016/S0032-3861(02)00818-2)
- [42] Massey K. L.: Permeability properties of plastics and elastomers. A guide to packaging and barrier materials. *Plastics Design Library*, New York (2003).

# Influence of ionic liquids on the dielectric relaxation behavior of CNT based elastomer nanocomposites

D. Steinhäuser<sup>1</sup>, K. Subramaniam<sup>2</sup>, A. Das<sup>3</sup>, G. Heinrich<sup>2,3</sup>, M. Klüppel<sup>1\*</sup>

<sup>1</sup>Deutsches Institut für Kautschuktechnologie e.V., Eupener Str. 33, 30519 Hannover, Germany

<sup>2</sup>Leibniz-Institut für Polymerforschung Dresden e.V., Hohe Str. 6, 01069 Dresden, Germany

<sup>3</sup>Technische Universität Dresden, Institut für Werkstoffwissenschaft Helmholtzstrasse 7, 01069 Dresden, Germany

Received 2 April 2012; accepted in revised form 24 June 2012

**Abstract.** The influence of an imidazolium type ionic liquid (IL) on the relaxation behavior of carbon-nanotube (CNT) based polychloroprene nanocomposites prepared by melt mixing has been investigated by broadband dielectric spectroscopy. It is demonstrated that the presence of the ionic liquid modifies the relaxation behavior of the pure rubber matrix and leads to a significant increase of the conductivity for the CNT/rubber composites. For the unfilled rubber, a distinct glass transition of the IL is observed for high concentrations demonstrating that the IL forms a separate phase. The increased conductivity of the CNT-filled rubber composites is related to a physical coupling between CNTs and rubber matrix mediated by IL leading to a better dispersion of the CNTs.

**Keywords:** nanocomposites, rubber, ionic liquid, dielectric spectroscopy, relaxation dynamics

## 1. Introduction

Electrically conducting rubber has attracted considerable attention due to the potential opportunity of combining the stretchable and deformable properties of the material with sufficient high electric conduction for various applications such as electromagnetic interference shielding materials, sensors and to avoid electrostatic charging. For example, a conductivity of 1 S/cm is typically sufficient for electromechanical interference shielding [1]. In technical rubber goods the low electrical conductivity of the polymer is improved by the incorporation of conductive fillers like carbon black. Polymer nano-composites can have a remarkable piezo-resistivity [2, 3]. Such materials are good candidates to be used as sensors with high sensitivity [4]. For example, a piezo-resistive rubber sensor vulcanized into the sidewall of a tire can monitor the actual state of a tire such as the tire pressure to a

control system. This kind of pressure control could be realized by measuring the variation of resistivity when the sensor passes through the contact area of a rolling tire reflecting the bending state of the sidewall. Such facilities would improve the security and drive stability of a vehicle, significantly.

For a sufficient high conductivity the building up of a filler network is necessary. This can be achieved above the percolation threshold describing the amount of conductive filler necessary to obtain an infinite cluster, which forms a conductive path through the whole sample. Depending on the structure and the size of conductive carbon black particles and the specific interaction with the used polymer, percolation thresholds in the range of  $8 \text{ vol}\% < \Phi_c < 20 \text{ vol}\%$  of carbon black are found [5, 6]. For special conductive carbon blacks the threshold can even go down to 3 vol% [7]. Recently, also single walled CNT and multi walled carbon-nanotubes

\*Corresponding author, e-mail: [Manfred.Klueppel@dikautschuk.de](mailto:Manfred.Klueppel@dikautschuk.de)

© BME-PT

(MWCNT) have been applied as conductive fillers for reaching the necessary conduction level [8–11]. Compared to carbon black, the percolation threshold of MWCNT is significantly lower due to the high aspect ratio of the tubes. It can be reduced theoretically down to  $\Phi_c = 0.1$  vol%, which can be achieved in case of optimal dispersion resulting in even higher conductivities as for highly filled carbon black composites [12]. In particular, the very small amount of CNTs necessary to reach high conductivities is an ideal candidate to be used for preparing highly conducting materials with non-conductive reinforcing fillers. Additionally, the use of non-conductive fillers like silica can improve the dispersion of the CNTs due to the increased shearing forces. It has been demonstrated that the incorporation of CNT in silica filled rubber results in a good dispersion of the CNT probably due to the high shear forces during the mixing process [13]. The materials show an enhanced mechanical stiffness and tensile strength, an increased modulus and a high electrical conductivity with quite low amounts of CNT ( $\Phi_c = 1$  vol%), though the tear resistance under dynamical loading is slightly reduced. The dynamic-mechanical and dielectric spectra have been analyzed to get more insight into the morphology and dynamics of the systems. Thereby, a better understanding of the conduction mechanism, the polymer-tube interaction and the filler networking in CNT-nanocomposites has been achieved.

In previous papers, the conductivity of MWCNT/rubber composites was found to be increased by applying imidazolium type ionic liquids as dispersion agent [10, 13, 14]. A chemical coupling between CNTs and the rubber matrix mediated by imidazolium type ionic liquids and sulfur bridges can be achieved in SSBR-BR/CNT systems [14] as depicted in Figure 1. For polychloroprene rubber (CR), the usage of 1-butyl 3-methyl imidazolium bis-(trifluoromethyl-sulphonyl)-imide (BMI) modified tubes leads to a physical coupling between CNTs and rubber evidenced by Raman spectroscopy, where the ion-dipole interaction persists probably between CR and BMI [14, 15]. A low amount of MWCNT in polychloroprene rubber showed a very high conductivity level of about 0.1 S/cm with a high stretchability of more than 500%. Transmission electron microscopy (TEM) demonstrated an improved dispersion of the BMI modified tubes in the rubber matrix.

In the present paper, we will extend these investigations by a detailed study of the dielectric properties of the IL-modified MWCNT/rubber composites. We will first investigate the modified relaxation behavior of the pure rubber matrix. In a second step we will consider the dielectric spectra of the MWCNT-filled samples more closely.

## 2. Experimental and methods

The samples were based on chloroprene rubber (CR, Baypren 611, Lanxess AG, Leverkusen, Ger-

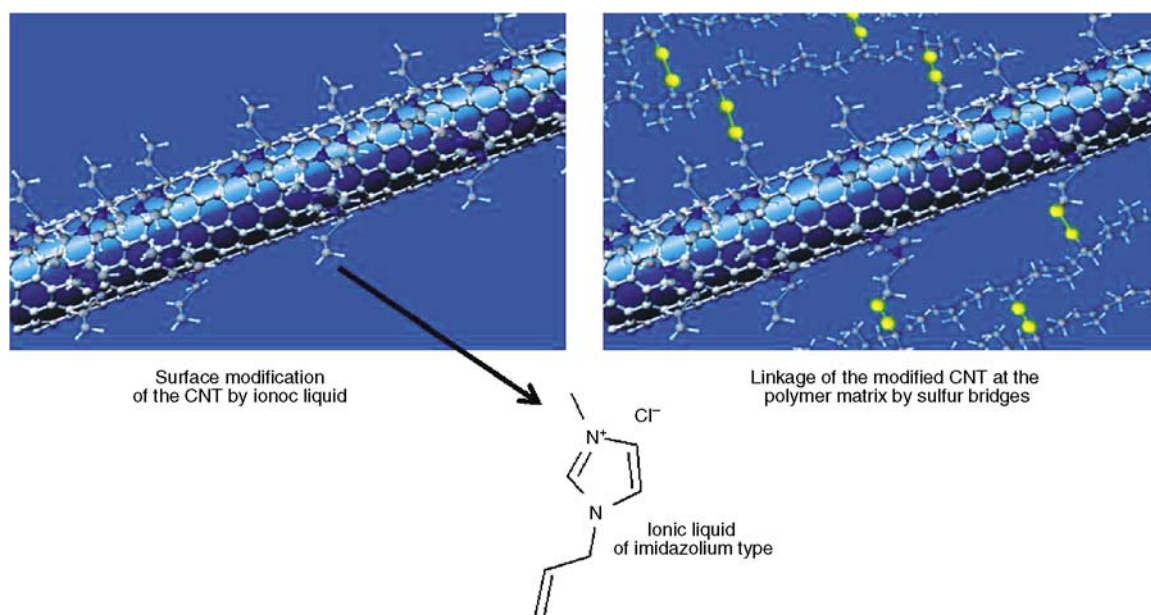


**Figure 1.** Schematic representation of the coupling between CNT and the rubber matrix mediated by imidazolium type ionic liquids and sulfur bridges

many). Each composite contained 0.5 phr stearic acid, 5 phr zinc oxide (ZnO), 4 phr magnesium oxide (MgO) and 1 phr ethylene thiourea. These chemicals are used on industrial grades. Table 1 shows the curing recipe and explanation for sample designation. For the CNT/CR composites, the commercial multiwalled carbon nanotubes (MWCNTs) Nanocyl 7000 (Nanocyl S.A, Sambreville, Belgium) has been used. The MWCNTs were modified with the IL, BMI (1-butyl 3-methyl imidazolium bis(trifluoromethylsulphonyl) imide, Sigma-Aldrich, Steinheim, Germany), by grinding them till a black paste was obtained. The MWCNTs were mixed with CR in a laboratory scale two roll mixing mill (Polymix 110L, size: 203 × 102 mm, Servitech GmbH, Wustermark, Germany) at 40°C with a friction ratio of 1:1.25. The vulcanization additives were incorporated into the matrix after the admixing of MWCNTs. The optimum cure time ( $t_{90}$ ) was determined in a moving die rheometer, shortly referred as MDR (Scarabaeus V50, Scarabaeus GmbH, Langgöns, Germany) at 160°C for 60 minutes. The mixed stocks were cured in a standard hot press at 160°C, 150 kN pressure and at an optimum cure time ( $t_{90}$ ) of the samples.

Dielectric investigations have been carried out by using a broadband dielectric spectrometer BDS 40 (Novocontrol GmbH, Hundsangen, Germany). The temperature was varied from –100 to 150°C in steps of five degrees using the temperature control system Novocool (Novocontrol GmbH, Hundsangen, Germany). At each temperature, a frequency sweep from 0.1 Hz to 10 MHz has been measured. The sample geometry was a disc shaped plate capacitor with a diameter of around 2 cm. The sample with a thickness of around 2 mm was placed between two gold-plated electrodes. To provide an excellent contact between sample and electrodes, thin gold layers have been sputtered onto the flat surface of the sample plate. The dielectric permittivity and the dielectric loss have been recorded for each sample in dependence on temperature and frequency.

### 3. Results and discussion

#### 3.1. Relaxation dynamics in neat chloroprene rubber

The dielectric loss  $\varepsilon''$  of neat CR rubber in dependence on temperature and frequency is shown in Figure 2a. The pronounced relaxation process can be related to the glass transition ( $\alpha$  process) due to the cooperative segmental motion of the chain, for which the characteristic temperature and frequency dependence is described by a Vogel-Fulcher behavior. At low temperature, the Arrhenius-activated  $\beta$  process can be observed which is due to local fluctuations of chain segments or side groups. The dielectric loss for CR rubber with IL, shown in Figure 2b, has an additional relaxation process below the glass transition of the rubber, which can therefore be associated with the ionic liquid. It has been reported that ionic liquids, which exhibit disordered and fragile structure, can also form a glassy-like state that could be traced by calorimetric measurements [16]. This glass transition of the IL was also observed previously by dynamic-mechanical analysis [14].

The  $\alpha$  process at three temperatures is compared in Figure 2c. The addition of BMI to the CR rubber does not change the peak position and the broadness of the  $\alpha$  process. Thus, the ionic liquid has no influence on the glass transition of the rubber matrix. This indicates that the two components are not very compatible and the solubility of the ionic liquid in the rubber matrix is low. In addition, the distinct presence of the  $\alpha$  process of BMI is a hint that microdomains of BMI exist in the rubber matrix. Hence, BMI forms partly a separated phase that has its own glass transition at temperatures smaller than the glass transition temperature of the rubber matrix.

The large rise of dielectric loss at small frequency and large temperatures seen in both investigated samples is probably generated by ion conduction and electrode polarization, which become often dominant above the glass transition. Ionic conductance probably results from mobile ions obtained

**Table 1.** Curing recipe and explanation for sample designation. All units are in phr (per hundred rubber).

Sample designation	CR rubber	ZnO	MgO	Stearic acid	Ethylene thiourea	MWCNTs	BMI
CT0	100	5	4	0.5	1	0	0
CT0BMI20	100	5	4	0.5	1	0	20
CT3BMI0	100	5	4	0.5	1	3	0
CT3BMI15	100	5	4	0.5	1	3	15

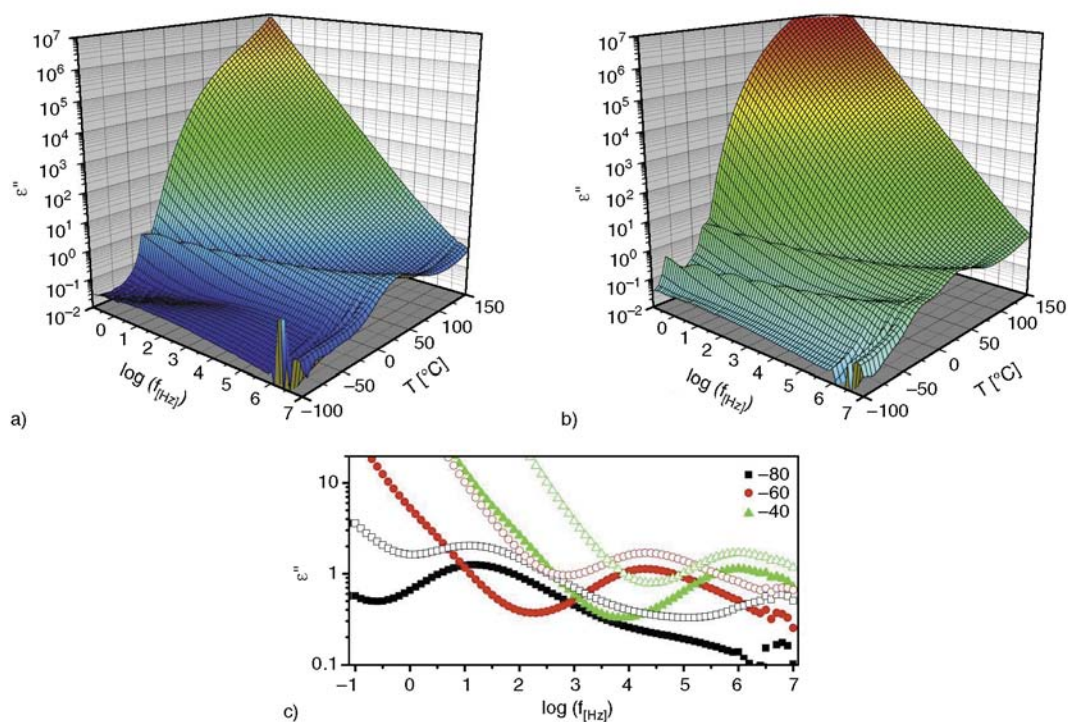


**Figure 2.** Dielectric loss of CR rubber a) without BMI (sample: CT0) and b) with BMI (sample: CT0BMI20). c) Comparison of the  $\alpha$  process. Closed symbols: CT0; Open symbols: CT0BMI20.

from addition of the processing agents zinc oxide, magnesium oxide and stearic acid. It might be possible that this large effect masks relaxation transitions in the high temperature range. In order to minimize it, an analyzing procedure has been developed by Wübbenhorst and van Turnhout [17]. This method is based on the Kramer-Kronig relations, one of which is Equation (1):

$$\varepsilon'' = \frac{\sigma_{dc}}{\varepsilon_0 \omega_0} + \frac{2}{\pi} \int_0^{\infty} \varepsilon'(\omega_0) \frac{\omega_0}{\omega^2 - \omega_0^2} d\omega \quad (1)$$

where  $\sigma_{dc}$  is the Ohmic conduction,  $\omega_0$  is the relaxation frequency and  $\varepsilon_0$  is the vacuum permittivity. It states that the real part  $\varepsilon'$  and the imaginary part  $\varepsilon''$  are carrying the same information about relaxation processes. Other than the imaginary part  $\varepsilon''$ , the real part of permittivity  $\varepsilon'$  has no contribution from the frequency-independent Ohmic conduction  $\sigma_{dc}$ . Therefore, determining the dielectric loss from the quantity  $\varepsilon'$  eliminates the part of conduction with ohmic behavior. In the analysis procedure of Wübbenhorst, the derivation of  $\varepsilon'$  with respect to the frequency  $\omega$  denoted as  $\varepsilon''_{deriv}$ :

$$\varepsilon''_{deriv} \approx -\frac{\pi}{2} \frac{\delta \varepsilon'(\omega)}{\delta \ln \omega} \quad (2)$$

is used in order to obtain narrow and sharp peaks and to eliminate ohmic conductivity. Equation (2) is almost exact and the derivative reproduces the measured frequency dependent  $\varepsilon''$  data for broad relaxation processes such as the glass process. Contrary, for narrow Debye-like processes a peak sharpening is observed and  $\varepsilon''_{deriv} \propto \omega^{-2}$  is obtained for large frequencies instead of  $\varepsilon''_{deriv} \propto \omega^{-1}$  [17].

The partial blocking of ions at the metallic electrodes leads to the pronounced contribution in the measured  $\varepsilon''$  at high temperature and low frequency. This electrode polarization refers typically to a Debye-like process with relaxation maximum below the measured frequency range. Therefore, Equation (2) is expected to sharpen this undesired peak and the contribution in the measured range is diminished, enabling the observation of other processes of dipolar origin.

The dielectric loss  $\varepsilon''_{deriv}$  evaluated by the derivative of  $\varepsilon'$  is shown for neat CR rubber in Figure 3a. An additional relaxation is clearly observed above the glass transition, which was masked in the measured dielectric loss  $\varepsilon''$  in Figure 2a by the dominant effects related to ion conduction and electrode polarization. A comparison of  $\varepsilon''_{deriv}$  for the both investigated samples, CT0 without IL and CT0BMI20



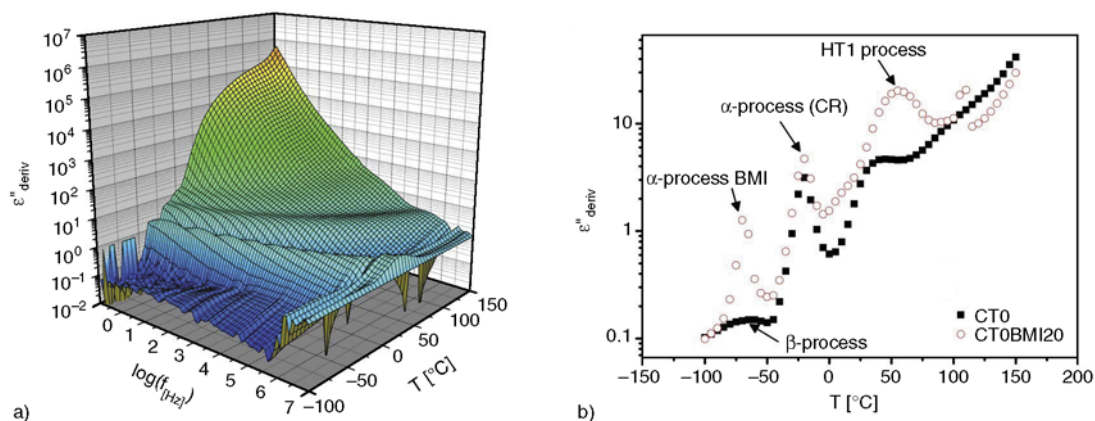


**Figure 3.** a) Dielectric loss from derivative of  $\epsilon'$  for neat CR rubber (sample: CT0). b) Dielectric loss  $\epsilon''_{deriv}$  for CT0 and CT0BMI20 at  $f = 1$  kHz.

with  $IL_c$ , can be seen in Figure 3b at 1 kHz. The glass transition of CR is clearly observed and is at the same temperature for both samples. Thus, the ionic liquid does not influence the glass transition of the rubber. The high temperature process, noted here as HT1, is obviously shifted to higher temperature for using BMI. This indicates that the ionic liquid hinders the relaxation belonging to this transition. At low temperatures, the  $\beta$  process is observed for CT0 and the  $\alpha$  process of BMI for CT0BMI20.

The dielectric spectra are fitted by Cole-Cole functions (Equation (3)):

$$\epsilon^*_{CC}(\omega) = \epsilon_\infty + \sum_j \frac{\Delta\epsilon_j}{1 + (i\omega\tau_j)^{\alpha_j}} \quad (3)$$

where  $\epsilon_\infty$  is the dielectric permittivity at infinite frequencies,  $\tau_j$  is the relaxation frequency,  $\Delta\epsilon_j$  is the relaxation strength and  $\alpha_j$  is the broadening parameter of the  $j$ -th relaxation process. The fit has been carried out for each temperature as shown in Figure 4 for 20°C. At this temperature, the  $\alpha$  process and the high temperature process HT1 are clearly visible.

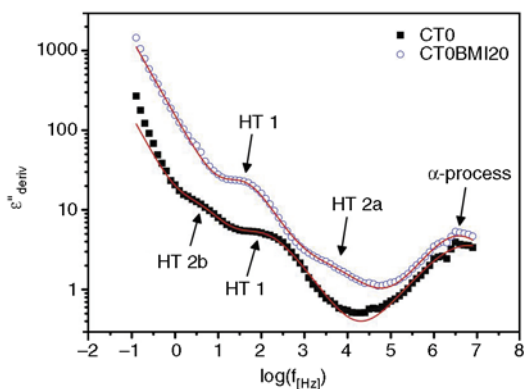


**Figure 4.** Fits of dielectric spectra with Cole-Cole functions at 20°C. The lines are fits according to Equation (3).

Additionally, another high temperature process for each of the both samples, noted here as HT2a and HT2b, is observable. These processes are broad and have relatively small relaxation strengths. The determination is therefore difficult and imprecise. It is also unclear whether these both processes have the same origin or a different one.

The activation diagram, the logarithm of the relaxation frequency versus the reciprocal temperature, is shown in Figure 5. For each of the both samples, four processes have been detected. The  $\alpha$  processes have been analyzed by the empirical Vogel-Fulcher-Tamman equation (Equation (4)):

$$f(T) = f_0 \exp\left(\frac{-E_A}{R(T - T_{FV})}\right) \quad (4)$$

where  $R$  is the gas constant. The activation energy  $E_A$ , the Vogel-Fulcher temperature  $T_{FV}$  and the relaxation rate  $\log f_0$  are the fit parameters. The results are summarized in Table 2. It has been found that the  $\alpha$  process of CR with the activation energy of about 10 kJ/mol does not change with the usage

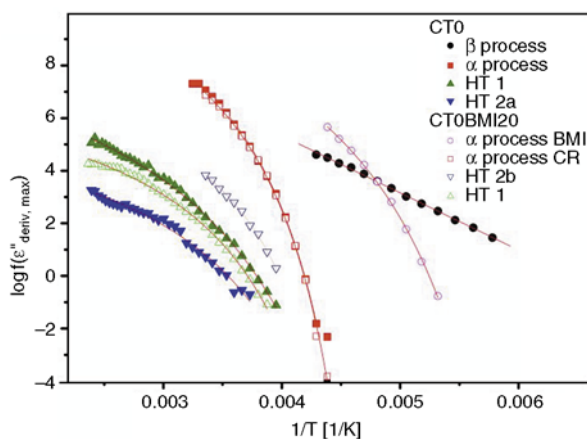


**Figure 5.** Activation diagram for the relaxation processes

**Table 2.** Activation parameters for CT0 and CT0BMI20

	$E_a$ [kJ/mol]	$\log f_0$	$T_{FV}$ [K]
<b>CT0</b>			
$\beta$ process	41.5	14	–
$\alpha$ process CR	10	12.2	196
HT1	13.2	8.1	179
HT2a	9.3	5.3	192
<b>CT0BMI20</b>			
$\alpha$ process CR	9.7	11.9	196
$\alpha$ process BMI	9.3	11.8	149
HT1	6.5	8.9	243
HT2b	7.6	7.9	204

of BMI. This indicates that the dynamics of the bulk polymer matrix is not affected by the presence of the ionic liquid. The  $\alpha$  processes of the BMI can also well be fitted with the Vogel-Fulcher-Tamman equation. The activation energy and the relaxation rate are comparable to that of the CR polymer, but the Vogel-Fulcher temperature is much smaller. The  $\beta$  process is well described by the Arrhenius relation (Equation (5)):

$$f(T) = f_0 \exp\left(\frac{-E_A}{RT}\right) \quad (5)$$

having an activation energy of about 41.5 kJ/mol. The  $\beta$  process is only observed in the neat rubber CT0. In CT0BMI20, the  $\beta$  process is probably covered by the BMI  $\alpha$  peak, which lies in the same temperature range.

It can be seen that all high temperature processes can well be described by a Vogel-Fulcher-Tammann behavior. The BMI clearly influences the high temperature process HT1. The relaxation rate is for both samples comparable, but the activation energy is smaller and the Vogel-Fulcher temperature is much larger for CT0BMI20 than for CT0. The origin of the relaxation process HT1 might be the formation of zinc clusters as recently reported in carboxylated nitril rubber (XNBR) [18]. In this study, it has been observed by dielectric relaxation spectroscopy and confirmed by IR spectroscopy that clusters are formed due to the presence of ZnO and carboxylic groups. In chloroprene rubber, a similar mechanism is imaginable between the polar side groups and the ZnO. The high temperature process could therefore be assigned to the thermal decay of zinc clusters. The ionic nature of the IL can stabilize

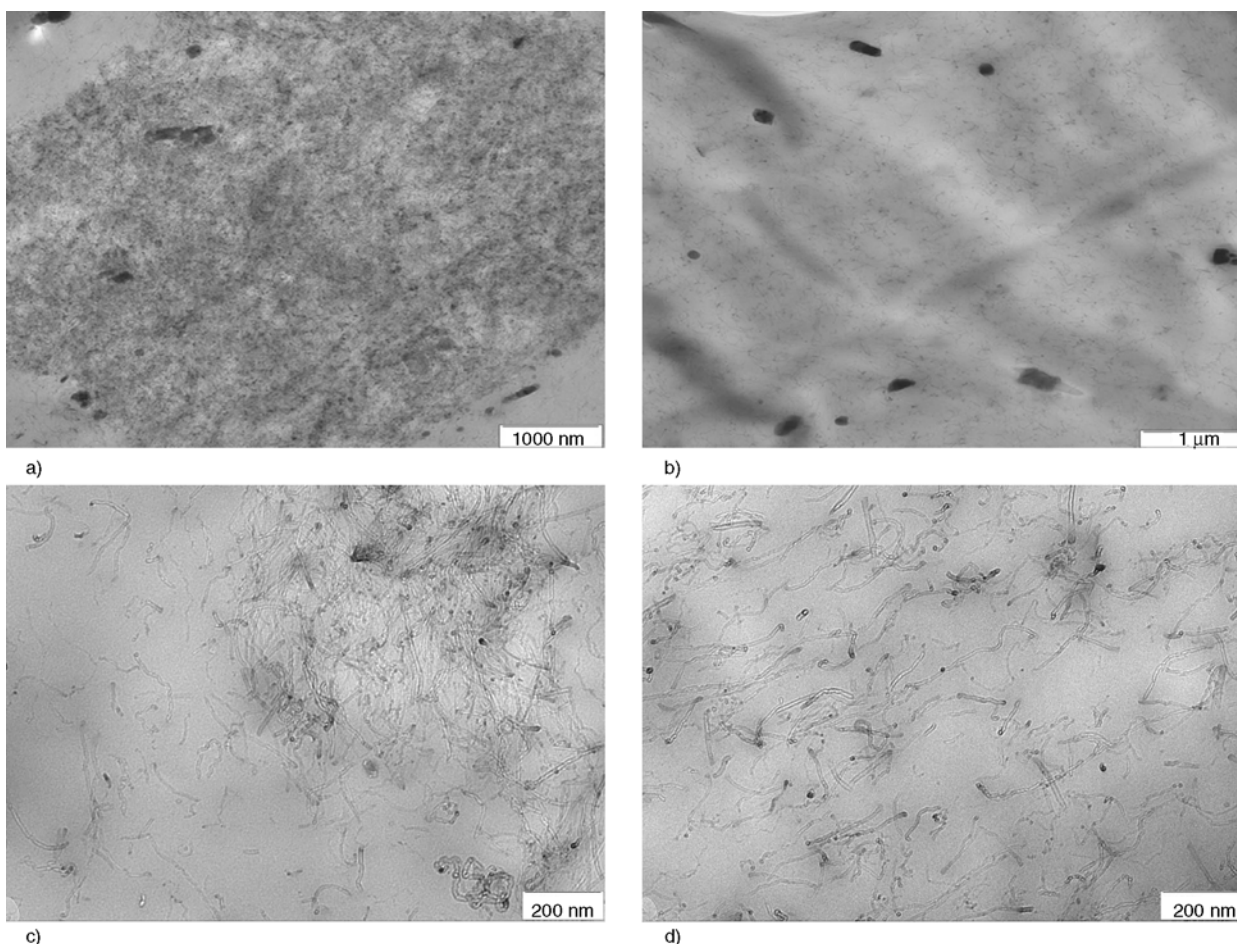
these clusters, explaining the shift to higher temperatures.

The used CR grade has a slight to medium tendency to crystallize [19]. Thus, a few crystalline regions might exist in the mostly amorphous polymer matrix. It is possible that the melting of these crystalline regions generates the less-pronounced, broad relaxation process HT2a in CT0. The melting temperature at long times of crystalline domains in chloroprene rubber is found at 30–70°C dependant on structural and geometrical isomerism [20] and lies therefore in the same temperature range as HT2a at low frequencies. This process is probably not observable in CT0BMI20 due to the higher electrode polarization and the shift of HT1 towards HT2a. HT2b in CT0BMI20 is maybe generated by the melting of BMI with melting point at 0°C that matches approximately HT2b at small frequencies.

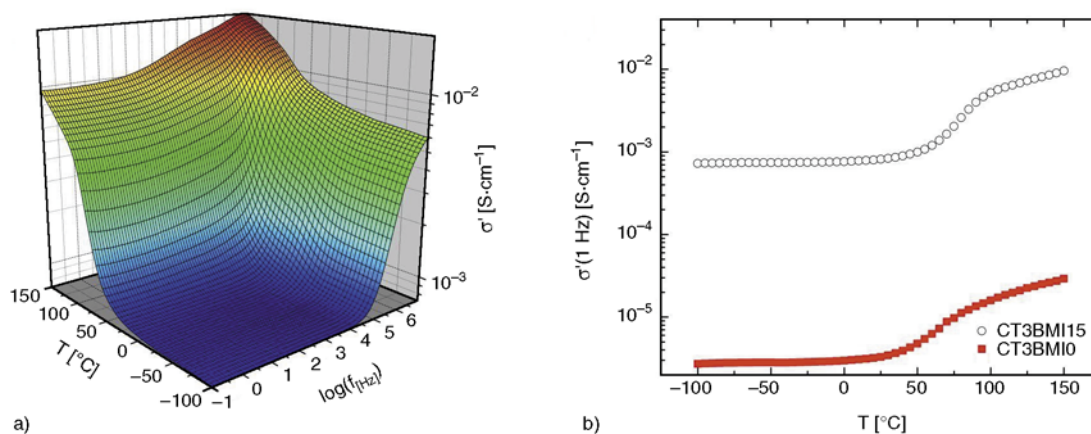
### 3.2. Dielectric properties of CNT filled rubber composites

Figure 6 illustrates the dispersion of 3 phr CNTs in the CR rubber matrix by TEM pictures. Considering the sample CT3BMI0 (Figure 6a and 6c), the dispersion state of the tubes is poor and a large amount of different sized agglomerates are seen. The tube agglomerates are also spaced apart without intertubular connection in many regions. The pristine MWCNTs have a tendency to form entangled bundles, which are apparently hard to separate only by the shearing force during mixing with the elastomer matrix. In contrary, the TEM picture of CT3BMI15 (Figure 6b) shows only small agglomerates. At higher magnification (Figure 6d), single CNTs are seen, which are well distributed over the entire image. Thus, a much better dispersion can be obtained by modifying the CNTs with BMI. Additionally, the intertubular contacts are increased. It has been recently discussed that the Van der Waals attraction among the tubes decreases due to cation- $\pi$  interaction between ILs and CNTs in modified tubes [10, 11]. This leads to disentanglement of CNTs that in turn increased the dispersion and the formation of a highly conductive CNT network.

In Figure 7a, the real part of conductivity is shown in dependence on temperature and frequency for the sample CT3BMI15, which contains 3 phr CNTs and 15 phr BMI. At small frequencies, a conductiv-



**Figure 6.** TEM images of CNT filled CR rubber. a) and c) CT3BMI0 without BMI. b) and d) CT3BMI15 with BMI. Scale bar: a), b) 1  $\mu\text{m}$  and c), d) 200 nm.



**Figure 7.** a) Real part of the conductivity of CT3BMI15. b) Conductivity at 1 Hz for CT3BMI0 (without IL) and CT3BMI15 (with IL).

ity plateau is observed which corresponds to the dc conductivity. The ac conductivity increases from the plateau into a disperse regime at about 10 kHz. The dc plateau is almost constant at small temperatures and increases strongly at around room temperature. The effect of ionic liquids on the dc conduc-

tivity is considered in Figure 7b. An improvement of the conductivity over more than two orders of magnitude has been found for CT3BMI15 with regard to CT3BMI0. Note that the slightly increased ion conduction due to the usage of BMI cannot explain that huge difference in the conductivity.

Neat CR rubber (sample CT0) and CR rubber containing BMI (CT0BMI20) have a conductivity at room temperature of  $\sim 10^{-10}$  S/cm  $\sim 10^{-9}$  S/cm, respectively. Thus, the ion conduction is insignificant compared to the much larger conductivity due to the electron transport through the CNT network.

One main reason for the much larger conductivity in the samples containing BMI is the improved dispersion. Indeed the conductivity is not only determined by the structure and number of conductive paths of the CNT network, but also affected by a contact resistance between neighboring CNTs. As pointed out by Fritzsche *et al.* [13], quantum mechanical tunneling of electrons between neighboring CNTs plays a dominant role for CNT/rubber composites. CNTs in the rubber matrix have no direct geometrical contact, but are separated by a thin polymer layer that limits the dc conductivity of the CNT network. Despite these small gaps between the CNTs, electrons can overcome these barriers by tunneling or hopping. The increase in conductivity above room temperature suggests that a transition from tunneling to thermal activated hopping takes place and therefore the transport mechanism between CNTs changes. This behavior has also been observed for carbon black/rubber composites [6].

In order to gain more information about CNT/CNT connections, the permittivity has been considered. The real part of permittivity at different temperatures can be seen in Figure 8. At small temperatures, a relaxation transition is found at relatively large frequencies. For CT3BMI15 the relaxation transition is sharper and at larger frequencies than for CT3BMI0. Additionally, the plateau of the permittivity at small frequencies has a much larger value for CT3BMI15, indicating a larger polarization in the modified

CNT/rubber composite. With increasing temperature, a large rise of permittivity at small frequencies becomes dominant. The high  $\epsilon'$ -values might be correlated to Maxwell-Wagner-Sillars relaxation that occurs due to accumulation of ions at the interfaces in inhomogeneous media. This effect becomes more important at larger temperatures since the thermal activated ion transport increases with increasing temperature.

The sharp relaxation transition at large frequencies can be traced back to a quantum mechanical tunneling process of electrons across small gaps between adjacent CNTs [13]. A relation between the relaxation frequency and the gap distance between neighboring filler particles has been derived, which says that larger relaxation frequencies means smaller gap distances. Consequently, the gaps between CNTs in the sample with IL (CT3BMI15) are smaller. Additionally, the sharper transition indicates a narrower distribution of gap distances. The much larger value of the relaxation strength for the IL modified CNT composite indicates that a larger amount of gaps exist which contribute to the polarization. This is consistent with the better dispersion and the more homogenous CNT network. The consequence of smaller gaps is that the quantum mechanical tunneling current over them is larger and thus the conductivity is increased. The main reasons for the improved conductivity of the IL modified CNT composite are therefore the smaller gaps between the CNTs and the better CNT networking.

The conductivity could additionally be influenced by the improved polymer-filler interaction due to BMI as coupling agent. The polymer in the nanoscopic gaps between neighboring fillers is expected to be glassy [6] because of immobilization of polymer chains by confinement between adjacent filler particles and adsorption of polymer segments at the surfaces. The stronger physical coupling by BMI probably affects the polymer dynamics in the gaps and therewith the dielectric properties. In order to estimate the influence of this effect on the conductivity, the measured permittivity of the CR without CNTs (CT0 and CT0BMI20) can be considered, which is for both samples around 4 in the glassy regime and around 10 in the elastic regime. Since the tunneling current is only proportional to the polymer permittivity [13], the influence on conductivity due to any changes in flexibility of the poly-

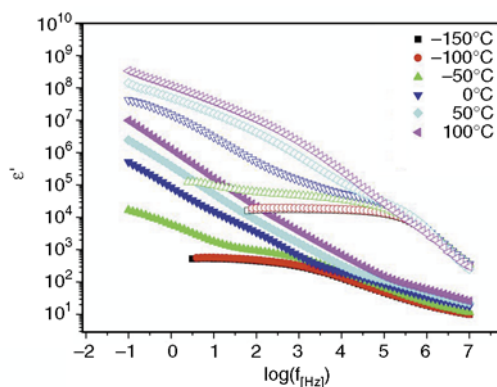


**Figure 8.** Real part of permittivity for CT3BMI0 (closed symbols) and CT3BMI15 (open symbols) at different temperatures

mer is relatively small compared to the improved conductivity of more than two orders of magnitude. The effect of the gap size with an exponential dependence of gap distance on the tunneling current is probably much larger.

#### 4. Conclusions

The dielectric spectra of unfilled chloroprene rubber and of IL/chloroprene rubber have been investigated. Besides electrode polarization, four relaxation processes have been detected for each of the both samples. It has been found that the glass transition described by a Vogel-Fulcher behavior does not change with the usage of ionic liquid, indicating that the both components are not compatible. The weakly pronounced, broad relaxation process at low temperature in pure CR rubber can be assigned to the  $\beta$  process due to rotational motion of side groups. For the sample containing IL, the  $\beta$  process is masked by an additional relaxation transition, which is much more pronounced. This process can be related to the  $\alpha$  process of the IL, whose disordered and fragile structure typically exhibits a glassy like state at low temperatures. The origin of one of the both observed high temperature processes might be the existence of zinc clusters.

The high electrical conductivity of the CNT-filled rubber composites can be related to the transport of electrons along conductive paths of the throughgoing CNT network. The temperature behavior of the conductivity suggests that the conduction mechanism between neighboring CNTs is quantum mechanical tunneling at low temperatures and thermal activated hopping above room temperature. The IL-modification of the CNTs leads to an increased conductivity that is related to smaller gap distance between neighboring CNTs and a better dispersion due to a physical coupling between CNTs and rubber matrix.

#### References

- [1] Chung D.: Materials for electromagnetic interference shielding. *Journal of Materials Engineering and Performance*, **9**, 350–354 (2000).  
DOI: [10.1361/105994900770346042](https://doi.org/10.1361/105994900770346042)

- [2] Kost J., Narkis M., Foux A.: Resistivity behavior of carbon-black-filled silicone rubber in cyclic loading experiments. *Journal of Applied Polymer Science*, **29**, 3937–3946 (1984).  
DOI: [10.1002/app.1984.070291226](https://doi.org/10.1002/app.1984.070291226)
- [3] Stübler N., Fritzsche J., Klüppel M.: Mechanical and electrical analysis of carbon black networking in elastomers under strain. *Polymer Engineering and Science*, **51**, 1206–1212 (2011).  
DOI: [10.1002/pen.21888](https://doi.org/10.1002/pen.21888)
- [4] Chen L., Chen G. H., Lu L.: Piezoresistive behavior study on finger-sensing silicone rubber/graphite nanosheet nanocomposites. *Advanced Functional Materials*, **17**, 898–904 (2007).  
DOI: [10.1002/adfm.200600519](https://doi.org/10.1002/adfm.200600519)
- [5] O'Farrell C. P., Gerspacher M., Nikiel L.: Carbon black dispersion by electrical measurements. *Kautschuk Gummi Kunststoffe*, **53**, 701–710 (2000).
- [6] Klüppel M.: The role of disorder in filler reinforcement of elastomers on various length scales. *Advances in Polymer Science*, **164**, 1–86 (2003).  
DOI: [10.1007/b11054](https://doi.org/10.1007/b11054)
- [7] Medalia A. I.: Electrical conduction in carbon black composites. *Rubber Chemistry and Technology*, **59**, 432–454 (1986).  
DOI: [10.5254/1.3538209](https://doi.org/10.5254/1.3538209)
- [8] López-Manchado M. A., Biagiotti J., Valentini L., Kenny J. M.: Dynamic mechanical and Raman spectroscopy studies on interaction between single-walled carbon nanotubes and natural rubber. *Journal of Applied Polymer Science*, **92**, 3394–3400 (2004).  
DOI: [10.1002/app.20358](https://doi.org/10.1002/app.20358)
- [9] Gojny F. H., Wichmann M. H. G., Fiedler B., Kinloch I. A., Bauhofer W., Windle A. H., Schulte K.: Evaluation and identification of electrical and thermal conduction mechanisms in carbon nanotube/epoxy composites. *Polymer*, **47**, 2036–2045 (2006).  
DOI: [10.1016/j.polymer.2006.01.029](https://doi.org/10.1016/j.polymer.2006.01.029)
- [10] Das A., Stöckelhuber K. W., Jurk R., Fritzsche J., Klüppel M., Heinrich G.: Coupling activity of ionic liquids between diene elastomers and multi-walled carbon nanotubes. *Carbon*, **47**, 3313–3321 (2009).  
DOI: [10.1016/j.carbon.2009.07.052](https://doi.org/10.1016/j.carbon.2009.07.052)
- [11] Lorenz H., Fritzsche J., Das A., Stöckelhuber K. W., Jurk R., Heinrich G., Klüppel M.: Advanced elastomer nano-composites based on CNT-hybrid filler systems. *Composites Science and Technology*, **69**, 2135–2143 (2009).  
DOI: [10.1016/j.compscitech.2009.05.014](https://doi.org/10.1016/j.compscitech.2009.05.014)
- [12] Shaffer M. S. P., Sandler J. K. W.: Carbon nanotube/nanofibre polymer composites. in 'Processing and properties of nanocomposites' (ed.: Advani S. G.) World Scientific Publishing Company, Singapore (2006).

- [13] Fritzsche J., Lorenz H., Klüppel M.: CNT based elastomer-hybrid-nanocomposites with promising mechanical and electrical properties. *Macromolecular Materials and Engineering*, **294**, 551–560 (2009). DOI: [10.1002/mame.200900131](https://doi.org/10.1002/mame.200900131)
- [14] Subramaniam K., Das A., Heinrich G.: Development of conducting polychloroprene rubber using imidazolium based ionic liquid modified multi-walled carbon nanotubes. *Composites Science and Technology*, **71**, 1441–1449 (2011). DOI: [10.1016/j.compscitech.2011.05.018](https://doi.org/10.1016/j.compscitech.2011.05.018)
- [15] Subramaniam K., Das A., Steinhauser D., Klüppel M., Heinrich G.: Effect of ionic liquid on dielectric, mechanical and dynamic mechanical properties of multi-walled carbon nanotubes/polychloroprene rubber composites. *European Polymer Journal*, **47**, 2234–2243 (2011). DOI: [10.1016/j.eurpolymj.2011.09.021](https://doi.org/10.1016/j.eurpolymj.2011.09.021)
- [16] Yamamuro O., Minamimoto Y., Inamura Y., Hayashi S., Hamaguchi H.: Heat capacity and glass transition of an ionic liquid 1-butyl-3-methylimidazolium chloride. *Chemical Physics Letters*, **423**, 371–375 (2006). DOI: [10.1016/j.cplett.2006.03.074](https://doi.org/10.1016/j.cplett.2006.03.074)
- [17] Wübbenhorst M., van Turnhout J.: Conduction-free dielectric loss  $\partial\epsilon/\partial\ln f$  – A powerful tool for the analysis of strong (ion) conducting dielectric materials. *Dielectrics Newsletter*, **14**, 1–3 (2000).
- [18] Fritzsche J., Das A., Jurk R., Stöckelhuber K. W., Heinrich G., Klüppel M.: Relaxation dynamics of carboxylated nitrile rubber filled with organomodified nanoclay. *Express Polymer Letters*, **2**, 373–381 (2008). DOI: [10.3144/expresspolymlett.2008.44](https://doi.org/10.3144/expresspolymlett.2008.44)
- [19] Kempermann T.: *Handbuch für die Gummiindustrie*. Bayer AG, Leverkusen (1991).
- [20] Batzer H.: *Polymere Werkstoffe*, Band III. Georg Thieme Verlag, New York (1984).

# Development of novel melt-compounded starch-grafted polypropylene/polypropylene-grafted maleic anhydride/organoclay ternary hybrids

R. Tessier<sup>1,2</sup>, E. Lafranche<sup>1,2\*</sup>, P. Krawczak<sup>1,2</sup>

<sup>1</sup>Ecole Nationale Supérieure des Mines de Douai, Department of Polymers and Composites Technology and Mechanical Engineering, 941 rue Charles Bourseul, CS 10838, F 59508 Douai, France

<sup>2</sup>Université Lille Nord de France, 59000 Lille, France

Received 18 April 2012; accepted in revised form 25 June 2012

**Abstract.** Starch-grafted polypropylene (PP-g-starch)/organoclay nanocomposites were melt-compounded using a co-rotating twin-screw extruder. Homopolymer or copolymer-based polypropylene-grafted maleic anhydrides (PP-g-MA) with different molecular weights and different maleic anhydride (MA) grafting levels were added at different weight contents as compatibilizer. Two organo-modified montmorillonites were used, the first one containing polar functional groups (Cloisite<sup>®</sup>30B) having affinity to the starch phase, and the other one containing non polar-groups (Cloisite<sup>®</sup>20A) having affinity to the polypropylene phase of the polymer matrix. Whatever the MA grafting level and the molecular weight and content of PP-g-MA, no significant immiscibility of PP-g-starch/PP-g-MA blends is evidenced. Regarding clay dispersion, adding a low content of ethylene-propylene copolymer-based PP-g-MA compatibilizer having a high MA-grafting level, and a polar organoclay (Cloisite<sup>®</sup>30B) is the most desirable formulation to optimize clay intercalation and exfoliation in PP-g-starch. Nevertheless, regarding the reinforcement effect, whatever the PP-g-MA compatibilizer, the addition of non polar organoclay (Cloisite<sup>®</sup>20A) is preferably recommended to reach higher tensile properties (modulus, yield stress, strength) without significant loss of ductility.

**Keywords:** nanocomposites, polymer blends, starch, clay, mechanical properties

## 1. Introduction

Ever-growing concern related to sustainability and ecology has been the key driving force for developing bio-based plastics. In single-use packaging applications, biodegradability is an advantage and poor mechanical properties remain acceptable. Automotive applications are however much more challenging as durable bioplastics are expected to meet very demanding requirements, such as high thermo-mechanical performance (strength and rigidity) often coupled with dimensional accuracy and stability [1]. The most widely spread bioplastics, namely biopolyamide 11, poly(lactic acid) and ther-

moplastic starch, are unfortunately often either too expensive or too sensitive to ageing and humidity, and are not rigid and resistant enough to be used to manufacture automotive plastic parts. The issue is therefore to reinforce bio-based plastics whose properties are not high enough to replace the fully petroleum-based polymers. This may be achieved for example by addition of cheap micro- or nano-scaled fillers (particles or fibres), so as to develop cost-effective composite or nanocomposite materials reaching the expected level of performance [1]. Considering this constraining application field, raw material producers have developed hybrid (bipha-

\*Corresponding author, e-mail: [eric.lafranche@mines-douai.fr](mailto:eric.lafranche@mines-douai.fr)

sic) polymers where a bio-based matrix is associated with a more conventional polyolefin matrix (polyethylene, polypropylene). In particular starch-grafted polypropylene may provide a suitable alternative solution to supply automotive industry with a durable ‘green’ thermoplastic [2]. Nevertheless, reaching the desired level of mechanical performance still requires further reinforcement by addition of nanofillers for instance, as it was done with the development of bio-based nanocomposites dedicated to packaging applications [3]. In that case, layered silicate nanoplatelets are commonly used and among the different types of clay, montmorillonite (MMT) is the most used nanofiller because of its low cost, natural abundance and high aspect ratio.

Biphasic thermoplastic matrices such as Gaïalene® (Roquette, France [2]) made of polypropylene (PP) grafted with starch at a 48/52 weight ratio form a complex polymer system with hydrophilic and hydrophobic phases in which clay has to be dispersed and exfoliated. Thermoplastic starch is hydrophilic. In that case, a better dispersion and exfoliation is usually obtained with native clay (Na<sup>+</sup>-MMT, unmodified sodium montmorillonite), which is naturally hydrophilic. Polar interactions are created between the silicate lamella and the hydroxyl groups of the starch [4–6].

The dispersion, intercalation and exfoliation of clay, and especially montmorillonite, in PP have also been widely investigated [7–17]. The exfoliation of clay platelets is an uphill task, particularly in non-polar hydrophobic polymers like PP because of the unfavourable enthalpic interaction with the highly hydrophilic clay, which prohibits the diffusion of polymer molecules into the intergallery space. Even if attempts have been made to use pristine (unmodified) clay [7], modification of clay with organic cations (by cationic exchange with the sodium cations of the mineral) and addition of compatibilizers such as maleic anhydride (MA) are common solutions used to improve the interaction between PP and clay nanoplatelets. Besides, proper choice of processing conditions may further improve clay dispersion [8]. The organic cations used for clay modification are usually alkyl ammonium cations with different chemical structures depending on the considered polymer matrix. Generally apolar alkyl ammonium cations are used in the case of apolar

polymers such as PP [10, 11]. It is now well admitted that clay dispersion in PP and interfacial adhesion are better with a non-polar clay modifier such as the one used in Cloisite®20A (Southern Clay Product) than with pristine (i.e. native) clay or polar clay modifier such as that used in Cloisite®30B (Southern Clay Product) [12]. Similarly, as for carbon nanotubes [18], it is well known that a better clay dispersion and exfoliation is achieved when PP-g-MA compatibilizers are used. Some authors [11–16] investigated the compatibilizer influence on the clay exfoliation. A high maleic anhydride grafting level enables a better molecular insertion between the lamella, but a molecular weight decrease of the polypropylene may be expected due to molecular chain breakage [10, 12, 17]. A higher compatibilizer molecular weight increases the melt viscosity [15], which may be favourable to break the clay tactoids, but may also hinder the diffusion mechanism of the polymer chain in clays interlayer space at low temperature. In practice, a balance between compatibilizer molecular weight and maleic anhydride grafting level is necessary to optimize clay exfoliation (even if full exfoliation cannot be obtained in PP matrices due to the huge polarity difference between the matrix and the clay) and thus mechanical properties [11, 12, 15].

Furthermore, some authors highlighted the interest of using solid nanoparticles (clays among others [19–21]) to improve the properties of polymer blends, the nanofiller playing the role of both structural reinforcement and compatibilizer. In particular in the case of clays, when the platelets are organo-modified, the nature of the surfactant can influence the location of clay platelets in immiscible polymer blends, affect the coalescence behaviour and, effectively, reduce the size of the dispersed phase, decrease the interfacial tension and improve the adhesion between the phases [22, 23]. However, whereas it is commonly admitted that organoclays may act as compatibilizers in the case of immiscible polymer blends, the exact mechanism involved is still unclear. Yousfi *et al.* [24] have recently shown that the key factor for organoclay compatibilization efficiency is the surfactant (organo-modifier) itself and not solely the presence of clay platelets.

In that context, the general objective of the present research program is to develop, based on a newly marketed biphasic starch-grafted polypropylene



matrix, compatibilized starch-grafted polypropylene/organoclay nanocomposites by melt-compounding so as to up-grade its mechanical performance. In particular, this paper aims at understanding the influence of both the PP-g-MA compatibilizer (weight content and maleic anhydride grafting level) and the organoclay modifier on the clay dispersion in the complex biphasic starch-grafted polypropylene matrix. The miscibility was evaluated by rheology and microscopy. Then, the intercalation and/or exfoliation were assessed by rheological analysis coupled to morphological observations. Finally, the resulting tensile properties were characterized.

## 2. Experimental

### 2.1. Materials

The material studied was a 52 wt% plant-based starch-grafted polypropylene (Gaiälene® 906PJ, Roquette, France) with an MFR of 30 g/10 min (190°C/10 kg), further named PP-g-starch. Three commercial maleated polypropylenes (Polypropylene-grafted maleic anhydride, PP-g-MA) were used: two homopolymers with graft efficiency of 0.5 wt% (Fusabond® P613, Dupont, Switzerland – further named PP-g-MA1) and 1 wt% (Orevac® CA100, Arkema, France – further named PP-g-MA2), and one ethylene-propylene copolymer with graft effi-

ciency of 1.4 wt% (Fusabond® P353, Dupont, Switzerland – further named PP-g-MA3), the ethylene content in the copolymer being 52 wt%. The clays were sodium montmorillonite modified with quaternary ammonium salt, one polar modified nanoclay (Cloisite®30B, Southern Clay Products Co., USA – further named C30B) and one non-polar modified nanoclay (Cloisite®20A, Southern Clay Products Co., USA – further named C20A). The main characteristics of the materials are summarized in Table 1.

### 2.2. Compounding conditions

The PP-g-starch/PP-g-MA and PP-g-starch/PP-g-MA/organoclay compounds were obtained by melt-blending in a twin-screw extruder (Haake PolyLab, Thermo Scientific, Germany) equipped with a 16 mm screw diameter and a length/diameter ratio  $L/D$  of 29:1, operating at 160–180°C and 200 rpm. Polymers were first mixed before introduction in the extruder. The clays were then introduced in the polymer melt just before a screw mixing zone (Figure 1). Raw materials were dried at 80°C during 4 hours in order to get a relative humidity of 8000 ppm. The composition of the compounds is detailed in Table 2.

**Table 1.** Main characteristics of materials used

Polymer material	Gaiälene® 906PJ (PP-g-starch)	Fusabond® P613 (PP-g-MA1)	Orevac® CA100 (PP-g-MA2)	Fusabond® P353 (PP-g-MA3)
Structure	Starch-grafted	Homopolymer	Homopolymer	PE/PP (52/48) copolymer
MFR (190°C; 2.16 kg) [g/10 min]	30 (10 kg)	120	10 (0.325 kg)	470
Melting point [°C]	157	162	167	135
Crystallization point [°C]	110	108	107	93
$M_w$ [g·mol <sup>-1</sup> ]	–	95 000	89 000	88 700
Density	1.12	0.903	0.909	0.904
Young's Modulus [MPa]	420	1170	1050	700
Grafting level [wt%]	52	0.5	1	1.4
<b>Organoclay</b>	<b>Cloisite®30B (C30B)</b>		<b>Cloisite®20A (C20A)</b>	
Organic modifier	Methyl, tallow, bis-2-hydroxyethyl, quaternary ammonium chloride, where HT is hydrogenated tallow (65% C18, 30% C16, 5% C14); Anion: Chloride		Dimethyl, deshydrogenated tallow, quaternary ammonium chloride, where HT is hydrogenated tallow (65% C18, 30% C16, 5% C14); Anion: Chloride	
Structure of organic modifier	$\begin{array}{c} \text{CH}_2\text{CH}_2\text{OH} \\   \\ \text{CH}_3\text{-N}^+\text{-T} \\   \\ \text{CH}_2\text{CH}_2\text{OH} \end{array}$		$\begin{array}{c} \text{CH}_3 \\   \\ \text{CH}_3\text{-N}^+\text{-HT} \\   \\ \text{HT} \end{array}$	
Modifier concentration [meq/100 g]	90		95	
X-ray $d_{001}$ [nm]	1.85		2.42	
% loss on ignition	30		38	

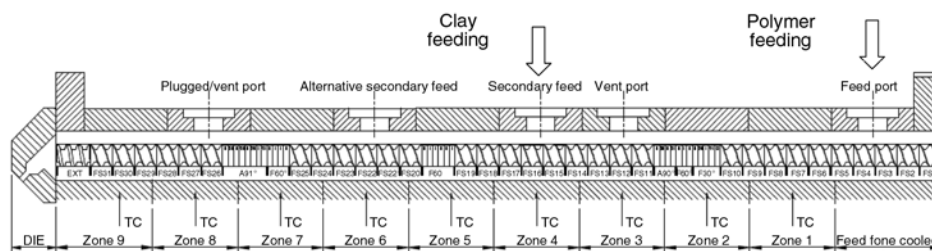


Figure 1. Screw profile of the extruder

Table 2. Sample designation and composition

Sample designation	PP-g-starch wt% content	PP-g-MA wt% content	Neat clay* wt% content
5PP-g-MA1 (or PP-g-MA2, PP-g-MA3)	95	5	
10PP-g-MA1 (or PP-g-MA2, PP-g-MA3)	90	10	
15PP-g-MA1 (or PP-g-MA2, PP-g-MA3)	85	15	
20PP-g-MA1 (or PP-g-MA2, PP-g-MA3)	80	20	
5PP-g-MA2 C30B (or C20A)	95	5	3.5
20PP-g-MA2 C30B (or C20A)	80	20	3.5

\*Neat mineral wt% content, determined from ignition loss tests to eliminate the surfactant weight fraction of organoclay (corresponds to 5 wt% Cloisite® organoclay)

The shear rate  $\dot{\gamma}$  imposed to the blends during compounding was estimated using an extrusion software package (Ludovic®, Sciences Computers Consultants, France). The computed value is  $120 \text{ s}^{-1}$ .

### 2.3. Moulding conditions

Dumbbell test specimens (ISO 1A) were moulded on an 800 kN clamping force injection-moulding machine (80-160E, Krauss Maffei, Germany). The moulding conditions are summarized in Table 3.

Table 3. Moulding conditions

Processing parameters	Set up value
Mould temperature [°C]	40
Melt temperature [°C]	180
Volume flow rate [ $\text{cm}^3 \cdot \text{s}^{-1}$ ]	46
Holding pressure [bar]	800
Back pressure [bar]	20
Screw rotation speed [ $\text{cm} \cdot \text{s}^{-1}$ ]	8.8

### 2.4. Mechanical testing

Tensile tests were performed on a tensile machine (Model 1185, Instron, USA) using an extensometer for strain measurement. Tests were conducted on five samples according to ISO 527 standard at  $20 \text{ mm} \cdot \text{min}^{-1}$  crosshead speed for the yield and ultimate properties measurement and at  $1 \text{ mm} \cdot \text{min}^{-1}$  for Young's modulus measurement. Samples were stored during 2 days at  $23^\circ\text{C}$  and 50% relative humidity before testing.

### 2.5. Rheological characterisation

Oscillatory shear rheological analysis was carried out at  $170$ ,  $180$  or  $200^\circ\text{C}$  under air atmosphere on compression-moulded circular samples (40 mm diameter, 2 mm thick) on a rotational rheometer (ARES, Rheometric Scientific, USA) with parallel plates. Linear domains of the materials were identified from strain sweeps and a common strain of 1% was then selected for the different samples whatever the testing temperature. Frequency sweeps were run from  $0.1$  to  $100 \text{ rad} \cdot \text{s}^{-1}$  in order to record the storage (elastic) modulus  $G'$  and the complex viscosity  $\eta^*$ .

### 2.6. Structural characterisation

X-ray diffraction (XRD) characterisation of the structure was carried out on clay powder or disks of 50 mm diameter and 2.3 mm thickness compression-moulded in a press (Dolouets 383, France; compression pressure of 10 MPa for 1 min and temperature of  $180^\circ\text{C}$ ). Wide-angle X-ray scattering experiments were carried out at room temperature in reflection mode. XRD curves were recorded on a diffractometer (D5000, Siemens, Germany) operating at 40 kV and 30 mA with a beam consisting of  $\text{CoK}\alpha$  radiation ( $\lambda = 1.78897 \text{ \AA}$ ). Data were collected in the  $2\theta$  region  $2$ – $10^\circ$  with a step size of  $0.04^\circ$  and a counting time of 30 seconds per step. The basal spacing of the organically modified layered silicate (organo-clay) before and after interca-

lation was estimated from the position of ( $d_{001}$ ) peak in the XRD diffractogram according to the Bragg equation ( $n\lambda = 2d\sin\theta$ ) where  $d$  is the spacing between silica layers of the clay (also called interlayer spacing),  $\lambda$  the wave length of X-ray,  $\theta$  the reflection angle of X-ray on the silica layer, and  $n$  is a whole number which represents the order of diffraction, taken 1 in our calculations.

Morphological analysis was performed on cryo-fractured surfaces of injection-moulded samples. A thin layer of gold was sputter deposited onto the sample. Imaging of the samples was carried out under high vacuum with a Scanning Electron Microscope (S-4300SE/N, Hitachi, Japan) operating at 10 kV.

Specimens for Transmission Electron Microscopy (TEM) were cut from bulk samples using a microtome (Ultracut UTC and EM FCS, Leica, Germany). Ultra-thin sections were cut using a diamond knife and collected on a 300 mesh copper grid. TEM images were obtained using a TEM instrument (CM20, Philips, The Netherlands) with a 200 kV acceleration voltage. Experiments were carried out at PSA research centre (PSA Peugeot Citroen, France).

### 2.7. Interfacial tensions characterisation

Surface energies (sometimes also called surface tensions as polymers may be liquid-like) of the blended polymers were measured by the sessile drop method using a goniometer (Digidrop, GBX, France). Experiments, consisting in measuring the contact angle of a liquid droplet on a solid substrate, were performed at ISPA (Institut Supérieur de Plasturgie d'Alençon, France). The measurements were carried out at room temperature in static mode under nitrogen atmosphere. The probe liquids were HPLC grade water (surface tension  $\sigma = 72.8 \text{ mJ}\cdot\text{m}^{-2}$  with polar component  $\sigma^p = 51.0 \text{ mJ}\cdot\text{m}^{-2}$  and dispersive component  $\sigma^d = 21.8 \text{ mJ}\cdot\text{m}^{-2}$ ), formamide ( $\sigma = 58.2 \text{ mJ}\cdot\text{m}^{-2}$  with  $\sigma^p = 18.7 \text{ mJ}\cdot\text{m}^{-2}$  and  $\sigma^d = 39.5 \text{ mJ}\cdot\text{m}^{-2}$ ), and diiodomethane ( $\sigma = 50.8 \text{ mJ}\cdot\text{m}^{-2}$  with  $\sigma^p = 49.5 \text{ mJ}\cdot\text{m}^{-2}$  and  $\sigma^d = 1.3 \text{ mJ}\cdot\text{m}^{-2}$ ).

The polymers surface energies ( $\sigma$ ) and their polar ( $\sigma^p$ ) and dispersive ( $\sigma^d$ ) components were determined according to Owens-Wendt theory [25]. The corresponding values are reported in Table 4 for the different materials constituting the blends (PP-g-starch being considered as a one and only phase having its own surface energy).

**Table 4.** Surface energies  $\sigma$  and their dispersive  $\sigma^d$  and polar  $\sigma^p$  components for the different blends constituents

Material	$\sigma$ [mN·m <sup>-1</sup> ]	$\sigma^d$ [mN·m <sup>-1</sup> ]	$\sigma^p$ [mN·m <sup>-1</sup> ]
PP-g-starch	30.4	30.4	0
PP-g-MA2	33.4	32.2	1.1
PP-g-MA1	32.9	32.2	0.7
PP-g-MA3	34.2	31.7	2.6

**Table 5.** Calculated interfacial tension  $\sigma_{12}$  of the blends

Blend	Interfacial tension $\sigma_{12}$ [mN·m <sup>-1</sup> ]
PP-g-starch/PP-g-MA2	7.41
PP-g-starch/PP-g-MA1	6.10
PP-g-starch/PP-g-MA3	10.42

The interfacial tension ( $\sigma_{12}$ ) between the constitutive materials (1 and 2) of the different polymer blends were then calculated from the polymers surface energies and their polar and dispersive components using Wu's harmonic relation (Equation (1)), which has been shown to be applicable to polymer melts [26, 27]. The calculated values are reported in Table 5 for the different PP-g-starch/PP-g-MA blends:

$$\sigma_{12} = \sigma_1 + \sigma_2 - \frac{4\sigma_1^d\sigma_2^d}{\sigma_1^d + \sigma_2^d} - \frac{4\sigma_1^p\sigma_2^p}{\sigma_1^p + \sigma_2^p} \quad (1)$$

Surface energies were measured and interfacial tensions calculated at room temperature and not at 180°C because forming a suitable droplet at such a high temperature was impossible in practice.

## 3. Miscibility of PP-g-MA compatibilizers with starch-grafted polypropylene

At first, the miscibility of the different PP-g-MA compatibilizers (differing by their maleic anhydride grafting level and their molecular weight) with the polymer matrix (PP-g-starch) was checked in order to define the most desirable formulation. The assessment of the miscibility was carried out for the different PP-g-starch/PP-g-MA blends by means of complementary rheological and microscopic characterisation methods.

### 3.1. Rheological assessment

Rheological methods have been frequently used to study the phase separation of partially miscible or immiscible (i.e. fully phase separated) polymer

blends. One of the most frequently used methods to judge whether the blend is fully miscible (i.e. behaves as a single-phase system with no phase separation) or in phase separated state is the time-temperature superposition (TTS) principle [28, 29]. The TTS principle states that, when studying the viscoelastic behaviour of a material (for instance complex viscosity or complex elasticity modulus), a change of temperature is completely equivalent to a shift of the logarithmic time scale (so-called time-shift); such a material is termed ‘thermo-rheologically simple’ [30]. It is usually believed that TTS principle fails for polymer blends in phase separated state, and works in miscible state [28, 29]. If an excellent superposition is obtained when plotting

the rheological master curves at a reference temperature, then the polymer blend is fully miscible; if not, it is assumed to be immiscible or partially miscible only.

The dynamic rheological behaviour of 95/5 and 80/20 wt% PP-g-starch/PP-g-MA blends was recorded at different temperatures, namely 170, 180 and 190°C. The master curves of complex viscosity  $\eta^*$  as a function of the shifted frequency  $a_T \omega$  at 180°C were plotted (Figure 2). A very good superposition is obtained for the blends containing PP-g-MA2 and PP-g-MA3 whatever the compatibilizer weight content. Their rheological behaviour depends neither on the temperature nor on the blend composition (i.e. PP-g-MA weight content), suggesting

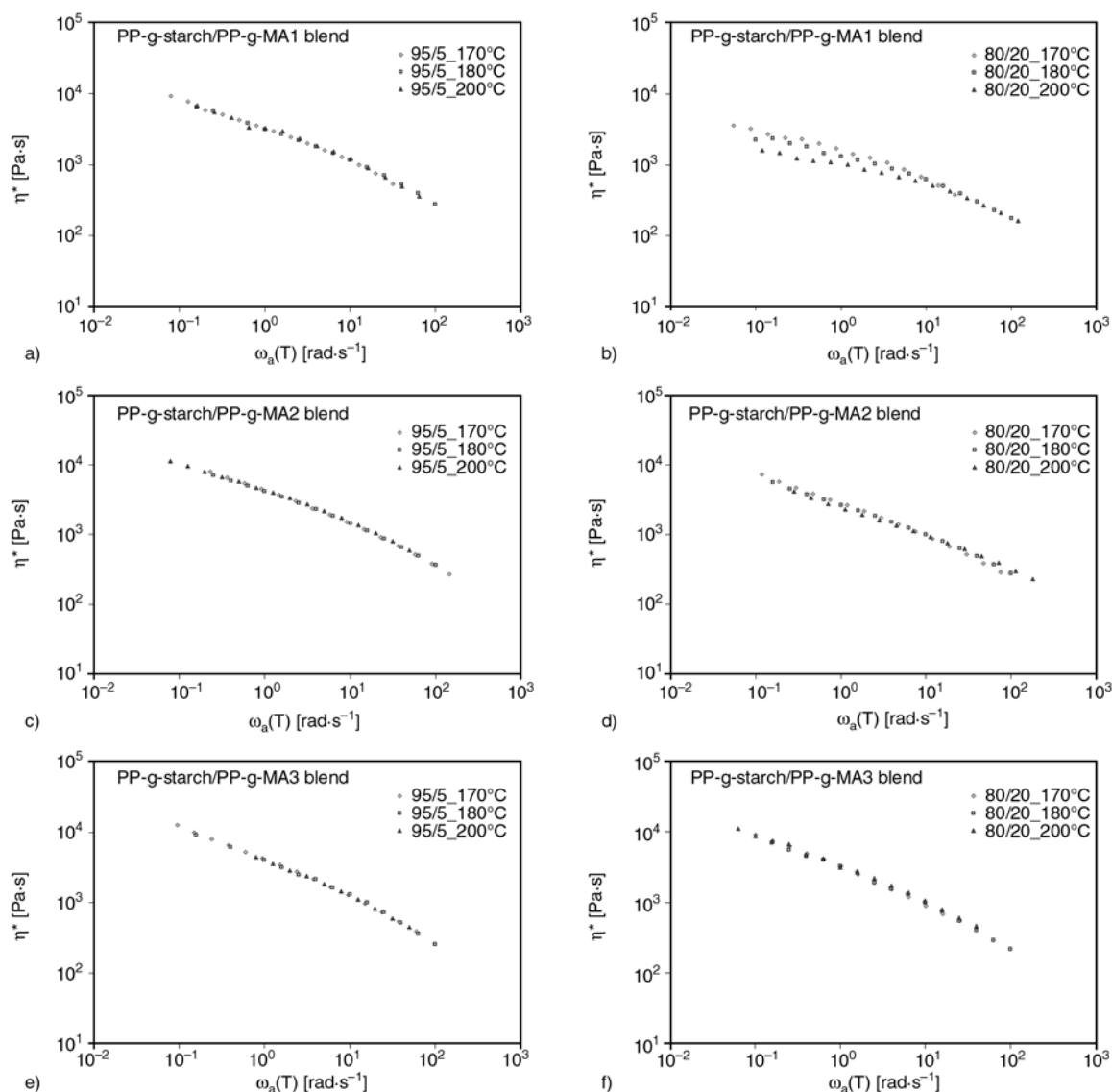


**Figure 2.** Complex viscosity master curves at the reference temperature of 180°C for PP-g-starch/PP-g-MA1 (a, b), PP-g-starch/PP-g-MA2 (c, d) and PP-g-starch/PP-g-MA3 (e, f) compatibilized blends at 95/5 wt% (a, c, e) and 80/20 wt% (b, d, f)

quite good miscibility. A peculiar behaviour is noticed in the case of the blend containing PP-g-MA1; a shift appears at lower frequencies depending on both the temperature and the PP-g-MA weight content. Such a deviation may be ascribed to a partial, lower miscibility of this blend, in particular when the compatibilizer weight content is high. A similar trend was also pointed out by other authors [10]. It is however worth mentioning that the failure of TTS principle is not a strict principle to judge the phase separation as it may fail in the miscible state also according to some authors [28]. Therefore, another complementary method was also implemented.

### 3.2. Microscopic assessment and prediction of dispersed particle size

As a method of direct observation, optical or electron micron microscopy has also been used quite often to show whether polymer blends are in homogeneous or phase separated states. SEM imaging of

neat PP-g-starch and of the three PP-g-starch/PP-g-MA blends were performed. Taking the neat biphasic PP-g-starch matrix (Figure 3a) as a reference (further considered being the continuous matrix phase), a PP-g-MA dispersed phase possibly appears upon compatibilizers' addition, depending on PP-g-MA type and content. SEM imaging of the three PP-g-starch/PP-g-MA blends does not show any significant immiscibility at the lower PP-g-MA compatibilizer content (5 wt%). At higher weight content (20 wt%), the dispersed phase size is high enough to be visible on microscopic images (Figure 3b, c, d), but strongly depends on the compatibilizer used. Based on representative SEM images, an equivalent diameter of dispersed phase was determined (typical order of magnitude only). For the PP-g-MA1 homopolymer-based compatibilizer, the size of the dispersed phase typically reaches more than 80  $\mu\text{m}$  (Figure 3b) whereas it is of about 35  $\mu\text{m}$  for the PP-g-MA2 homopolymer-based compatibilizer (Figure 3c) and of 25  $\mu\text{m}$  for the PP-g-MA3 copolymer-

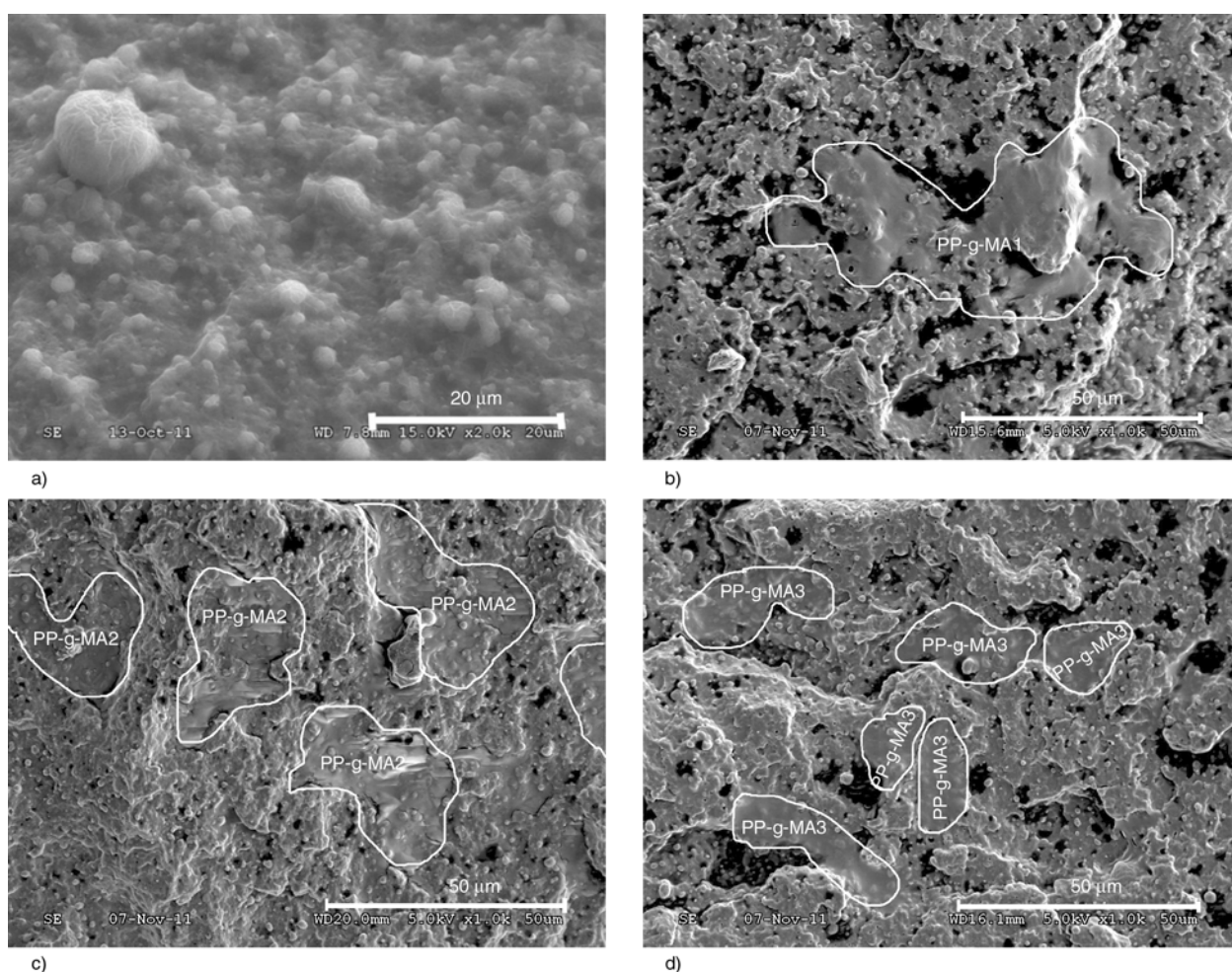


**Figure 3.** SEM images of cryo-fractured surfaces of (a) neat PP-g-starch; (b) 80/20 wt% PP-g-starch/PP-g-MA1; (c) 80/20 wt% PP-g-starch/PP-g-MA2; (d) 80/20 wt% PP-g-starch/PP-g-MA3

based compatibilizer (Figure 3d). These particle size differences may explain the difference of rheological behaviour of the blends observed previously, and especially the peculiar behaviour of PP-g-MA1 based blends (see 3.1.).

The average particle size in incompatible polymer blends may be predicted using the theory being developed by Wu (Equation (2)) [26]. The dispersed-drop size is the smaller when the interfacial tension is the lower and the components viscosity ratio is the closer to unity. Serpe *et al.* [31] further modified Wu's equation in order to take into account the influence of the dispersed phase concentration and the blend viscosity on blend morphology (Equation (3)):

$$D \approx \frac{4\sigma_{12}}{\dot{\gamma}\eta_{\text{blend}}} \left( \frac{\eta_{\text{disp}}}{\eta_{\text{cont}}} \right)^{\alpha} \quad (2)$$

$$D \approx \frac{\frac{4\sigma_{12}}{\dot{\gamma}\eta_{\text{blend}}} \left( \frac{\eta_{\text{disp}}}{\eta_{\text{blend}}} \right)^{\alpha}}{1 - (4 \cdot (\Phi_{\text{disp}} \cdot \Phi_{\text{cont}})^{0.8})} \quad (3)$$

where 'D' is the diameter of the droplet of dispersed phase,  $\sigma_{12}$  the interfacial tension between the two components of the blend at a temperature equal to the mixing temperature,  $\dot{\gamma}$  the shear rate during mixing,  $\eta_{\text{disp}}$  the dispersed phase viscosity,  $\eta_{\text{cont}}$  the continuous (matrix) phase viscosity,  $\eta_{\text{blend}}$  the blend viscosity, and  $\phi_{\text{disp}}$  and  $\phi_{\text{cont}}$  the volume fractions of dispersed and continuous matrix phases.  $\eta_{\text{disp}}/\eta_{\text{cont}}$  and  $\eta_{\text{disp}}/\eta_{\text{blend}}$  are named viscosity ratio and corrected viscosity ratio.  $\alpha$  is an experimental parameter, and has a value of nearly 0.84, which is positive if the corrected viscosity ratio is larger than one and negative if the viscosity ratio is smaller than one.

Dynamic viscosity measurements (Figure 4) show that the rheological behaviour of PP-g-MA3 com-

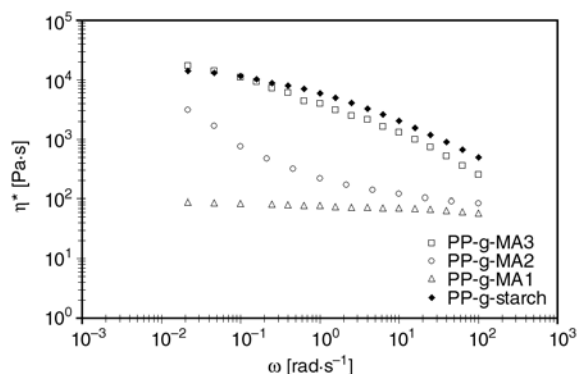


**Figure 4.** Dynamic rheological behaviour of the blend constituents

patibilizer is similar to that of neat PP-g-starch at the reference temperature (180°C) in the 0.01–100 rad·s<sup>-1</sup> frequency range. This means that the finest dispersed-droplet size is expected in that case. At the processing shear rate ( $\dot{\gamma}=120$  s<sup>-1</sup>), the blend viscosities of the two homopolymer compatibilizers (PP-g-MA1 and PP-g-MA2) are similar and lower than the PP-g-starch viscosity; the dispersed droplets should be larger. The theoretical particle sizes of the dispersed phase were calculated from the Serpe's model (Equation (3)) for each blend. They are around 2 to 4 μm for the 95/5 wt% PP-g-starch/PP-g-MA blends. The theoretical particle diameter of PP-g-MA1 is two times higher than that of the other compatibilizers, but the differences remains low in the considered shear rate range. When PP-g-MA content reaches 20 wt%, the theoretical particle diameter increases up to 7.5, 8.8 and 20 μm for PP-g-MA3, PP-g-MA2 and PP-g-MA1 compatibilizers respectively (Figure 5). The hierarchy previously obtained on the basis of representative SEM observations (25, 35 and 80 μm respectively) is confirmed. The differences between experimental and theoretical values may be explained by the fact that the interfacial tensions values used in computations were determined at room temperature and not at the mixing temperature for practical reasons (see 2.7.).

To summarize, even if major immiscibility of the compatibilizers used with PP-g-starch was not evidenced, the PP-g-MA3 copolymer compatibilizer gives the best results in terms of dispersed particle sizes and thus of miscibility thanks to its rheological behaviour close to that of the PP-g-starch matrix. The addition of PP-g-MA1 compatibilizer leading

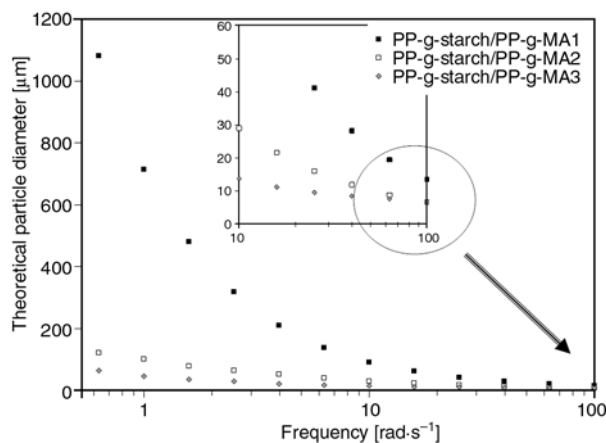


**Figure 5.** Calculated diameter of 20 wt% PP-g-MA dispersed phase in the PP-g-starch matrix as function of frequency

to lower miscibility (large dispersed particle size), further investigations will be carried out using PP-g-MA2 homopolymer-based and PP-g-MA3 copolymer-based compatibilizers.

#### 4. Reinforcement of starch-grafted polypropylene with nanoclay

In a second development step, nanoclay was added to the compatibilized starch-grafted polypropylene, aiming at forming ternary PP-g-starch/PP-g-MA/organoclay nanocomposites with improved mechanical properties. Dispersion, intercalation and exfoliation of nanoclay is a key factor to achieve this goal.

##### 4.1. Assessment of clay dispersion, intercalation and exfoliation in ternary PP-g-starch/PP-g-MA/clay hybrids

When assessing the structure of nanocomposites, the main issue is to get a representative evaluation of the filler dispersion degree at a relevant scale. Microscopy is widely used but provides local and qualitative assessment only. Alternatively, dynamic (oscillatory) rheology may provide a semi-quantitative evaluation of the dispersion degree of nanofillers such as carbon nanotubes or layered silicates (montmorillonite among others) in the bulk [8, 18, 32–35]. Also, X-ray diffraction (XRD) analysis allows quantifying the intercalation in the bulk by measuring the clay platelets interlayer distance [35].

##### *Influence of clay organo-modification*

Transmission Electron Microscopy (TEM) shows that, whatever the material formulation, clay is locally well dispersed (see for example Figure 6a and 6c for 5PP-g-MA3 C30B and 5PP-g-MA2 C20A references respectively). The presence of clay tactoids and several individual clay platelets indicates an intercalated structure with partial exfoliation (Figure 6b and 6d). No significant difference is visible at this local scale between the different materials. As a consequence, rotational rheology and XRD were used in this section to further investigate the effect of the clay surfactant and PP-g-MA compatibilizer on nanoclay dispersion, intercalation and exfoliation and to get a more global assessment.

The dynamic rheological analysis (Figure 7) does not reveal any major difference between the two organo-modified polar (C30B) and non-polar (C20A) clays whatever the PP-g-MA compatibilizer

type, the secondary plateau of storage modulus tending to appear in both cases. Nevertheless, compared to its non-polar counterpart, the polar organo-modified clay (C30B) has a higher storage modulus and a slightly lower terminal slope in the low frequency domain, which suggests a better clay dispersion degree, intercalation and/or exfoliation in that case. Actually, it is well admitted that the exfoliated and/or disordered intercalated silicate layers form a network type structure rendering the system highly elastic as revealed by the appearance of a secondary plateau for the dynamic storage modulus ( $G'$ ) in the low frequency regime (i.e. frequency independent behaviour at the lower frequencies) or at least a lower terminal slope in  $G'$  vs. frequency ( $\omega$ ) plot. This gradual change of the behaviour from liquid-like to solid-like is mainly correlated to the extent of dispersion and distribution of the nanofillers that form a three-dimensional percolating network.

Based on XRD analysis (Figure 8), the space gallery was determined using the Bragg law for the organoclays and the blends containing nanoclay. A decrease in the degree of coherent layer stacking (i.e. a more disordered system) of the clay would lead to a peak broadening and an intensity decrease in the XRD diffractogram. The primary ( $d_{001}$ ) diffraction peaks of neat C20A and C30B are located around  $2\theta = 4$  and  $5.4^\circ$  respectively, which gives interlayer spacing (d-spacing) of 1.55 and 0.81 nm respectively. Upon addition of C20A clays into PP-g-starch/PP-g-MA blend, the XRD peak shifts to lower angles around  $2\theta = 2.56^\circ$  (or even vanishes tending to form a shoulder in case of PP-g-MA3) indicating an increase in interlayer spacing due to polymer intercalation within clay platelets (confirmed by TEM imaging, Figure 6d). The average distance between the platelets then becomes about 2.99 nm instead of 1.55 nm before intercalation. In the case of the C30B-based blends, the absence of the signal in the XRD pattern tends to suggest the existence of clay platelets exfoliation.

The maleic anhydride of the PP-g-MA compatibilizer can interact with both the polar organo-modified clay (C30B) and the starch phase of the matrix according to the chemical reactions presented in Figure 9. The C30B surfactant has two hydroxyl groups ( $-\text{OH}$ ) that can react with the PP-g-MA anhydride ( $-\text{CO}-\text{O}-\text{CO}-$ ) to give an ester ( $-\text{COO}-$ ) and an acid ( $-\text{COOH}$ ) (Figure 9a and 9b). The acid

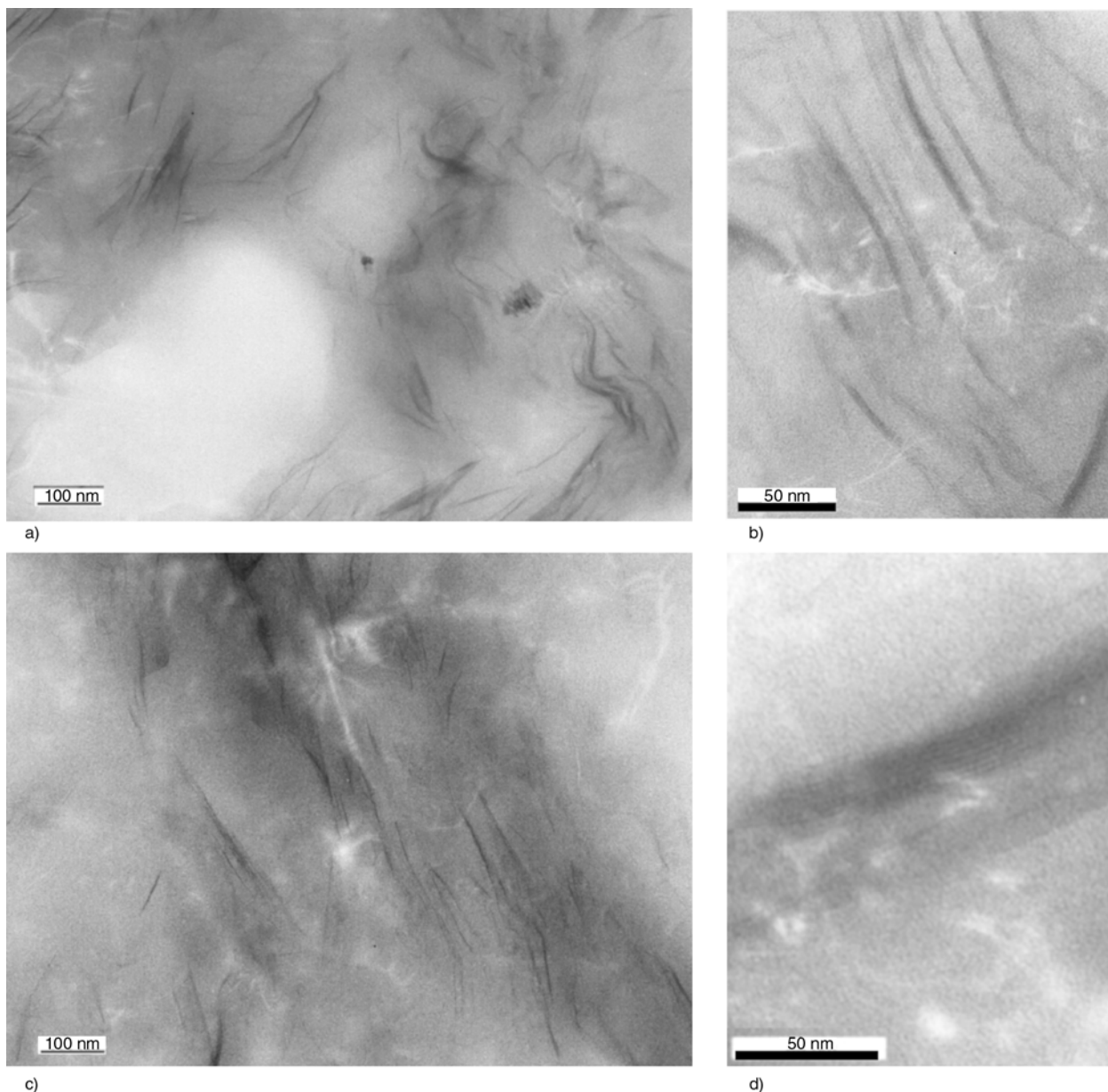


**Figure 6.** TEM images of PP-g-starch/PP-g-MA/organoclay hybrids. (a, b) 5PP-g-MA3 C30B, (c, d) 5PP-g-MA2 C20A, at lower (a, c) and higher (b, d) magnifications

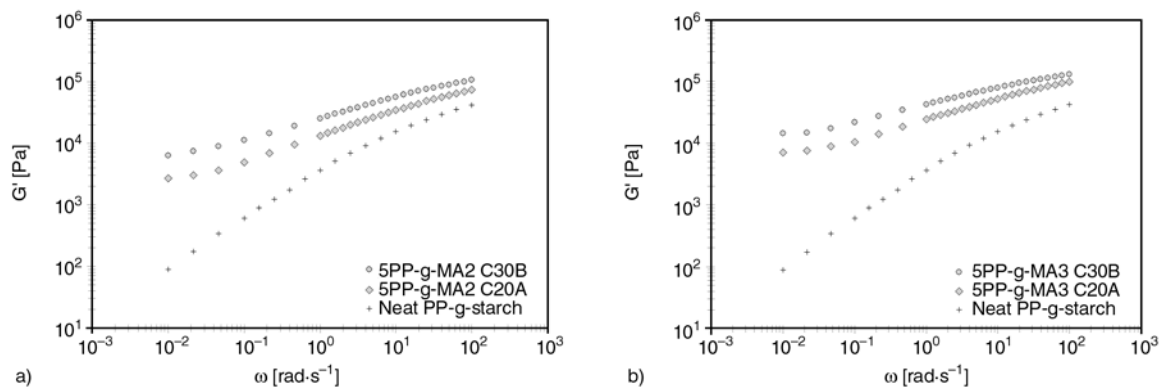


**Figure 7.** Influence of MA-grafting level of PP-g-MA (1 wt% for PP-g-MA2 and 1.4 wt% for PP-g-MA3) on storage modulus of PP-g-starch/5 wt%PP-g-MA/organoclay hybrids for different organoclays: (a) C30B ; (b) C20A



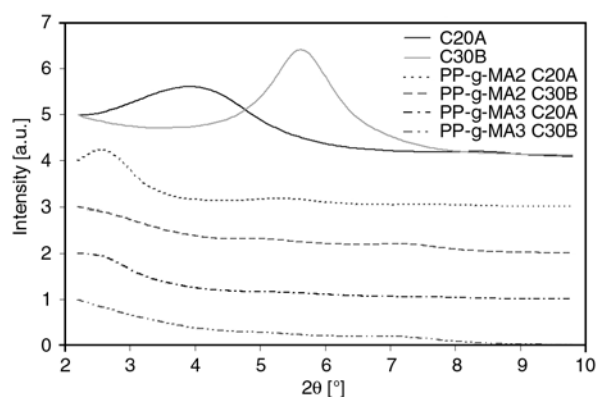


**Figure 8.** Influence of clay organo-modification (C20A or C30B) on X-ray diffraction patterns of PP-g-starch/5 wt% PP-g-MA/organoclay hybrids for different PP-g-MA

group can then react with the second hydroxyl of the surfactant (or coming from another part of the surfactant) to form a second ester and a water molecule (Figure 9c). On the other hand, maleic anhydride can react with the numerous hydroxyl groups of the starch which is mainly constituted of amylose and amylopectine. All these chemical reactions favour the formation of a surfactant/PP-g-MA/starch network making the platelet separation, intercalation and exfoliation (at least partially) possible and therefore increasing the dynamic storage modulus. In the case of the non-polar organo-modified clay (C20A), the long alkyl chains of the surfactant intercalate the platelets to form a paraffin film facilitating the exfoliation, as suggested by Alexandre and Dubois [36]. This is supported by the fact that, as mentioned above, the initial inter-platelet distance of this non-polar modified montmorillonite (C20A) is higher than that of its polar modified counterpart (C30B) (1.55 nm against 0.81 nm). In case of C20A,

the exfoliation mechanism is more mechanically driven (by polypropylene chain insertion) than chemically driven.

Globally, whatever the PP-g-MA compatibilizer, the addition of polar organoclay (C30B) seems to be preferable rather than non-polar organoclay (C20A) as the former allows achieving better clay dispersion degree and exfoliation level and therefore higher dynamic storage modulus.

#### *Influence of PP-g-MA content and MA-grafting level*

Increasing the MA-grafting level of PP-g-MA from 1 wt% (PP-g-MA2) to 1.4 wt% (PP-g-MA3) increases the storage modulus and slightly decreases the terminal slope in the low frequency domain (Figure 10), apparently slightly more for C20A than for C30B organoclay. This suggests that PP-g-MA3 has a better ability to promote clay intercalation and partial exfoliation of the non-polar organoclay (C20A) that is confirmed by XRD analysis (vanishing of the C20A residual peak, shoulder appearing at low angles, Figure 8). As PP-g-MA2 and PP-g-MA3 have similar molecular weights (89 000 and 88700 g·mol<sup>-1</sup> respectively), a higher molecular mobility and lower rigidity of the PP-g-MA3 maleated ethylene-propylene copolymer (compared to the maleated homopolymer PP-g-MA2) due to the 52 wt% ethylene content in the copolymer, may also contribute to explain this better efficiency.

Increasing the PP-g-MA compatibilizer weight content from 5 to 20 wt% is either not significant (in the case of PP-g-MA2) or detrimental (in the case of PP-g-MA3) (Figure 11). In particular for C20A, the storage modulus drops by nearly a decade when

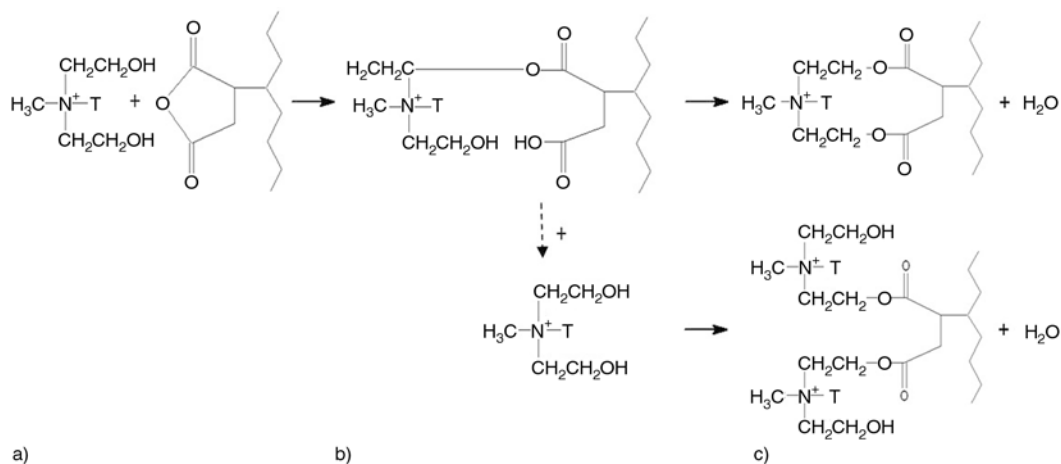


**Figure 9.** Expected chemical reactions of C30B polar organo-modified clay and PP-g-MA compatibilizer (a) to form an ester and acid groups (b); final ester chemical structure (c)

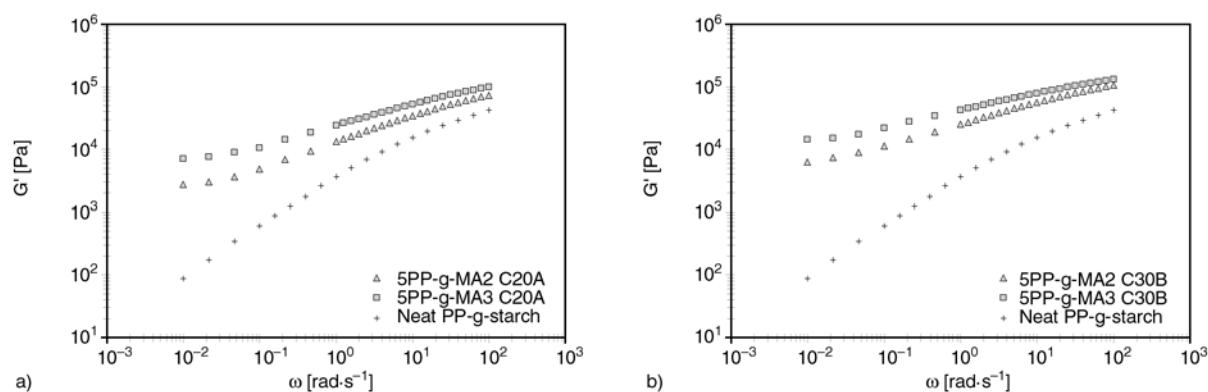


**Figure 10.** Influence of MA-grafting level of PP-g-MA (1 wt% for PP-g-MA2 and 1.4 wt% for PP-g-MA3) on storage modulus of PP-g-starch/5 wt %PP-g-MA/organoclay hybrids for different organoclays: (a) C30B; (b) C20A

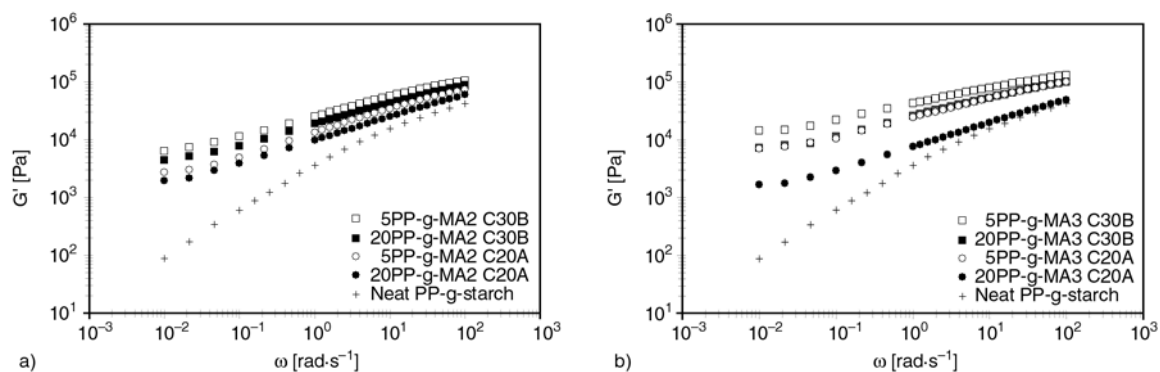


**Figure 11.** Influence of PP-g-MA content (5 or 20 wt%) on storage modulus of PP-g-starch/PP-g-MA/organoclay hybrids for different organoclays (C30B or C20A) and PP-g-MA types: (a) PP-g-MA2; (b) PP-g-MA3

the PP-g-MA3 content is multiplied by 4. This may be ascribed to the lower modulus of the PP-g-MA based on ethylene-propylene copolymer. The XRD patterns do not show any significant differences when PP-g-MA weight content increases (therefore not reported here).

To summarize, adding at moderate weight content (5 wt%) an ethylene-propylene copolymer-based PP-g-MA compatibilizer having high MA-grafting level and a polar modified montmorillonite (C30B) seems to be the most desirable combination to optimize the clay dispersion, intercalation and exfoliation in PP-g-starch/PP-g-MA/organoclay hybrids.

#### 4.2. Mechanical properties of ternary PP-g-starch/PP-g-MA/clay hybrids

The tensile mechanical properties of the ternary PP-g-starch/PP-g-MA/organoclay hybrids were determined and are plotted as a function of the maleic anhydride fraction in the total PP phase (i.e. PP contained in both PP-g-starch and PP-g-MA) in Figures 12 (Young’s modulus), 13 (yield stress), 14 (strength, i.e. stress at break) and 15 (elongation at

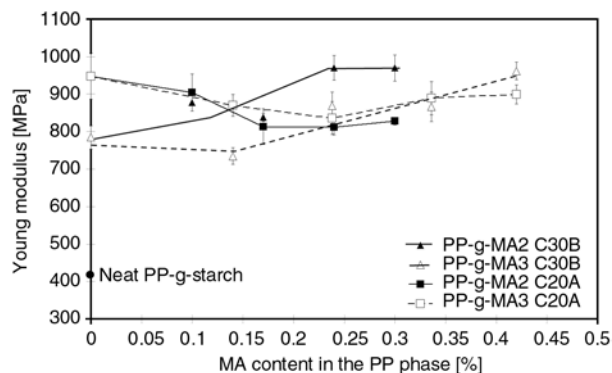


**Figure 12.** Influence of clay organo-modification (C20A or C30B) and PP-g-MA compatibilizer on nanocomposites Young’s modulus

break). The weight content of the added PP-g-MA is therefore taken into account in an implicit manner. Addition of 3.5 wt% of mineral (neat mineral corresponding to 5 wt% organoclay) into PP-g-starch clearly increases its tensile modulus (Figure 12) by 100 or 130% depending on the organoclay type (polar organo-modified C30B or non-polar organo-modified C20A, respectively). However, addition of polar PP-g-MA compatibilizer induces opposite

effects depending on the clay surfactant polarity. Whereas the modulus increases (up to +20%) as a function of MA fraction for polar C30B-based compounds, it decreases (up to –15%) for non-polar C20A-based compounds. These results confirm that clay platelets intercalation is mechanically-driven in the case of CA20 (no possible chemical reactions) and chemically-driven in the case of C30B (existence of chemical reactions between the maleic anhydride of PP-g-MA and the hydroxyl groups of the surfactant).

Similarly, addition of nanoclay into PP-g-starch increases its tensile yield stress (Figure 13) by 10 or 15%, depending on the organoclay type (polar organo-modified C30B or non-polar organo-modified C20A, respectively). Besides, the yield stress further increases significantly (up to +15%) as a function of the MA fraction increase for both organoclay types.

The effect of nanoclay addition on ultimate properties is quite different and strongly depends on clay organo-modification type. Addition of 3.5 wt% of mineral into PP-g-starch changes its strength (Fig-

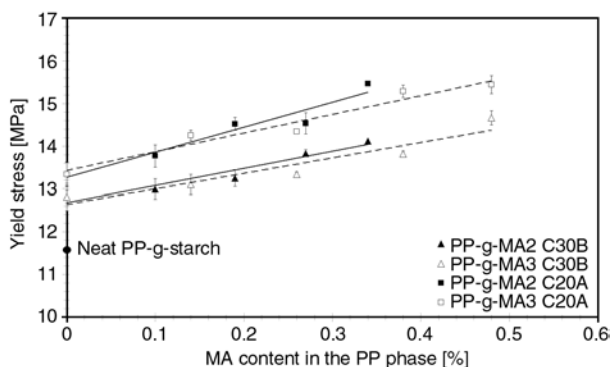


**Figure 13.** Influence of clay organo-modification (C20A or C30B) and PP-g-MA compatibilizer on nanocomposites yield stress

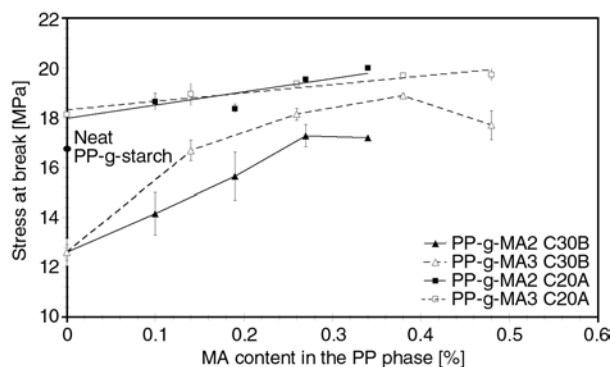


**Figure 14.** Influence of clay organo-modification (C20A or C30B) and PP-g-MA compatibilizer on nanocomposites strength (stress at break)

ure 14) in a manner being either detrimental or favourable, by –25 or +6.5%, depending on the organoclay type (polar organo-modified C30B or non-polar organo-modified C20A, respectively). As for the strength, addition of compatibilizer at growing MA level then increases the strength significantly: moderately for C20A-based materials (up to +10%) and very importantly for C30B-based materials (up to +36 or even +48% depending on the compatibilizer type, possibly above the initial value of neat PP-g-starch for PP-g-MA3).

As expected, the elongation at break is also affected (Figure 15). Adding 3.5 wt% of mineral has almost no effect on PP-g-starch ductility (elongation at break decreases by –10% only) for C20A, whereas it strongly reduces deformation ability (elongation at break drops by –40%, from about 600% to less than 375%) for C30B due to the presence of clay aggregates in the sample. In this latter case, addition of PP-g-MA compatibilizers makes it possible to limit to [–20%;–10%] or even to nearly avoid (case of PP-g-MA3) the loss of ductility.

Such an increase in tensile yield stress and strength may be ascribed to improved matrix/clay interfacial interactions [10], better miscibility between PP-g-MA and PP-g-starch macromolecules and improved interfacial affinity between polymer phases brought by clays surfactant (well known double role of clay acting as structural reinforcement and compatibilizer in polymer blends [19–23] as shown by Yousfi *et al.* [24]).

The efficiency differences in term of usage properties improvement observed between non-polar C20A and polar C30B organoclays, the former having affinity with PP phase and the latter with the starch phase of PP-g-starch matrix [11, 12], may be

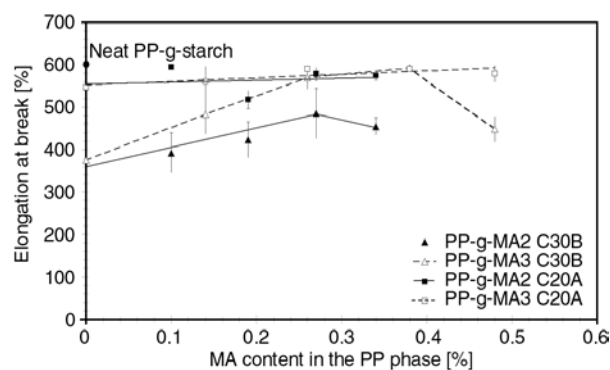


**Figure 15.** Influence of clay organo-modification (C20A or C30B) and PP-g-MA compatibilizer on nanocomposites elongation at break

explained considering the chemical composition and structure of PP-g-starch. The long PP chain mobility may be assumed being higher than that of grafted starch chains because of steric hindrance issues. Moreover, considering the PP/starch weight ratio within PP-g-starch (48% PP and 52% starch) and the respective molecular masses of PP ( $42.08 \text{ g}\cdot\text{mol}^{-1}$ ) and starch ( $162 \text{ g}\cdot\text{mol}^{-1}$ ) repeating units, the molar ratio is 1/0.28. When the material is subjected to tensile loading, the PP segments predominantly sustain stresses and strains whereas grafted starch segments follow this main skeleton chain movement and mostly undergo shear and compression. Considering C20A/PP and C30B/starch above-mentioned affinities, it makes sense to suppose that the non-polar modified clay (C20A) is preferentially dispersed in the PP phase whereas the polar modified clay (C30B) is mainly dispersed in the starch polar phase. Despite better exfoliation obtained with C30B clay within the starch phase, previously evidenced by XRD and dynamic rheology, C20A intercalated clay efficiently reinforces the phase (PP) governing the PP-g-starch deformation, damage and fracture mechanisms under tensile loading.

As a consequence, whatever the PP-g-MA compatibilizer (PP-g-MA2 or PP-g-MA3), the addition of non-polar organoclay (C20A) is preferably recommended rather than polar organoclay (C30B) to achieve higher tensile properties (modulus, yield stress, strength) without significant loss of ductility in PP-g-starch/PP-g-MA/organoclay hybrids.

## 5. Conclusions

Novel nanocomposites based on durable, 52 wt% plant-based, starch-grafted polypropylene (PP-g-starch) and organo-modified montmorillonite compatibilized with polypropylene-grafted-maleic anhydride (PP-g-MA) were successfully prepared by melt-compounding in a co-rotating twin-screw extruder. Two types of organoclay (same montmorillonite with different surfactants) were considered: Cloisite<sup>®</sup>30B having affinity with the starch phase due to its polar functional groups, and Cloisite<sup>®</sup>20A having affinity with the polypropylene phase of the polymer matrix due to its non-polar groups. Homopolymer or copolymer-based

PP-g-MA with different molecular weights and different maleic anhydride (MA) grafting levels was added at different weight contents as compatibilizer to improve clay dispersion.

Whatever the formulation, no significant immiscibility of PP-g-starch/PP-g-MA blends is evidenced. The best miscibility is however observed for low content of the ethylene-propylene copolymer-based PP-g-MA, which combines the lowest molecular weight and the highest MA-grafting level, and has a rheological behaviour (viscosity) close to that of PP-g-starch.

Regarding clay dispersion, adding a low content of ethylene-propylene copolymer-based PP-g-MA compatibilizer having a high MA-grafting level, and a polar organoclay (Cloisite<sup>®</sup>30B) is the most desirable combination to optimize clay intercalation and exfoliation in PP-g-starch. Nevertheless, regarding the reinforcement effect (i.e. improvement of tensile properties), the addition of non-polar organoclay (Cloisite<sup>®</sup>20A) is preferably recommended to reach higher tensile properties (modulus, yield stress, strength) without significant loss of ductility. Considering the PP/starch molar ratio (1:0.28), PP/Cloisite<sup>®</sup>20A affinity is expected to promote preferential dispersion of clay within the dominant PP phase, which governs the overall mechanical behaviour in tension, whereas Cloisite<sup>®</sup>30B is assumed being mainly dispersed within the starch phase with less or no benefit on the tensile behaviour.

## Acknowledgements

This work was carried out in the frame of the 'MATORIA' project dedicated to development of new materials from renewable resources for the automotive industry. The authors are indebted to the French Ministry of Economy, Finance and Industry, DGCIS Department, for its financial support (Contract n°08 2 90 6249). Thanks are also due to ROQUETTE Frères (France) for kindly supplying starch-grafted polypropylene (Gaialene<sup>®</sup>), to ISPA for the interfacial tension measurements, and to PSA Peugeot Citroen (France), leader of the MATORIA project, for TEM imaging. The authors also gratefully acknowledge the support and contribution of CISIT (International Campus on Safety and Intermodality in Transportation), the Nord-Pas-de-Calais Region and the European Community (FEDER, European Funds for Regional Development) for funding of the twin-screw extruder.

## References

- [1] Rusu D., Boyer S. A. E., Lacrampe M-F., Krawczak P.: Bioplastics and vegetal fiber reinforced bioplastics for automotive applications. in ‘Handbook of bioplastics and biocomposites engineering applications’ (Ed.: Srikanth Pilla) 397–448, Wiley, New York (2011). DOI: [10.1002/9781118203699.ch15](https://doi.org/10.1002/9781118203699.ch15)
- [2] Corpart J. M.: ROQUETTE, Gaïalene<sup>®</sup>. in ‘International business directory for innovative bio-based plastics and composites’ (eds.: Carus M., Thielen M.) 66–67, Nova-Institute GmbH and Bioplastics Magazine, Hürth (2011).
- [3] Soulestin J., Prashantha K., Lacrampe M. F., Krawczak P.: Bioplastics based nanocomposites for packaging applications. in ‘Handbook of bioplastics and biocomposites engineering applications’ (ed.: Srikanth Pilla), 77–120, Wiley, New York (2011). DOI: [10.1002/9781118203699.ch4](https://doi.org/10.1002/9781118203699.ch4)
- [4] Chen B., Evans J. R. G.: Thermoplastic starch–clay nanocomposites and their characteristics. *Carbohydrate Polymers*, **61**, 455–463 (2005). DOI: [10.1016/j.carbpol.2005.06.020](https://doi.org/10.1016/j.carbpol.2005.06.020)
- [5] Park H-M., Li X., Jin C-Z., Park C-Y., Cho W-J., Ha C-S.: Preparation and properties of biodegradable thermoplastic starch/clay hybrids. *Macromolecular Materials and Engineering*, **287**, 553–558 (2002). DOI: [10.1002/1439-2054\(20020801\)287:8<553::AID-MAME553>3.0.CO;2-3](https://doi.org/10.1002/1439-2054(20020801)287:8<553::AID-MAME553>3.0.CO;2-3)
- [6] Park H-M., Lee W-K., Park C-Y., Cho W-J., Ha C-S.: Environmentally friendly polymer hybrids. Part I: Mechanical, thermal, and barrier properties of thermoplastic starch/clay nanocomposites. *Journal of Materials Science*, **38**, 909–915 (2003). DOI: [10.1023/A:1022308705231](https://doi.org/10.1023/A:1022308705231)
- [7] Aloui M., Soulestin J., Lacrampe M-F., Krawczak P., Rousseaux D., Marchand-Brynaert J., Devaux J., Quiévy N., Sclavons M.: A new elaboration concept of polypropylene/unmodified montmorillonite nanocomposites by reactive extrusion based on direct injection of polypropylene aqueous suspensions. *Polymer Engineering and Science*, **49**, 2276–2285 (2009). DOI: [10.1002/pen.21474](https://doi.org/10.1002/pen.21474)
- [8] Rajesh J. J., Soulestin J., Lacrampe M. F., Krawczak P.: Effect of injection molding parameters on nanofillers dispersion in masterbatch based PP-clay nanocomposites. *Express Polymer Letters*, **6**, 237–248 (2012). DOI: [10.3144/expresspolymlett.2012.26](https://doi.org/10.3144/expresspolymlett.2012.26)
- [9] Sharma S. K., Nema A. K., Nayak S. K.: Polypropylene nanocomposite film: A critical evaluation on the effect of nanoclay on the mechanical, thermal, and morphological behavior. *Journal of Applied Polymer Science*, **115**, 3463–3473 (2009). DOI: [10.1002/app.30883](https://doi.org/10.1002/app.30883)
- [10] Dubnikova I. L., Berezina S. M., Korolev Y. M., Kim G-M., Lomakin S. M.: Morphology, deformation behavior and thermomechanical properties of polypropylene/maleic anhydride grafted polypropylene/layered silicate nanocomposites. *Journal of Applied Polymer Science*, **105**, 3836–3850 (2007). DOI: [10.1002/app.26665](https://doi.org/10.1002/app.26665)
- [11] López-Quintanilla M. L., Sánchez-Valdés S., Ramos de Valle L. F., Medellín-Rodríguez F. J.: Effect of some compatibilizing agents on clay dispersion of polypropylene-clay nanocomposites. *Journal of Applied Polymer Science*, **100**, 4748–4756 (2006). DOI: [10.1002/app.23262](https://doi.org/10.1002/app.23262)
- [12] López-Quintanilla M. L., Sánchez-Valdés S., Ramos de Valle L. F., Guedea Miranda R.: Preparation and mechanical properties of PP/PP-g-MA/Org-MMT nanocomposites with different MA content. *Polymer Bulletin*, **57**, 385–393 (2006). DOI: [10.1007/s00289-006-0555-x](https://doi.org/10.1007/s00289-006-0555-x)
- [13] Svoboda P., Zeng C., Wang H., Lee L. J., Tomasko D. L.: Morphology and mechanical properties of polypropylene/organoclay nanocomposites. *Journal of Applied Polymer Science*, **85**, 1562–1570 (2002). DOI: [10.1002/app.10789](https://doi.org/10.1002/app.10789)
- [14] Hong C. H., Lee Y. B., Bae J. W., Jho J. Y., Nam B. U. K., Hwang T. W.: Molecular weight effect of compatibilizer on mechanical properties in polypropylene/clay nanocomposites. *Journal of Industrial Engineering Chemistry*, **11**, 293–296 (2005).
- [15] Wang Y., Chen F-B., Wu K-C.: Twin-screw extrusion compounding of polypropylene/organoclay nanocomposites modified by maleated polypropylenes. *Journal of Applied Polymer Science*, **93**, 100–112 (2004). DOI: [10.1002/app.20407](https://doi.org/10.1002/app.20407)
- [16] Wang Y., Chen F. B., Li Y-C., Wu K-C.: Melt processing of polypropylene/clay nanocomposites modified with maleated polypropylene compatibilizers. *Composites Part B: Engineering*, **35**, 111–124 (2004). DOI: [10.1016/S1359-8368\(03\)00049-0](https://doi.org/10.1016/S1359-8368(03)00049-0)
- [17] Hasegawa N., Kawasumi M., Kato M., Usuki A., Okada A.: Preparation and mechanical properties of polypropylene-clay hybrids using a maleic anhydride-modified polypropylene oligomer. *Journal of Applied Polymer Science*, **67**, 87–92 (1998). DOI: [10.1002/\(SICI\)1097-4628\(19980103\)67:1<87::AID-APP10>3.3.CO;2-9](https://doi.org/10.1002/(SICI)1097-4628(19980103)67:1<87::AID-APP10>3.3.CO;2-9)
- [18] Prashantha K., Soulestin J., Lacrampe M. F., Claes M., Dupin G., Krawczak P.: Multi-walled carbon nanotube filled polypropylene nanocomposites based on masterbatch route: Improvement of dispersion and mechanical properties through PP-g-MA addition. *Express Polymer Letters*, **2**, 735–745 (2008). DOI: [10.3144/expresspolymlett.2008.87](https://doi.org/10.3144/expresspolymlett.2008.87)

- [19] Ray S. S., Pouliot S., Bousmina M., Utracki L. A.: Role of organically modified layered silicate as an active interfacial modifier in immiscible polystyrene/polypropylene blends. *Polymer*, **45**, 8403–8413 (2004). DOI: [10.1016/j.polymer.2004.10.009](https://doi.org/10.1016/j.polymer.2004.10.009)
- [20] Ray S. S., Bousmina M.: Compatibilization efficiency of organoclay in an immiscible polycarbonate/poly(methyl methacrylate) blend. *Macromolecular Rapid Communications*, **26**, 450–455 (2005). DOI: [10.1002/marc.200400586](https://doi.org/10.1002/marc.200400586)
- [21] Ray S. S., Bousmina M.: Effect of organic modification on the compatibilization efficiency of clay in an immiscible polymer blend. *Macromolecular Rapid Communications*, **26**, 1639–1646 (2005). DOI: [10.1002/marc.200500447](https://doi.org/10.1002/marc.200500447)
- [22] Calcagno C. I. W., Mariani C. M., Teixeira S. R., Mauler R. S.: The role of the MMT on the morphology and mechanical properties of the PP/PET blends. *Composites Science and Technology*, **68**, 2193–2200 (2008). DOI: [10.1016/j.compscitech.2008.03.012](https://doi.org/10.1016/j.compscitech.2008.03.012)
- [23] Kusmono, Mohd Ishak Z. A., Chow W. S., Takeichi T., Rochmadi: Influence of SEBS-g-MA on morphology, mechanical, and thermal properties of PA6/PP/organoclay nanocomposites. *European Polymer Journal*, **44**, 1023–1039 (2008). DOI: [10.1016/j.eurpolymj.2008.01.019](https://doi.org/10.1016/j.eurpolymj.2008.01.019)
- [24] Yousfi M., Soulestin J., Vergnes B., Lacrampe M-F., Krawczak P.: Compatibilization of immiscible polymer blends by organoclay: Effect of nanofiller or organo-modifier? *Macromolecular Materials and Engineering*, in press (2012). DOI: [10.1002/mame.201200138](https://doi.org/10.1002/mame.201200138)
- [25] Owens D. K., Wendt R. C.: Estimation of the surface free energy of polymers. *Journal of Applied Polymer Science*, **13**, 1741–1747 (1969). DOI: [10.1002/app.1969.070130815](https://doi.org/10.1002/app.1969.070130815)
- [26] Wu S.: Formation of dispersed phase in incompatible polymer blends: Interfacial and rheological effects. *Polymer Engineering and Science*, **27**, 335–343 (1987). DOI: [10.1002/pen.760270506](https://doi.org/10.1002/pen.760270506)
- [27] Wu S.: Interfacial and surface tensions of polymers melts and liquids. in ‘Polymer interface and adhesion’ (ed.: Wu S.) Marcel Dekker, New York, 67–132 (1982).
- [28] Yu W., Li R., Zhou C.: Rheology and phase separation of polymer blends with weak dynamic asymmetry. *Polymer*, **52**, 2693–2700 (2011). DOI: [10.1016/j.polymer.2011.04.024](https://doi.org/10.1016/j.polymer.2011.04.024)
- [29] Bai L., Li Y-M., Yang W., Yang M-B.: Rheological behavior and mechanical properties of high-density polyethylene blends with different molecular weights. *Journal of Applied Polymer Science*, **118**, 1356–1363 (2010). DOI: [10.1002/app.32329](https://doi.org/10.1002/app.32329)
- [30] Schwarzl F., Staverman A. J.: Time-temperature dependence of linear viscoelastic behavior. *Journal of Applied Physics*, **23**, 838–843 (1952). DOI: [10.1063/1.1702316](https://doi.org/10.1063/1.1702316)
- [31] Serpe G., Jarrin J., Dawans F.: Morphology-processing relationships in polyethylene-polyamide blends. *Polymer Engineering and Science*, **30**, 553–565 (1990). DOI: [10.1002/pen.760300908](https://doi.org/10.1002/pen.760300908)
- [32] Dorigato A., Pegoretti A., Penati A.: Linear low-density polyethylene/silica micro- and nanocomposites: Dynamic rheological measurements and modelling. *Express Polymer Letters*, **4**, 115–129 (2010). DOI: [10.3144/expresspolymlett.2010.16](https://doi.org/10.3144/expresspolymlett.2010.16)
- [33] Prashantha K., Soulestin J., Lacrampe M. F., Krawczak P., Dupin G., Claes M.: Masterbatch-based multi-walled carbon nanotube filled polypropylene nanocomposites: Assessment of rheological and mechanical properties. *Composites Science and Technology*, **69**, 1756–1763 (2009). DOI: [10.1016/j.compscitech.2008.10.005](https://doi.org/10.1016/j.compscitech.2008.10.005)
- [34] Soulestin J., Rashmi B. J., Bourbigot S., Lacrampe M-F., Krawczak P.: Mechanical and optical properties of polyamide 6/clay nanocomposite cast films: Influence of the degree of exfoliation. *Macromolecular Materials and Engineering*, **297**, 444–454 (2012). DOI: [10.1002/mame.201100202](https://doi.org/10.1002/mame.201100202)
- [35] Touchaleaume F., Soulestin J., Sclavons M., Devaux J., Cordenier F., Van Velthem P., Flat J. J., Lacrampe M. F., Krawczak P.: Efficient one-step melt-compounding of copolyetheramide/pristine clay nanocomposites using water-injection as intercalating/exfoliating aid. *Express Polymer Letters*, **5**, 1085–1101 (2011). DOI: [10.3144/expresspolymlett.2011.106](https://doi.org/10.3144/expresspolymlett.2011.106)
- [36] Alexandre M., Dubois P.: Polymer-layered silicate nanocomposites: Preparation, properties and uses of a new class of materials. *Materials Science and Engineering R: Reports*, **28**, 1–63 (2000). DOI: [10.1016/S0927-796X\(00\)00012-7](https://doi.org/10.1016/S0927-796X(00)00012-7)